

University of
Strathclyde
Engineering

DESIGN CONSIDERATIONS FOR LIGHT WEIGHT MECHANICAL
PARTS

ENGD THESIS

Space Mechatronic Systems Technology Laboratory
Design, Manufacture and Engineering Management
University of Strathclyde, Glasgow

30th October, 2021

Thomas Alistair Michael
MCMMASTER

Registration Number: 201473964

thomas.mcmaster@strath.ac.uk

Declaration of Academic Honesty

This thesis is the result of the author's original research. It has been composed by the author and has not previously been submitted for examination which has led to the award of a degree.

Signed

Dated

Declaration of Author's Rights

The copyright of this thesis belongs to the author under the terms of the United Kingdom Copyright Acts as qualified by the University of Strathclyde Regulation 3.51. Due acknowledgement must always be made of the use of any material contained in, or derived from, this thesis.

Acknowledgements

To Richard Wright, for sparking my imagination in engineering.

To Graham Ross, Malcolm Ritchie and Archie Morton, who kept that spark going.

To my entire family, for my upbringing, enduring love, support and encouragement.

To my fellow students, especially Andrew Campbell and Andreas Reimer, for their assistance, suggestions and companionship.

To Dorothy and Xiu, for giving me the opportunity to study the EngD and the advice and support throughout it.

To Tiffany, whose support, kind words and love kept me going when I was going through low points - terima kasih.

Published Papers

The author has published three papers during the course of the PhD:

1. McMaster, Thomas and Yan, Xiu. Oct. 2017. The design of a robotic arm link using functionally graded materials: A case study. 68th International Astronautical Congress, Adelaide, Australia.
2. McMaster, Thomas and Yan, Xiu. Oct. 2017. A methodology for design of lightweight robotic arm links in harsh environments. 68th International Astronautical Congress, Adelaide, Australia.
3. McMaster, Thomas and Yan, Xiu. Sept. 2018. Development of a heat flow code to simulate production of a functionally graded material robotic gripper using the additive manufacture process. 16th Mechatronics Forum International Conference, Glasgow, United Kingdom.

Abstract

Context and Background Lightweight design is important for many engineering fields due to the increased energy efficiency and process performance that it can result in. Functionally graded materials (FGMs) give a key contribution to lightweight design when low mass along with a **gradual** change in a second primary constraint is required, such as alleviation of a large temperature gradient. With the evolution of additive manufacturing (AM), FGM use for light weighting is rising in practicality. Therefore, research into combining FGMs with AM is required, and should include topics relevant to these, including form, material choice and structural design. The work is tested on robotic arm links due to the ever-increasing adoption of automation, and the practical accessibility of them for the researcher.

Aim of Research The aim of the research is to investigate the mass reduction of robotic arm links by merging second moment of area calculations, structured cells, topology optimisation, functionally graded materials and additive manufacture in various combinations.

Key Work The main output of this work is a set of design guidelines that have been written to assist engineers with combining FGMs, topology optimisation, structured cells and high-level AM restrictions. Within the field of lightweight design, the guidelines are use-case agnostic. The design guidelines have been trialled using test cases, each aimed at individual elements of the guidelines. The objective of the first test case is to discover if FGMs will reduce stresses in parts constructed of dissimilar materials when used in conjunction with high-level AM constraints. The second test case trails the various computational testing sections required in the guidelines, including part sectioning rules and material distribution techniques. The third test case incorporates heat flow simulation during AM deposition of the FGMs, including the three heat transfer mechanisms and interaction with the print bed of AM hardware. The final test case assesses the entirety of the design guidelines, re-examining the aspects tested in the second and third test cases, together with a technique to decide whether structured cells or topology optimisation should be used based on the use case of the part, and a first pass at inspecting the residual stresses in the additively manufactured part once it has cooled.

Conclusions Overall, the use of FGMs along with lightweight structural design techniques and high level AM restrictions are computationally-successful at reducing the mass in robotic arm links. While the design guidelines are use case agnostic, they

make most sense used in fields of engineering that have a substantial requirement for light weight design, such as aerospace and space. Ideally, physical testing would have been used to increase validity of the design guidelines. Unfortunately, funds were not available, and thus it physical testing is deemed the next step for this work in the future.

Nomenclature

Material Properties

ϕ_B^e	Bending factor
ρ	Density
σ_{ave}	Average stress
σ_{max}	Maximum stress
σ_f	Material yield strength
E	Young's modulus
I	Second moment of area
L	Length
m	mass
K_t	Stress concentration factor

Acronyms

ABS	Acrylonitrile Butadiene Styrene
ALM	Additive Layer Manufacture
AM	Additive Manufacture
AMS	Adaptive Meshing Strategy
BCC	Body Centred Cubic
BESO	Bi-Directional Evolutionary Structural Optimisation
CAD	Computer Aided Drawing
CF	Carbon Fibre
CFRP	Carbon Fibre Reinforced Polymer
CVD	Chemical Vapour Deposition
DED	Direct Energy Deposition
DMLS	Direct Metal Laser Sintering

EBM Electron Beam Melting
EPD Electrophoretic Deposition
ESO Evolutionary Structural Optimisation
FDM Fused Deposition Modelling
FE Finite Element
FEA Finite Element Analysis
FGM Functionally Graded Material
GF Glass Fibre
GFRP Glass Fibre Reinforced Polymer
HVOF High Velocity Oxygen Fuel
IN625 Inconel 625
IN718 Inconel 718
LENS Laser Engineered Net Shape
ME Material Extrusion
MJP MultiJet Printing
PBF Powder Bed Fusion
PC Polycarbonate
PLA Polyactic Acid
PM Powder Metallurgy
RP Rapid Prototyping
SHS Self-propogating High-temperature Synthesis
SIMP Solid Isotropic Microstructure with Penalisation
SLA Stereo Lithography
SLM Selective Laser Melting
SLS Selective Laser Sintering
SPS Spark Plasma Sintering

SS316L Stainless Steel 316L

STL StereoLithography/Standard Tessellation Language (backronym)

SUMC Segments of Unique Material Composition

TI64 Ti-6Al-4V

TO/T.O Topology Optimisation

UTS Ultimate Tensile Strength

UV Ultra Violet

WAAM Wire Arc Additive Manufacturing

Contents

Statement of Academic Honesty	1
1 Introduction	18
1.1 Background to research	18
1.1.1 Why light weighting is important	18
1.1.2 Why FGMs are important in the context of lightweight design	19
1.1.3 How this thesis looks to investigate lightweight design	19
1.2 Aim and Objectives	20
1.3 Thesis Overview/Structure	21
2 Literature Review	22
2.1 Form	22
2.2 Evolution of link form	23
2.2.1 Conclusions	25
2.3 Structure	26
2.3.1 Current research into lightweight robotic arm link structure	26
2.3.2 Structured cells	32
2.3.3 Topology optimisation	40
2.3.4 Conclusions	45
2.4 Material	46
2.4.1 Properties attractive for lightweight design	46
2.4.2 Metals	47
2.4.3 Polymers	48
2.4.4 Ceramics	49
2.4.5 Functionally graded materials	50
2.4.6 Conclusions	59
2.5 Manufacturing Technique	60
2.5.1 Manufacture of FGMs	60
2.5.2 Additive manufacture	63
2.5.3 Multi-material ability	68
2.5.4 Conclusions	79

2.6	Cost	80
2.6.1	Conclusion	85
2.7	Knowledge gap map	86
3	Scope of Research	87
3.1	Aim and Objectives	87
3.2	Research Question	87
3.3	Research Methodology	88
3.4	Assumptions	91
3.5	Linking literature and research question to first experiments	92
3.5.1	Form	92
3.5.2	Structure	93
3.5.3	Materials	93
3.5.4	Manufacturing Technique	95
4	Test case 1 - preliminary tests	96
4.1	Introduction	96
4.2	Choosing the test case	96
4.2.1	Model of test case	96
4.2.2	Link parameters	97
4.2.3	Primary constraints	98
4.2.4	Secondary constraints	98
4.3	Developing the testing strategy	98
4.4	Single material without topology optimisation	99
4.4.1	Model set up	99
4.4.2	Solver set up	100
4.4.3	Results and conclusion	100
4.5	Single material while applying topology optimisation	101
4.5.1	Model set up	101
4.5.2	Solver set up	104
4.5.3	Results and conclusion	105
4.5.4	Single material conclusions	107
4.6	Dual material - set up	107
4.6.1	Models used	108
4.6.2	Materials used	108
4.7	Dual material - radial	109
4.7.1	Model set up	112
4.7.2	Solver set up	112
4.7.3	Experiments conducted	113

4.7.4	First testing group results and conclusions	113
4.7.5	Second testing group results and conclusions	115
4.8	Dual material - along tube	116
4.8.1	Model set up	116
4.8.2	Solver set up	116
4.8.3	Experiments conducted	116
4.8.4	First testing group results and conclusions	116
4.8.5	Second testing group results and conclusions	118
4.8.6	Dual material conclusions	119
4.9	Automated FGM without topology optimisation	120
4.9.1	Importance of FGM	120
4.9.2	Model setup	120
4.9.3	Setup itself	122
4.9.4	Solver setup	125
4.9.5	Results and conclusions	125
4.10	Automated FGM while applying topology optimisation	127
4.10.1	Model setup	127
4.10.2	Solver setup	127
4.10.3	Results and conclusions	127
4.11	Summary of preliminary test case results	129
4.12	Outcomes of preliminary test case	130
5	Design guidelines for FGM mechanical parts	131
5.1	Introduction	131
5.1.1	Reasons for design guidelines	131
5.1.2	Design guidelines creation	131
5.1.3	Design guideline constraints	133
5.1.4	Defining the focus of the design guidelines	134
5.2	Form: Detailed description	136
5.2.1	Introduction	136
5.2.2	STEP 1 - UNDERSTANDING DESIGN TASK	136
5.2.3	STEP 2 - INFLUENCE OF FORM	140
5.3	Structure: Detailed Description	152
5.3.1	Introduction	152
5.3.2	Constraints on internal structure	152
5.3.3	STEP 3 - CHOICE OF INTERNAL STRUCTURE TECH- NIQUE	153
5.4	Material: Detailed Description	156

5.4.1	Introduction	156
5.4.2	STEP 4 - PART SEGMENTATION	157
5.4.3	STEP 5 - THEORETICAL MATERIAL MIXING	168
5.4.4	STEP 6 - MATERIAL CHOICE	180
5.5	Computational Testing: Detailed Description	186
5.5.1	Introduction	186
5.5.2	STEP 7 - COMPUTATIONAL TESTING: PRE-PROCESSOR	187
5.5.3	STEP 8 - COMPUTATIONAL TESTING: PROCESSOR . . .	202
5.5.4	STEP 9 - COMPUTATIONAL TESTING: POST-PROCESSOR	207
5.5.5	Introduction	208
5.6	Manufacturing Technique: Detailed Description	209
5.6.1	STEP 10 - ACTUAL MATERIAL MIXING	209
5.6.2	STEP 11 - MANUFACTURING: PROCESSING	212
5.6.3	STEP 12 - MANUFACTURING: POST-PROCESSING	217
5.7	Diagram of complete design guidelines	218
5.7.1	Conclusion	220
6	Test case 2 - verification of Computational testing segments of design guidelines	222
6.1	COMPUTATIONAL TESTING: PRE-PROCESSOR	223
6.1.1	Model Definition	224
6.1.2	Structured cells vs TO	228
6.1.3	Part Segmentation (from STEP 4: PART SEGMENTATION)	228
6.1.4	Theoretical material mixing (from STEP 5: THEORETICAL MATERIAL MIXING)	230
6.1.5	Apply materials	233
6.1.6	Apply solver requirements	234
6.1.7	Use instructions to apply topology optimisation	235
6.1.8	Conclusion	237
6.2	COMPUTATIONAL TESTING: PROCESSOR	237
6.2.1	Pre-processor FEA data check	238
6.2.2	FEA elementary processing	238
6.2.3	Pre-processor T.O data check	239
6.2.4	FEA and TO detailed processing	239
6.2.5	Conclusion	241
6.3	Results	241
6.3.1	Mass	242
6.3.2	Thermal	243

6.4	COMPUTATIONAL TESTING: POST-PROCESSOR	244
6.4.1	Part smoothing	244
6.4.2	Validation	245
6.5	Conclusions	247
7	Heat flow guidelines	248
7.1	Introduction	248
7.2	Code	248
7.2.1	Aspects to be modelled	248
7.2.2	Assumptions for model	248
7.2.3	Variables used in simulation	249
7.2.4	Graphical user interface	250
7.2.5	Conclusion	251
7.3	Steps in code	251
7.3.1	Segmenting the part	252
7.3.2	Applying FGMs	252
7.3.3	Creating the print bed and meshing the part	252
7.3.4	Creating the tool path	253
7.3.5	Deactivating deposition segments	253
7.3.6	Creating the heat transfer conditions	254
7.3.7	Heating the material	255
7.3.8	Reactivating deposition segments	255
7.3.9	Applying a radiative surface heat flux	258
7.3.10	Conclusion	260
8	Test case 3 - Implementing the heat flow guidelines	261
8.1	Using guidelines	261
8.1.1	Step 1 - Segmenting the part	261
8.1.2	Step 2 - Applying the FGMs	262
8.1.3	Step 3 - Creating and attaching the print bed	262
8.1.4	Step 4 - Creating the tool path	262
8.1.5	Step 5 - Deactivating the deposition segments	263
8.1.6	Step 6 - Heat transfer conditions	263
8.1.7	Step 7 - Heat print bed and deposition segments	264
8.1.8	Step 8 - Sequentially reactivate the deposition segments	264
8.1.9	Step 9 - Set nozzle velocity and heat source conditions	265
8.1.10	Step 10 - Apply radiative surface heat flux	269
8.1.11	Step 11 - Set cooling rate for part	270
8.1.12	Conclusion	270

8.2	Addition of residual stress	270
8.3	Fitting heat flow into design guidelines	271
8.4	Conclusion	275
9	Testing the entire design guidelines	276
9.1	Introduction	276
9.2	Model	276
9.3	Step 1 - Understanding Design Task	276
9.3.1	Elicit design requirements from design task	277
9.3.2	Validate design task/requirements	278
9.3.3	Conclusion	281
9.4	Step 2 - Influence of form	281
9.4.1	Influence of geometric features	281
9.4.2	Influence of Core Volume	281
9.4.3	Influence of cross section alteration	281
9.4.4	Influence of material placement	284
9.4.5	Conclusion	284
9.5	Step 3 - Choice of Internal Structure Technique	285
9.5.1	Assessing the geometry	285
9.5.2	Assessing the loading conditions	285
9.5.3	Assessing part shape	285
9.5.4	Conclusion	285
9.6	Step 4 - Part Segmentation	287
9.6.1	Choose FGM Extremity locations	287
9.6.2	Measure FGM Extremity Distance line	287
9.6.3	Calculate FGM blending distance	287
9.6.4	Take note of segmentation rules	289
9.6.5	Conclusion	289
9.7	Step 5 - Theoretical Material Mixing	289
9.7.1	Take note of mixing constraints	290
9.7.2	Calculate complete FGM distance	290
9.7.3	Use calculations for above complete FGM distance	291
9.7.4	Use layer stacking rules	291
9.7.5	Conclusion	292
9.8	Step 6 - Material Choice	292
9.8.1	Translate design constraints into material properties	293
9.8.2	Optimise material properties linked to design constraints	293
9.8.3	Combine material properties onto material charts	293

9.8.4	Create material group charts	295
9.8.5	Screen materials based on design constraints	296
9.8.6	Choose most optimal materials	297
9.8.7	Conclusion	297
9.9	Step 7 - Computational Testing: Pre-Processing	297
9.9.1	Decide form of structured cell	298
9.9.2	Use steps to create part	299
9.9.3	Segment part	300
9.9.4	Apply materials	300
9.9.5	Apply solver requirements	300
9.9.6	Conclusion	300
9.10	Step 8 - Computational Testing: Processing	300
9.10.1	Pre-processor FEA data check	301
9.10.2	FEA elementary processing	302
9.10.3	FEA detailed processing	304
9.10.4	Conclusion	304
9.11	Step 9 - Computational Testing: Post-Processing	304
9.12	Step 10 - Heat Flow Testing	304
9.12.1	Step 1 - Segmenting the part	305
9.12.2	Step 2 - Applying the FGMs	305
9.12.3	Step 3 - Creating and attaching the print bed	305
9.12.4	Step 4 - Creating the tool path	305
9.12.5	Step 5 - Deactivating the deposition deposition segments	305
9.12.6	Step 6 - Heat transfer conditions	305
9.12.7	Step 7 - Heat print bed and deposition segments	306
9.12.8	Step 8 - Sequentially reactive the deposition segments	306
9.12.9	Step 9 - Set nozzle velocity and heat source conditions	306
9.12.10	Step 10 - Apply radiative surface heat flux	306
9.12.11	Step 11 - Set cooling rate for part	306
9.12.12	Conclusion	308
9.13	Conclusion	309

10 Discussion 310

10.1	Reflection on research questions	310
10.1.1	Q1) What effect does altering form have on the possibility of incorporating TO, structured cells and FGMs?	310
10.1.2	Q2) If AM manufacturing restrictions are put in place, are the stress-reduction benefits of FGMs present?	311

10.1.3	Q3) Does FGM + TO mixing work?	311
10.1.4	Q4) Does FGM + structured cell mixing work?	312
10.1.5	Q5) How effective are these mixing techniques? Use physical testing to find this out.	312
10.1.6	Q6) If the above techniques can be used to reduce the mass in robotic arm links?	312
10.2	Reflection on research methods used	313
10.2.1	Literature Review	313
10.2.2	Case study	313
10.3	Reflection on overall approach	314
11	Summary of conclusions, contributions to knowledge and future work	316
11.1	Summary of conclusions	316
11.2	Contributions to knowledge	318
11.3	Future Work	318
12	Appendix A: Python Code	320
12.0.1	Calculating number and thickness of layers	320
12.0.2	Partitioning the part	321
12.0.3	Material creation	324
12.0.4	Building print base for heat flow	326
12.0.5	Meshing part	326
12.0.6	Writing raster scan path for heat flow	327
12.0.7	Deactivating print deposits	328
12.0.8	Creating heat transfer conditions	328
12.0.9	Heating, depositing and cooling segments	329
13	Appendix B: Physical Experimentation	331
13.1	Experimental Aim	331
13.2	Test block	331
13.3	Test coupon creation	333
13.3.1	Making test block	334
13.4	Cutting the test coupons	334
13.5	Tooling	334
13.6	Experiments to be conducted	335
13.6.1	Tensile test	335
13.6.2	Micro hardness test	335
13.6.3	XRD	336
13.6.4	EBSD	336

13.6.5	Residual stress test	336
13.7	Conclusion	336

Chapter 1

Introduction

1.1 Background to research

1.1.1 Why light weighting is important

Mechanical devices are integral to “modern” life, as we know it. Ever increasingly alongside this integration is the drive for devices to be lighter. As the title suggests, a backbone of the work in this thesis is lightweight design. There are two central benefits to light weighting when compared to identical processes using heavier components - increased energy efficiency and increased process performance. This section will discuss the importance of these two aspects lightweight design, through the eyes of the researcher.

1.1.1.1 Energy efficiency

One of the key drivers for parts being lighter is the energy efficiency; parts which are lighter require less energy to overcome inertia, and therefore require less energy input to perform their function when compared to a heavier part with equal function. One outcome of this increased energy efficiency results in a reduced environmental impact. The drive to reduce environmental impact is not only a moral one; it also has a financial incentive - mechanical devices (either entire systems or subsystems) are cheaper for the customer/operator to use on a daily basis, due to the aforementioned lower energy costs.

1.1.1.2 Process performance

As stated above, lighter products need less energy to overcome inertia when compared to a heavier product with an equal function.

For moving parts in a system, for example robotic arm links on a robot, this lighter weight results in the ability to be able to accelerate faster than a heavier part given the same input energy. In a production setting, turn, this increased acceleration means that processes can be performed faster, and thus throughput performance increased.

For a complete system, for example a car, this lighter weight could result in performance increases in terms of handling, acceleration and fuel efficiency, assuming changes are made to other sub-systems in order to capitalise on the new reduced mass.

1.1.2 Why FGMs are important in the context of lightweight design

There are many options for reducing component weight and in turn increasing energy efficiency and process performance, and therefore many research avenues. One topic which is of particular interest is the **gradual** combination of different materials and/or geometries during manufacture. Two or more materials and/or geometries **gradually** blended together are known as functionally-graded materials. These are of significant interest in the field of light weighting, as they allow the task-specific advantageous properties of different materials/geometries to be capitalised upon and the task-specific disadvantageous properties to be minimised, while greatly minimising effects seen at boundaries of dissimilar materials/geometries, such as high stresses. In the context of light weighting, this could be a temperature sensitive part which requires a material that can be exposed to high temperatures. This material could be comparatively dense when compared to other materials, so there is a desire to only use it as a facing material, and use a less dense material as the main body of the component. However, rather than applying the dense material as a coating, and having to deal with the associated stresses at the boundary layer, the two materials could be gradually blended, reducing the mass, reducing the stresses, and creating a FGM. Combining FGMs with other lightweight design techniques, such as topology optimisation, further increases the argument for FGMs in lightweight design - in a structural application, topologically-optimised designs can be created that use the different material property values (e.g, density, stiffness) of the differing constituent materials to ensure that a part can be even lighter than that made from a single material. Due to the benefits that FGMs can bring to light weighting, it is decided that they will be included in this thesis.

1.1.3 How this thesis looks to investigate lightweight design

The light weighting of mechanical parts is a non-trivial process, with many variables involved. As technology evolves, the possibilities to light weight increase, but with greater possibility comes more unanswered challenges. One such technology that is evolving and lends itself to light weighting is additive manufacturing, especially when combined with topology optimisation - the idea that the material can be redistributed within a design space to maximise or minimise material values of interest. This combination of additive manufacture and topology optimisation is particularly useful in light weight design due to the design freedom it both offers and then subsequently creates, meaning that forms and structures (such as complex structured cells) that were previously impossible to physically produce, are now possible. The increasing adoption of additive manufacture has brought about greater opportunities for light weighting. However, in order to design light weight mechanical parts that can have widespread

use, many topics must be thought of, including but not limited to: cost, structure, material and additive manufacturing boundaries. These topics, and how to combine them, will be the basis of this thesis.

Combining these elements brings challenges, both theoretical and practical. On a theoretical front, issues with material interaction, structural optimisation, FGM simulation and their inter-relationships must be addressed. On a practical level, cost of manufacture, material cross-contamination and AM technology capabilities all have an effect. In order to combine these aspects, a set of design guidelines is presented in the thesis, along with case studies to evaluate parts of the guidelines. The work that the guidelines suggest would see greatest benefit in engineering sectors that have both very stringent mass requirements, and a fairly high ceiling on cost due to the complexity that is required to manufacture the parts per the guidelines, such as space and aerospace. However, from a theoretical point of view, the guidelines can be applied to any engineering sector that deals with mechanical structures that could benefit from light weighting.

In this thesis, it was decided that this sector would be robotics, specifically robotic arm links, due to the ever-increasing adoption of robotics and automation in manufacturing and the previously mentioned desire to reduce mass of parts in order to lower energy consumption and therefore reduce environmental impact. It is conceded that the value-addition of lightweight design is not as high for robotic arm links as it would be for a spacecraft component, for example, but due to the accessibility of robotic-related case studies and knowledge via the supervisor, it was decided that this would be the best compromise.

Due to the nature of robotic arm links it was decided that “form”, in particular the impact that the second moment of area has on form, should also be included as a topic of research. This, alongside the topics previously mentioned, established the background of the research, allowing aims of the project to be developed.

1.2 Aim and Objectives

The aim and objectives of the research were based on the research topics set out in section 1.1 and the findings during the literature search. The aim is:

To investigate the mass reduction of robotic arm links by merging second moment of area calculations, structured cells, topology optimisation, functionally graded materials and additive manufacture in various combinations.

The objectives reflect the aim of the project, and are as follows:

1. Run a preliminary case study to test selected ideas derived from literature.

2. Write a methodology that incorporates all the ideas from the literature that aims to help designers reduce the mass of robotic arm links.
3. Test the methodology using a case study and computer simulations.
4. Use additional case studies to further test the methodology, and investigate points that make up the research question. This will be done using computer simulations.
5. Verify aspects of the methodology using physical experiments (creation and testing of TO-FGM parts).

1.3 Thesis Overview/Structure

Omitting this introduction, the thesis is broken into five main areas which are spread across 10 chapters. The five areas are as follows:

- I. **Literature review.** This chapter cover the literature read to gain knowledge of the project, form the research question, and bound the project in order for it to be manageable.
- II. **Preliminary test case.** This chapter is a first test of some of the ideas that came out of the literature review.
- III. **Design guidelines.** An outcome of the preliminary test case is the need for a set of guidelines for the process of combining the topics addressed during the literature review. This chapter has many sections - each one describing a different step in the design guidelines.
- IV. **Further test cases.** There are three further test cases, covered over four chapters. The test cases assess various stages of the design guidelines in order to check their robustness.
- V. **Discussion, conclusions and future work.** The final two chapters cover the discussion, the contributions to knowledge made during the project, a summary of the conclusions made at other stages during the document, and future work that could lead on from where this project ends.

Chapter 2

Literature Review

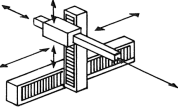
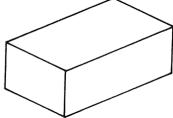
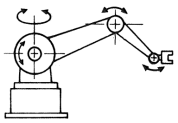
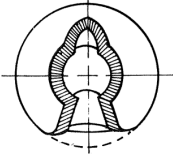
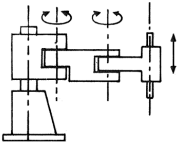
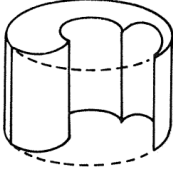
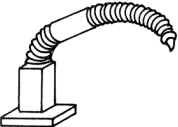
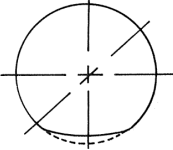
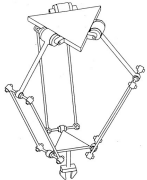
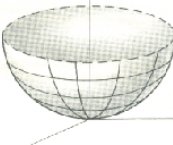
The literature review was conducted without following any set technique, and as such, can be classified as a traditional literature review (Jesson, Matheson and Lacey, 2011). Without a set technique (i.e. formal methodology), the literature exploration could cover a broad spectrum of topics. This was considered beneficial when forming a wide basis of the research focus definition.

The literature review will cover the four areas of lightweight robotic arm design discussed previously. It will start by focussing on form, followed by structure, material and manufacturing technique. It will conclude with a discussion of cost, an important factor to take into consideration when manufacturing.

2.1 Form

The form of a robot arm describes its overall shape, and therefore the task it will undertake. It can be viewed from both the perspective of the entire robot arm, or from the link itself. The form of the entire robot arm refers to its mechanical layout. Altering this form vastly alters the tasks that the robot will be able to undertake, as summarised in table 2.1 which shows five common industrial robot arm forms.

Table 2.1: Common robot arm forms

Robot Type	Configuration	Work Envelope	Primary Use
Cartesian			Pick and place
Horizontal Jointed-Arm			Assembly, Spray Painting, Spot Welding, Material Handling
SCARA			Pick and place requiring horizontal compliance
Multiple Joint / Continuum			Tasks requiring extreme flexibility
Delta			High speed pick and place, typically of light, small items

2.2 Evolution of link form

When first introduced into industry in 1961^[1], robotic arms were far stiffer and therefore heavier than need be. This was to ensure repeatability and accuracy within their work envelope (the entirety of the volume the arm can reach between its minimum and maximum range). The reason was due to past control algorithms and systems that were relatively slow and cumbersome - computing power was lower and robotic movements therefore simpler^[2]. Robot performance nowadays is constrained by the maximum torque, inertia and speed that the actuators can apply and withstand^[3], rather than the constraints of repeatability, accuracy and rigidity which used to arise from poorer control systems^[2].

However, from first appearance, links of many robotic arms look to have not been innovated to any great degree - many have rectangular or square cross sections, as seen when comparing horizontal jointed robot arms from 1991 and 2005, respectively, in

Figure 2.1, or when looking at a modern collaborative robot in Figure 2.2. Indeed, similar circular and square geometries are also used on “lightweight” robots (those which aim to achieve a payload ratio nearing 1:1), such as the the Kinova JACO²^[4] and the LWA 4P^[5] - the from which the consumer sees on these robots is an aesthetic cover for the structural components beneath. The main factor in the increasing success of “lightweight” robots are the advanced control systems, as they have to be able to keep all links in specific orientations at all times in order to ensure they are positioned to maximise their payload potential^[6;7].

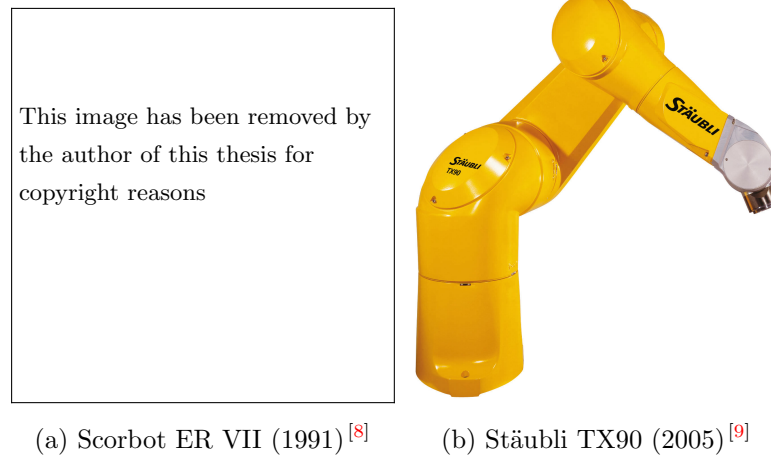


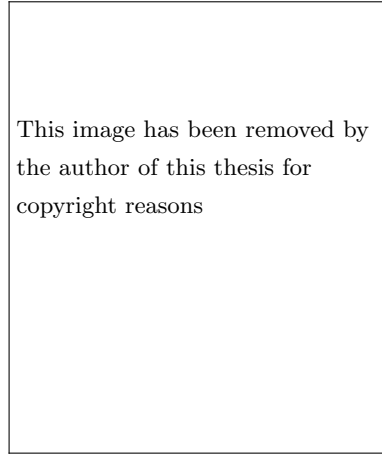
Figure 2.1: Design evolution of horizontal jointed robot arms



Figure 2.2: A modern robot, showing circular cross section links^[10]



(a) Kinova JACO2^[4]



(b) Schunk LWA 4P^[5]

Figure 2.3: Contemporary Robot Arms

The reason that robotic arm links still predominantly use circular and square cross sections is the rotational independence that these two shapes offer - the stiffness of these cross sections is completely independent of loading direction for a circle, and nearly independent of loading direction for a square. This is very important for robotic arms with multiple links, as the dynamic load on the arm at any instant can be acting in one of an infinite number of directions. Indeed, using specially designed modular joints, researchers have been able to make “lightweight” arms using circular cross section links^[11].

However, not all robot configurations move in the same work envelope, as shown in Table 2.1. Those which do not operate in spherical work envelopes can have links which theoretically deviate further away from the circular and square cross section, as each link has instantaneous dynamic loads that are more constrained in terms of direction when compared to those that have spherical work envelopes. For example, a horizontal jointed robotic arm should always have circular or square cross sectional links, as the instantaneous dynamic loads can be in any direction, but a SCARA robot can have links which are more elliptical or rectangular, as the instantaneous dynamic loads are acting in fewer directions.

2.2.1 Conclusions

The reason that circular and square cross sections for robotic arm links are still popular is well understood - the larger the orientation range of the robotic arm, the greater benefit a circular or square cross section will be, due to its stiffness independence. Therefore, work on form in this thesis should concentrate on robot configurations whose links do not operate in a large orientation range, such as SCARA robots, or bespoke

robots constrained similarly to SCARA robots. **A gap in knowledge is therefore seen in further optimisation of form shapes and dimensions for robot links with small orientation ranges.**

2.3 Structure

The structure of a lightweight robotic arm in this thesis refers to the internal structure of the link. Currently, the walls of most robotic arm links are solid. This section of the literature review will look into how to alter this structural configuration, and make the links hollow within. This change should increase the strength to mass ratio of the link, and therefore is important for creating a lightweight arm. There are two areas that will be focussed on: structured cells and topology optimisation. However, before this investigation begins, a review of past research into structural work for lightweight robotic arms will be done.

2.3.1 Current research into lightweight robotic arm link structure

As discussed in section 2.1, circular and square/rectangular cross sections are used due to their relative independence to dynamic loads when compared to other shapes. Work on robotic arm link structure has therefore aimed to keep these overall forms, and only optimise the structures where possible. Zhou and Bai^[12] worked on the inclusion of structural optimisation into robotic arm design. The research converted structural dimensions, kinematic dimensions, gearbox parameters and motor parameters into design variables, and then solved an optimisation problem that aimed to minimise weight. The structural dimension variables are shown in figure 2.4. The process was successful at altering the structural dimensions of the robotic arm link, though the possible alterations were limited to sizing of slots in a circular cross section link (not alterable). The authors concluded that future work should incorporate more advanced structural design techniques, such as topology optimisation^[12].

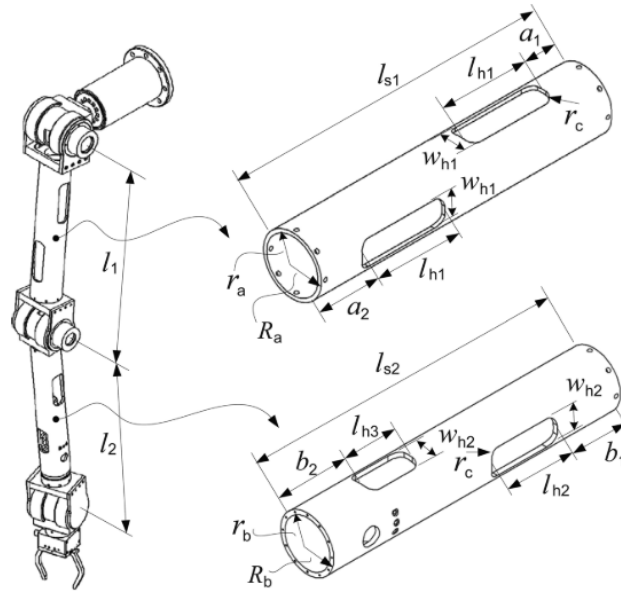
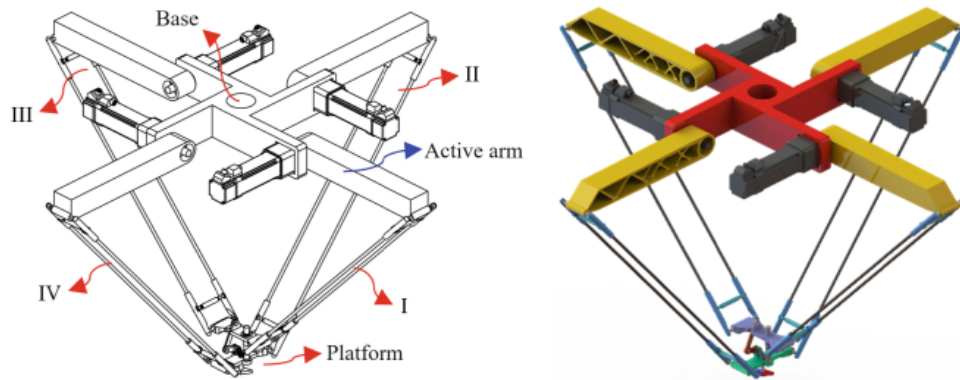


Figure 2.4: Structural design parameters of robotic arm links^[12]

A similar process was used to modify a UR5 robotic arm, controlling the length of the links, but not creating slots within^[13], and also concluded that work on the link morphology would be advantageous. Work by Yin et al.^[14] took the idea of Zhou and Bai^[12] and combined it with the ability to alter the width and thickness of the circular arm links, and the governing dimensions in the joints.

As time has progressed, so has the complexity of structural optimisation of robotic arm links. More recent work has focussed on introducing topology optimisation, as Zhou and Bai^[12] suggested for future work.

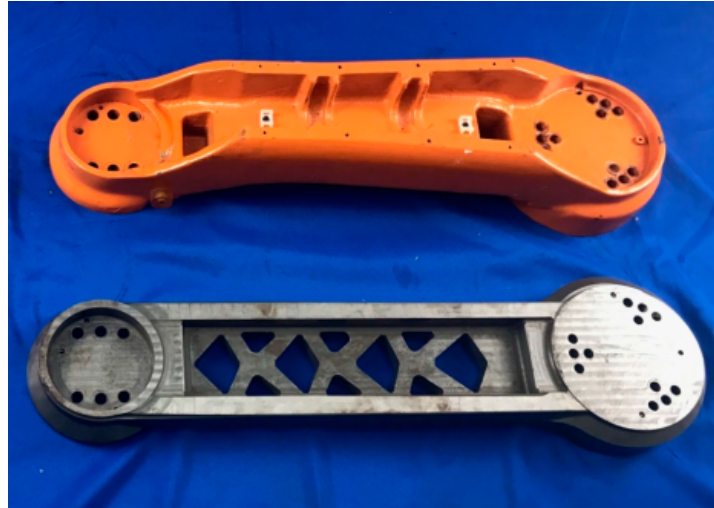
Meng et al.^[15] used TO in order to reduce the mass of active links in a delta robot. The researchers wrote the optimisation code in MATLAB (based on the SIMP method, discussed in section 2.3.3.2) before transferring the final design to CAD software. Figure 2.5 shows the active link before and after it has been topologically optimised, and also highlights the main aspects of the robot (the four limbs, the base and the platform). The resulting active link was not only lighter (a volume reduction of 30%), it also showed an increase in the static stiffness and dynamic response of the robot. In comparison to other robot configurations (e.g, horizontal jointed-arm), the movement of the active links in a delta robot is relatively constrained, and thus the researchers could model it as a cantilever beam. Despite this constraint, the use of TO to alter the structure of robotic arm links shows promise.



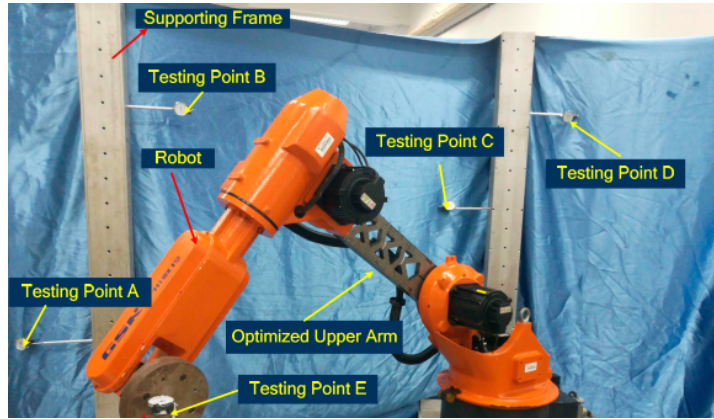
(a) Before the active link was topologically-optimised (b) After the active link was topologically-optimised

Figure 2.5: Cross section examples for manipulator ram arm^[15]

An example of work on a robot with relatively unconstrained links was done by Yao et al.^[16]. In this work, the researchers used topology optimisation to reduce the mass of one link in a GSK RB20 horizontal jointed-arm robot. The results showed a 17.9% decrease in mass, an increase in the natural frequency at all orders, and a reduction in deflection and Mises stress when dynamically-analysed in the worst position (outstretched horizontally). Figure 2.6a shows the original arm side by side with the topologically-optimised arm. Figure 2.6b shows the arm fitted to the robot, along with the testing points used to test repeatability and accuracy. This real world example shows that tangible benefits from using TO in robotic arm links structures are achievable.



(a) The two arms



(b) The new arm fitted to the robot

Figure 2.6: The original arm vs the topologically-optimised arm^[16]

Extending the concept of altering the structure in order to reduce the mass of links in a horizontal jointed arm robot, Lv et al.^[17] used topology optimisation to modify four links in a six degree of freedom robot. The optimisation routine took into account two limit conditions - both outstretched horizontally, with the final link rotated through 90° between each limit condition. The final result reduced the mass by 26.5%, while adhering to imposed stiffness requirements, and was therefore reported to increase the dynamic response of the robot. Similar work on multiple robot links has also been undertaken by other researchers, all reporting reduced mass and increased dynamic response^[18;19]. Figure 2.7 shows the parts topologically-optimised by Lv et al.^[17].

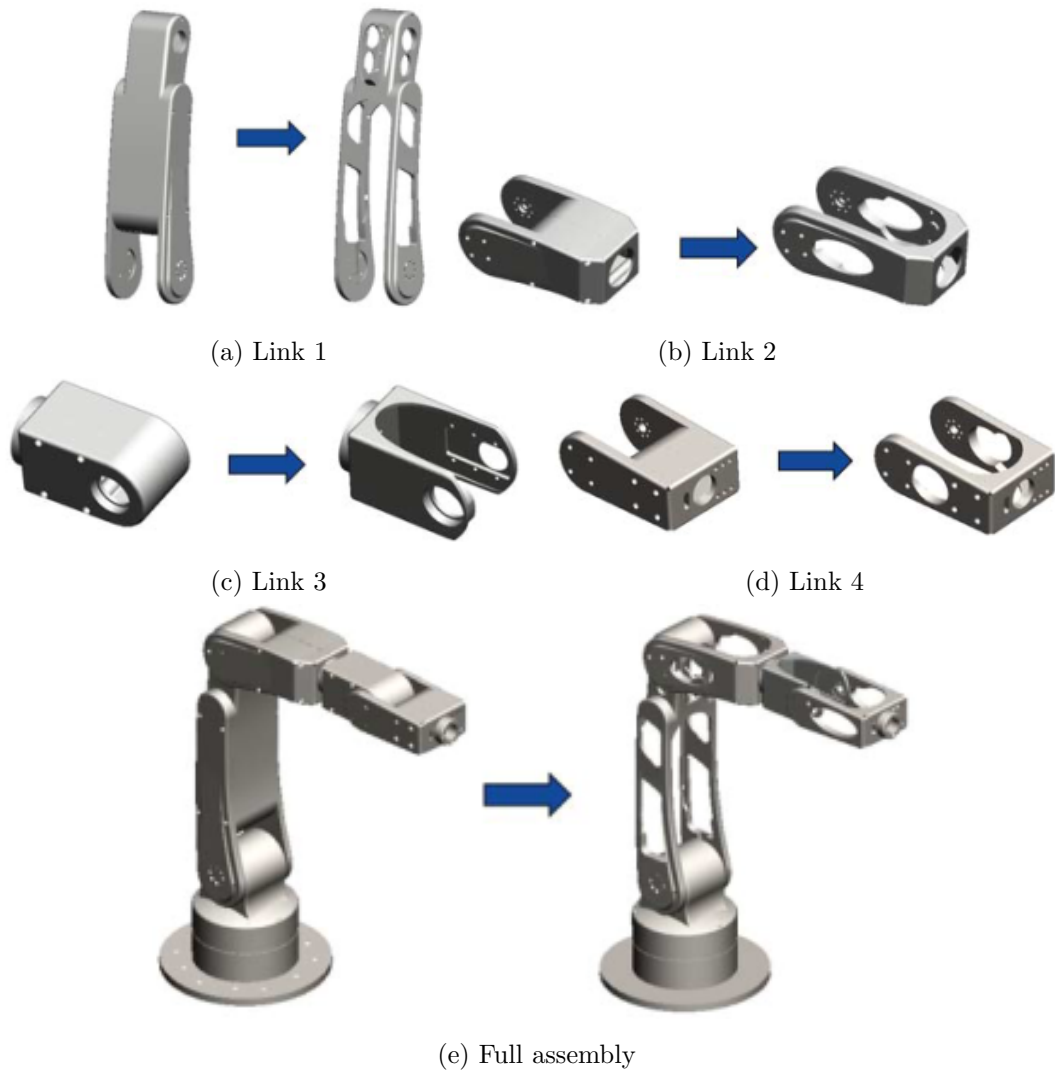


Figure 2.7: Topologically-optimised final assembly^[17]

As shown in the above examples, structural optimisation of arms can be undertaken on small desktop robots and larger industrial robots. Luo et al.^[20] took this one step further, demonstrating that heavy-duty manipulator arms can also benefit from structural optimisation. In this case a friction stir welding ram arm. The researchers were able to reduce the mass of the arm by over 50%, while optimising vibration resistance (increasing the natural frequency of the arm further away from operating frequency) and stiffness. This process led to improvements to the precision of the friction stir welder. In order to achieve this, the researchers used shape optimisation - tested various cross sections (Figures 2.8a and 2.8b) for the arm and hole geometries in the outer wall.

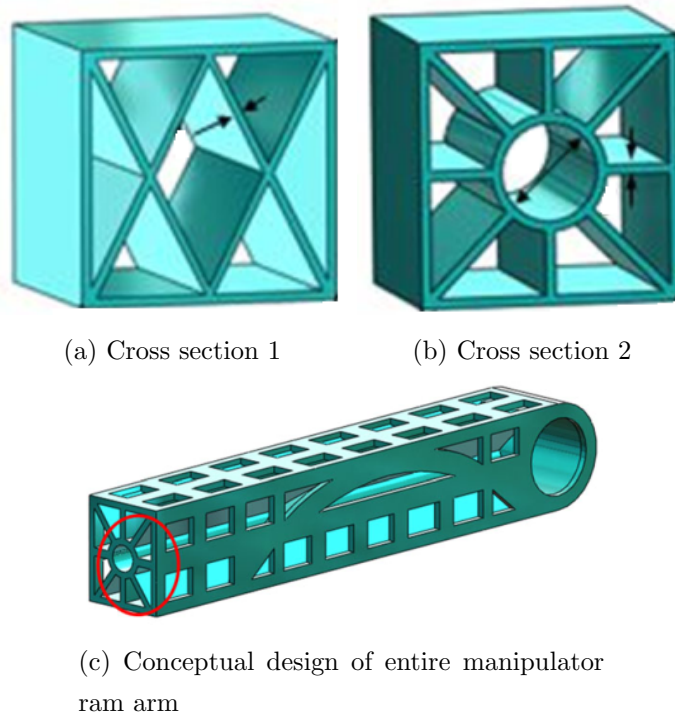


Figure 2.8: Cross section examples for manipulator ram arm^[20]

Figure 2.8c shows a conceptual design for the manipulator ram arm with differing slot shapes and sizes in the outer wall, and highlights the chosen cross section. Figure 2.9 shows the installed ram arm on the friction stir welder.



Figure 2.9: Finalised manipulator ram arm installed on friction stir welder^[20]

As seen, many of these examples of structural optimisation have used structured cells and topology optimisation, however, none have used them in the solid wall of hollow-centred links - a potential knowledge gap. This next section of the review will discuss

both structured cells and topology optimisation, detailing the main subsets of each.

2.3.2 Structured cells

Structured cells, also known as optimised cells or lattice structures, are specially designed geometries that give high strength to mass ratios with low relative densities [21–28]. Strength to mass ratio and relative density are two important concepts for structured cells, and lightweight design in general. Strength to mass ratio refers to the strength of a material (its ability to resist plastic deformation when loaded) divided by the density of the same material. The higher this ratio, the greater force a material **of the same mass** can take without plastically deforming, compared to a material with a lower ratio. On the other hand, relative density, in the case of structured cells, refers to the total possible volume of the cell that is actually populated with material. A cell completely “full” of material would have a relative density of 100%, while a cell that is only half “full” would have a relative density of 50%. Many structured cells have relative densities of less than 15%, which indicates that over 85% of most structured cells are void of material.

Rather than using solid walls in a part, optimised cells can be used between the wall skins. They give the benefits mentioned above (high strength to mass ratio with low relative densities) to the entire part [29–34]. Fabrication of these cells is possible (though complex) with investment casting [28] amongst other techniques, but is easiest with additive manufacture, as the layerwise manufacturing lends itself to the intricate and more complicated geometric detailing required.

Structured cells can have many forms. One possible classification technique is to label them as CAD-based (either strut-based or plate-based), implicit surface-based or topology optimisation-based. The choice/design of structured cell should depend on the loading situation of the part, such as compression tension or in-plane bending, and the task required of the part.

2.3.2.1 Strut based

A 3D strut-based structured cell can conceivably be any shape or part-shape that fits one of the 14 3D Bravais lattices [35]. When designing the internal structure of the lightweight robotic arm link, it is important to set the cell height, strut thickness and strut angle, as all three have a large effect on the structural rigidity [32]. The skin thickness will also have a large influence on the structural rigidity of the arm link, so should also be taken into account. These four variables will control the failure mode from yielding to buckling in either the skin or the struts. They are illustrated in figure 2.10.

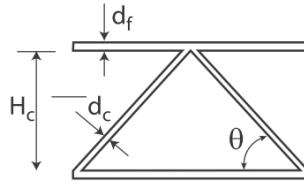


Figure 2.10: Cell Height [32]

Three common strut-based cells are shown below, all of which could be used in the lightweight robotic arm link.

Tetrahedral

As the name suggests, it uses many tetrahedral elements to create the core. Tetrahedral truss cores have typical relative density values of $\approx 2\%$. This density can be controlled using the following equation:

$$\bar{\rho} = \frac{2\pi}{\sqrt{3} \cos^2 \omega \sin \omega} \left(\frac{h}{l} \right)^2$$

where \$l\$ is the length of each leg and \$h\$ is the cross-sectional dimension, as can be seen in Figure 2.11. \$\omega\$ is the angle between the leg and the outer skin.



Figure 2.11: Tetrahedral Design [26]

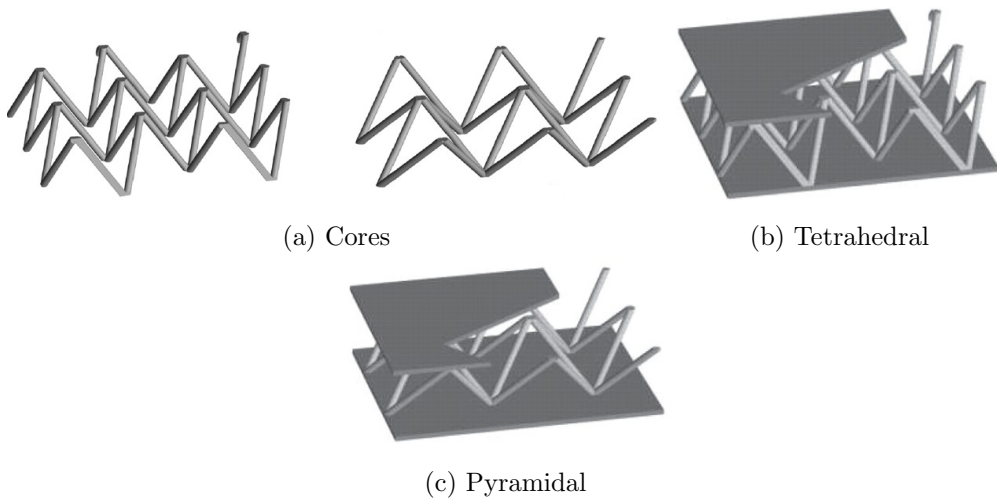


Figure 2.12: Tetrahedral and Pyramidal Core Comparison [21]

Pyramidal

The pyramidal truss core also has low typical values of relative density. It can be found using the following equation:

$$\bar{\rho} = \frac{2\pi}{\cos^2 \omega \sin \omega} \left(\frac{h}{l} \right)^2$$

The main difference between the tetrahedral and pyramidal core is the inclusion of a fourth member leg in each “set”, as can be seen in Figure 2.12a.

3D Kagomé

3D kagomé truss cores have values of relative density $\approx 2\%$ ^[36]. Unlike tetrahedral and pyramidal truss cores, kagomé cores display isotropic material behaviour, and therefore outperform tetrahedral and pyramidal cores when made to the same relative density^[28]. The 3D kagomé truss also differs from the previous two because it does not “continuously” cover the skin surfaces. That is, there are gaps between each kagomé element. The gap is typically equal in length to the width of the base of the kagomé itself. To ensure that relative density ($\bar{\rho}$) is the same in kagomé as it is in the other truss cores, the length of kagomé legs is half of that of tetrahedral cores^[23].

The relative density can be found using the following equation:

$$\bar{\rho} = \frac{3\pi}{\sin \omega} \left(\frac{R_c}{B} \right)^2$$

where ω is the angle between the truss leg and the outer skin (acute angle), R_c is the radius of the each leg and B is the distance between the centre of kagomé truss elements. These are shown in Figure 2.13.

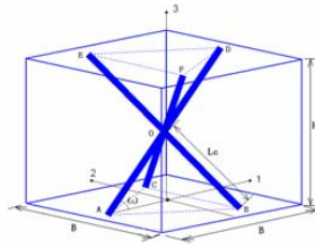


Figure 2.13: Kagomé design^[37]

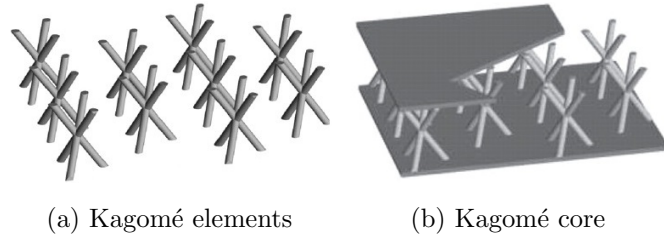


Figure 2.14: 3D Kagomé^[21]

2.3.2.2 Plate based

Plate based structured cells are assembled from plates rather than struts. Due to this construction technique, they have higher relative density values than strut based structured cells. The higher relative density results in stiffer parts when compared to the strut based cells. Three common plate based cells are shown below.

Corrugated

The corrugated sandwich core is the construction method used in cardboard. It has two outer skins with a central core made from a crimped/bent solid section. The relative density of the core is given by:

$$\bar{\rho} = \frac{t}{0.5l \sin 2\omega + t \cos \omega}$$

where ω is the angle between the core member and the outer skin, t is the thickness of the core member and l is the length of each core member. This is shown in Figure 2.15.

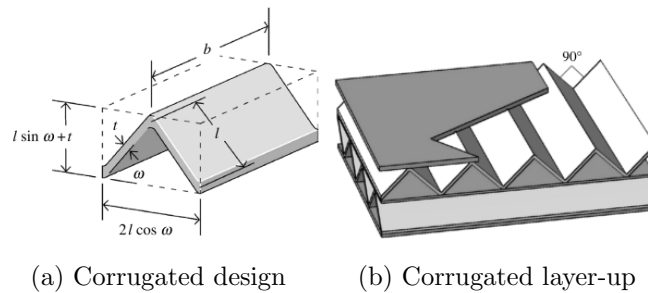


Figure 2.15: Corrugated Core^[21]

Diamond

Diamond cores have are constructed so as the cross section resembles many stacked diamonds. The relative density of the core is given by:

$$\bar{\rho} = \frac{2t}{l \sin 2\omega}$$

where t is the thickness of each member in the core, l is the length of each member and ω is the angle between the member and the outer skin. An image of a diamond core is shown in Figure 2.16.

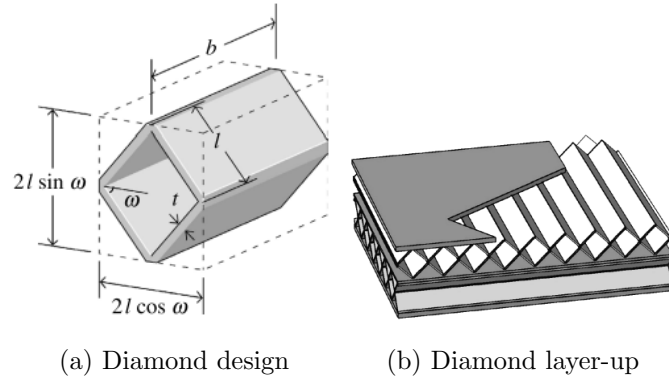


Figure 2.16: Diamond Core^[21]

Honeycomb

Honeycomb cores represent a honeycomb when viewed. The cross sectional shape of the honeycomb is most commonly hexagonal, and as such the core structure resembles many stacked hexagons when viewed. The relative density of the core is given by:

$$\bar{\rho} = \frac{8t}{3(\sqrt{3}l + 2t)}$$

where t is the honeycomb wall thickness and l is the length of one of the six honeycomb walls. An image of this is shown in Figure 2.17.

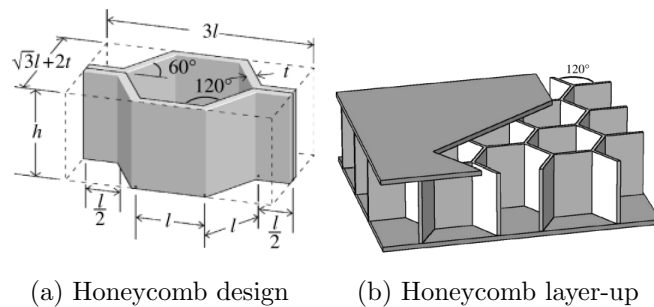


Figure 2.17: Honeycomb Core^[21]

A prediction of strength to relative density of selected strut based and plate based cellular structures is shown in figure 2.18. As expected, the lower the relative density, the lower the strength of the structured cell. This knowledge can be used to estimate the best structured cell to choose, dependent on the requirements of the specific lightweight robotic arm link.

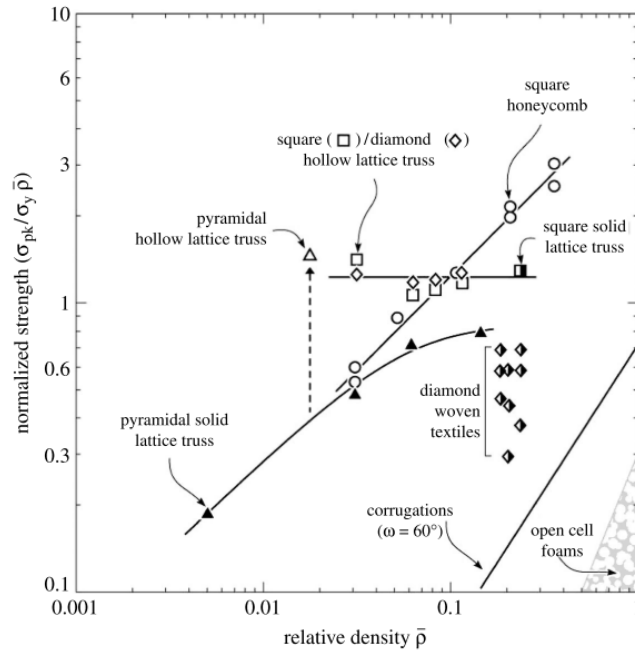


Figure 2.18: Strength vs density of selected strut and plate based cells^[21]

Both strut-based and plate-based structured cells are viable options for lightweight robotic arm links. As the geometries are not task-specific, there may be situations/parts that require a more bespoke solution, such that topology optimisation may give.

2.3.2.3 Implicit surface based

Surface based cells differ from CAD based cells above in their appearance and behaviour. A common use of surfaced based structured cells is interfacing with bone - the surfaces of the cell are designed to allow bone to bond with the cells^[38-42]. Additive manufacture is used to create the structures, however, the process parameters need further investigation to create surfaces with the finish for bone adhesion/growth. The geometry of these structured cells is also chosen to reduce the stiffness and weight of orthopedic implants - many metallic implants fail as the implant is too stiff compared to the surrounding bone^[38]. Over time, this “stress shielding” by the implant results in weaker bones, as they are not getting the required stimulation to regrow and strengthen^[41]. Through careful design of the surfaces, the elastic properties of the structured cells can be lowered to in line with those of trabecular bone and the yield stress can be kept high enough to exceed cortical bone^[40]. The design of the implicit surface cells is shown in figure 2.19.

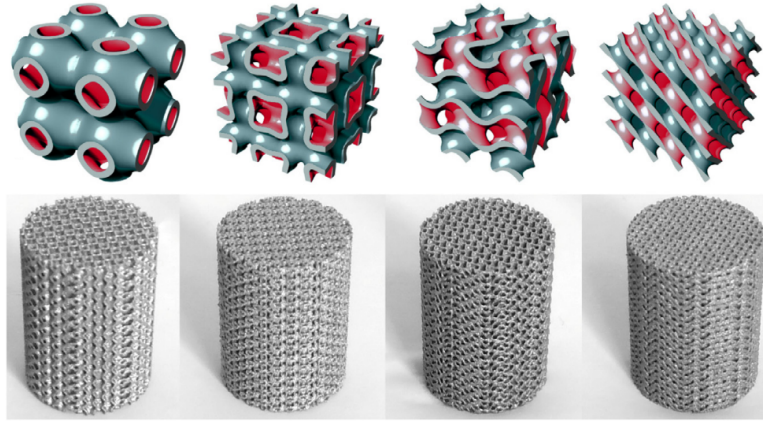


Figure 2.19: Implicit surface cells and layer-up^[40]

As mentioned, implicit surface based cells are primarily designed for integration with bones. Their strength to mass ratio is not as high as other structured cells, and therefore they will not be used in the design of lightweight robotic arm links.

2.3.2.4 Topology optimisation based

Topology optimisation is the re-organisation of material within a given design space. It allows for the creation of cells with great complexity that are bespoke to the design task, as the objectives of the optimisation are set (e.g, minimising mass), and the constraints that must be adhered to are given (e.g, maximum strain on part)^[43].

Wang et al. used level set topology optimisation to create structured cells^[43]. A level set function describes a surface. The level set method describes this surface using the contour of said surface as it is moved through a plane, allowing a complex 3D surface to be represented as many 2D “slices”^[44]. An example is shown in figure 2.20. Notice the difference between layers 50 and 52 (a and b) where parts of the cross section in layer 50 are no longer represented in layer 52, and similarly between layers 90 and 120 (c and d) where d has a larger footprint and the two halves are no longer connected (as in c) due to being further through the part build in the vertical direction.

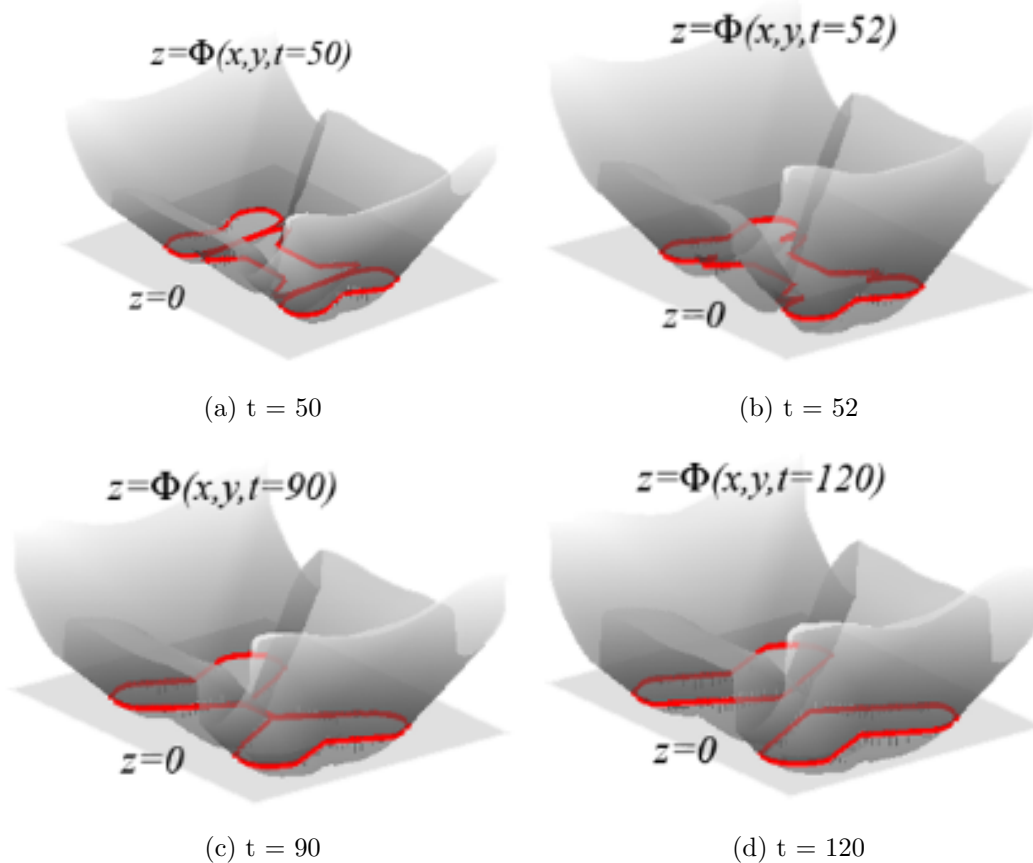


Figure 2.20: Level set method, showing the plane moving and the contour changing.^[45]

These cells were optimised for bone growth using porosity, permeability and stiffness as metrics. The basic principles of the level set method make it powerful to describe shapes which have a complex topology, as the objective functions and constraints depend solely on the solid-void interface of each individual layer. However, there are limitations - firstly, subsequent optimisation cycles must lead on from current boundaries^[44], and secondly, it is computationally intensive, and thus only acceptable if all cells within the part will be identical^[43].

Huang et al. created topologically-optimised structured cells using the BESO technique^[46] - a topology optimisation technique which alters the solid-void ratio of a part during each design cycle. Objective functions and constraints are set akin to other topological optimisation techniques. Each cell computes a criterion value for each objective function. The cells with the highest criterion values are removed from the part (turned from solid to void), and the criterion values for all remaining cells re-calculated^[47]. De-activated cells can be re-activated in a later cycle if their criterion value comes within admissible limits (turning from void to solid). This is the difference between ESO and BESO (which cannot reinstate cells). Similar to the work by Wang et al., the work is computationally intensive.

If different cell structures are needed in areas of the part (for varying loads, for example), creating the cells using topology optimisation is not advisable. It would take a great deal of time to find the different cell shapes required for each area. However, as a technique for finding new design ideas for structured cells, it is a powerful technique^[46]. Examples of these cells is shown in figure 2.21. This strength of topologically optimised cells may be used for finding designs of cells for a lightweight robotic arm link, however, the topology optimisation will not be used for all the cells, as this would take too long. Topology optimisation should instead be used on the part as a whole, as this will require far less time and computing power.

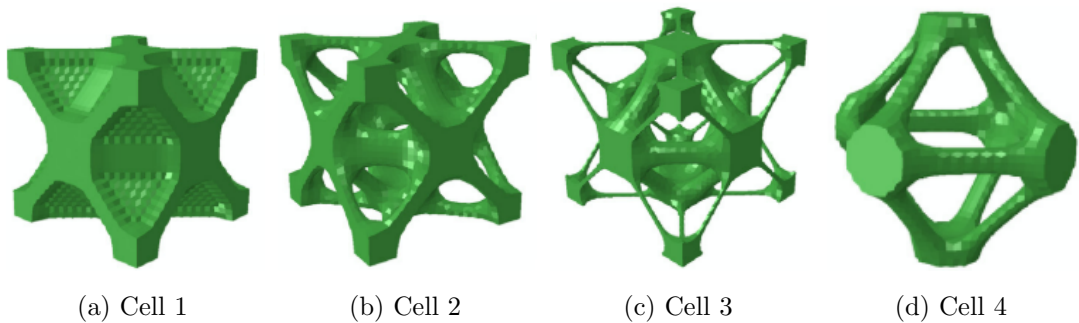


Figure 2.21: Examples of topologically optimised structured cells^[46]

2.3.3 Topology optimisation

As introduced in section 2.3.2.4, the aim of topology optimisation (T.O) is to remove/re-distribute material in order to maximise or minimise material values of interest. Topological optimisation and additive manufacture go hand-in-hand due to T.O's ability to produce intricate, non-intuitive designs. There are many algorithms available, two of which were briefly discussed above. This review will look at the widely used algorithms.

2.3.3.1 ESO and BESO

As mentioned in section 2.3.2.4, evolutionary structural optimisation (ESO) solves topological optimisation problems by altering the void-solid ratio; selectively removing elements during each optimisation cycle. The elements which are removed depend on the parameter being solved for, for example minimum compliance or minimum mass. Elements with the lowest criterion value for this given parameter will be converted from solid to void.

Bi-directional evolutionary structural optimisation (BESO) builds on ESO. The major difference is the allowance to re-instate elements that had previously been classified as voids and make them solids once again. Reinstatement of an element is decided by the criterion value - elements are replaced adjacent to those elements which currently have

a high criterion value during that optimisation cycle^[47]. This is powerful, as it means that latter material removal can be checked against previous, and once the structure goes outwith the design limits, said previous material can be re-instated to bring the structure back within design limits.

Aremu et al.^[48] built on the BESO algorithm with an adaptive meshing strategy (AMS). The AMS is designed to alter the mesh as the optimisation routine runs. Areas of the structure which have not been altered from void \Leftrightarrow solid between optimisation cycles will have the mesh coarsened while areas that are seeing changes between void \Leftrightarrow solid will have the mesh refined. To minimise mesh quality deterioration, Laplacian smoothing is used^[48]. Filtering of the elemental strain energy densities eradicates checkerboarding in the structures - a phenomenon that arises in topology optimisation due to discretisation errors caused by mathematical instability in FE software with conventional element shapes (quadrilaterals, triangles, wedges, etc)^[47;49]. This causes a “checkerboard” pattern of areas with very high density next to those with very low density. This pattern is incorrectly interpreted by TO solvers as having a high overall stiffness, and thus the solver thinks it is an optimised solution. Figure 2.22 shows a checkerboard example and highlights how it is not only of low stiffness in the real world, but also very difficult to manufacture - each square of the checkerboard only touches another at its corners. This phenomenon is still an active research field in topology optimisation, as solvers try and reduce its effects without increasing the complexity (and thus time required) of the solver^[50;51].



Figure 2.22: An example of checkerboarding, showing how a part with this structure has low stiffness, and is difficult to manufacture^[52]

In order to filter the elemental strain energy to eradicate checkerboarding via AMS, a target area for each element is decided upon for each optimisation cycle. The elemental strain energy density of the element with an area closest to this value was is as a threshold value. All solid elements with strain energies below this threshold value are made into voids by reducing their Young’s modulus to 1% of the material Young’s modulus. Setting this value rather than totally removing the elements makes it much easier to later reincorporate them^[53]. Any elements which are already void are reinstated if their strain energy is above the threshold value for this cycle. To ensure that the AMS does not produce an infinite number of tiny elements, a minimum area boundary is set. At

each cycle, the smallest 1% of elements were removed to ensure that elements did not distort.

Aremu et al.^[48] found that the AMS routine improved the efficiency of BESO T.O, with each method returning similar strain energies, but AMS being able to do it in less time. It was also seen that AMS was far less sensitive to changes in input characteristics (starting number of elements, minimum area, etc) than BESO, meaning AMS can produce smoother structures than BESO with less computational time. Figure 2.23 shows the AMS algorithm results, with a large number of smaller elements visible at boundary regions compared to BESO where elements are of similar area all over the structure.

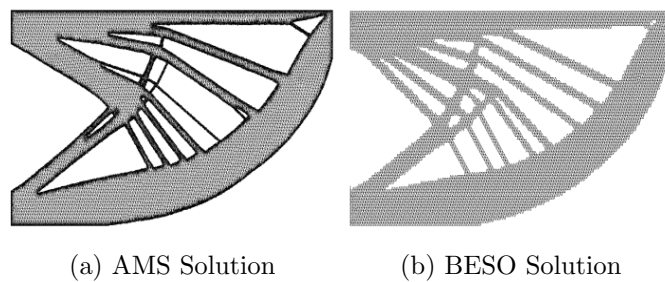


Figure 2.23: AMS vs BESO Solution^[48]

The AMS BESO algorithm compliments additive manufacture, as coarse meshes can produce smooth models that can be converted into construction files for additive manufacture hardware^[48]. This could be a powerful technique for creating lightweight robotic arm links.

Work on incorporating BESO into additive manufacture has been done. by Aremu et al.^[53], amongst others. The work focussed on the importance of the filter radius, R , and the evolution rate, ν . The filter radius is the radius of a sphere that has the same centre as an element in the structure. The evolution rate is the fraction which aids to compute the target volume for each optimisation cycle. Carrying out experiments that had the target volume altered and then the filter radius altered,^[53] found that filter radius was a significant factor while evolution rate was not. The filter radius should be made as low as possible in order to achieve high complexity parts with detailed features. The evolution rate should be made high, as this will increase computation speed. Figure 2.24 shows the dependence on the two input parameters.

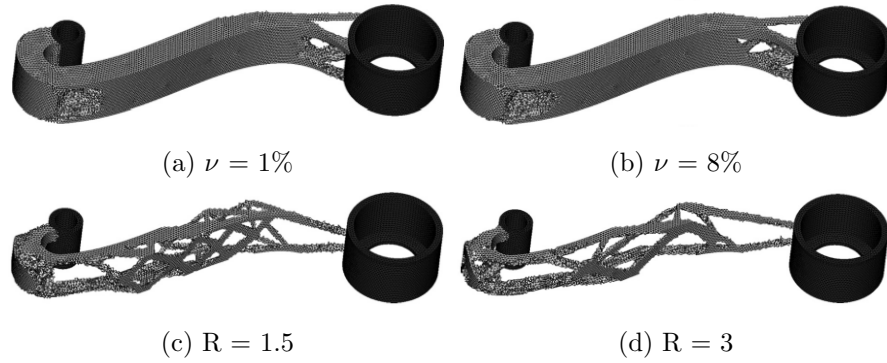


Figure 2.24: Influence of ν and R ^[53]

Despite the ability of BESO, and the benefits of the AMS algorithm written by Aremu et al.^[53], there is one inherent problem with BESO - the inability to correct for disastrous errors in certain situations, as shown in Figure 2.25^[47].

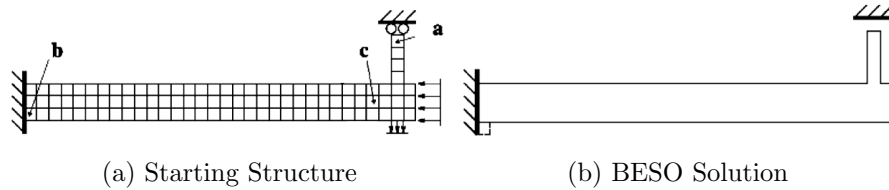


Figure 2.25: BESO Failure^[47]

The objective function is to minimise strain energy (and therefore get a part with maximum stiffness). Looking at Figure 2.25a, ESO suggests to remove element “a” first, increasing the strain energy value by 1100%. This is non-optimal, as to remove element “c” would only increase strain energy by 1.89%. BESO fails to remedy the loss of element “a” caused by ESO, because element “b” now has the highest criterion value (strain energy) and therefore it places an element where the dashed outline sits (Figure 2.25b) in an attempt to reduce the criterion value. However, element “a” is still missing^[47]. This shows that ESO and BESO still have limitations. This thesis is not aimed at creating new topology optimisation algorithms. Due to this inherent disadvantage of the BESO technique, a different T.O algorithm will be used if needed when creating lightweight robotic arm links.

2.3.3.2 SIMP

The Solid Isotropic Microstructure with Penalization (SIMP) method optimises parts by varying density. This is the main difference between SIMP and ESO/BESO, which optimises by altering the void-solid ratio. Despite taking time to be accepted by the scientific community over homogenisation routines, SIMP has become the de-facto standard in most optimisation software^[47], as well as the near exclusive solving method

in the seminal text “Topology Optimization: Theory, Methods, and Applications” from Bendsøe and Sigmund^[54]. This is possibly due to the fact that it uses an Eulerian solving approach, meaning that the part does not need to be remeshed every time boundaries between the void-solid regions change^[49].

Also known as the power-law, the SIMP method is described by

$$\rho = s^{1/p} \quad \text{for } p > 1$$

One disadvantage of the SIMP algorithm is grey-scaling, whereby regions of the optimised part are neither completely solid, not completely void, but instead are of “intermediate density”. To avoid grey-scale results, a high value of p (penalisation factor) is used. This means that ρ (the density) will tend to 0 (void) or 1 (solid). In order to overcome the zero-stiffness regions (those that are “truly” void in computational terms), the SIMP method has been modified to represent void areas as materials with very low Young’s modulus (akin to the technique in the BESO method).

Because the mesh does not need to be re-calculated when the boundary between solid and void regions change does not mean that the part is independent of remeshing; a part with a finer mesh will generally produce a closer-to-optimal result. Ideally, this mesh dependent behaviour should not exist^[49]. One method to eradicate it is to use filters, including perimeter controls, density filters and projection filters. However, these filters often create smooth void-solid transition regions which appear as intermediate density regions. Projection or continuation methods can be used to remove these intermediate density regions^[49].

The continuation method determines whether an intermediate density region should be void or solid. This is done by *continuing* to increase the penalisation value (p) from $p=1$ (a unique solution) upwards during the optimisation cycles to reduce intermediate density regions into regions of localised void-solid and therefore get closer to a “0-1” design that does not stray far from the global optimum^[47;49]. Another adoption of the continuation method is to reduce the filter radius during each optimisation cycle. This can result in break down of elements if introduced too soon however, and is therefore not favoured^[49]. While the continuation method encourages “0-1” designs, regions of intermediate density may remain. To remove this requires a threshold value. This value is usually set to $\rho = 0.5$. When below this value, the region is considered void, when above this value it is considered rigid. This simplification inevitably distorts the results, however results remain *reasonably* good^[49].

An additional filter is used to remove the checkerboard effect. The filter stops checkerboarding by setting a length scale to eradicate any “large” elements. The AMS spoken about in 2.3.3.1 also eradicates checkerboarding.

Although the SIMP method does have intermediate density region problems, it is noted

these can be addressed using filters. For this reason, as well as the integration of SIMP into Abaqus™ FE analysis software, SIMP will be chosen as the T.O algorithm, if T.O is required when creating lightweight robotic arm links.

2.3.3.3 Genetic Algorithms

Genetic algorithms are currently not widely used^[55]. A large reason for this is the computational power they require and the inefficiency they demonstrate for simple single objective problems, where other optimisation routines are far more logical to use^[47;56]. Hiller and Lipson^[55] argue that genetic algorithms have a place in solving functionally complex optimisation problems, such as those that arise when working on continuum problems with multiple materials. A solution to a three-material (blue, yellow, red), multi objective (low weight, low density, given load) cantilever problem is shown in Figure 2.26.

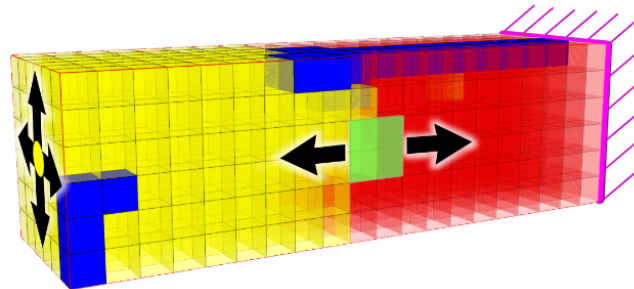


Figure 2.26: Genetic Algorithm Solver^[55]

This type of algorithm is powerful in that it can solve multi-material solutions to a far better standard than BESO currently can, as seen from the findings from Huang and Xie^[57]. The computational time and checkboarding of the result in Figure 2.26 are unsolved issues with genetic algorithms however, and work on complex multi-material optimisation problems for BESO and SIMP are expected to render genetic algorithms a niche technology. For this reason, genetic algorithms will not be investigated any further in this thesis.

2.3.4 Conclusions

It has been demonstrated in literature that structured cells, and TO especially, are able to successfully reduce the mass of robotic arm links, and, in many cases, increase natural frequency response, stiffness and dynamic response. However, no work to date has used TO or structured cells in the outer walls or links - it has always been used through the bulk volume. The form of a lightweight robotic arm can be complimented with lightweight internal structures cells, of which there are many types. The choice

of cell should be determined by the loading on the arm link. The structured cells increase the strength to mass ratio of a part, and are most advantageous when the part is geometrically-simple. If this is the case, the use of structured cells within lightweight robotic arm links is a possibility. On the other hand, topology optimisation has been seen to create geometrically-elaborate results, and is useful if loading and/or geometry of the part is complex. There are multiple TO algorithms available, each with strengths and weaknesses. From literature, the SIMP method is seen to be the most robust and widely used technique, and will therefore be used if TO is necessary. **A knowledge gap exists on using structured cells and TO predominantly within the walls robotic arm links, both independently of one another, and co-existing.**

2.4 Material

The material used to create a lightweight robotic arm link will, unsurprisingly, alter the final mass of the part. As noted in section 2.3, additive manufacture will be required to make many of the structural features reviewed. Therefore, focus will be on materials that are commercially available for additive manufacture hardware. This section of the review will begin with looking at what properties are attractive for lightweight design, then focus on the suitability of different material groups for use in lightweight design. It will finish with considering the possibility of combining multiple materials into one part.

2.4.1 Properties attractive for lightweight design

When designing lightweight structures, there are certain material properties which are attractive, and certain which are not. Often it is best to measure these properties as ratios, as it gives an impartial, unbiased comparison of how materials stack up against one another. For lightweight applications, the ratio should always include density. The task of the part will determine if a high ratio is needed, or a low ratio. Two common ratios used for lightweight part design are:

- **Strength to mass ratio.** Depending on the arrangement of the ratio, this returns materials that are very light but require a large load before permanent deformation, and every combination up to very heavy, but permanently deform with fairly low loads. For a lightweight robotic arm link, it is expected that materials with a high strength to mass ratio will be preferred, as the links may be moving large payloads, or have multiple dependent links attached to them (which will manifest as a large load)
- **Stiffness to mass ratio.** This is a measure of how elastic or rigid the part is

compared to its density. Certain materials (such as rubber) have a low stiffness to mass ratio as they are very flexible, while other materials (such as diamond) have a very high stiffness to mass ratio, as they are very rigid. For a lightweight robotic arm link, it is expected that materials with a high stiffness to mass ratio will be preferred, as the links should not easily deform. If the link did deform easily, accuracy and repeatability of the robot arm would be very poor.

These properties are also called “specific strength” and “specific stiffness”.

2.4.2 Metals

As mentioned, only materials commercially available for additive manufacture (AM) will be focussed on. The largest driver of AM metals is currently the aerospace sector, followed by the medical and then automotive sectors^[58]. For this reason, most research on metals has looked at structural materials with high specific stiffness and strength values. This is advantageous for a lightweight robotic arm link, as it will also require materials with these material properties. Table 2.2 lists the metals currently in commercial printing^[59].

Table 2.2: Commercially-Printed Metals

Metal	Grade
Titanium Alloy	Ti-6Al-4V Grade 23 ELI
Nickel Alloy	Inconel 625
Nickel Alloy	Inconel 718
Aluminium Alloy	Al10SiMg
Cobalt Chrome	Co28Cr6Mo
Stainless Steel	316 L
Stainless Steel	17-4 PH
Cobalt Chrome	Bego (Dental)
Titanium Alloy	TiMG1 (Medical)
Gold	
Silver	

2.4.2.1 Future Possibilities

As mentioned, metallic AM is currently focussed on structural applications and future applications will therefore aim to fabricate structural metals not currently printed. The ability to create a stable powder with small particles is mandatory if a metal is to be used for AM.

As mentioned by West et al.^[60], the future of metal AM lies in increasing the understanding of the effects of printing parameters such as grain size distribution and grain shape. When these are better understood, development of new deposition materials can begin.

2.4.2.2 Advantageous situations

Metals are advantageous in the following situations:

1. When high stiffness is required. If a part application requires high stiffness, metals can provide this
2. Temperature resistance. Most engineering metals have high melting points, and therefore are advantageous for a part which may be exposed to high temperatures
3. High toughness. Most engineering materials have high toughness; that is, they can absorb energy without sudden, catastrophic failure.
4. High electrical and thermal conductivity. Metallic objects conduct electricity very effectively. If the part needs to be thermally and/or electrically conductive, constructing it from metal is a good idea.
5. High strength

2.4.3 Polymers

Many properties of polymers are distinctly different to those of metals. The uses for polymers in engineering applications are therefore usually quite different. Polymers were the first additively manufactured materials and presently the majority of parts created use polymers^[61]. Table 2.3 shows the polymers currently being printed commercially.

Since polymers have been researched more intensively than metals, more AM fabrication techniques exist for them. 3D Printing, Stereolithography (SLA), Fused Deposition Modelling (FDM) and Polyjet are all polymer technologies, although other techniques can also be used.

2.4.3.1 Advantageous situations

1. Low density. Engineering polymers have lower densities than engineering metals. If the application does not demand heavy loads, a polymer may be sufficient. If this is the case, the part may end up being lighter using a polymer when compared to a metal.

Table 2.3: Commercially Printed Polymers

Polymer	Grade
ABS (Acrylonitrile butadiene styrene)	C ₈ H ₈ :C ₄ H ₆ :C ₃ H ₃ N
PLA (Polylactide)	C ₃ H ₄ O ₂
PC (Polycarbonate)	C ₁₅ H ₁₆ O ₂
Polyamide (Nylon)	C ₁₂ H ₂₂ N ₂ O ₂
Nylon 12	(CH ₂) ₁₁ C(O)NH
Glass-filled Nylon	Various
Epoxy Resin	Various
Wax	Various
Photopolymer Resins	Various

2. High corrosion resistance. Polymers tend to be more chemically inert when compared to metals, and as such do not corrode in as many environments, for example, oxygen-rich environments
3. High electrical insulation. If it must be ensured that a part cannot conduct electricity, engineering polymers are a good choice of construction material.
4. Non magnetic. Engineering polymers do not contain any iron, and therefore they are not ferromagnetic. Depending on the situation, this could be advantageous.

2.4.4 Ceramics

In recent years, commercial additive manufacturing hardware has become capable of depositing ceramics in combination with polymers to create a composite. The properties of ceramics are different from either metals or polymers. Many AM systems are capable of depositing ceramics and powders have existed for many years. The lack of ceramics in AM is attributed to the lack of understanding of ceramic AM^[58]. Table 2.4 details the ceramics that have been commercially printed.

Table 2.4: Commercially Printed Ceramics

Polymer	Grade
Glass/Silica	Various
Porcelain	Various
Silicon-Carbide	Various

2.4.4.1 Advantageous situations

1. Extreme hardness. Ceramics are extremely hard, and therefore are far more resistant to plastic deformation than metals or polymers.
2. High wear resistance.
3. High stiffness. Stiffness of ceramics is very high, meaning they will not deform as much when compared to polymers or metals. However, they have comparatively low fracture toughness, so will fail catastrophically once crack propagation begins.
4. High electrical and thermal insulation
5. Non magnetic

2.4.5 Functionally graded materials

Mankind first created alloys from pure metals over 6000 years ago. While still in wide use today, alloys have limitations including restricted metal combinations due to thermal compatibility^[62]. Composites were created to overcome this issue - they allow multiple materials of different physical properties to be combined. However, composites can founder under severe conditions by de-laminating due to the large difference in properties at the material boundaries (e.g, different thermal properties). Functionally graded materials (FGM) eliminate this issue as the materials are designed to gradually blend into one another. This allows FGM materials to be configured for unique applications. Bamboo, palm trees, bone and mollusc shells are all natural examples of FGMs^[63]. These materials are created by nature, so the difficulty arises when numerically modelling them, not creating them. Much work has gone into simulating bamboo, for example, as it is environmentally-friendly building material^[64-67].

Modern engineering FGMs were first used by the Japanese Space Agency in 1984 to construct a 10 mm thermal barrier capable of shielding a 1000 K gradient^[68;69]. Computed using finite element software, the FGM modelling technique has been used to reduce stresses and improve performance of road surfaces^[70] and many multi material parts including notched plates^[71], pressure vessels^[72;73] and fuel cells^[74].

2.4.5.1 Importance of FGMs in lightweight design

As discussed during the background to research in section 1.1, FGMs can play an important role in lightweight design. Most uses for lightweight FGMs are highly specialised, as they are situations whereby low mass is required alongside **gradual** change in a second primary requirement, including energy manipulation or structural compliance

(similar to topology optimisation). Such situations do exist however, as demonstrated in this section.

Li et al.^[75] used porosity-based FGMs to alter the shape of a structured cell that would be used in a quad-copter arm. The arm needed to be as light as possible, while maintaining stiffness requirements. Using FGMs, the researchers found that they were able to reduce the mass further when compared to either the current design or a truss design, and also increase structural stiffness to enhance the performance. The results were also preferable to those gained from standard topology optimisation solvers, as the part had lower max stresses for comparable volume fractions, and could also be additively manufactured without the need for the support structures that both the truss and topology optimisation would require. Figure 2.27 shows the design space, the truss design, and the FGM re-design.

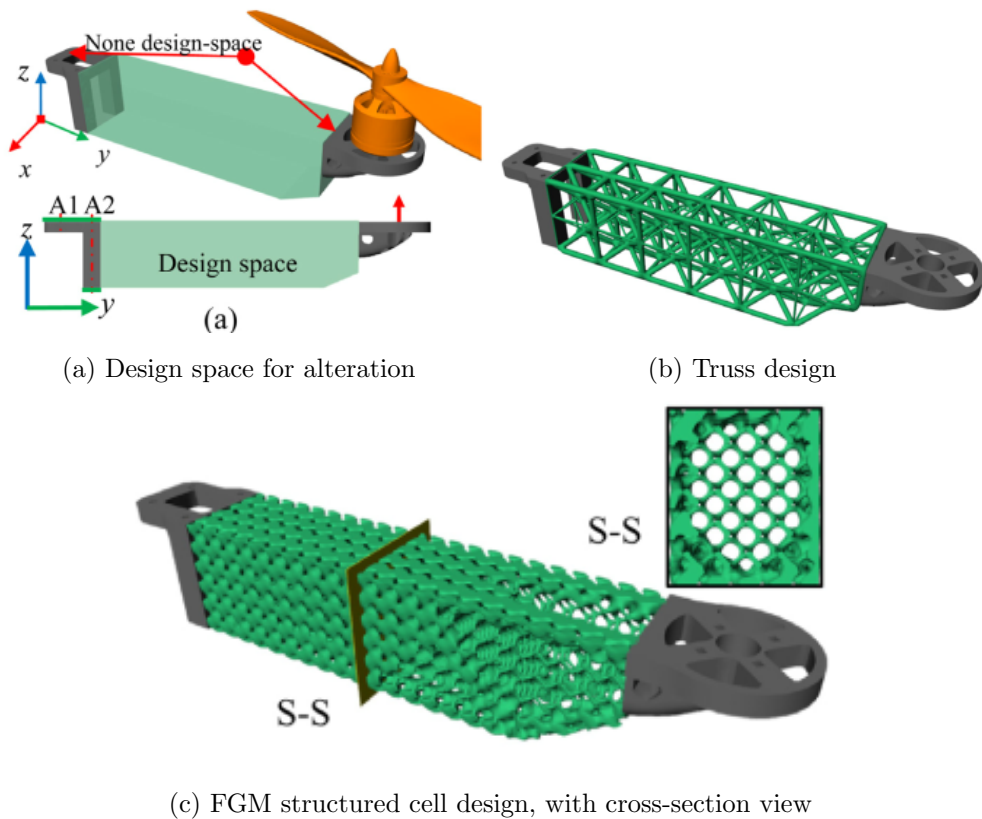


Figure 2.27: Optimisation stages of a lightweight quad-copter arm

Chen and Zheng^[76] used composition-based FGMs to create lightweight micro architectures from metamaterials with varying Poisson's ratios. The Poisson's ratio of the created metamaterial was directly dependent on the Young's modulus values of the constituent materials, and could range from extreme negative values, to zero, as shown in Figure 2.28. This is unlike most metamaterial architectures whose Poisson's ratio is dictated by geometry. Therefore, through careful choice of the constituent materials,

the researchers produced parts with varying elasticity, from soft elastomers, to hard, brittle polymers. As mentioned, high energy manipulation alongside low mass is a key use of FGMs. One possible application of this work is flexible armour - by selection of the correct materials, the functionally-graded micro-architecture can be both light, and able to absorb and dissipate large amounts of energy.

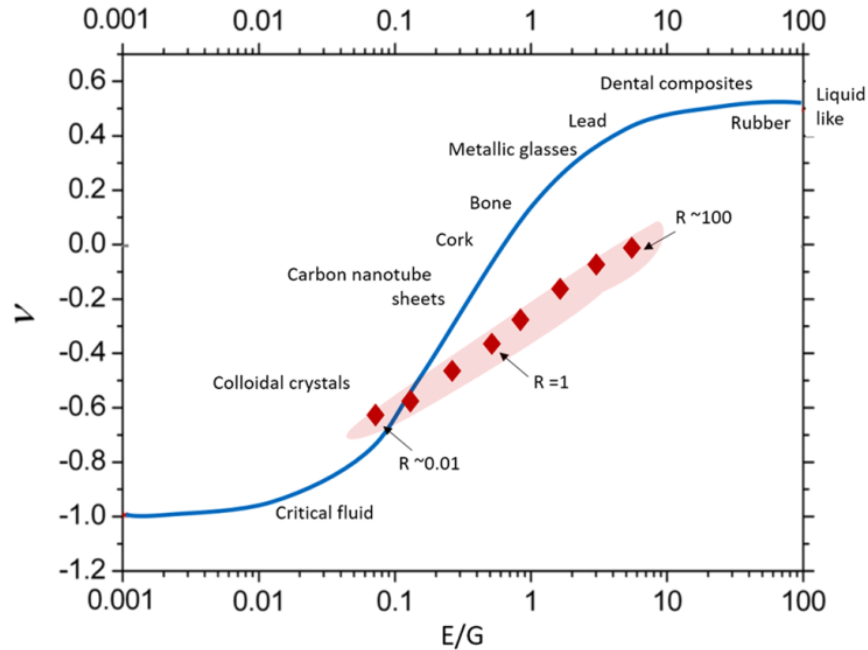


Figure 2.28: Poisson's ratio vs. Young's modulus/Shear modulus of micro architecture metamaterials in comparison with bulk materials. R refers to Young's modulus gradient within the micro-architecture of the metamaterials. [76]

Another example of energy manipulation alongside low mass is the original use of FGMs, credited to the Japanese space agency for a space plane thermal barrier. As known, space craft need to be as light as possible due to the high costs associated with leaving Earth's atmosphere. However, when space planes re-enter the atmosphere, extreme temperatures are experienced on the external surfaces due to air friction. However, the fuel temperature for the space plane must be kept low, and therefore there is a requirement to shield the fuel tanks against a 1000 K gradient through a 10 mm wall thickness, as shown in Figure 2.29. In order to keep mass to a minimum and avoid the high stresses due to differences in thermal expansion, the concept of grading materials together was conceived, as shown in Figure 2.30. The researchers used chemical vapour deposition to create a silicon carbide-graphite FGM, and discovered that it had far greater thermal resistance and thermal fatigue life when compared to pure silicon carbide deposited directly onto a graphite substrate. Without this FGM, the skin of the plane would either have to be far thicker (and thus heavier), or have higher thermal

stresses, and thus fail faster.

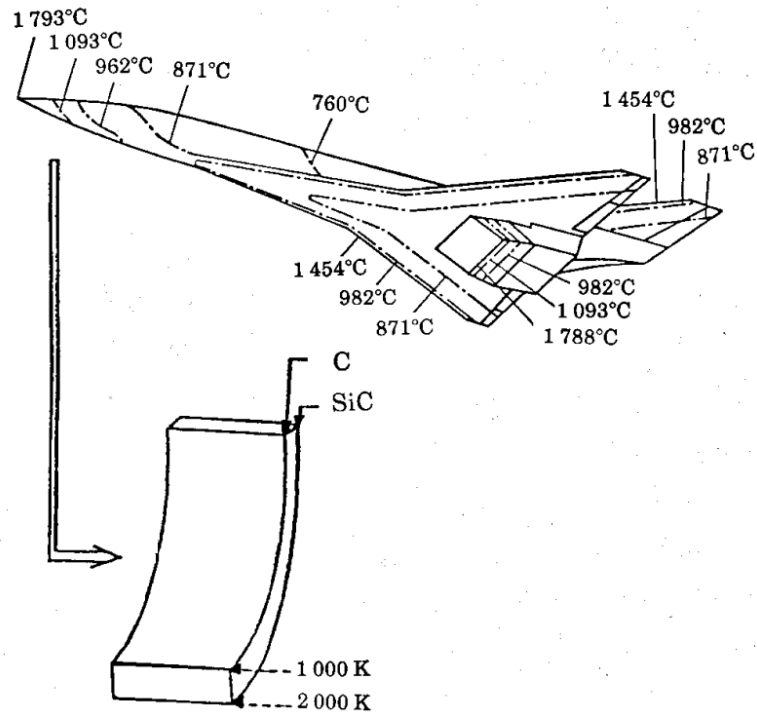


Figure 2.29: Schematic for the requirement of a 1000 K gradient through a 10 mm wall thickness^[77]

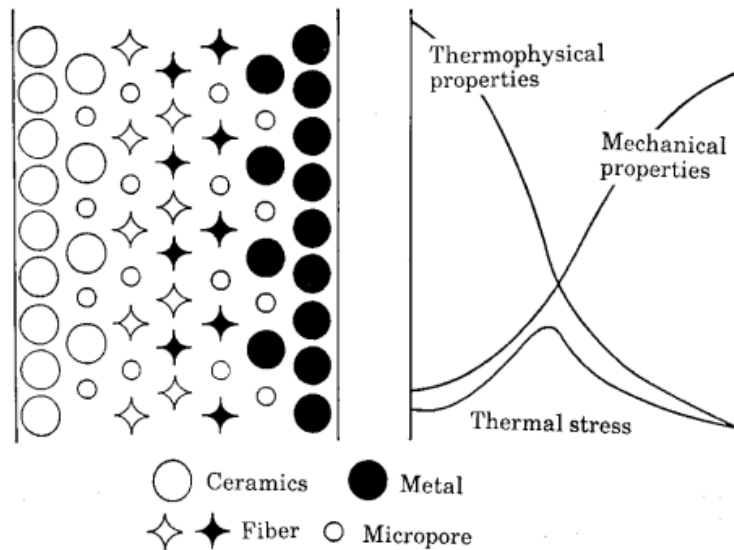


Figure 2.30: The original FGM concept^[77]

Biomedical applications have also received interest from FGMs. Hazlehurst et al.^[78] used porosity-based FGM techniques to control the stiffness and reduce the mass of femoral stems. This technique is powerful, as it not only reduced the mass of the

implant and thus stresses on surrounding body parts, it also showed promise being able to accurately match the stiffness of the bone the implant would be interacting with, thus reducing potential bone fractures. The parts ended up being 48% lighter and 60% more flexible when compared to conventional implants. Figure 2.31 shows the conventional implant, and the FGM design.

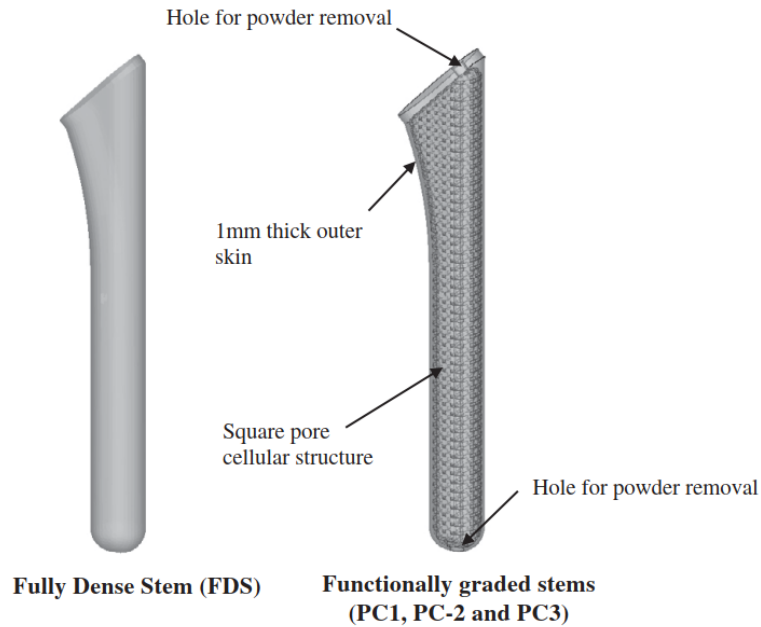


Figure 2.31: The fully dense implant compared to the FGM re-design^[78]

Work related to this is demonstrated in section 2.5.3.3, using FGMs to create implants with increased bio-compatibility.

As shown, FGMs are extremely useful for lightweight applications when a second primary requirement must be gradually changed in order to maximise its benefit - usually in order to minimise stress mismatches. The practicality of FGMs has increased in recent years due to the advances of manufacturing techniques able to produce them, and will continue to increase as more work is undertaken, be that on manufacturing, modelling, or representation^[79]. The next sections describe the main characteristics, and differences within each.

2.4.5.2 FGM classification

FGMs can be classified in two ways. The first is by geometry - either “thin” or “bulk”. “Thin” include coatings, often deposited using vapour deposition or plasma spraying. “Bulk” include 3D parts and can be produced using powder metallurgy and centrifugal methods. However, AM is best suited to fully realise the potential of bulk FGM. Laser AM techniques are currently most widespread in FGM^[62].

The second classification of FGMs uses what is being graded. Microstructure-, composition- and porosity-gradation are the three broad categories^[80]. In reality, all FGMs are homogeneous sections combined into a heterogeneous part when viewed at a small enough scale. However, the distinction of “continuous” and “discontinuous” is used to categorise different FGMs when viewed at a larger scale^[62], as the individual layers are still visible/noticeable, be it percentage change of material in a composition based FGM or visible porosity variation in a porosity based FGM^[81]. This is visualised in figure 2.32.

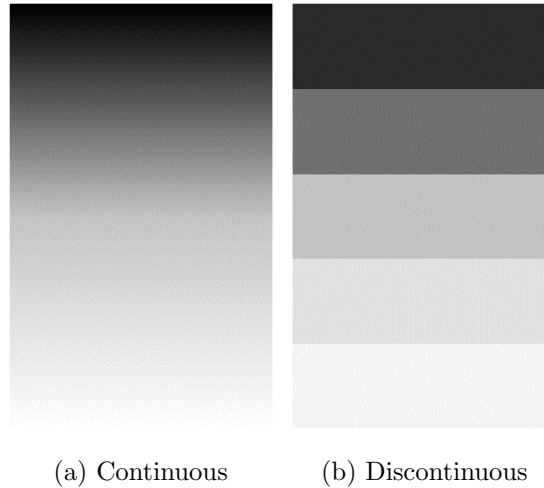


Figure 2.32: Continuous vs Discontinuous representation

The FGM is created by updating the material properties at each Gauss point of the finite element, unlike traditional finite elements that have constant material properties throughout each element^[80]. Much work on FGMs begins with numerical simulation, followed by physical prototyping. This can create problems when manufacturing - the closer to a true “continuous” gradation that is created when simulating the part, the more difficult it is to physically create the part.

2.4.5.3 Material gradation options

2.4.5.3.1 Microstructure gradation Microstructure gradation is only possible when using AM to create the parts, and therefore is the most niche of the three FGM techniques. Popovich et al.^[82] using SLM to vary the microstructure in an Inconel part. The microstructure was controlled by altering the laser power and scanning speed of the SLM hardware. Changing the microstructure allowed the surface of the part to become more wear resistant (but more brittle) and the bulk of the part to become tougher^[82]. As this change was gradual, residual stresses are minimised. Figure 2.33 shows the graded microstructure, with the size of grains visibly changing over the build direction.



Figure 2.33: Microstructure gradation^[82]

2.4.5.3.2 Composition gradation Grading by composition is a common FGM technique, used when combining one material into another. This can be applied to bulk parts, or surface coatings^[83]. As with the other gradation techniques, the stresses between the material layers will be lower as the degree of grading continuity increases. A visualisation of graded composition is shown in figure 2.34.

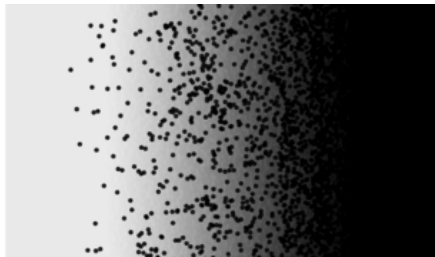


Figure 2.34: Composition gradation^[84]

2.4.5.3.3 Porosity gradation Porosity gradation is only realistically possible with additive manufacture, due to the complexity of altering shapes and difficulty other manufacturing technologies would have with this. Porosity gradation can be combined with composition gradation to achieve a part which alters material and geometry. As mentioned, porosity gradation can be described as either continuous or discontinuous. An example of both is shown in figure 2.35.

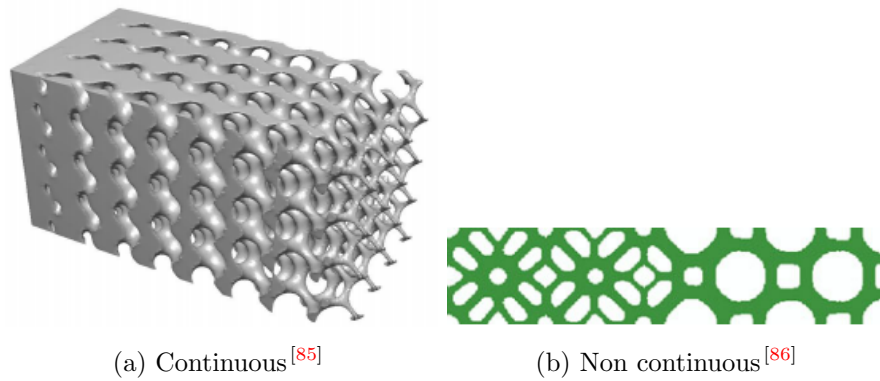


Figure 2.35: Porosity gradation

2.4.5.4 Material representation approaches

It is difficult to represent the materials of a FGM on current CAD software^[83], as the material may spread across mesh boundaries that are created to represent the geometry of the part. Irrespective of the how the material is distributed within an FGM, at any point within the part, the summation of all the composition materials must be equal to 1. Mathematically, this is represented as $M_X = [m_1, m_2, \dots, m_n]$, where M_X is the material composition at point X in the part (which must be equal to 1) and m_n is one of the composition materials^[87;88]. While physically impossible for a point in a part to have properties that are the sum of other material properties, this approach is a fine assumption to make when working at the macro-level^[83]. If FGM is used for constructing lightweight robotic arm links, this technique will be used.

Material can be distributed in a FGM using four techniques - geometry-independent functions, distance-based functions, blending functions and sweeping functions. Geometry independent functions do not take into account the shape the material is filling, and the material grades in the directions of the coordinate system chosen. Though slightly primitive, this is an extremely robust technique, as it only depends on the volume fractions of the composition materials^[89]. Distance-based functions are designed to create FGMs at set distances from geometric features of a part^[90]. An example is shown in figure 2.36, where a surface coating is gradually blended into the body of the material.

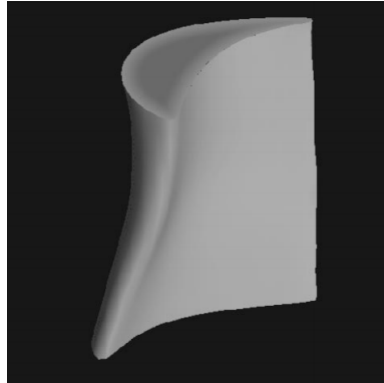


Figure 2.36: An example of distance based FGM^[89]

Blending functions are used when multiple features at different distances from one another need material blended at a set composition rate, for example, between the two edges of an hourglass-shaped part^[91]. The sweeping technique works just as it does in other situations - a 2D version of the FGM is created, and then swept around the part by following an edge. Allowing the sweep in multiple dimensions means that the cross section does not have to be constant^[89].

If FGMs are to be used when making a lightweight robotic arm link, the material distribution will need considering. A geometry-independent function may be chosen, as it does not depend on the shape of the part, and implementation is very robust.

2.4.5.5 FGM representation approaches

FGM representation has to take into account both the material and the geometry. There are two ways to represent FGM parts. The first, sequential representation, models the part as a solid object with no material information then subsequently adds the material information (the FGM itself)^[83]. Work to characterise sequential representation has been done^[92]. It starts with the geometry, and then partitions the part up into areas that will be most efficient for material definition. An image of this process is shown in figure 2.37.

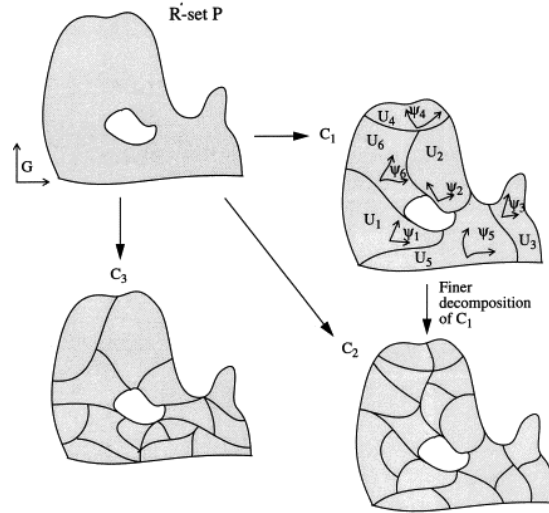


Figure 2.37: Partitioning for sequential representation Kumar et al. [92]

The second technique is parallel representation, whereby the geometry and material are established simultaneously. The volume of the part is broken into smaller volumes whose form is decided by both the geometry and material requirements. The shape of these small volumes dictates how they are represented, be it using voxels [93] or polyhedrons [94].

If FGM is to be used, a sequential representation will most likely be used, as the lightweight robotic arm link may well have a form defined before materials are examined.

2.4.6 Conclusions

Looking at material properties, both the strength to mass ratio and stiffness to mass ratio are important when choosing materials for a lightweight robotic arm link. All classes of materials have their own advantages when used for a lightweight design task, as there are many potential material requirements, depending on the loads, geometry and environment the arm will be operating in. Combining materials using functional grading allows advantageous properties of different materials to be realised. As such, they may be used when designing a lightweight robotic arm link. **Many knowledge gaps exist in the field of FGMs, but, for the purposes of lightweight robotic arm link design, a potential gap is discovering if FGMs can be used in a range of applications, and how well, if at all, they integrate with other lightweighting techniques, such as structured cells and topology optimisation.**

2.5 Manufacturing Technique

As seen in 2.4.5, functionally graded materials vary their material and/or porosity over distance. For this reason, they are of significant interest to lightweight design, as heavier materials can be placed only where required. Therefore, this section on manufacturing technique will focus on functionally graded materials

2.5.1 Manufacture of FGMs

Manufacture of FGMs can be broken down into gas-based, liquid-based or solid-based [95]. Some technologies are more versatile than others. Some of the prominent technologies in each category will be briefly described below.

2.5.1.1 Gas-based

2.5.1.1.1 Chemical vapour deposition Chemical vapour deposition (CVD) can be used to make thin/coating FGMs only [81;95;96]. It uses a gas (typically bromide, hydride or chloride) to accelerate the FGM coating particles onto the surface of the bulk structure. Altering the deposition temperature, gas pressure, flow rate, types of gas and gas ratio controls the grading of the FGM [97]. CVD allows accurate control of material composition at a low temperature, which gives a near net shape finished product [95;98;99].

2.5.1.1.2 Thermal spraying Although time consuming, thermal spraying can be used to make bulk FGMs as well as thin FGMs [95]. This covers a range of spraying techniques including flame, HVOF, detonation gun (all energised by a chemical source), wire ARC and plasma (both energised by an electrical source). As such, a variety of deposition temperatures, speeds and thus coating qualities can be made with thermal spraying [100]. Functionally graded thermal barrier coatings are commonly made with thermal spray processes [101–106], as the FGM limits the thermal stresses between the coating and the substrate.

2.5.1.2 Liquid-based

2.5.1.2.1 Centrifugal casting Centrifugal casting is a bulk-only FGM technique which can only make cylindrical parts [62]. When spun, the centripetal forces grade the different molten materials based on their density and the structure is slowly solidified to hold the as-produced structure in place [107–109]. A diagram of the process is shown in figure 2.38a.

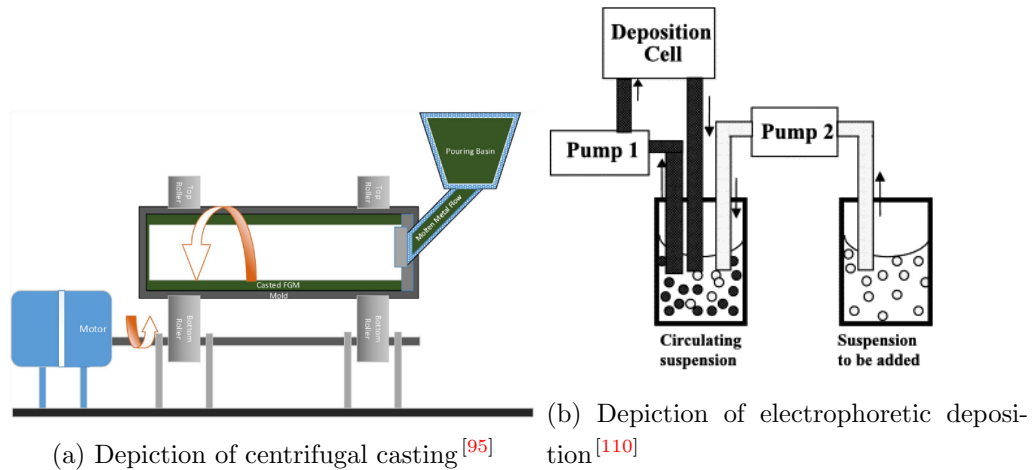


Figure 2.38: Liquid-based FGM production techniques

Altering the pouring temperature, mould temperature and rotation speed control the FGM characteristics^[111]. Metal and metal ceramics have both been created using centrifugal casting^[112–116]. However, despite studies into the manufacturing principles of centrifugally-casted FGMs^[117], precise control of the final material composition remains a great challenge^[95].

2.5.1.2.2 Combustion Creating FGMs using combustion covers any technique which chemically reacts two raw materials at high temperatures, including reactive combustion forging, reactive casting and reactive SHS extrusion. It is a bulk only FGM technique that is extremely simple - the raw materials are powdered, mixed and then combusted. To begin combustion, a point heat source is directed at one location until an exothermic chemical reaction occurs (at a high temperature). The remaining powder then subsequently undergoes the chemical reaction via a chain reaction. Combustion FGMs are quick to produce and extremely well consolidated^[95]. The form of parts possible is limited by the arrangement limitations of the powdered material. Ceramic FGMs are often investigated using combustion techniques, due to the high temperatures needed to chemically react them^[118–121].

2.5.1.2.3 Electrophoretic deposition Electrophoretic deposition (EPD) covers electrocoating, cathodic/anodic electrodeposition and e-coating. It can be used to make both thin and bulk FGM parts^[95]. Only electrically conductive materials can be used. The FGMs are placed into a suspension and the substrate (also in the suspension) is then electrified, which causes the FGMs to bond onto the substrate. It is a versatile FGM coating technology, as the substrate being coated can be extremely complex in shape. To alter the composition of the coating, the concentration of the materials in the suspension can be changed. This factor, combined with its simplicity and short

processing time, are advantages of this process^[122]. However, these advantages are diminished when making bulk parts - the thickness of the part is directly correlated to the length of time the electricity is running. Making parts thicker therefore requires extra time, and bulk parts can only be formed into simple solid geometries (mainly plates). For this reason, most EPD FGMs are coatings. A diagram of the process is shown in figure 2.38b.

2.5.1.3 Solid-based

2.5.1.3.1 Spark plasma sintering Contrary to its name, spark plasma sintering (SPS) uses neither a spark, nor plasma^[123]. The process uses an electrical current passed through two graphite dies to heat and squeeze a compacted powder. Different materials require different strengths of electrical current to process them. Since the current is easily controlled using SPS and therefore different temperatures can be easily obtained, it is a useful technique for creating FGMs^[95]. It is capable of making bulk FGM parts^[124–128], not coatings on existing parts. However, it can make nano-scale standalone parts (which many FGM processes cannot), as the combination of heat and pressure means that heating rates, processing times and cooling rates can be very high^[129]. The short time at high temperature also mean that unwanted chemical reactions between the constituent materials are minimised^[130]. The ability to re-heat in order to soften and incorporate regions of the FGM which did not melt as intended during the first heat cycle is also advantageous^[127;131]. The major disadvantage of SPS is the inability to produce intricate designs such as lattice structures.

2.5.1.3.2 Powder metallurgy Powder metallurgy (PM) is a bulk FGM technique. To create the FGM, the constituent powders are stacked into a mould, compacted and then sintered, either with or without pressure applied to the mould^[132;133]. Altering the sintering temperature, dwell time and pressure will affect the quality of the FGM. As such, the chemical composition and microstructure of the FGM can be well controlled using PM^[134]. Akin to SPS, the process is not able to make intricate bulk FGM pieces due to the process setup.

Studies comparing SPS and PM have found that SPS can produce slightly more dense parts that have significantly higher bending strengths when compared to PM parts^[135]. The properties of PM parts can be improved via further heat treatments, though^[136].

2.5.1.3.3 Additive manufacture Depending on the specific technology, additive manufacture can be either a thin or bulk FGM technique. The process for different AM hardware alters, but follows a similar idea - the material is deposited layer by layer where it then solidifies, either by chemical reaction (UV polymerisation, sintering, or

cooling from molten to name three techniques)^[83]. Some of the AM techniques listed above are more convenient for making FGMs than others^[137] - if the technique requires material changeover and cleaning between printing different materials, it is not as convenient as a technique which does not require said steps^[81]. A large benefit with certain AM hardware is its ability to produce intricate geometries^[38;138]. Compared with the technologies mentioned above, additive manufacture has been shown as more precise and accurate^[139], and therefore it is nowadays the predominant technique for producing FGMs^[38]. Other advantages when compared to include greater utilisation of material, production speed and lower energy requirements^[81].

2.5.1.4 Conclusions

Of the manufacturing options for FGMs, additive manufacture gives the greatest flexibility to FGM creation. For this reason, as well as its ability to produce any conceivable form with a wide range of internal structures, from many materials which are currently used in lightweight applications, it will be taken forward for further research.

2.5.2 Additive manufacture

Parts created when material is removed from a solid block are called “subtractive” processes. Parts created using moulds are known as “formative” processes. Both of these classes come under the banner of “traditional manufacture”. This section will describe manufacturing processes that add material rather than removing it: so called “additive manufacture”.

2.5.2.1 Overview

Since 1986^[140], layer-by-layer manufacturing techniques have been in development. Additive manufacture (also known as additive layer manufacture (ALM)) is the production of three dimensional objects from a digitally-generated file. A key factor of AM is its ability to produce final parts - a fundamental difference when compared to rapid prototyping (RP). As mentioned in section 2.5.1.3.3, while the production (building) method can vary, the basic process flow of AM is similar for all technologies.

There are many different AM techniques that have been developed, each with its own advantages and disadvantages. In order to formalise the techniques, the ASTM created a set of standards to place all AM techniques into seven categories^[141]. These are listed below:

1. Vat Polymerisation
2. Material Extrusion

3. Material Jetting
4. Binder Jetting
5. Powder Bed Fusion
6. Direct Energy Deposition
7. Sheet Lamination

Ideally, the properties required from the part should influence which AM hardware is used. However, often there is no choice of hardware available (often due to financial constraints). The process parameters of available hardware can often be altered to produce a wide range of mechanical properties^[38]. The importance of process parameters should not be overlooked - they can have a very significant impact on the mechanical ability of any AM part^[142-145]. A selection of these are briefly discussed below.

2.5.2.2 Vat Polymerisation

Vat polymerisation covers StereoLithography, Digital Light Processing and Continuous Digital Light Processing - the common trait being the use of UV light to cure the part. Due to the necessity of UV curability, the parts are made from photopolymer resins. The first layer covers the entire surface of the building platform. This allows for any supporting structures that may be needed to be constructed as the build progresses. It also anchors the different features of the part in place^[146]. An SLA set up is shown in Figure 2.39a. The build platform is lowered layer-by-layer into the resin container for each subsequent layer to be printed. Once all layers are printed the un-cured resin in the container is drained, allowing it to be reused. To make parts more accurately the process can be inverted, with the UV light shone through a clear panel on the underside of the resin container^[147]. This improves surface finish, amongst other issues. Figure 2.39b shows a schematic for an inverted system.

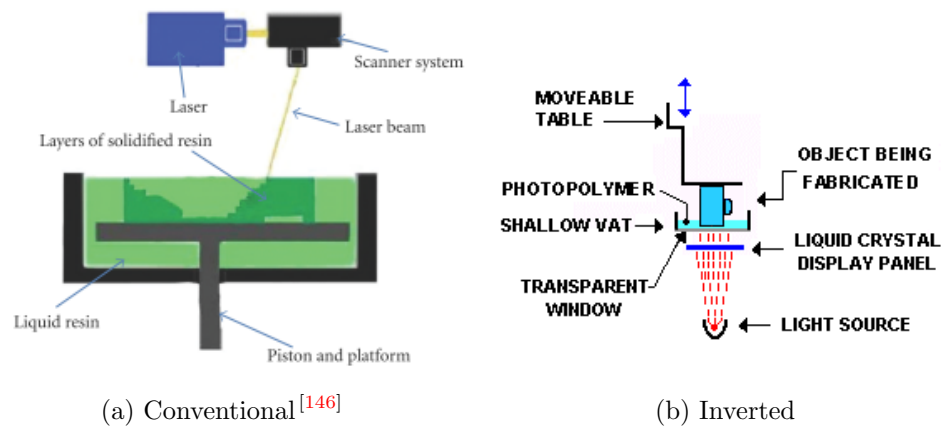


Figure 2.39: SL Set-ups

Overexposure to the UV light is a source of error for SL. It causes over curing in parts which leads to warping and undesired final features. Because it is a liquid-based process, errors from poor resin flow control can also lead to features being cured which are not intended^[148].

2.5.2.3 Material Extrusion

Material extrusion covers fused deposition modelling (FDM), a polymer and composite AM technology. A roll of filament is fed to a deposition head and melted prior to being extruded in a bead. A schematic of an FDM set up is shown in Figure 2.40.

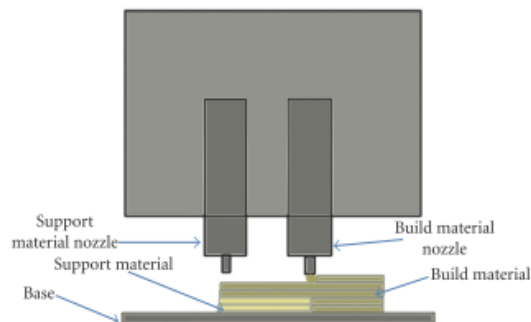


Figure 2.40: FDM Setup^[146]

The equipment is cheap when compared to other AM systems, however the resolution is worse^[146]. This is due to the minimum bead dimensions that are possible, typically 0.25 mm. As a result, the staircase effect can be significant in FDM parts and post processing is often needed to create the required surface finish. Warping can also be a problem due to the thermal gradient when FDM is operational^[146]. Multiple nozzles can easily be used simultaneously, meaning that multi material parts can be created

with ease. At least two nozzles are typically used - one to supply support material and the other to supply the build material.

2.5.2.4 Powder Bed Fusion

Powder bed fusion covers powders fused with laser (SLS, DMLS), electron beam (EBM) and a combination of laser and binding agent (MJP). This review will focus on those fused with laser only.

Selective Laser Sintering (SLS) and Direct Metal Laser Sintering (DMLS) are powder bed fusion processes which use a point-wise laser scanning technique to fuse layers of material into the final 3D object (see Figure 2.41). The layer thickness is variable, but can be as thin as 0.1mm. The powder is fed from cartridges and then rolled (using anti-clockwise rotating rollers) onto the build platform. The build platform itself is kept at an elevated temperature (just below the part materials melting temperature/glass transition temperature) using an IR heater or resistive heating coil to reduce laser power consumption (less power required to reach material fusion) and reduce thermal shock in the part, which reduces the risk of warping.

When the thermal stresses are above the material strength, plastic deformation and thus distortion occurs. As seen in Figure 2.42b, parts are often built on a solid substrate to further reduce curling and thermal stress issues^[150]. Once the powder has been rolled on the powder bed, the laser is activated and a small melt pool created. The size and stability of the melt pool will dictate the porosity and surface roughness, and thus must be carefully optimised^[150]. The laser

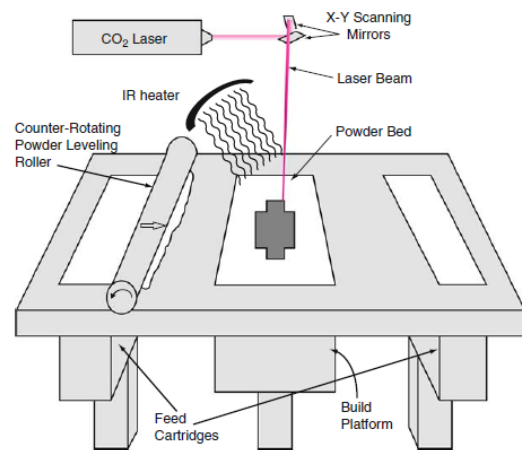


Figure 2.41: Selective Laser Sintering^[149]

is directed using galvanometers (motor-mounted mirrors) to ensure that the particles fuse in a set order. The surrounding material that is heated (but not laser fused) acts as a support for the part being built^[150]. Between each layer, the build platform is lowered by the distance equal to the height of one layer, allowing the anti-clockwise roller to deposit the subsequent layer. This distance must be carefully chosen - too small and the build will be prohibitively time-consuming, too large and the staircase effect will be too significant (see Figure 2.42a). The staircase effect arises from the conversion of the 3D CAD file into layers - these layers are an approximation of the nominal shape of the part and as such become surface roughness defects. The problem is more pronounced when curves are

being created [151].

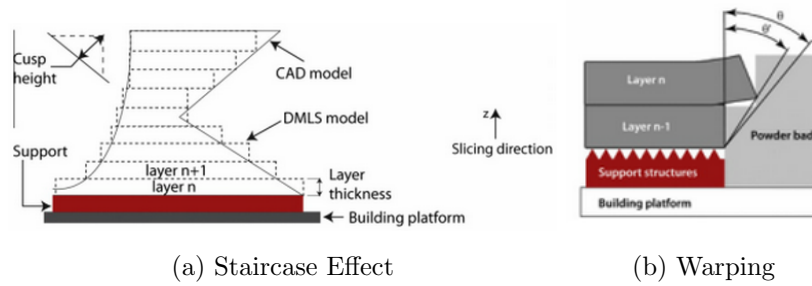


Figure 2.42: PBF Problems [151]

2.5.2.5 Direct Energy Deposition

Unlike PBF methods which use an anti-clockwise roller to position and grade the powder particles before melting, direct energy deposition (DED) delivers the feedstock moments before it is melted (a “just-in-time” process), similar to material extrusion. The difference between DED and material extrusion is the flexibility of the deposition head - it is usually fitted to a five or six DoF manipulator, not on fixed axes (as is the case with material extrusion). The feedstock can either be powder or wire.

Laser Engineering Net Shaping (LENS) is powder DED technique. Through the use of multiple powder feeds, many different materials can be delivered to the melt zone at once. Because the particles are fully melted by the high-power laser, the subsequent parts are very dense [152] with mechanical properties that can exceed those generated when using “traditional” manufacturing methods [153]. The design of the powder feeding nozzle must be carefully undertaken, as it plays a decisive role in the deposition process [154].

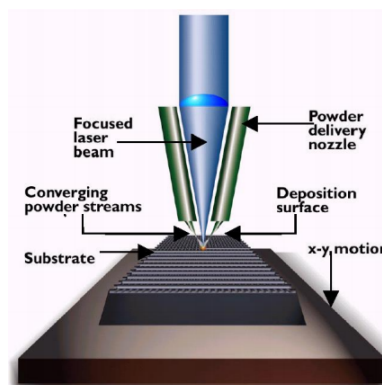


Figure 2.43: Laser Engineering Net Shaping [149]

Since it uses a CNC-style set-up, LENS is capable of producing large (up to 1500 mm in length) freeform objects. The direct material feed makes LENS far more qualified

than PBF methods for making FGM parts^[38;137].

Wire Arc Additive Manufacture (WAAM) is a wire DED technique. As such, all feedstock material is used (it all reaches the melt area), meaning the process is 100% efficient in terms of material usage. This also means that the deposition volume can accurately be tracked, as it is exactly equal to the volume of wire which has been used. Wire-deposition generally has a higher purity than powder DED (LENS) because it is less prone to contamination from foreign particles due to its lower surface area^[155]. It also has a higher deposition rate and is easier to transport and store than powder. However, being in wire form also results in difficulties when the part to be created is complex, as the wire diameter and feed rate have a large impact on the possible dimensions and geometries. These properties are far more difficult to control in wire fed deposition than powder fed deposition.

Complex geometries are difficult to create since wire parameters which control high accuracy alongside low porosity are difficult to regulate and alter as required^[156]. FGM is also difficult due to the nature of the feedstock (it is not as easy to “mix” wire feeds as it is powder feeds)^[38].

2.5.3 Multi-material ability

Section 2.4 showed that additive manufacture was far more flexible at creating FGM parts when compared to other FGM technologies, such as powder metallurgy and centrifugal casting^[96;157]. This section discusses which additive manufacturing techniques have been used to create FGMs.

2.5.3.1 Vat polymerisation

Since polymers were the dominant printing material during the infancy of AM (when RP was the main use of layer-wise construction), a great deal of work has gone into the creation of multi-polymer structures^[158;159]. Work at the W.M. Keck Center for 3D Innovation has assessed both the performance of multi material polymer parts and the practicality of physically printing them using Vat polymerisation^[160]. When using SLA, the printing surface must be immersed in the photopolymer. This requirement makes it more work intensive than direct energy AM techniques, as vats of different photopolymers are typically needed to be switched out when a different material is needed to be printed. The W.M. Keck Center developed an SLA machine that has a carousel, meaning that up to three different materials can be printed autonomously (no need for human interaction to switch out photopolymer vats). The machine can be seen in Figure 2.44a.

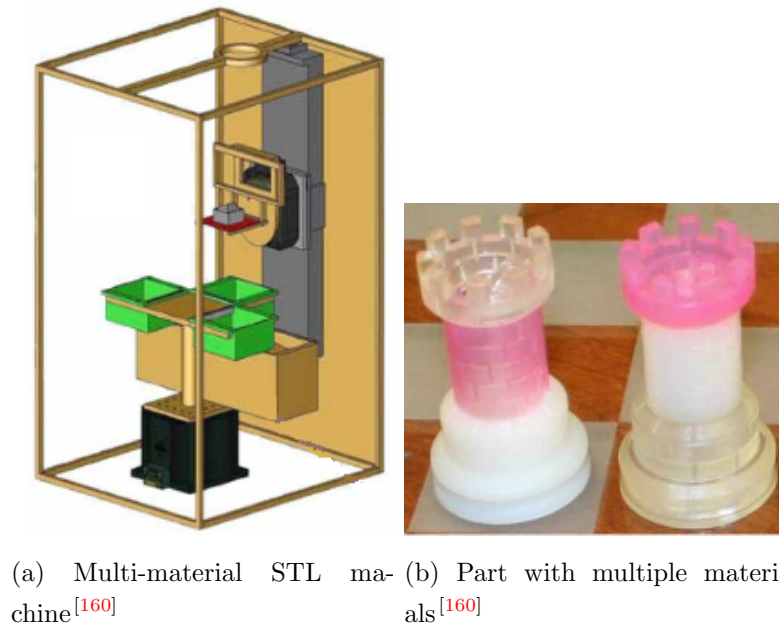


Figure 2.44: Multi-material ability

This machine has given great flexibility to multi-material STL printing as it makes printing of multiple materials on the same layer easy^[160]. This can be seen in Figure 2.44b. However, it must be noted that these parts are purely aesthetic, not structural components.

More recently, vat polymerisation has been used to make porosity-graded FGMs, more common with non-direct energy techniques, such as vat polymerisation. Yu et al.^[159] used SLA to fabricate both graded and uniform Schwarz Primitive and gyroid structures (see Figure 2.45) - two implicit surface-based cell designs (Section 2.3.2.3). In both cases, it was found that the graded structures absorbed more energy to at the densification than the uniform structures, despite the earlier onset of densification itself. These structures are geometrically complex, especially when porosity-graded. The results showed that SLA could accurately produce the parts, showing the possibility of SLA as a viable FGM technology for lightweight design in applications requiring energy absorption.

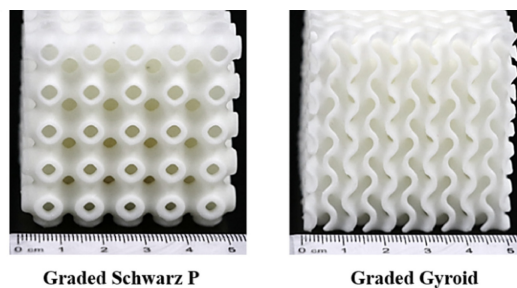


Figure 2.45: Implicit surface-based porosity-based FGMs created with SLA^[159]

Mahbod and Asgari^[158] similarly used SLA to create porosity-based FGMs. The researchers were aiming to test the mechanical response of a new unit cell design - a double diamond dodecahedron (see Figure 2.46). Using SLA, the researchers fabricated uniform and porosity-graded versions of the unit cell. In agreement to Yu et al.^[159], the FGM unit cell deformed layer by layer in sequence of decreasing porosity (from thinnest to thickest strut). In contradiction to the work from Yu et al.^[159], the researchers found that the functionally graded cells absorbed less energy than the uniform cells, showing the importance of cell geometry when designing for particular applications. This work, along with that from Yu et al.^[159] shows the capability of SLA to produce highly intricate FGMs with surface finishes of high quality when compared to other AM techniques.

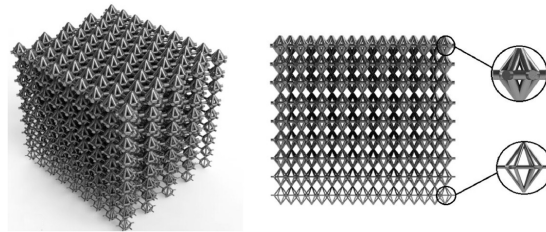


Figure 2.46: Double diamond dodecahedron unit cell design^[158]

2.5.3.2 Material extrusion

Unlike indirect AM processes, material extrusion can be modified comparatively simply to produce composition-based FGM parts - the build nozzle needs supplied with various required constituent materials for the build. Ren et al.^[161] developed such a machine, with three inks being fed into the deposition head via an inline mixing device, see Figure 2.47. A proof of concept composition-based FGM was first made with different coloured dyes in 1D, 2D and 3D, followed by two further tests - one which increased percentage of Al_2O_3 in 3D to build experience in solid particle addition, followed by one which altered the mechanical properties of the build using the third ink which altered the material hardness and modulus. By combining this grading complexity with gray-scale representation techniques discussed in Section 2.3, Ren et al.^[161] have shown it is possible to fabricate parts with composition that gradually changes in any given 3D space. However, in order for this ME FGM technology to be usable for production of consumer parts, work must first be done to enhance the print precision and shape complexity.

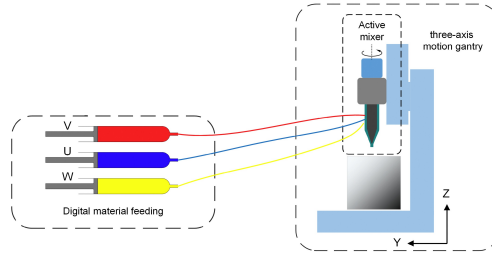


Figure 2.47: Multi material ME setup^[161]

Using the same multi-material feed concept as Ren et al.^[161], Kokkinis et al.^[162] also used ME to create parts with composition based FGMs that could be fine tuned in a 3D space. The research aimed to create bioinspired composition gradients from synthetic materials for discs in the human spine in order to produce a soft core with stiff edges. As with the work by Ren et al.^[161], the print precision requires further research, however, the 3D flexibility of ME FGM is extremely high in comparison to other AM FGM techniques - see Figure 2.48. For this reason, research into ME FGM shape complexity is a worthwhile endeavour.

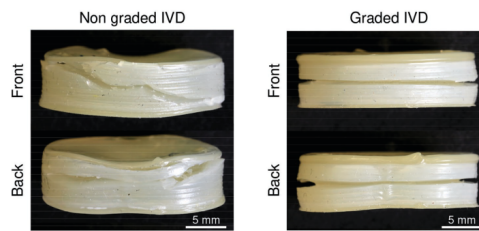


Figure 2.48: Poor print precision and shape complexity of ME FGMs^[162]

Material extrusion has been an AM technology at the forefront of carbon fibre AM research. Work at the Oak Ridge National Laboratory has created carbon fibre parts using AM using FDM technology^[163]. The bonding between fibre and matrix was not perfect due to the two components flowing differently to one another and thus voids were seen. However, it was found that increasing the fibre content decreased the voids between FDM beads due to increased thermal conductivity through the fibres. The overall result was an increase in inner bead porosity but a decrease in intra bead porosity, as seen in Figure 2.49^[163]. Despite this, the level of fibre orientation and molecular orientation was higher than that seen when carbon fibre is produced using compression or injection moulding and thus the overall tensile strength of AM parts and TM parts are comparable. In order to improve the performance of FDM composites further work is needed on fibre preparation methods, as currently the mixing process (of the fibres and the matrix) breaks the fibres. This results in more fibres which leads to a greater number of inner bead voids and thus weaker parts. Once this is done, alterations to both fibre and matrix can be researched in order to enhance bonding

between the two parts^[163].

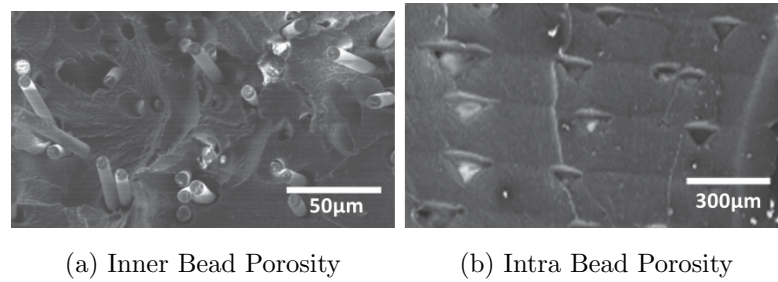


Figure 2.49: FDM Composite Voids^[163]

Further work at Texas Tech University found the influence of carbon fibre percentage on mechanical properties of thermoplastic parts^[164]. It was seen that carbon fibre inclusion improved flexural properties of parts compared to the pure plastic parts. It was also seen to increase tensile strength and Young's modulus but decrease toughness, yield strength and ductility. However, until mixing strategies and adhesion between fibre and matrix are improved, porosity remains a large barrier for FDM printing with carbon fibres alongside other materials^[164].

2.5.3.3 Powder bed fusion

As described in section 2.5.2.4, powder bed fusion lays down a layer of material before selectively melting certain areas. Because of this, composition-based FGMs are more complex to create when compared to DED, as a large portion of mixed material will not be used, and mixing many different material compositions and then separating post-build (when possible) is not cost-effective. Therefore, most PBF FGM work is porosity gradation with one material.

Li et al.^[165] used SLM to create porosity-graded FGMs from pure iron, in order to improve biodegradability of implants in the human body when compared to traditional metal implants. Using a diamond truss core as the repeated cell, the thickness of the struts was altered - the length was kept constant - see Figure 2.50. It was seen during in-vitro testing that the biodegradability of the implant altered depending on the thickness of the struts, with far increased biodegradability rates in areas of the implant with thinner struts, showing the great potential of SLM as a bone substituting material. As noted, the possibility to further increase biodegradability of implants using SLM can most probably be further improved with changes to the unit cell design.

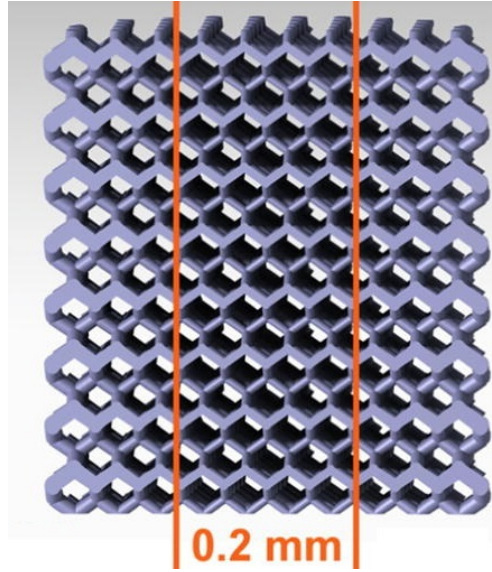


Figure 2.50: Porosity-based FGM created using SLM for bone integration^[165]

Porosity-gradation can be used to alter energy absorption of structures. Al-Saedi et al.^[166] used SLM to create F2BCC unit cell structures from Al-12Si, both uniform and porosity-based FGM, whose strut thickness again changed, while strut length remained constant - see Figure 2.51. Akin to findings from Yu et al.^[159] with SLA, it was found that, despite entering onset densification under lower loads, the FGM structure could absorb more energy compared to a F2BCC unit cell structure with uniform struts - the cumulative energy absorption per unit volume rose exponentially with strain in the FGM structure, compared to bi-linearly in the uniform structure. The FGM structures also collapsed more predictably when compared to the uniform structures, with the thinner struts collapsing first. These two features make porosity based FGM structures made with SLM very attractive for energy absorption tasks.

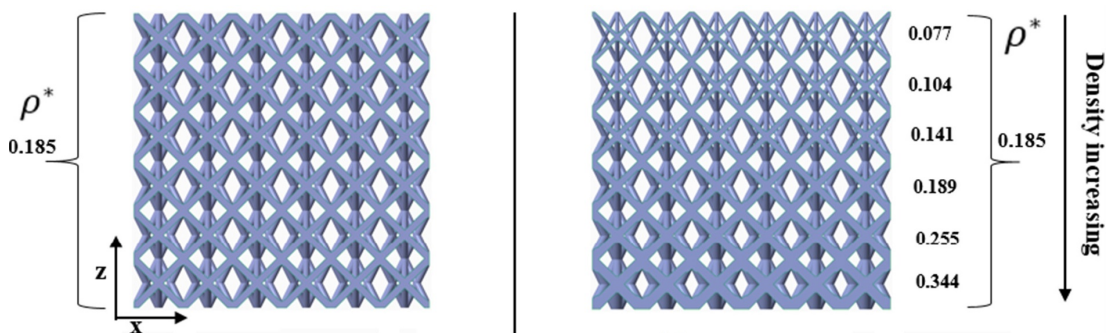


Figure 2.51: Uniform vs porosity-based FGM using SLM for energy absorption^[166]

Despite the inherent process characteristics of PBF making composition-based FGMs a complex undertaking, research has been attempted.

Work by Liu et al.^[167] modified an SLM machine to deposit two metals. This was achieved by adding a central divider to the deposition head. Powder A would flow down one side of the divider and not mix with powder B, which would flow down the other side of the divider. The lasers would then individually melt the powders^[167]. The set up was tested on 316L stainless steel and C18400 copper. The team discovered that depositing copper was difficult due to the high reflectivity and thermal conductivity of the material. These properties led to copper depositions with large voids, cracks and unmelted particles within them. Altering SLM parameters such as scan speed, laser power and hatching space could improve the copper structure^[167]. The diffusion zone between the stainless steel and the copper was successful, with a large diffusion zone (15 times thicker than the deposition layer thickness) and strong metallurgical bonding. The result was hardness and tensile strength values that lie between those of stainless steel and copper^[167].

More recently, Tan et al.^[168] have attempted to make a tungsten-copper FGM, with the hope of using it as a plasma-facing material in a fusion reactor. However, the lack of bespoke equipment (unlike that used by Liu et al.^[167]) meant that the powders were not mixed - the W powder was instead deposited on bulk copper. As such, the resulting thin interfacial FGM layer was created solely by the Marangoni effect (mass transfer between liquids based on surface tension differences - schematic in Figure 2.52). This thin FGM layer, along with the large difference in thermal expansion coefficient between the two constituent materials, led to large residual stresses. Therefore, the importance of material compatibility, especially thermal expansion coefficient, can not be overlooked.

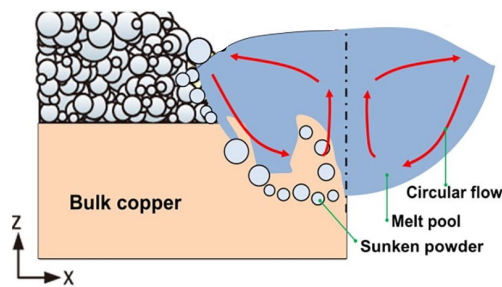


Figure 2.52: Schematic of the Marangoni effect^[168]

2.5.3.4 Direct energy deposition

Powder-based direct energy deposition has been used for many FGM experiments, due to the relative ease required to alter the percentage of each material in the blend when compared to other AM techniques. Multi material research in recent years has focussed on improving aspects of the physical build, including reduction of cracking, unmelted powder due to different properties of the constituent materials and control of process

parameters^[169–171].

Zuback et al.^[172] used powder-based DED to create a graded bond between stainless steel (austenitic) and a nickel-chromium ferritic alloy. Under traditional joining techniques, the transition between the two dissimilar alloys creates a step change in the carbon content, and thus premature failure occurs. The two materials were graded at 10% intervals and each interval was roughly 4 mm thick, see Figure 2.53. The AM parameters were kept constant during the build. It was seen that the carbon diffusion rate was “significantly diminished” using the FGM technique when compared to a traditional joining technique.

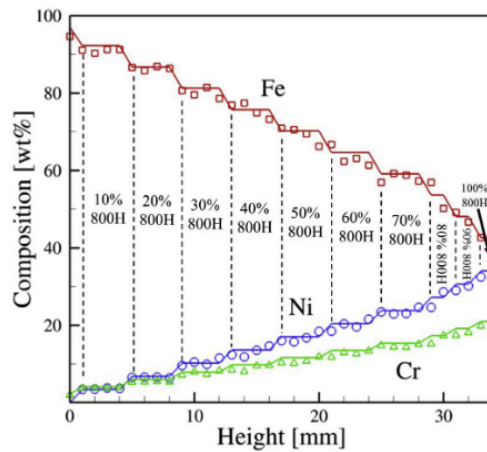


Figure 2.53: Chemical composition in austenitic-ferritic FGM^[172]

Kim et al.^[173] also conducted powder-based DED FGM tests to bond austenitic stainless steel (SS316L) with ferritic steel (P21) in order to see if the bonding characteristics and resultant mechanical properties were enhanced when compared to a non-FGM bond. Unlike Zuback et al.^[172] who used 10% grading intervals, Kim et al.^[173] used a 50% grading interval, therefore having only two interfaces at which material composition changed. Despite this, the findings showed that the intermediate layer had enhanced mechanical properties when compared to those measured in the single material areas, including continuous yielding behaviour and higher ultimate tensile strength, as seen in Figure 2.54. The higher yield stress was an unexpected result, possibly due to the accidental creation of an alloy. Nonetheless, the ability of DED to produce a stable FGM was demonstrated.

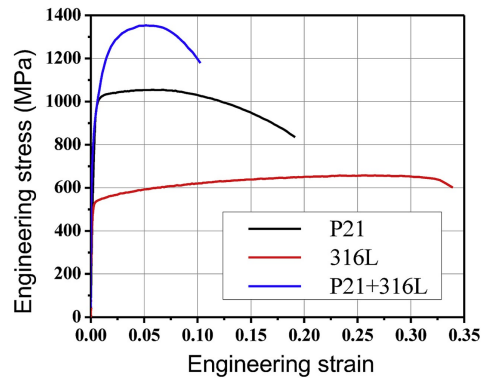


Figure 2.54: Engineering stress-strain curves of three constitutive layers^[173]

Bobbio et al.^[174] used powder-based DED to form a Ti-6Al-4V to SS304L functionally graded part with the addition of vanadium to stop Fe-Ti phases forming. The two material powders were graded at 25% intervals, and each interval was roughly 8 mm thick. However, while attempting to limit the Fe-Ti phases forming, brittle σ -FeV formed, resulting in a crack, as seen in Figure 2.55. This highlights the importance of material combinations in FGMs - a known issue in the field which needs addressed.

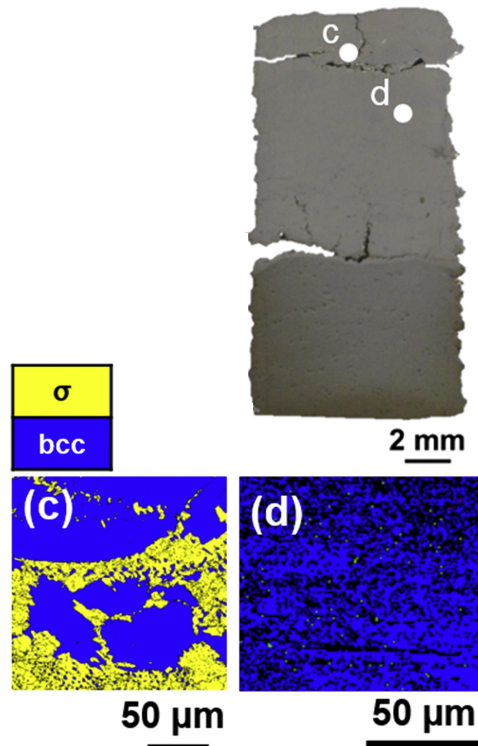


Figure 2.55: Chemical composition in austenitic-ferritic FGM^[174]

Su et al.^[175] have done comprehensive research on the impact of grading interval on the mechanical properties of Inconel 718 and 316L stainless steel on composition-based

FGMs. The work graded the parts from 100% Inconel 718 to 100% 316L stainless steel at 5%, 10% and 20% intervals. Results showed that micro-hardness increased as the grading interval decreased, indicating that the smoother the transition from one material to another, the better the the bond between the two materials is^[175]. The as deposited parts and tensile specimen template are shown in Figure 2.56. Interestingly, this was not the case for tensile strength or elongation, which were best at 10% grading intervals. The outcomes show that it is therefore important to choose the grading interval dependent on the mechanical response that is required of the application.

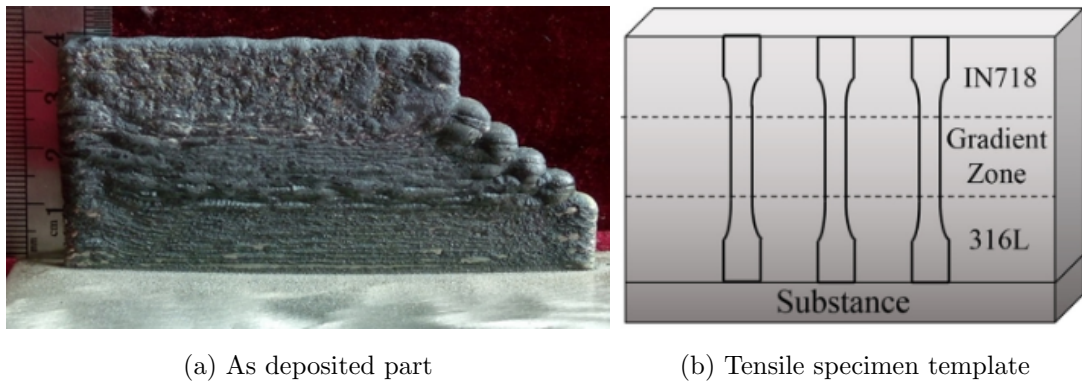


Figure 2.56: The as deposited part with layers of constituent and blended material clearly visible, and tensile specimen template

Liu et al.^[176] have theorised that the success or failure of an FGM DED build is closely related to the dilution that occurs during the DED process - the amount of alloying elements that are redistributed from previous deposition layers as a result of the laser partially remelting the previous layers. Therefore, if the dilution can be controlled via process parameters, part failure can be reduced. Ideally, the dilution ratio should be high - that is, the laser should remelt as much of the previous layer as possible when depositing the current layer, to allow the alloying elements in each layer to mix as thoroughly as possible - see Figure 2.57. This is demonstrated successfully by fabricating a Ti/Ti-6Al-4V FGM^[176].

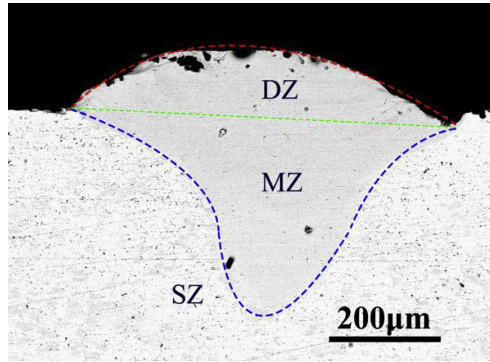


Figure 2.57: Cross section showing the parameters in the dilution ratio (DZ, deposition zone, MZ, melting zone, SZ, substrate zone) [176]

Powder-based DED has also been used to create FGMs containing ceramics. Zhang and Bandyopadhyay [177] used the LENS technique to create a Ti-6Al-4V/ Al_2O_3 FGM. The LENS process parameters were changed during deposition of the different layers, aiding the build process. Measured hardness values of the Al_2O_3 were higher than those seen in literature when created with other techniques, such as spark plasma sintering, or pressing followed by heat treatment [177]. Hardness values of the Ti-6Al-4V/ Al_2O_3 section lay between those of the constituent materials, as expected - see Figure 2.58.

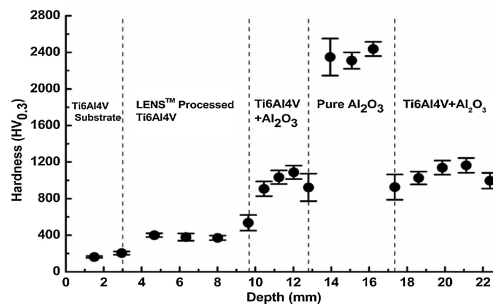


Figure 2.58: Microhardness profile of Ti-6Al-4V/ Al_2O_3 FGM [177]

Zhang et al. [178] have also used powder-based DED to create FGMs containing ceramics. This experiment created a Ti-6Al-4V/TiC FGM with a maximum volume of 30% TiC. The TiC was graded at 10% intervals. As expected, the Young's modulus increased and UTS decreased as the percentage of TiC increased [178] - see Figure 2.59. As with the result from Zhang and Bandyopadhyay [177], a further result of note was the ability to directly fabricate metal-ceramic FGMs with DED, as most ceramic production processes require intensive post-processing.

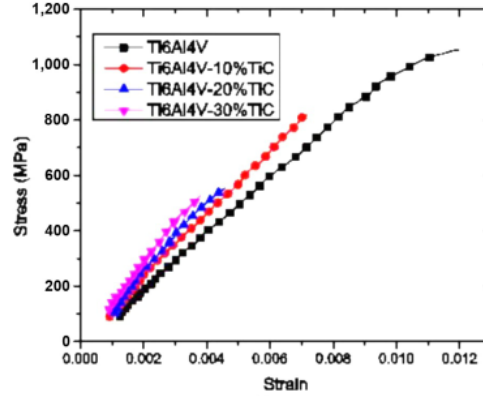


Figure 2.59: Stress vs strain of a Ti-6Al-4V/TiC FGM at varying compositions)^[178]

While powder-based DED is used far more than wire-based DED for making FGMs, experiments with WAAM have been undertaken. Chandrasekaran et al.^[179] used WAAM to create a composition-based FGM for harsh marine environments using duplex stainless steel and carbon-manganese steel. When compared to X-52 carbon manganese steel, the graded layer of the FGM was seen to have similar yield strength and increased ultimate strength, and more importantly, no enrichment of chromium across the graded layer into the carbon-manganese steel. This FGM shows increases in both strength and durability when compared to X-52 carbon manganese steel, highlighting its potential use case for marine applications.

2.5.4 Conclusions

The outcomes of the FGM literature show that there are many theoretical benefits to FGMs, and many examples of successful implementation. As noted by Reichardt et al.^[180], development during the 2010s transformed AM from a prototyping technology to a full-scale manufacturing process. However, FGM development is an ongoing task^[169;180;181].

There is no dispute among FGM researchers that further work is required, however, depending on the author, next steps should focus on different aspects of FGMs. The next steps highlighted by Yan et al.^[169] include the need for a universal database that gives information for designing the joining process, and a universal process plan of how to build physical FGMs. Reichardt et al.^[180] believes enhanced material understanding is required next in order to achieve chemical, metallurgical and thermal stability when attempting to combine selected materials from a wide range. Saleh et al.^[181] have collated the next steps, including material, simulation and mass production requirements, as shown in Figure 2.60.

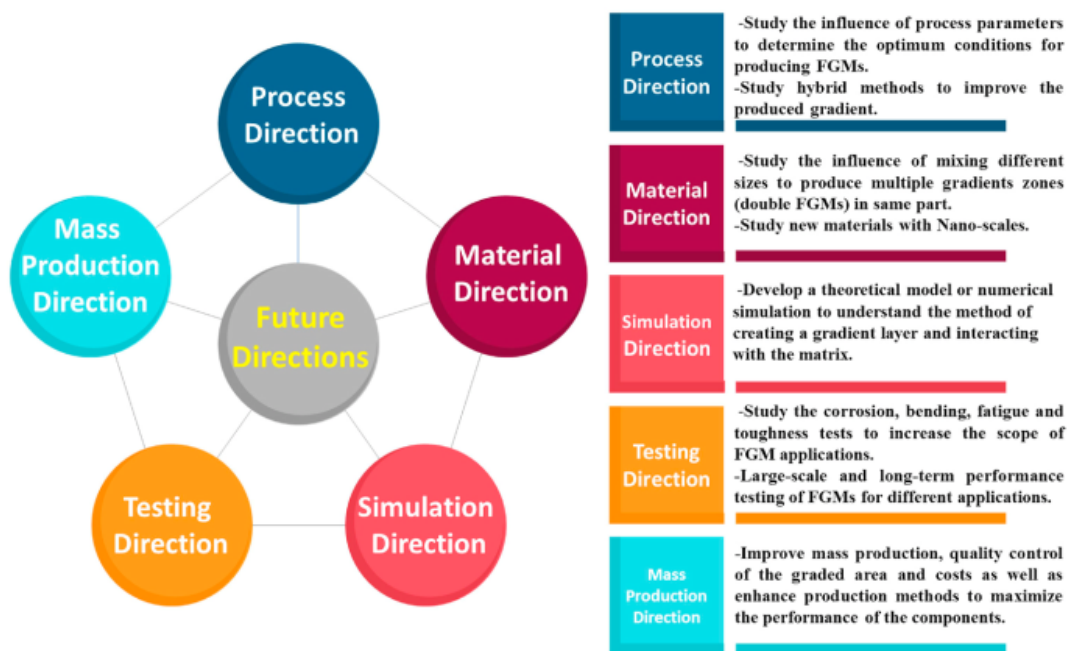


Figure 2.60: A broad spectrum of future research directions for FGMs) ^[181]

This project is not looking to develop new manufacturing methods, rather use existing/emerging technology. For that reason, these future FGM steps will not be attempted in this thesis. Rather, **using additive manufacture along with FGMs will help to close the other knowledge gaps seen**, as it allows the creation of the highly complex designs that result from many of the ideas seen in earlier sections of the literature. The choice of technology is dependent on the material(s) being used.

2.6 Cost

The first four sections of this review cover the design and physical manufacturing of FGM parts. However, up to this point, no consideration has been given to the cost of production. This is an important factor, as the greater the manufacture cost, the more compelling the reasoning must be for that particular manufacturing technique over another.

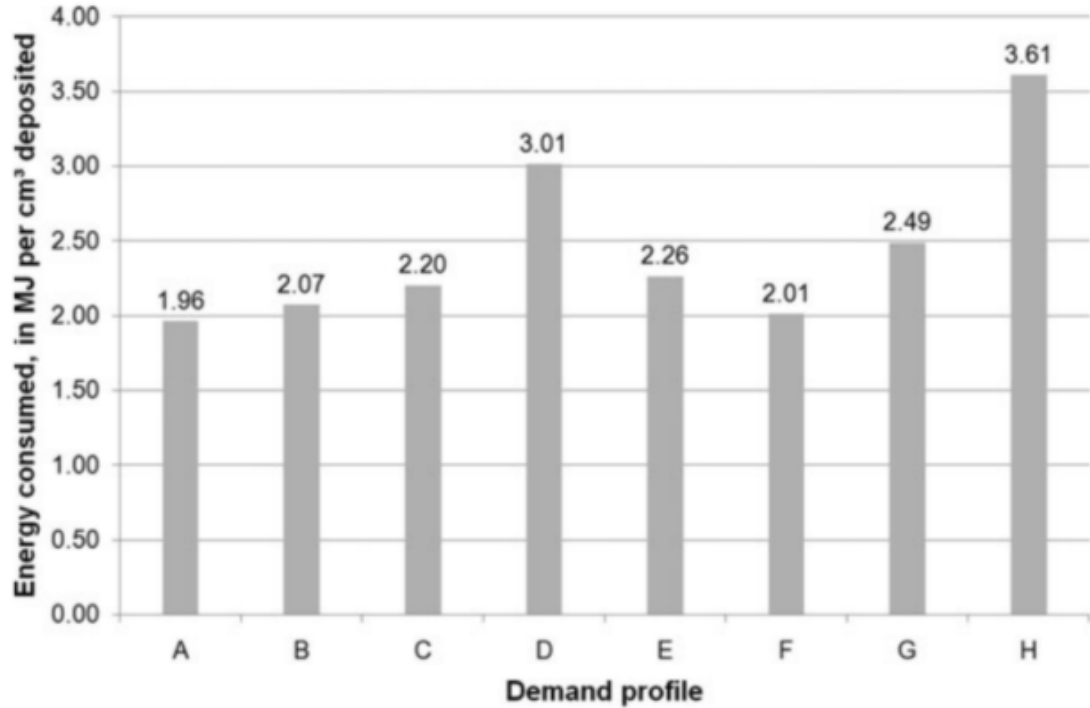
As with many technologies, as AM has matured, research has been done to reduce the cost of the processes ^[182]. This increasing technology maturity is central to reducing the cost, because, as widely agreed, the main disadvantages when compared to traditional manufacturing are the high costs - material, machine, energy and post-processing being the main ones ^[182-184]. Some example solutions of problems unique to AM are explained below. Examples of generic manufacturing issues (surface finish, for example) will not be discussed, despite their relevance to AM cost reduction.

The first example of a cost reduction technique for AM is build space optimisation. Baumers et al.^[185] studied the effects of quantity and variety of parts and thus use of available machine capacity. The findings showed that, unlike traditional manufacturing methods, process efficiency and thus per part cost, is affected by both of these variables - the more efficiently the build space is used, the lower the relative cost of each part. In order to best understand cost reduction, Baumers et al.^[185] wrote an algorithm that aims to minimise energy consumed per cm³ of material deposited using part size and part demand as variables. The authors also compared the results to a single part build - a common use of an AM machine. This energy use for different set ups is shown in Figure 2.61.

Demand profile	Quantity of parts demanded					Build volume floor area occupation (voxels)	Description
	Bearing block	Turbine wheel	Belt link	End cap	Venturi		
A	∞ (2)	∞ (5)	∞ (8)	∞ (1)	∞ (69)	92.59%	Uniform demand, excess
B	5 (2)	5 (5)	5 (5)	5 (4)	5 (5)	79.80%	Uniform demand, high
C	3 (2)	3 (3)	3 (3)	3 (3)	3 (3)	62.27%	Uniform demand, intermediate
D	1 (1)	1 (1)	1 (1)	1 (1)	1 (1)	26.32%	Uniform demand, low
E	∞ (3)	—	—	—	—	50.07%	Excess demand, largest part
F	—	∞ (10)	∞ (13)	—	—	82.37%	Excess demand, medium parts
G	—	—	—	∞ (45)	∞ (100)	97.53%	Excess demand, small parts
H	1 (1)	—	—	—	—	16.69%	Single-part build, bearing block

Notes: Values in parentheses show the actual number of parts inserted by the build volume packing algorithm. ∞ = infinity.

(a) Different tests conducted to test energy efficiency vs used build volume



(b) Energy consumed vs per cm³ of built material

Figure 2.61: Relationship between energy efficiency and used build volume in AM^[185]

As can be seen, the energy consumed per cm³ of material reduces as the percentage of build volume used increases. Due to this phenomenon, column H (a single part build) is the least energy efficient.

The authors have expanded this field of research in recent years. Whereas the original work focussed on improved cost and energy modelling for DED AM exclusively by comparing used build volumes, later work has focussed on direct comparison to

traditional manufacturing methods, using the original build volume optimisation work to show that, in specific circumstances where the part is complex and would require multiple traditional manufacturing processes, the belief that AM is only cheaper on small production runs compared to traditional manufacturing methods does not hold completely true^[186], as spare build space can be assigned to parts from other jobs - so called “synthetic” builds. By doing this, costs of the original “main” part are reduced further compared to a build volume of only the “main” part geometries, as the spare build volume capacity is used. As Figure 2.62 shows, this efficient use of the build volume keeps the cost per part lower than traditional manufacture for larger part runs - “blower units” being the main part in this instance. This approach, while theoretically robust, might fall down in real world situations, however, as there will often not be part demand to fill the entire build volume.

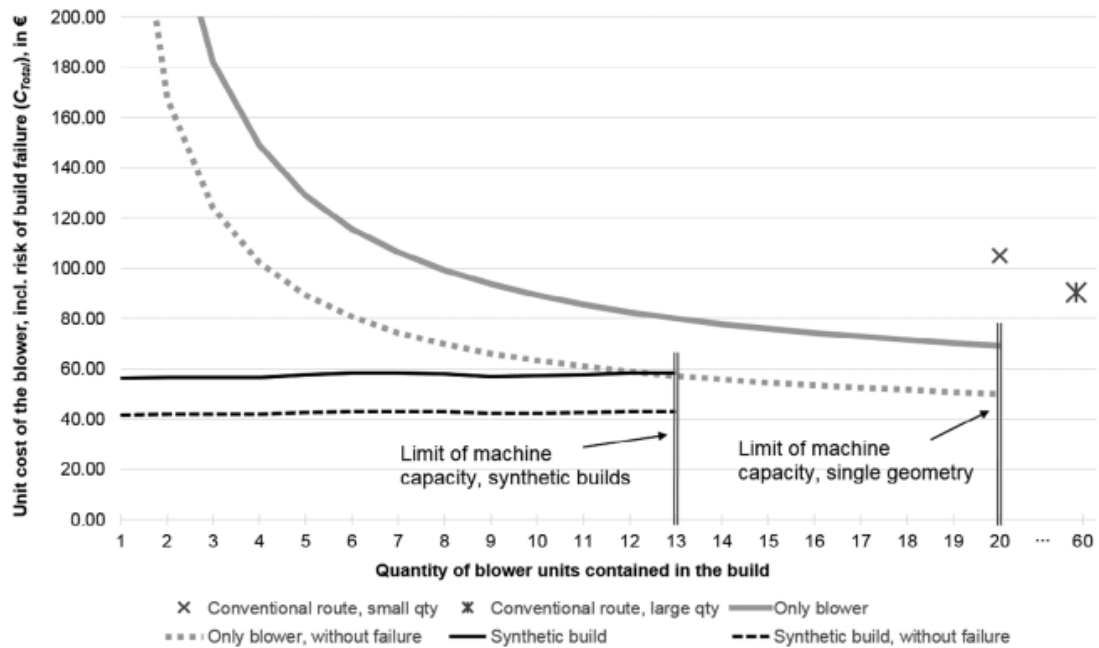


Figure 2.62: Unit cost comparison of using the “synthetic build” algorithm vs single repeating part build vs traditional manufacture^[186]

Interestingly, the most recent work from the authors has slightly contradicted the earlier results, showing that while increased build volume efficiency does reduce relative per part costs, there is an upper limit to the build volume efficiency percentage, above which there is no discernible reduction in per part costs^[187] - this helps towards addressing the real world scenario of lacking demand for fully-packed build volumes. The upper limit to build volume efficiency is due to build failure modes which become more common as the build volume is packed more densely, as first discussed in Baumers and Holweg^[182]. The authors show however, that this lower build volume utilisation has no negative

effect on the cost per part (Figure 2.63) and thus they still believe that DED AM is cheaper compared to traditional manufacture for complex parts that would require several traditional processes, as argued in Baumers et al. [186].

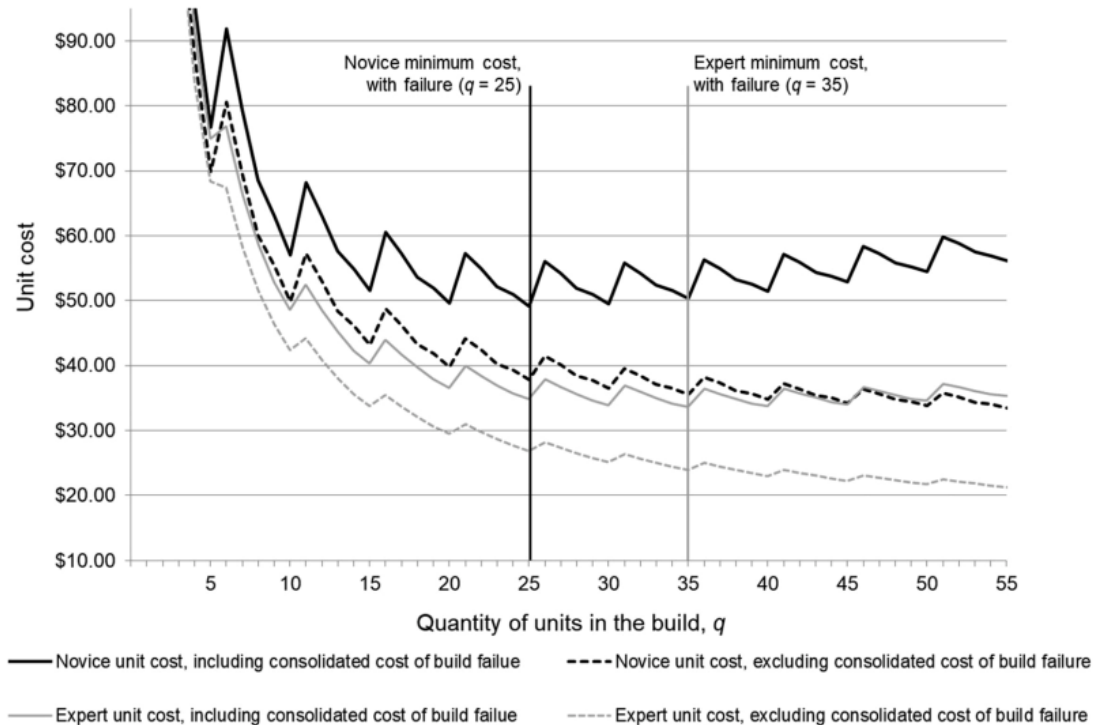


Figure 2.63: Unit cost comparison, showing a plateau in unit cost occurs before full utilisation of the build volume, with AM experts making parts quicker and hence cheaper than novices [187]

As mentioned, material and energy costs are two disadvantages of AM when compared to traditional manufacture, in many circumstances. Due to this, Fritz and Kim [188] have conducted research into reducing surface area and support material via optimisation of multiple variables - in this case density-based topology and build orientation. By experimenting with the build orientation in tandem with the topology, the authors found that they could successfully reduce deposited surface area and support material, and thus reduce material usage, print time, and thus cost. However, the solver suffered from local minima, even in the simple example that it was tested on, and therefore it is postulated that a large number of initial designs would be needed for a more complex topologically optimised structure. Additionally, it was seen that this method, while conceptually successful, led to structural performance issues as manufacturability increased. While this structural issue could be resolved with other TO solvers, it would not be possible to combine them with the orientation optimisation, thus making the technique unusable. While an interesting concept, further work is required before this technique can be used to reduce AM costs in real world applications.

In parallel to the technology improvements, improvements to cost models are also being made. Advocates of AM argue that one of the reasons it is more expensive than traditional manufacture is the comparatively accurate cost modelling that is possible with AM compared to traditional manufacture, due to the layers of complexity and ambiguity that lead to information loss in the supply chain of traditional manufacture^[186]. It is true that cost modelling has greatly improved in accuracy since the early 21st century. Early cost models focussed solely on machine costs^[189]. Later work focussed on the inclusion of energy consumption and time^[185], material processing, and part post-processing^[190;191], thus giving, in the eyes of the authors, accurate cost models for the near end-to-end process chain of specific AM processes. These processes are chiefly direct energy deposition and powder bed fusion, due to their relative dominance in real-world engineering applications when compared to other AM processes, however, work on cost modelling for other processes (such as vat polymerisation^[192]) has also been carried out. However, as noted in recent literature covering this topic, despite the large amount of work that has gone into cost modelling to date, a satisfactory overarching cost model for AM has yet to be made^[193]. This is obviously a demanding task due to the differences in function of the seven AM categories and processes within each, however, until this is done, the reach of AM into mainstream manufacturing is unlikely.

2.6.1 Conclusion

Despite techniques to reduce the cost of AM and the fact that cost models are increasing in accuracy (to the point that some argue the models are more transparent than those for traditional manufacture), it cannot be disputed that AM is an expensive technology, especially from a customer perspective. As noted by Liao and Cooper^[194], unless production numbers are small, conventional production is cheaper, as upfront tooling costs are absorbed over the duration of production. This supports the prevailing industry view that AM is of greatest benefit on either small production runs^[195], for making parts whereby the savings in feedstock material are significant, or for parts that conventional production techniques cannot be used, such as geometrically complex FGMs^[196], going against earlier research from Baumers et al.^[197] which argued that as industries emerge, economies of scale are a structural characteristic which is gradually achieved. At the current price, AM technology may not be financially-practical for robotic arm links, however, as noted in the introduction, robots are the chosen use-case for a range of factors. The work in this thesis is therefore conceptual, and little real-world application to robotic arm links is foreseen until AM costs reduce. As this work is conceptual, practical costs of simulation and production of lightweight FGM parts will not be taken into account in this work. However, the work itself will still have contex-

tual use in other engineering fields with greater requirement for weight-minimisation, less financial restriction, and increased environmental complexity, such as space and aerospace.

2.7 Knowledge gap map

Collated from the knowledge gaps of each review section, the knowledge gap map in figure 2.64 can be constructed. This map shows all gaps found when undertaking the literature review. The gaps which were deemed outside the scope of the project are marked in red. Those which are being taken forward to form the research question are marked in green.

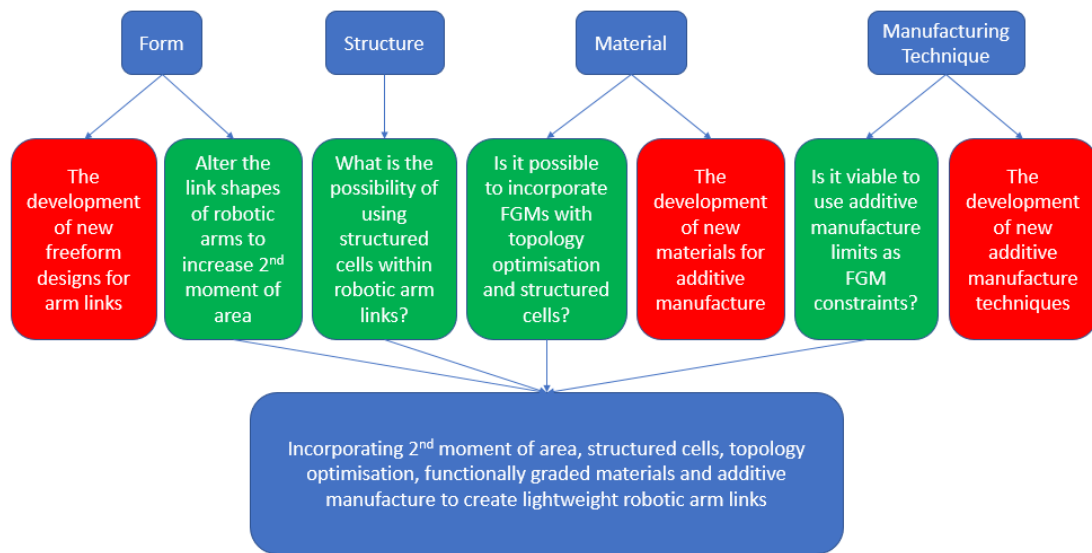


Figure 2.64: A map showing the gaps in knowledge found during the literature review

The knowledge gap map can be supplemented with a more in depth research focus procedure, shown in Figure 2.65.

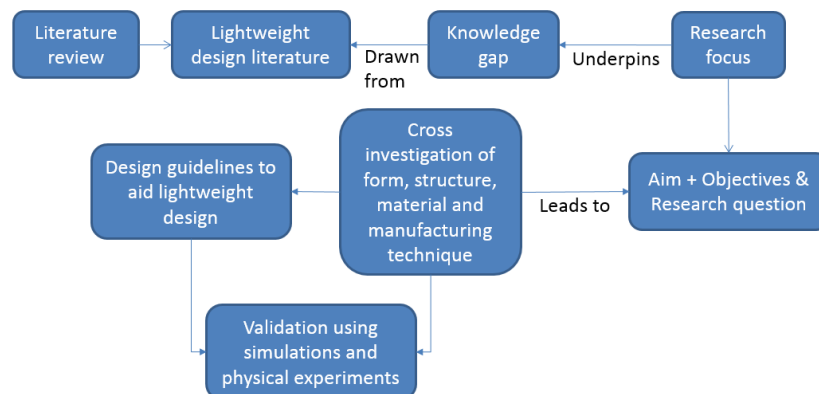


Figure 2.65: An updated research focus definition

Chapter 3

Scope of Research

3.1 Aim and Objectives

The aim and objectives of the research were laid out in section 1.2, but are repeated here for the sake of clarity. The aim is:

To investigate the mass reduction of robotic arm links by merging second moment of area calculations, structured cells, topology optimisation, functionally graded materials and additive manufacture in various combinations.

The objectives are:

1. Run a preliminary case study to test selected ideas derived from literature.
2. Write a methodology that incorporates all the ideas from the literature that aims to help designers reduce the mass of robotic arm links.
3. Test the methodology using a case study and computer simulations.
4. Use additional case studies to further test the methodology, and investigate points that make up the research question. This will be done using computer simulations.
5. Verify aspects of the methodology using physical experiments (creation and testing of TO-FGM parts).

3.2 Research Question

The scope of this project will be refined using the knowledge gaps collated in the knowledge gap map in section 2.7. Form of robotic arm links is very important, as the stiffness of links is dependent on the cross section. However, since form of robotic arm links is already well understood and researched it will not receive as much interest as the structure and material sections, which both have multiple avenues of research discovered during the literature review. As noted, developing a new manufacturing technique is outside the scope of the project, however, the manufacturing restrictions of additive manufacture should be used when developing new internal structures. All four sections of the literature will combine to develop the specific research question, though certain aspects will be of greater importance.

The following points need to be answered in this project, and will be used to create the final research question:

1. What effect does altering the second moment of area have on the possibility of incorporating TO, structured cells and FGMs?
2. If AM manufacturing restrictions are put in place, are the stress-reduction benefits of FGMs present?
3. Does FGM + TO mixing work?
4. Does FGM + structured cell mixing work?
5. How effective are these mixing techniques? Use physical testing to find this out.
6. If the above techniques can be used to reduce the mass in robotic arm links?

The overall research question can thus be phrased:

how effectively can topology optimisation, structured cells, FGMs, alterations to form and additive manufacture be merged in order to reduce the mass of robotic arms?

While work has been done on combining functionally graded materials and topology optimisation^[86], and functionally graded materials and additive manufacture^[38;81;82;198], work is yet to take all three aspects and consider the limitations of the manufacturing technique as a foundation of possible part creation. The study in this thesis aims to ultimately test that the three aspects can be combined together successfully.

3.3 Research Methodology

The research methodology will link the research question breakdown in section 3.2 with the upcoming chapters in the thesis that encompass the main body of work. The six points in the research question are shown in Figure 3.1.

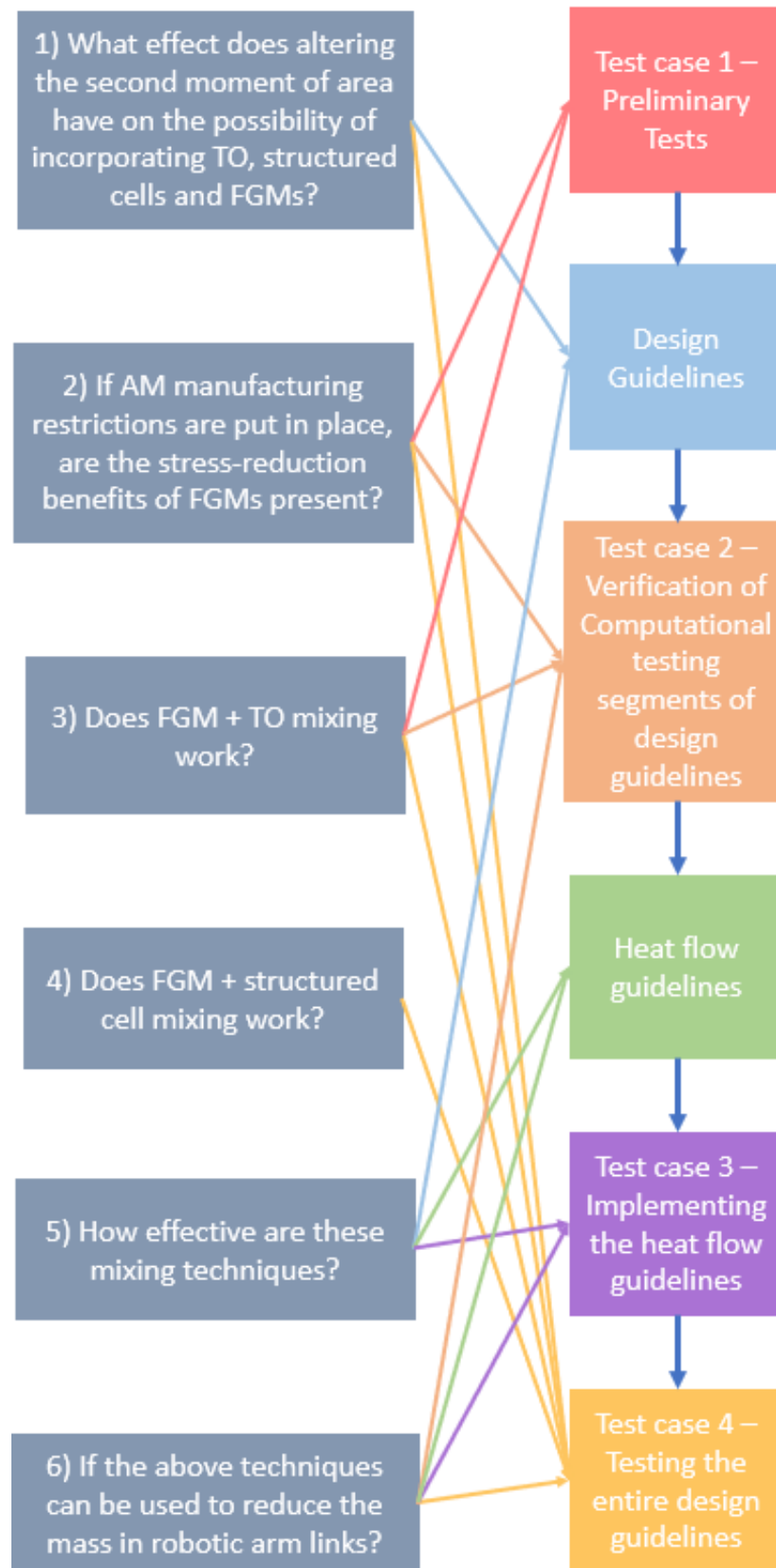


Figure 3.1: Linking research questions to stages of work

This main steps within each work stage are shown in Figure 3.2 colour-coded to match the colours used in Figure 3.1.

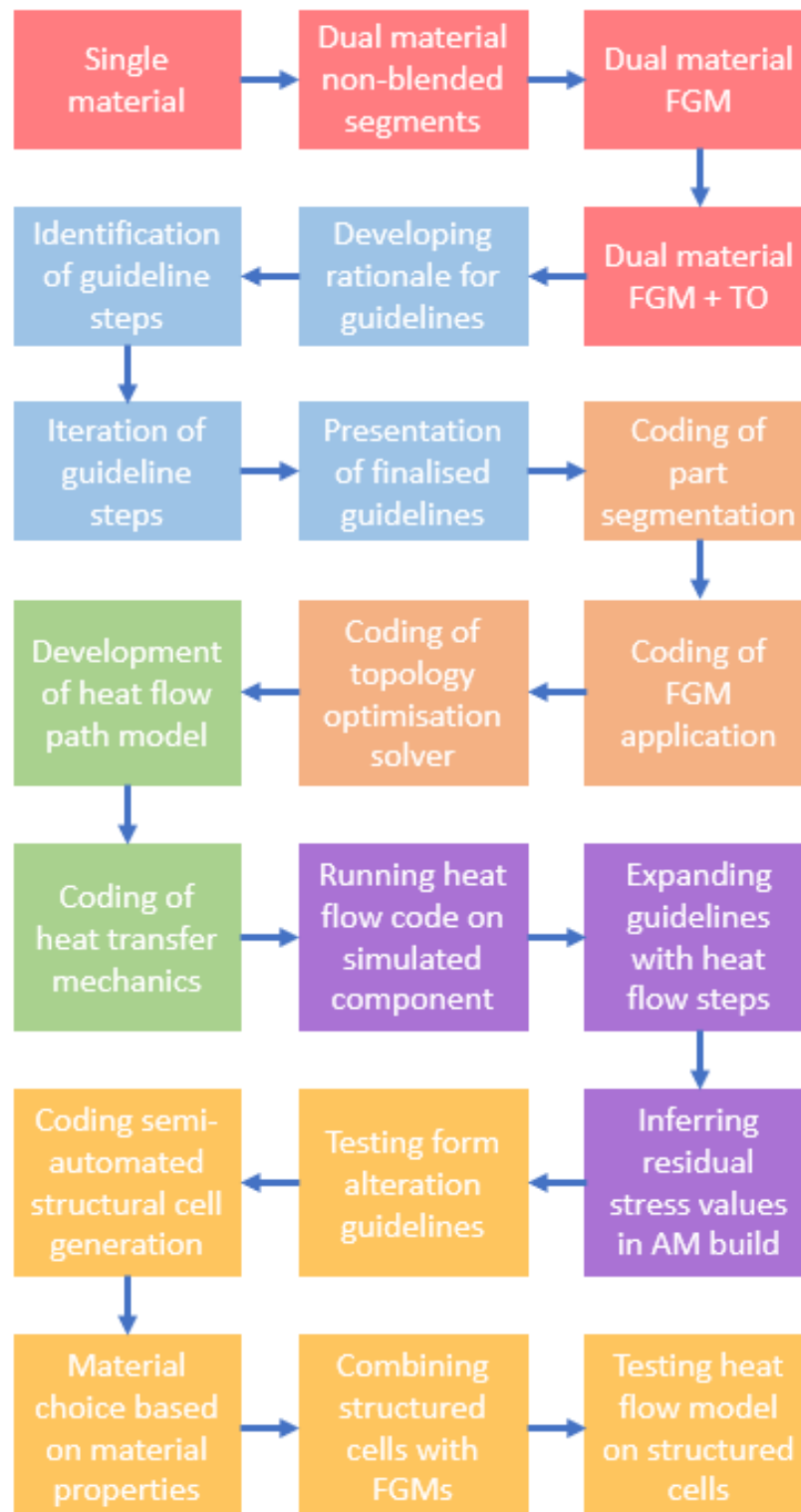


Figure 3.2: Breaking down work stages into main tasks

3.4 Assumptions

In order to bound the project, the following facets are deemed outside the scope of study:

- **Material bonding characterisation and properties, of both identical and non-identical materials, during additive manufacture.** Investigating the bonding characteristics of materials would make this project far wider-reaching. In order to understand this, the following would be needed:
 1. **Validation of material combinations.** Material combinations that could not be written off due to knowledge of chemical reaction would need to be validated. This would need to be done using rounds of physical manufacture.
 2. **Development of build parameters.** Those material combinations which did physically bond would need to have the build parameters developed. This would require iterations of controlled, designed additive manufacture experiments to ensure validity.
 3. **Investigation of material properties.** Once build parameters had been developed from the list of viable material combinations, the material properties of each combination would need to be investigated. This would require multiple specimens for each combination, followed by physical testing of the specimens.

This is not a materials science project, and thus, the following compromises have been made:

- **Select only materials which have been successfully additively manufactured.** To begin with, only materials which have already been successfully additively manufactured **on a commercial scale** will be used in test cases in this thesis.
- **Split materials into groups based on assumption of successful bonding.** From the list of commercially-successful materials for AM, they will be put into groups based on their thermal expansion coefficient and melt temperature. This is a known oversight, as it does not take into account any chemical instability that may be present between materials that have similar melting temperatures. However, a boundary is required, and the check of melt temperature and thermal expansion coefficient has been chosen as this boundary.
- **Material properties will be based on a interpolation of constituent material properties.** As said, this is not a materials science project, and

in order to find actual material properties, a large set of physical experiments would need to be done as highlighted above. Therefore, the material properties of any “successful” combination will be based on the interpolation of the two constituent materials. Properties in a blended part will alter as a function of distance along the part, in line with literature^[83]. **However, in order to be able to compare material combinations to one another in terms of material property, the “mid point” of interpolated limits will be used as the data point.** As examples:

1. If blending from 0% “material A”/100% material B to 100% material A/0% material B, the material properties for this blend for comparison to other materials would be taken at 50% material A/50% material B.
2. If blending from 0% “material A”/100% material B to 60% material A/40% material B, **the material properties for this blend for comparison to other materials** would be taken at 70% material A/30% material B.

For more information, see section 5.4, with attention to section 5.4.3.

- **Functionality unique to individual additive manufacturing techniques.** Any manufacturing restrictions put in place resulting from AM hardware (for example, a minimum resolution value) are assumed to affect all AM hardware. No hardware-specific limitations are going to be put in place.
- **The cross comparison of different topology optimisation techniques.** Only TO algorithms available on the chosen FE software are going to be tested - the ability of different algorithms will not be investigated.

3.5 Linking literature and research question to first experiments

This section aims to link the outcomes of the literature review and updated research question to the first stage experiments in this thesis - the preliminary tests in section 4.

3.5.1 Form

To fully utilise the potential form of a lightweight robotic arm link, the cross section must not be overlooked. As mentioned, a gap in knowledge is to look into further refinement of form for such links. One key parameter for this is deemed to be the second moment of area, as it affects the stiffness of the link. This will be investigated during the project, however, the first steps will be to develop understanding of combining FGMs and how, if at all, they can be combined with TO.

3.5.2 Structure

In literature, it has been seen that topology optimisation and structured cells have been used in robotic arm links. As shown, both of these methods have the ability to reduce the mass of a robotic arm link. However, all work demonstrated has used both techniques on the bulk volume of the links. If the links are to remain hollow in order to allow internal cabling and mechanisms to be fitted within, the two techniques must be investigated for use predominantly in the outer wall. As such, a knowledge gap exists. Investigation of the usability/suitability of either/both of these techniques in different loading situations should be prioritised.

3.5.3 Materials

The literature in section 2.4 showed that the choice of material had a large impact on the properties of a part. Materials that are still in development for additive manufacture could not give results in the same degree of consistency as those already commercially available. As such, development of new materials for additive manufacture is not within the scope of this thesis.

The choice of materials for any test case in this thesis had to be made with manufacturing constraints in mind. To that end, the capabilities of a prominent additive manufacturing company were investigated. The outcome of this investigation found the materials shown in Table 3.1 were all printed commercially, and therefore chosen for testing.

Table 3.1: Tested Materials

Category	Material
Metals	Ti-6Al-4V
	Inconel 625
	Inconel 718
	Stainless Steel 316L
	Al6061-T6
Ceramics	CF
	GF
Composites	CFRP
Polymers	ABS
	Nylon 6,6
	Polycarbonate
	PLA

As noted in section 3.4, material bonding characteristics were out with the boundaries of this thesis. That being said, preliminary research was done on material combinations to better understand what materials would realistically be bonded to one another. This preliminary research was undertaken via a small literature study that concluded that thermal expansion coefficient and melt temperature were the two most significant properties that determine how well different materials will bond with one another.

However, it was realised that combining materials as FGMs is experimental in itself, and therefore all combinations would need validated. Some could be written off straight away - any polymer/metallic combination, for example. However, any combination that could not be written off due to thermal expansion coefficient and melt temperature differences would need physical testing. Build parameters for each tested combination would need to be iterated and validated. Of those combinations that successfully combined, material properties of each would then need to be repeat tested and validated. This process would be financially non-viable, and therefore, a compromise was reached to split the materials based on their thermal expansion coefficient and melt temperature alone. As stated in the assumptions, this is a realised oversight of the project, as there is a possibility that the alloys of some of these combinations could be chemically-unstable. However, a boundary on the research had to be put in place, and due to the reasons listed above, the decision to base the material groupings on thermal expansion coefficient and melt temperature differences alone was chosen as the boundary.

This restriction resulted in three broad testing groups that would be taken forward into the preliminary test case - one containing high temperature metals, one containing low temperature metals, and one containing polymers. Literature showed ceramics had been combined with both metals and polymers, and for that reason the two ceramic fibres (CF and GF) were added to all testing groups. Short (chopped) fibres would be used for mixing with the other materials, and therefore the benefits of long, ideally-oriented fibred would not be seen. CFRP was also added to the lower temperature categories, as a commercial group had claimed the ability to be able to print this. The groups, rearranged from Table 3.1 are shown in Table 3.2.

Table 3.2: FGM Testing Groups

Group 1 - High temperature metals	Group 2 - Low temperature metals	Group 3 - Polymers
Inconel 625	Al6061-T6	CFRP
Inconel 718	CFRP	GF
Stainless Steel 316L	CF	CF
Ti-6Al-4V	GF	PLA
CF		Polycarbonate
GF		Nylon 6,6
		ABS

These three testing groups will be used as the starting point for materials in any lightweight robotic arm link.

3.5.4 Manufacturing Technique

As stated in the literature review, this project does not aim to develop a new manufacturing technique. Instead, the manufacturing technique work will define limitations and best practices for additive manufacture of lightweight robotic arm links. These limitations and best practices will be incorporated into the other sections of the literature review, in order to ensure any design produced will be physically-manufacturable. As such, the impact of the manufacturing technique work will be limited in this project, and not focussed on to the same degree as the outcomes from the earlier section of the literature review.

Chapter 4

Test case 1 - preliminary tests

4.1 Introduction

The literature review in Sections 2.1 - 2.5 highlighted gaps in the four key areas of lightweight design - form, structure, material and manufacturing technique. These gaps became the inputs for the detailed research question, developed in section 3.2. The aim of this chapter is to take the research question and the outcomes of the literature from section 3.5 and test points of them at a preliminary stage; that is, to confirm that certain ideas within it are sound. This will be done using a test case.

4.2 Choosing the test case

Since this is a preliminary test case, the complexity of the test part does not have to be too bold or enterprising. As such, it is going to test the following:

1. If the current mass of the test case can be reduced while still satisfying mechanical requirements.
2. That FGMs can reduce stresses within parts when compared to not blending the materials.
3. If TO and FGMs can be combined, and if possible, to what degree.

As mentioned, the researcher is part of the SMeSTech laboratory. In order to eliminate external influences (lead times, suppliers, etc), the test case was chosen from equipment already in the laboratory. At the time of research, the laboratory had recently developed a two-link robotic arm. One of the links of this robotic arm was deemed an appropriate test case, as it had capacity for mass reduction, the dimensions for incorporating bulk FGMs and the design itself readily available.

The form of the part in this test case would not be altered from its original shape. Investigation of the impact of form will be kept for later work, once the outcomes of the above points are established.

4.2.1 Model of test case

The robotic arm which contained the link chosen for the preliminary test case is shown in figure 4.1. Highlighted on this figure is the link that will be studied as the preliminary

test case. It is a hollow cylindrical pipe 500 mm in length, with an inner diameter of 40 mm and an outer diameter of 46 mm, as shown in Figure 4.2.

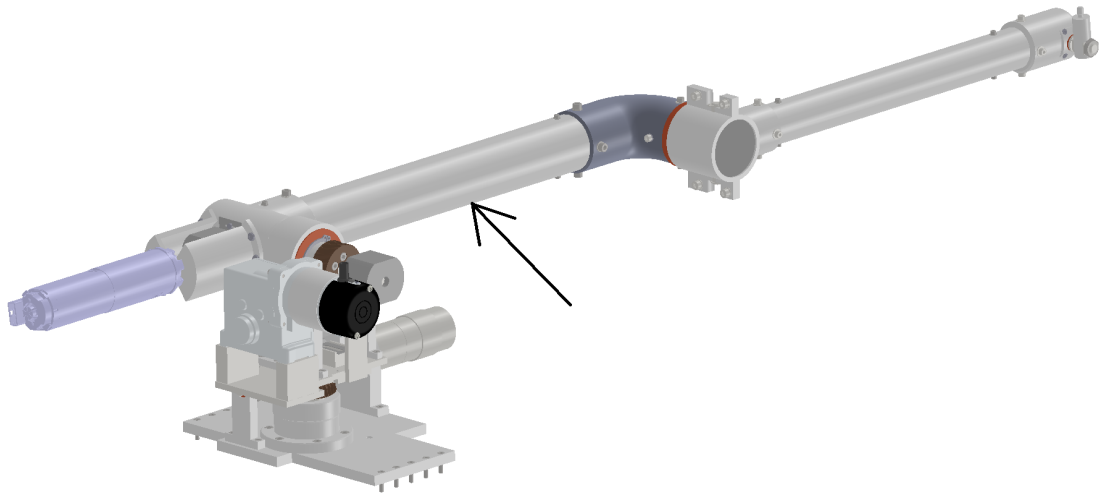


Figure 4.1: Robotic arm from which test case was taken from

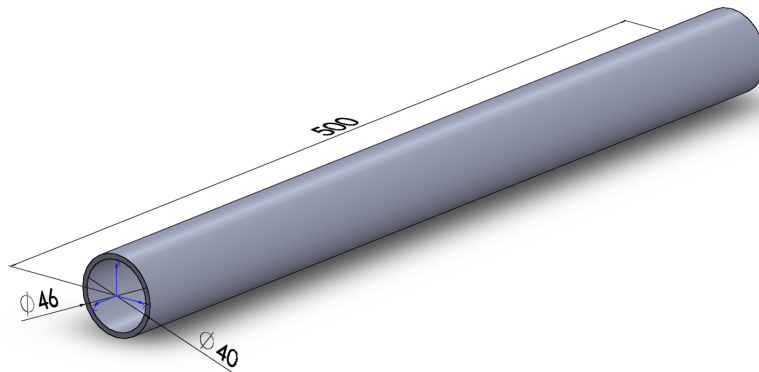


Figure 4.2: Original Model

4.2.2 Link parameters

At the time of research, the link had the parameters shown in table 4.1.

Table 4.1: Test case parameters

Parameter	Value
Material	Al 6061
Mass	0.547 kg
Length	0.5 m
Cross section	Circular
Wall thickness	0.003 m

These parameters were used to model the part on Abaqus CAE™ in preparation for finite element testing. In order to accurately set up the model in the finite element software, the constraints to simulate physical function were needed.

4.2.3 Primary constraints

1. One end of the model was fully fixed to simulate the end of the link that is attached to the base of the robot.
2. The free end of the arm link had a load of 11.5 N applied around the x axis to simulate loading on the arm.
3. The free end of the arm link had a displacement constraint of 0.25 mm

4.2.4 Secondary constraints

1. The arm should be made as light as possible.
2. The arm link must be physically manufacturable.

Once the test case was chosen and the initial evaluation was done, the testing strategy had to be developed.

4.3 Developing the testing strategy

A clear testing strategy was needed to understand the mechanisms of TO and FGM. The tests were developed to incrementally test the proof of two concepts; the first that TO reduces the mass of the part while adhering to mechanical constraints, and the second that FGMs would reduce stress concentrations when compared to not blending the materials. The testing strategy was decided as follows:

1. Test single materials without applying topology optimisation. This is the most basic test - applying each material to the arm link in turn and not removing any material. This gave a base point for each material. CF and GF will not be tested, as they require a bonding matrix.
2. Test single materials while applying topology optimisation. This built on the first test. However, rather than not removing any material, TO was used to remove material to set values. Again, CF and GF will not be used.
3. Dual material tests. These will be the first tests with combined materials, built manually in the finite element software. The materials will not be gradually

blended. Their objective is to show the high stress concentrations between dissimilar materials. They will test material combination possibilities in two different orientations:

- (a) Test dual materials by changing materials “along” the tube. The tube is split into two sections only. In this case, the tube is split into two equal halves.
 - (b) Test dual materials by changing materials “radially” on the tube. Again, the tube will be split into two sections only. In this case, the tube is split into two radially, in effect making two concentric cylinders, one larger than the other.
4. Semi-automated FGM. These will be follow up FGM tests, created using a Python™ script. These will test the FGM principle in greater detail than the manual FGM tests.
- (a) Segmenting parts “along” the tube.
 - (b) Segmenting parts “radially” on the tube.
 - (c) Segmenting parts both “along” and “radially” on the tube.
 - (d) Segmenting parts both “along” and “radially” on the tube while applying topology optimisation.

With the testing strategy decided, the materials that would be tested needed to be chosen. It was decided to test all materials found during the literature search of commercially-available AM materials, which are listed in Table 3.2. This would give the researcher an unbiased view of how the different materials perform, and ensure that no materials were excluded without reason.

4.4 Single material without topology optimisation

The first experiment in this preliminary test case was to apply each material to the arm link (shown in Figure 4.2) and simulate the primary constraints listed in section 4.2.3. The objective of this experiment was to gain a performance benchmark for each material. The maximum Von Mises stress and maximum displacement measured in the part are recorded. All commercially available materials (those in Table 3.1) would be simulated.

4.4.1 Model set up

The model used in this first experiment is the same as that shown in figure 4.2 - a hollow, solid wall cylinder. It is meshed using 16,800 quadratic wedge elements,

as seen in figure 4.3. Quadratic elements were chosen over linear elements due to the increased number of nodes (at midsurfaces as well as corners). This allows more accurate modelling of parts, especially during large deformation experiments, such as those in this test case.

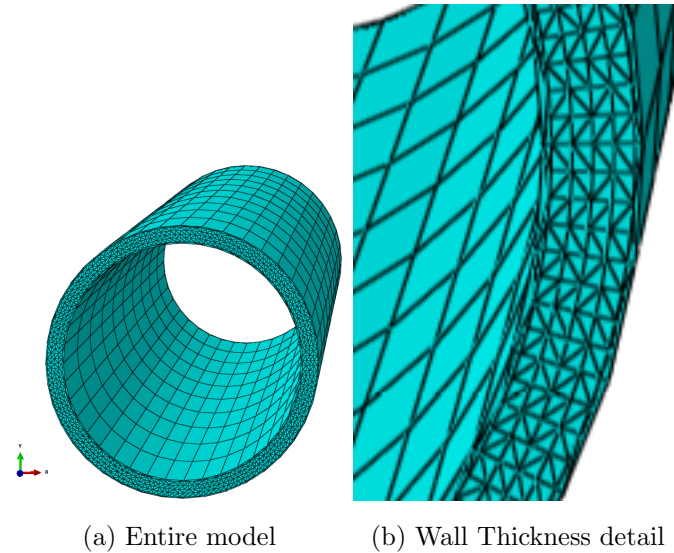


Figure 4.3: Original Model

4.4.2 Solver set up

The solver set up is simple for this test, as follows:

1. The material is applied to the entire part
2. The temperature during testing is set at room temperature (300 K).
3. The primary constraints listed in section 4.2.3 are applied as follows:
 - The fully fixed end of the arm link is modelled as an encastre boundary condition. It is in place from the initial step of the model.
 - The bending moment is applied as a moment around a point at the concentric centre of the free end of the arm link. The free end surface is constrained to move identically to the central point. This occurs during a step subsequent to the initial step.

The simulation was run once for each individual material.

4.4.3 Results and conclusion

The values for maximum displacement, density and mass of the part of the 11 simulations are shown in Table 4.2.

Table 4.2: Solid Tube Single Material Results

Material	Maximum Von Mises Stress (Pa)	Maximum Displacement (m)	Density (kg/m ³)	Equivalent Mass (kg)
Ti-6Al-4V	3.65E+06	1.41E-04	4430	8.98E-01
Inconel 625	3.66E+06	7.69E-05	8440	1.71E+00
Inconel 718	3.66E+06	8.01E-05	8193	1.66E+00
Stainless Steel 316L	3.67E+06	8.26E-05	8000	1.62E+00
Al6061-T6	3.66E+06	2.33E-04	2700	5.47E-01
CFRP	3.74E+06	2.22E-04	1600	3.24E-01
ABS	3.65E+06	6.42E-03	1040	2.11E-01
Nylon 6,6	3.64E+06	5.30E-03	1150	2.33E-01
Polycarbonate	3.65E+06	4.58E-03	1300	2.63E-01
PLA	3.65E+06	7.24E-03	1200	2.43E-01

As can be seen, the polymer tubes have the lowest mass and the greatest deflection. The ceramic tubes have a higher mass but deflect less and the metal tubes are the heaviest but deflect the least. These different deflections are due to the difference in stiffness of each material. These results give a basis of performance for the materials in the two testing groups when applied to this test case. The next step will be to study the performance of these materials when used in conjunction with topology optimisation.

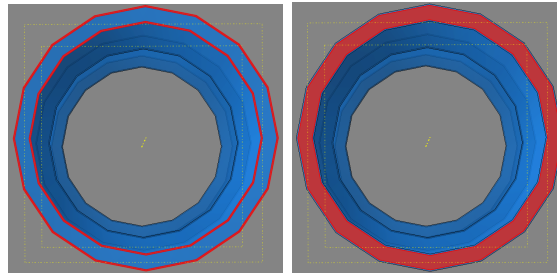
4.5 Single material while applying topology optimisation

This second test is an incremental change from the first test. The only difference is the application of topology optimisation in order to minimise the mass of the arm link - one of the secondary constraints of this test case (section 4.2.4). A SIMP-based topology optimisation algorithm integrated into Abaqus™ will be used to do this. The objective of this test is first to investigate whether TO is a valid option for reducing mass while adhering to a displacement constraint, and second, to begin choosing which materials are suitable for this test case, and which are not.

4.5.1 Model set up

In preparation for topological optimisation, the model was separated into two regions - a “frozen area” that would not be altered during the optimisation (the inner and outer walls of the cylinder), and an “optimisation area” that would be altered by the optimisation algorithm (the volume between the inner and outer walls of the cylinder).

These two areas are seen in Figure 4.4. The images show the end of the cylinder on a plane parallel to the reader’s page. The cylinder then extrudes “into the page”. The two small red rings in Figure 4.4a indicate the inner and outer walls of the cylinder being kept frozen, the single large red ring in Figure 4.4b indicates the volume between the inner and outer walls being “optimised”.



(a) Frozen Area (b) Optimisation Area

Figure 4.4: Segmented Regions

The same 16800, quadratic wedge mesh was used in experiment two as experiment one. Two concepts used in this model will now be introduced - choosing the feature size, and the “volume remaining” principle.

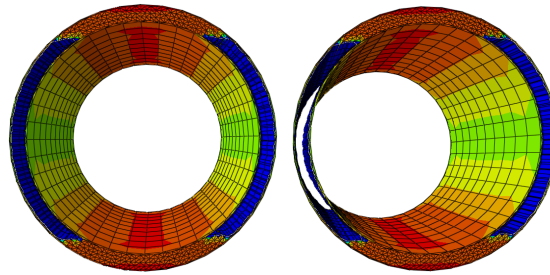
Choosing Feature Size

The effect of allowed feature size in a topologically-optimised part was tested to monitor the impact it would have on output parameters. The TO solver in Abaqus™ allows three feature size constraints to be set - a minimum size, a maximum size, or a size envelope (both minimum and maximum size constraints). A small test using the model set up in section 4.5.1 was used to measure the effect of feature size. Ti-6Al-4V was chosen as the test material. The test conditions and results are shown in Table 4.3.

Table 4.3: Choosing Feature Size

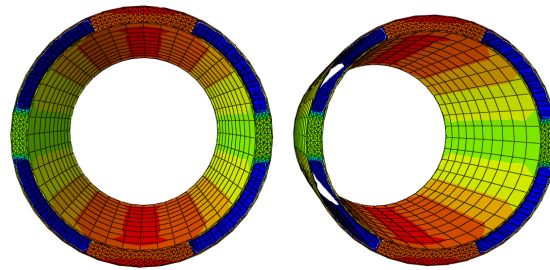
Feature Size (mm)		Stress (MPa)	Displacement (mm)
Minimum	Maximum		
0.25	N/A	5.555	0.3268
0.25	16	6.618	0.3904
0.25	06	7.472	0.4414

The results of these tests are shown in Figures 4.5, 4.6 and 4.7. Two orientations for each test, illustrating the hollowed internal structure, are shown.



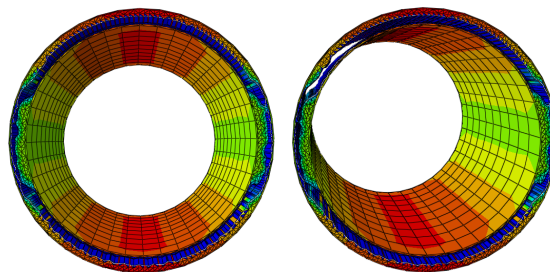
(a) Orientation 1 (b) Orientation 2

Figure 4.5: 0.25 mm Min, No Max



(a) Orientation 1 (b) Orientation 2

Figure 4.6: 0.25 mm Min, 16 mm Max



(a) Orientation 1 (b) Orientation 2

Figure 4.7: 0.25 mm Min, 6 mm Max

As seen, as the maximum feature size is reduced, the maximum stress and maximum displacement both increase. This is the reason **no maximum feature size was set**.

“Volume Remaining” Concept

To describe the material removal process, the term “volume remaining” will be used. As an example, when the tube has a solid wall, it has 100% “volume remaining”. As more material is removed by the TO algorithm, the “volume remaining” value decreases. Two example results from these tests are shown in Figure 4.8, the first with 30% volume

remaining and the second with 60% volume remaining. As seen, the frozen area remains in both. The difference in volume remaining is seen in the optimisation area.

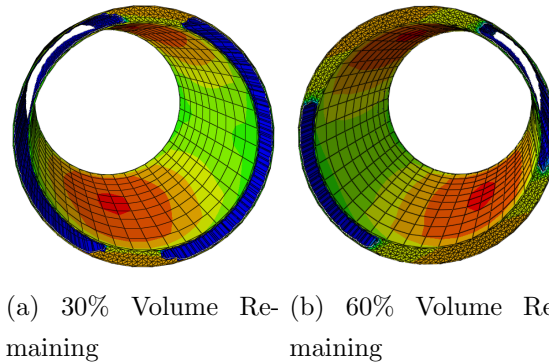


Figure 4.8: Demonstrating “Volume Remaining” Concept

4.5.2 Solver set up

The solver set up is identical to that for experiment one (section 4.4.2), with the addition of the topology optimisation algorithm. To solve the TO problems, the TO solver has to be set up with appropriate inputs, as follows:

1. All areas were included in the optimisation (neither load regions nor boundary condition regions were left out).
2. Two design responses were set - strain energy and volume.
3. The objective function was set as: **Minimise the strain energy**.
4. The constraint was set as: **Volume at a fraction of the initial value**. 13 volume fractions were tested per material, starting at 20% and increasing at 5% increments to 80%.
5. Two geometric constraints were set - the frozen area in 4.4 and a minimum feature size of 0.25 mm (minimum achievable resolution in AM is ≈ 0.1 mm).

The choice of volume fraction was made using a simple test, as explained below.

Choosing volume fraction

The range of volume fraction for testing was chosen via simple testing. A single material (Ti-6Al-4V) was assigned to the part. All inputs to the T.O solver were kept as in section 4.5.2. 18 tests were done, in which the “volume at a fraction of the initial value” was altered by 5% each time, between the value of 5% and 95%. The resulting displacement was plotted against the volume. This is shown in figure 4.9.

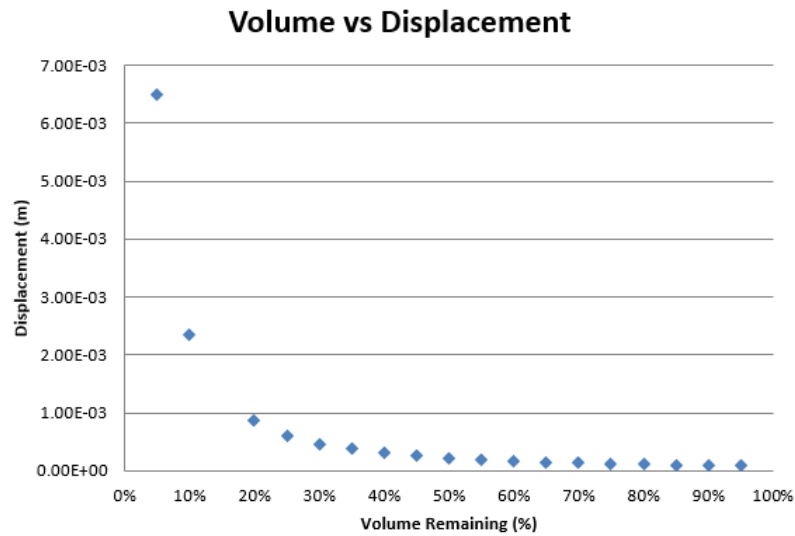


Figure 4.9: Choosing volume fraction

The results show an exponential increase in displacement when less than 20% of the material remains. 20% was thus chosen as the minimum material remaining percentage for all further tests. At the other end of the graph, the displacement change becomes almost 1 μm after 65%. Due to computational resources, it was decided that tests should not be done to 95%. However, in order to pick up any behaviour in different materials, it was decided that tests should go beyond 65%. A level of 80% was thus chosen.

4.5.3 Results and conclusion

The results of the single material TO tests are shown in Figure 4.10.

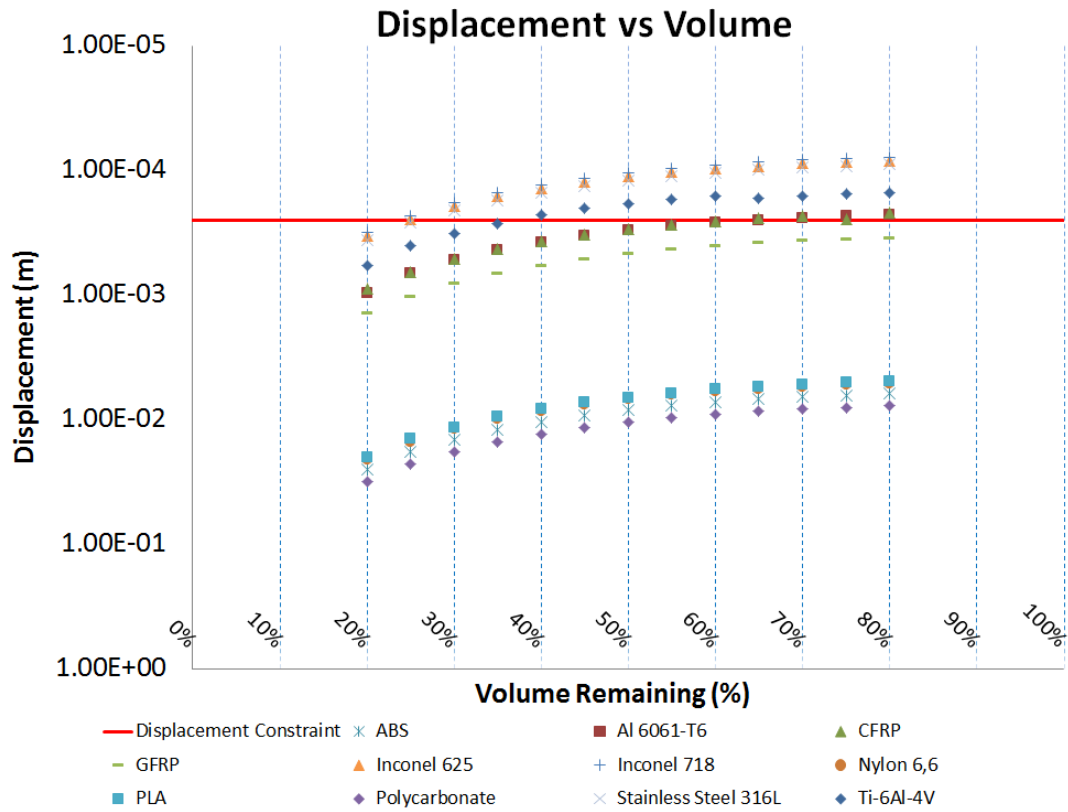


Figure 4.10: Single Material Results

Figure 4.10 has the 0.25 mm displacement constraint shown as a red horizontal line. Any points ABOVE this line have a displacement that is within acceptable limits. Table 4.4 lists, to the closest 5% “volume remaining” value (due to the testing resolution outlined in section 4.5.2), all materials (in order from heaviest to lightest) that are above this line and therefore within the displacement constraint. For simplicity, only the first result for each material that satisfies the displacement constraint is listed.

Table 4.4: Acceptable Materials

Material	Original Mass (kg)	Volume Remaining (%)	New Mass (kg)
Stainless Steel 316L	1.62	30	0.486
Inconel 625	1.71	25	0.428
Inconel 718	1.66	25	0.415
Ti-6Al-4V	0.898	40	0.359
Al6061-T6	0.547	65	0.356
CFRP	0.324	75	0.243

As shown in Table 4.4, TO has a substantial impact on the mass of the part. Due to their

lower stiffness, no polymers have met the displacement constraint. Currently, CFRP is the lightest possible material for use as the robotic arm link. However, this mass value could potentially drop further if CFRP were mixed with a lighter (albeit more flexible) material. This hypothesis will be tested in the latter experiments of this test case. It can be seen that the lower the volume, the greater the deformation. Assuming that the displacement constraint can be met, TO is a valid option for reducing mass. However, depending on the geometry of the part, structured cells may give better results, as will be explored in section 5.3.3.

4.5.4 Single material conclusions

The conclusion of single material testing showed that the mass of a part can be reduced using TO while adhering to certain constraints. The mass values from the experiments in sections 4.4 and 4.5 are shown in table 4.5. The values in green indicate that the displacement is lower than the constraint of 0.25 mm, or the mass is below the value of the current mass of the Al6061-T6 robotic arm. The values in red indicate the displacement is above the constraint of 0.25 mm or the mass is above the value of the current mass of the Al6061-T6 robotic arm.

Table 4.5: Single Material Conclusions

Material	Solid		TO		
	Displacement [mm]	Mass [kg]	Displacement [mm]	% Material Remaining	Mass [kg]
Inconel 625	0.0769	1.71	0.245	25	0.428
Inconel 718	0.0801	1.66	0.230	25	0.415
Stainless Steel 316L	0.0826	1.62	0.208	30	0.486
Ti-6Al-4V	0.141	0.898	0.228	40	0.359
Al6061-T6	0.233	0.547	0.249	65	0.356
CFRP	0.222	0.324	0.241	65	0.211
Polycarbonate	4.58	0.263	-	-	-
Nylon 6,6	5.3	0.233	-	-	-
ABS	6.42	0.211	-	-	-
PLA	7.24	0.243	-	-	-

4.6 Dual material - set up

As concluded in section 4.5.3, the performance of the robotic arm link could be further improved upon if two materials were mixed together. However, before work on FGMs

can begin, the performance of non-blended dual material parts must be studied, as noted in section 4.3. The results of this experiment will be useful to understand the ability of FGMs and where they lie in terms of performance when compared to single materials. It is hypothesised that these tests will show the large stress concentration and non-uniform bending that occur without FGM, and thus pave the way for the argument of using FGMs.

These experiments were also tested on the model in figure 4.2. This section describes the set up for the tests.

4.6.1 Models used

The two directions for material placement, as described in section 4.3, were as follows:

- along the tube from one end to another, and
- radially on the face from the inner circumference to the outer circumference.

In the solver, each material must have its own layer (multiple materials cannot be assigned to the same layer). The two directions are shown in Figure 4.11.

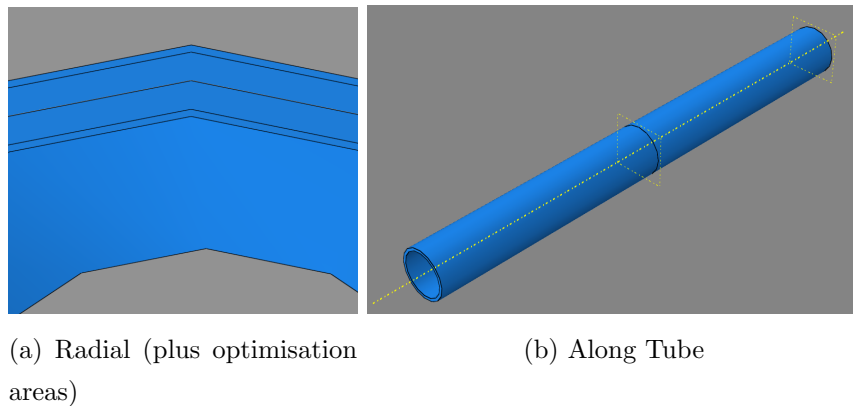


Figure 4.11: Segmentation Procedures

4.6.2 Materials used

Every material from each material testing group (Table 3.2) would be placed into the models. This meant that every material from each material group was tested in every material combination it could practically be in, and every position it could be in. This would be done for both the “along tube” and “radial” configurations. CF and GF would be omitted from these tests, as they cannot be used without a matrix. As a result, there would be 16 tests (4 materials, 2 positions) done for the “high temperature metals”, 4 tests (2 materials, 2 positions) done for the “low temperature metals” group, and 25 tests (5 materials, 2 positions) for the second material testing group.

Once these tests were finished, a pareto line would be fitted to each set of results to screen out any materials which are deemed non-optimal.

4.7 Dual material - radial

This experiment was the first of the two focusing on dual materials, while keeping materials in two distinct groups. The objective was to study the performance of materials in the radial direction, and use this as a comparison to the other direction - along the length of the tube.

Before the model was set up, it was decided that different configurations of radial material combinations should be tried. There are two configurations tried, A and B, both shown below.

Radial configuration testing

The tests intend to find which configuration of material placement will give a smaller deflection for a known load. Figures 4.12 and 4.13 show the two configurations. The images show the end of the cylinder on a plane parallel to the reader's page. The cylinder then extrudes "into the page".

In configuration A, the "frozen areas" of the model used during the topology optimisation test in section 4.5 are set as the first material and the "optimisation areas" are set as the second material, as shown in Figure 4.12.

In configuration B, the inner radius sections are set as the first material and the outer radius sections are set as the second material, as shown by the red rings in Figure 4.13. The "frozen" and "optimisation" areas remain the same as in configuration A.

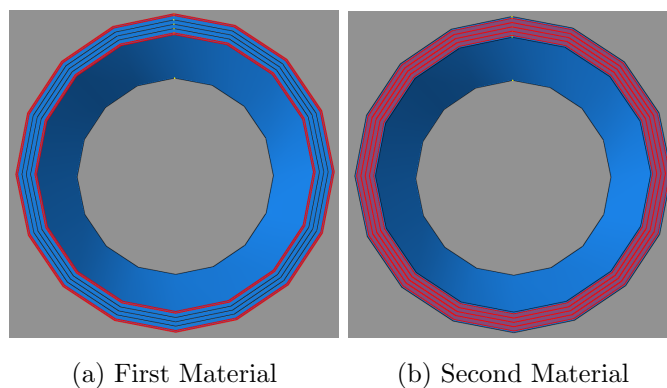


Figure 4.12: Configuration A. The red rings show the areas being highlighted in each image.

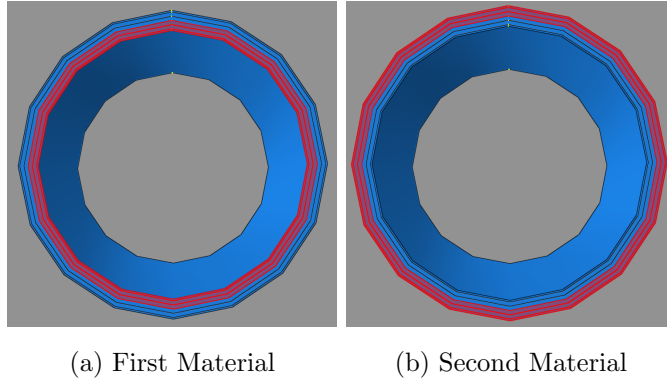


Figure 4.13: Configuration B. The red rings show the areas being highlighted in each image.

As this is only a test to choose the optimal configuration, only two materials are tested - Al6061-T6 and Ti-6Al-4V. Every combination of these two materials will be tested, as shown in Table 4.6. Tests on volume remaining vs displacement and mass vs Von Mises stress will be done.

Table 4.6: Dual Material Combinations

First Material	Second Material
Al6061-T6	Ti-6Al-4V
Ti-6Al-4V	Al6061-T6

Radial configuration results and conclusion

Firstly, the results of the volume vs displacement tests are shown in Figure 4.14.

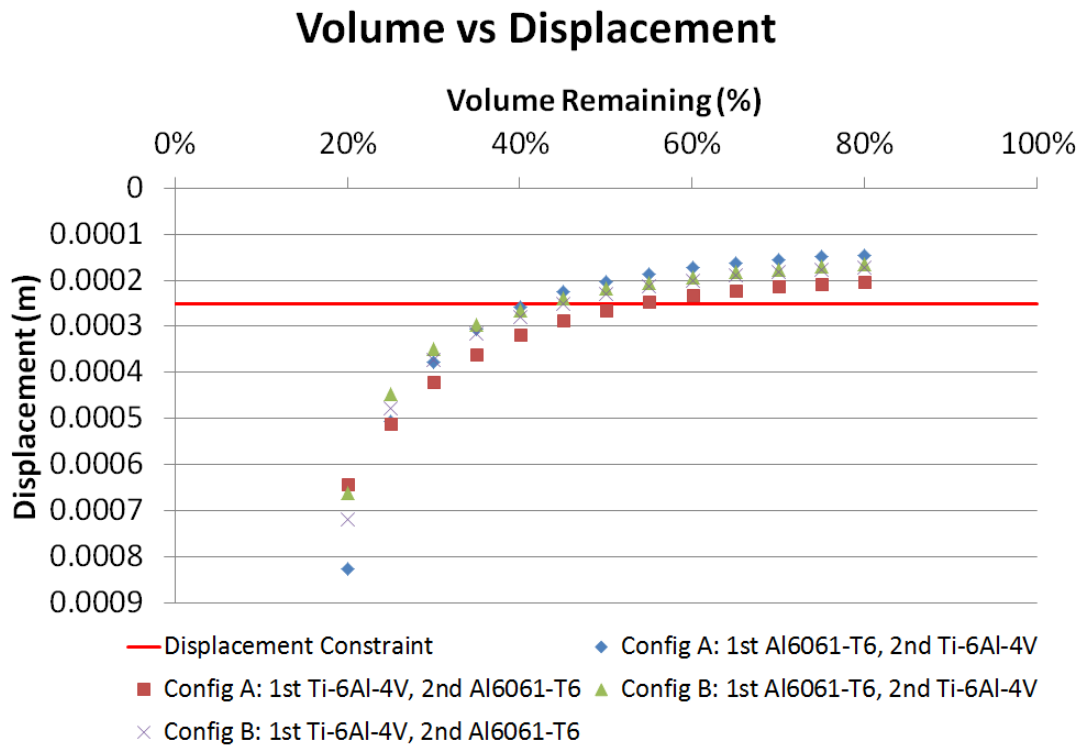


Figure 4.14: Volume vs Displacement

Both configurations show that when the stiffer material is placed further from the centroid of the part, the part itself will be stiffer. As configuration A places material furthest from the centroid, it is not surprising it has the highest and lowest displacement results for a given volume, depending on the configuration of the two materials. Configuration B results lie in between the configuration A results - the orientation of materials in configuration B has less effect on the displacement for a given volume. A part which has the stiffer part further from the centroid is therefore preferable. Secondly, the mass vs stress results are seen (Figure 4.15).

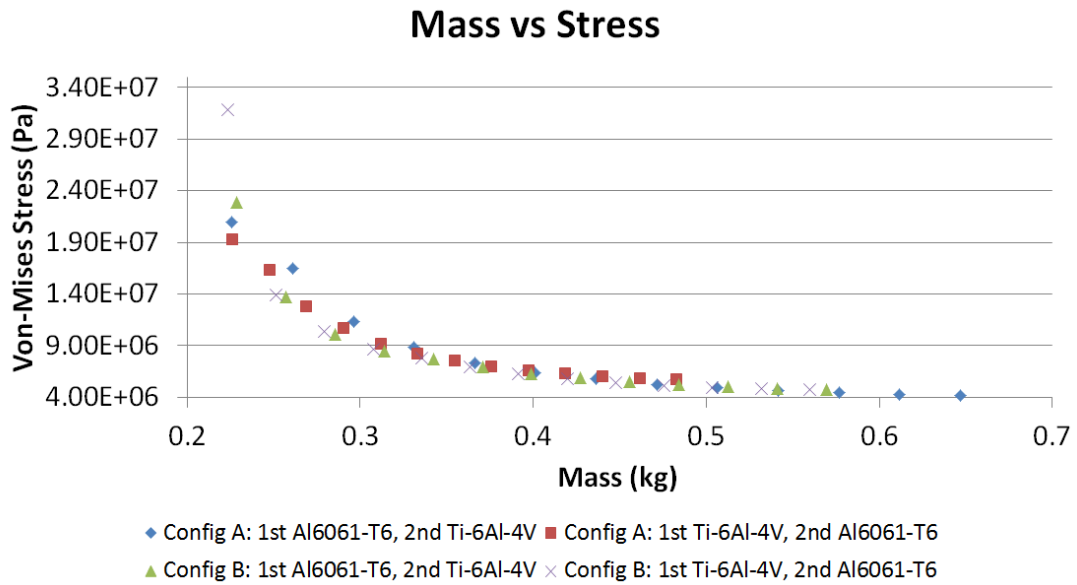


Figure 4.15: Mass vs Stress

The stresses for configuration A parts change more markedly with adjustments to the mass of the part, when compared to configuration B parts. Because the stresses change more gradually for configuration B, this set up is preferable.

While lightweight parts are of primary concern, the stresses should also be minimised, as areas of high stress are the first to fail when created with additive manufacture. Configuration A also has two material changes (Material A \rightarrow Material B \rightarrow Material A) whereas configuration B has one material change (Material A \rightarrow Material B). The less number of material changes, the better the performance of the additive manufacturing process. For these reasons, configuration B is chosen as the better option.

4.7.1 Model set up

The model for the third experiment was built upon the model from experiment two (section 4.5), and thus also used topology optimisation. The main difference was the third experiment was set up to simulate two materials that altered radially, compared to experiment two which tested one material.

As discussed in section 4.7, the model will be split into two concentric cylinders. Aside from this, it will be the same model as used in section 4.4.1, meshed with 16,800 quadratic wedge elements.

4.7.2 Solver set up

The solver was set up identically to experiment two (section 4.5.2).

4.7.3 Experiments conducted

Due to the multiple materials, there will be three batches of experiments run, one for each material testing group listed in table 3.2. Despite concluding in section 4.7 that the model set up with the stiffer material furthest from the centroid was preferred, all viable material combinations were tested for completeness. Therefore, 45 tests were done in total - 16 for the high temperature metals, 4 for the lower temperature metals, and 25 for the polymers. For succinctness, the high and low temperature values are shown on the same graph.

4.7.4 First testing group results and conclusions

The 20 combinations are shown in Figure 4.16. Since all 20 combinations are tried, there are times when both parts of the tube (inner surfaces and outer surfaces) are the same material. In these instances, they are recorded as “pure” in the legend. Using configuration B convention, when the material is the first material, it is called the “inside” material. For example, “Inconel 718 Inside” is represented by four purple diamonds in Figure 4.16 - each purple diamond has Inconel 718 as the inside material and one of the remaining three materials from the “high temperature metals” as the second/outer material.

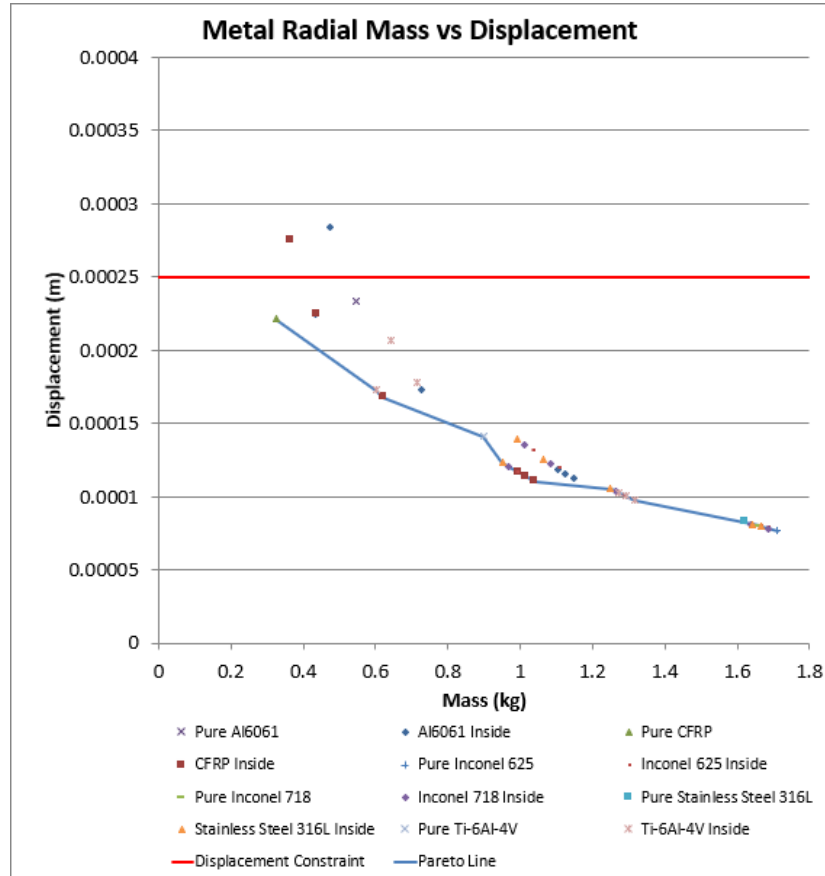


Figure 4.16: Metals 2 Layer Radial Comparison

The pareto front on 4.16 picks out the most efficient material combinations in terms of mass vs displacement when the material is altered radially.

It is seen that Al6061-T6 does not appear on the pareto front, so it will be ignored from further testing. This proves that the current use of pure Al-6061-T6 for the arm link is not the most suitable material, neither for minimising displacement nor minimising mass.

All remaining materials feature an equal number of times on the pareto front, their combination dependent on the displacement value - a lower overall displacement requires stiffer, more dense materials than a higher overall displacement. Because all remaining materials featured an equal number of times, they are all possible contenders to be combined for the arm link, based on the displacement constraint set in section 4.2.3. Therefore, they will all be taken forward for further testing.

Stresses increase as more material is removed from the part, as seen in figure 4.15. This is expected, and is due to the greater deformation and therefore greater tensile and compressive forces that the part is experiencing.

The objective of these tests was to study the performance of materials in the first testing group while in the radial configuration. The stresses recorded from this test

will be used as comparison for the along tube experiment in section 4.8 and the FGM experiment in section 4.9.

4.7.5 Second testing group results and conclusions

Figure 4.17 is very similar to Figure 4.16, except it represents the 25 possible configurations from polymer group rather than the 20 possible configurations from the combined metal groups. The legend follows the same logic as Figure 4.16.

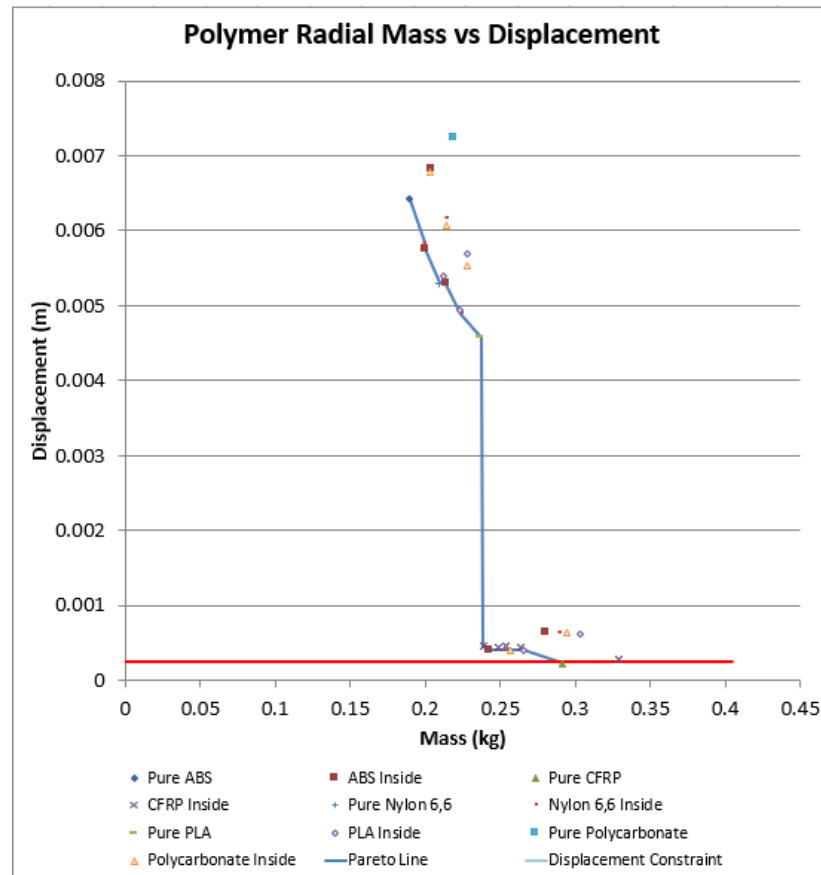


Figure 4.17: Polymers 2 Layer Radial Comparison

The pareto front on Figure 4.16 picks out the most efficient material combinations in terms of mass vs displacement when the material is altered radially.

This pareto front contains no polycarbonate, so this material is screened out. Once again, all remaining materials are seen an equal number of times. The combinations containing CFRP are seen at the bottom of the graph (more dense, but with low displacement), the combinations containing two polymers are seen towards the top of the graph (less dense, but with high displacement). All five polymer-CFRP combinations sit just above the displacement constraint, and although only an approximation of the FGM performance (which will be enhanced due to reduced stresses), the only mate-

rial currently stiff enough to satisfy the displacement constraint is pure CFRP. This result is the identical as that found in section 4.5, in which the polymers also failed the displacement constraint. The objective of this experiment was to compare the performance of these radial tests to the along tube tests. Due to this, the polymers will be removed from further testing if they also fail the displacement constraint in the “along tube” configuration.

4.8 Dual material - along tube

This fourth experiment is aimed to test the influence of altering the material half way along the length of the arm link, compared to altering the material half way through the wall thickness, as was done in section 4.7. This test is important, as it helps to build the argument for FGM use, and explores further design options for reducing the mass of the test case part.

4.8.1 Model set up

The model for the fourth experiment was similar to that in experiment three 4.7. The only difference was the placement of the two materials being simulated.

As discussed in section 4.7, this model would be split into two equal cylinders, placed end on end. Unlike in experiment three (section 4.7), there was no need to find the optimal configuration of material layout in this experiment because there were only two possible positions -left hand end or right hand end, and both were already integrated into the testing set up. Aside from the alteration in material position, it will be the same model as used in section 4.7.1, meshed with 16,800 quadratic wedge elements.

4.8.2 Solver set up

The solver was set up identically to experiment three (section 4.7.2).

4.8.3 Experiments conducted

These experiments follow the same procedure as those in experiment three (section 4.7.3) with the same materials, undertaking 36 tests for the first testing group and 25 for the second testing group, again for a total of 61 tests.

4.8.4 First testing group results and conclusions

Similar to the radial tests in section 4.7, Figure 4.18 shows the performance of the metals. “Pure” parts are, again, those made solely of that one material. As described in section 4.4.2, one end face of the tube is fixed in the analysis, while the other end

has a bending moment applied. The segment of the tube closest to the fixed face is referred to as the “base” in the legend. For example, in Figure 4.18, “Al6061 Base” is represented by five yellow circles. Each yellow circle has Al6061-T6 as the material for the first half of the tube closest to the “base” face and one of the remaining four materials from group one as the material for the second half of the tube - the segment nearest the face where the bending moment is applied.

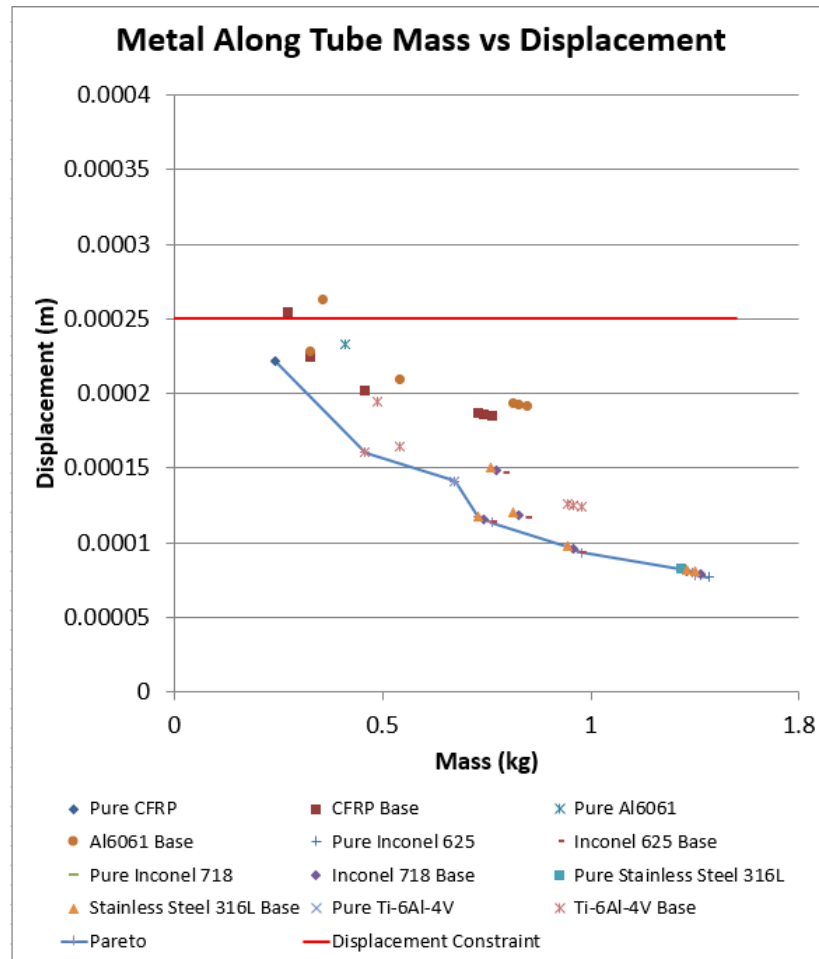


Figure 4.18: Metals 2 Layer Along Tube Comparison

The graph shows that when the material with the higher stiffness is placed at the end of the arm link that is fixed and the material with the lower stiffness is placed at the end of the arm link that has the bending moment applied, the overall structure deflects less than when the two materials switch positions. This is expected, as displacement will be greater influenced by the end of the tube closer to the “base”, so the stiffer the material at this end, the lower the overall displacement of the tube will be.

The pareto front on Figure 4.18 picks out the most efficient material combinations in terms of mass vs displacement when the material is altered along the length of the tube.

Similar to Figure 4.16, Al6061-T6 does not feature in any of the material combinations along the pareto front. Again, all remaining materials appear an equal number of times on the pareto front. This reinforces the intention made in section 4.7.4 to take all remaining materials forward for further testing.

The objective of these tests was to get an approximate result of the performance of materials in the first testing group while in the along tube configuration and compare them to the performance of the radial configuration. Comparing figures 4.18 and 4.16, it can be seen that the two configurations behave near-identically. For that reason, it was decided that both configurations would be taken forward and combined during the FGM tests.

Although also present in the radial simulations of section 4.7, the large stress concentration and non uniform bending profile between the two dissimilar materials could be more easily seen in the along tube configuration. An example is shown in Figure 4.19.

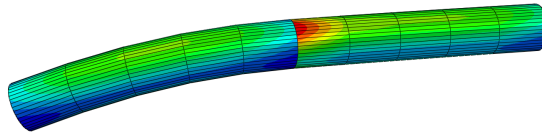


Figure 4.19: Stress concentration and non-uniform bending

As seen, the maximum stress is at the boundary where the two materials meet. Also of note is the fact the right hand side of the tube remains near-straight, while the left hand side displaces significantly across its length. These two problems are the basis of argument to investigate functionally graded materials (FGMs).

4.8.5 Second testing group results and conclusions

Figure 4.20 is very similar to Figure 4.18, except it represents the 25 possible configurations from group two rather than the 36 possible configurations from group 1. The legend follows the same logic as Figure 4.18.

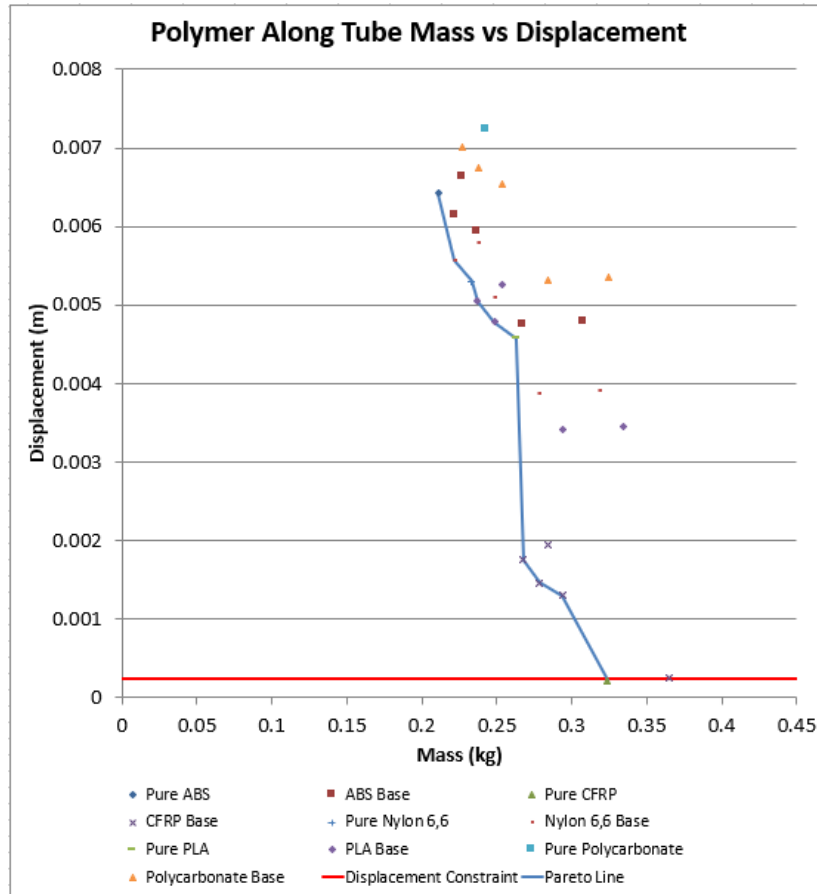


Figure 4.20: Polymers 2 Layer Along Tube Comparison

The pareto front on Figure 4.20 picks out the most efficient material combinations in terms of mass vs displacement when the material is altered radially.

The objective of this experiment was to compare the performance of these radial tests to the along tube tests. Similar to the pareto front in figure 4.17, figure 4.20 also does not contain polycarbonate along the pareto front. As with all pareto charts above, all materials on the pareto front are equally represented. However, compared to figure 4.17, the polymer-CFRP combinations sit further above the displacement constraint line. This fact, in addition to there being no polymers below the displacement constraint during single material testing in section 4.5, radial dual material experiment in section 4.7.5 or this experiment, mean that all polymers will be removed from further testing.

4.8.6 Dual material conclusions

The dual material experiments gave several pieces of useful information, to both the test case itself, and to the argument for use of FGMs in general when combining two materials:

- Polymers are no longer considered for this test case due to displacement constraint
- Configuration B for radial material blending is favourable to configuration A
- Metals and CFRP will be taken forward for further testing
- Stress concentration and non-uniform bending make dual material parts unfavourable

4.9 Automated FGM without topology optimisation

The objective of this experiment was to investigate the viable use of FGMs to reduce stress concentrations in the test case when made from two dissimilar materials. The results of the stresses seen in this experiment would be compared to those in the dual material experiments from sections 4.7 and 4.8.

4.9.1 Importance of FGM

Functionally graded materials alter the material gradually between two points/surfaces. This keeps stresses to a minimum while gaining the benefit of properties from different materials, such as the durability of ceramics with the ductility of polymers. Crude gradation of material results in stress peaks at material boundaries, as seen in figure 4.19 where the tube has been graded into two layers.

4.9.2 Model setup

As reported in section 4.8.4, material will be blended in both the radial and along tube directions simultaneously, due to the similar performance of both configurations. Before blending begins, a decision of the number of layers of material in each direction must be made.

Choosing number of layers

Radial The robotic arm link was separated into 2, 10, 20 and 30 radial layers. A close up of the 2 and 30 layer models are shown in Figure 4.21.

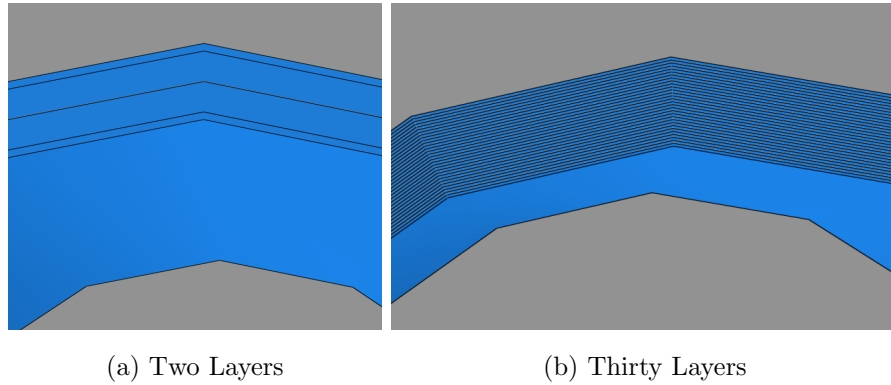


Figure 4.21: Radial Segmentation

Along Tube Again, the model was separated into layers, this time 2, 10, 20, 30 and 40 along tube layers. A close up of the 2 and 40 layer models are shown in Figure 4.22.

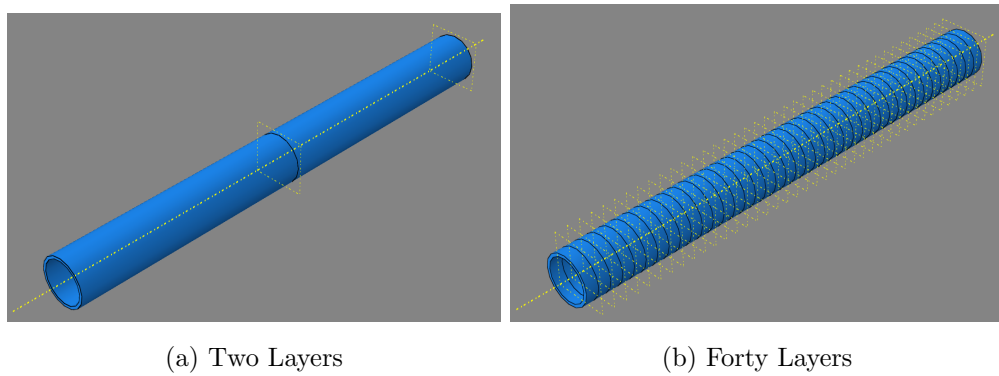


Figure 4.22: Along Tube Segmentation

Results The results from these tests are shown in the graphs in Figures 4.23 and 4.24.

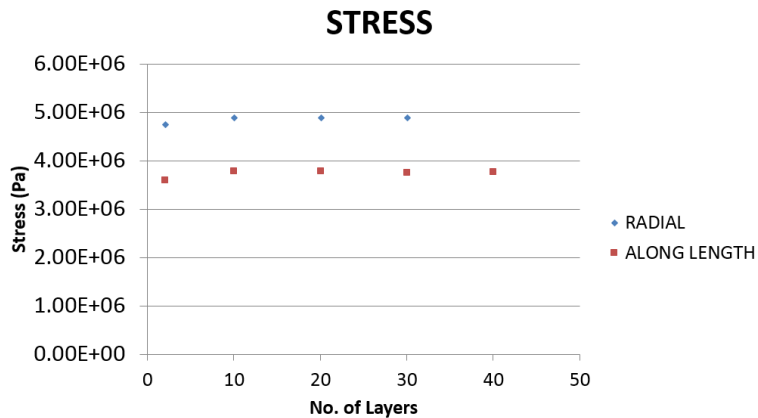


Figure 4.23: Stress Testing Results

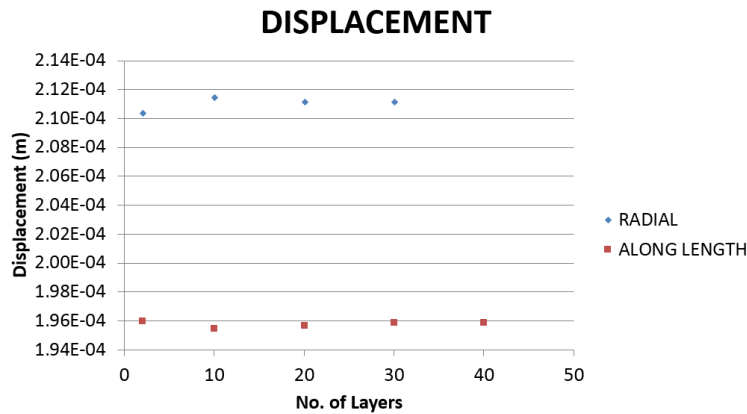


Figure 4.24: Displacement Testing Results

As can be seen in figure 4.23, the stress plateaus for both directions once there are 10 or more layers. Figure 4.24 shows that the displacement does not plateau as neatly as stress, however, it is very similar between 20 and 30 layers for the radial testing direction, and between 30 and 40 layers in the along length direction. As 30 layers is the minimum common value for all testing scenarios, 30 layers will be made in both directions in the model.

4.9.3 Setup itself

4.9.3.1 Material creation

As previously mentioned, the material properties cannot alter **within** any segment, only **between** them. This means that there must be a unique material for every segment within this test case.

Material gradation in this test case is very simplistic. To keep consistency, CF and GF will not be included in this test, although they could be. The values of relevant material properties of the two constituent materials are interpolated at every segment to give “new” material properties, based on the percentage contribution of each constituent material at the particular segment. To better explain, two examples are given - in tables 4.7 and 4.8.

Table 4.7: 6 layer material property example

Segment Number	Material A (%)	Material B (%)	Youngs Modulus (GPa)	Density (kg/m3)	Poisson's Ratio
1	0	100	193	8000	0.25
2	20	80	177.16	7286	0.2684
3	40	60	161.32	6572	0.2868
4	60	40	145.48	5858	0.3052
5	80	20	129.64	5144	0.3236
6	100	0	113.8	4430	0.342

Table 4.8: 11 layer material property example

Segment Number	Material A (%)	Material B (%)	Youngs Modulus (GPa)	Density (kg/m3)	Poisson's Ratio
1	0	100	193	8000	0.25
2	10	90	185.08	7643	0.2592
3	20	80	177.16	7286	0.2684
4	30	70	169.24	6929	0.2776
5	40	60	161.32	6572	0.2868
6	50	50	153.4	6215	0.296
7	60	40	145.48	5858	0.3052
8	70	30	137.56	5501	0.3144
9	80	20	129.64	5144	0.3236
10	90	10	121.72	4787	0.3328
11	100	0	113.8	4430	0.342

As seen, every value is interpolated between the properties of the two constituent materials, in this case stainless steel 316L in segment 1 and Ti-6Al-4V in the final segment. The greater the number of segments, the lower the change in material properties between each segment, and thus the lower the stress concentrations.

4.9.3.2 Model partitioning

It was decided in section 4.9.2 that the arm link would be segmented into 30 slices both radially and along its length, for a total of 900 segments. The arm link is 500 mm in length and 3 mm thick, so each segment would be 16.67 mm long and 0.1 mm thick. A resolution of 0.1 mm can be achieved by AM technology - an important concern of the test case, as laid out in the secondary constraints (section 4.2.4).

A model of the test case is shown in figure 4.25.

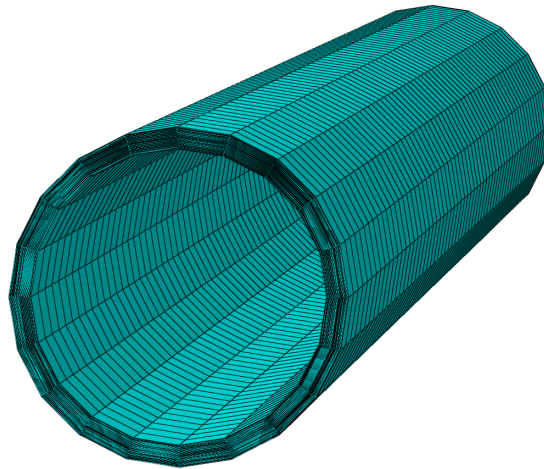


Figure 4.25: Mesh for FGM model

Due to the increased complexity of this model, it is meshed with 72,000 quadratic wedge elements, compared to 16,800 used on the earlier tests.

4.9.3.3 Material allocation

Taking the model from figure 4.2 and slicing it along the y-z plane gives figure 4.26. Using figure 4.26 as a guide helps to describe the material allocation.

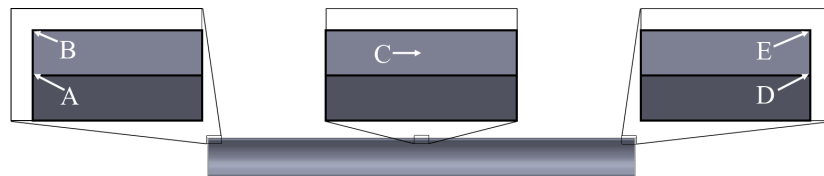


Figure 4.26: Original model sliced

The material will gradate from the lower left corner (point A in figure 4.26) to the top right corner (point E in figure 4.26). The material mixture in each segment will be linear function of the total distance between these two points. As such, the smoothness of material gradation is a direct function of the number of segments in the part. The higher the number of segments, the smaller the change in material mixture percentage between each segment. Altering the number of segments therefore directly controls the smoothness of stress concentrations.

The material mixture percentages at the five points in figure 4.26 are shown in table 4.9.

Table 4.9: Material Percentages

Point	Material A (%)	Material B (%)
A	100	0
B	99.4	0.6
C	50	50
D	0.6	99.4
E	0	100

These material mixture percentages are used as the interpolation multipliers to calculate the “new” material properties, as demonstrated in tables 4.7 and 4.8.

4.9.4 Solver setup

To create and apply 900 materials manually was deemed to be very labour intensive. For that reason, a script was written to automate the solver set up. The script does several steps to speed up the solver set up process, including:

1. partitioning the test case into 900 segments
2. creating a section for each of the 900 segments in preparation for material assignment
3. applying a material to each segment, the parameters of which depend on the distance the segment lies along the furthest measurable distance in the part
4. fully fixing one end of the arm link during the initial step of the model
5. applying the bending moment around a central point of the other end of the arm link during a step subsequent to the initial step.

4.9.5 Results and conclusions

The objective of this experiment was to show that the stresses reduce in the test case when the materials are gradually blended as compared to section 4.7 or 4.8 when the materials are not blended. In order to accomplish this, the results from 4.8 will be compared to the results from this experiment.

Table 4.10 shows the results of this comparison.

Table 4.10: Performance of FGM tube compared to dual material tube

Material	Stress (MPa)		Mass (kg)		Displacement (mm)	
	Dual Material	FGM	Dual Material	FGM	Dual Material	FGM
Inc 625+Inc718	4.04	3.69	1.658	1.658	0.112	0.108
Inc 625+SS 316L	4.01	3.68	1.638	1.638	0.115	0.109
Inc 625+Ti64	4.08	3.70	1.283	1.283	0.134	0.128
Inc 718+Inc 625	4.01	3.69	1.658	1.658	0.116	0.110
Inc 718+SS 316L	4.02	3.69	1.614	1.614	0.117	0.112
Inc 718+Ti64	4.06	3.70	1.258	1.258	0.138	0.132
SS 316L+Inc 625	4.03	3.69	1.638	1.638	0.117	0.112
SS 316L+Inc 718	4.01	3.69	1.614	1.614	0.119	0.114
SS 316L+Ti64	4.06	3.70	1.239	1.239	0.141	0.135
Ti64+Inc 625	4.12	3.72	1.283	1.283	0.163	0.156
Ti64+Inc 718	4.10	3.72	1.258	1.258	0.166	0.159
Ti64+SS 316L	4.15	3.72	1.239	1.239	0.168	0.161

As expected, the mass in the two tests is identical, as there is the exact same percentage (50%/50%) of both constituent materials in every test.

The maximum displacement is lower in the FGM tests than the dual material tests. This is due to the difference in deformation characteristics between the two tests. The dual material parts deform significantly over the length where the less stiff material is present, as was seen in figure 4.19. Comparatively, the FGM parts deform uniformly over the entire length of the robotic arm link, as seen in figure 4.27.

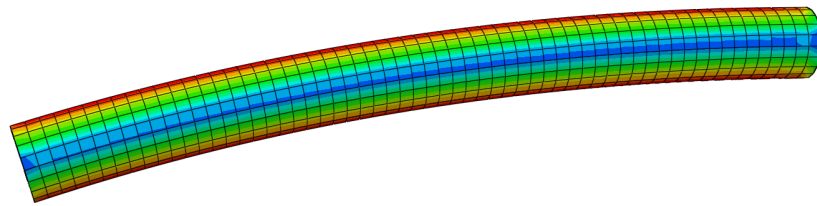


Figure 4.27: Uniform deformation characteristics of FGM part

As mentioned, the objective of this experiment was to show that the stresses reduce in the test case when the materials are gradually blended. The difference in stress between the two tests is seen in table 4.10. As seen, the stresses are lower in every FGM part when compared to the dual material counterpart. Of interest is the difference in performance between the between the tests - the maximum stress values for the FGMs are much more consistent (there is less spread in values) when compared to the dual

materials. While not verified, the reason is believed to be related to the material interface of the different tests. stress concentration on the dual material parts. The stress at the material interface of the dual material part can alter far more unpredictably, as the stress is a direct result of the two materials being brought together. There is a large range of stiffness values between the different materials. Therefore, the maximum stress values are also over a wide range of possible values, depending on the two materials brought together. The maximum stress is lower in the FGM parts because the difference in material properties at each material interface is far less distinct when compared to the dual material parts. This is significant, as it further shows that blending materials is more advantageous in terms of stress distribution and displacement behaviour when compared to the parts made with two distinct material regions.

4.10 Automated FGM while applying topology optimisation

The remaining experiment of this test case was to apply topology optimisation to the FGM study in section 4.9. The objective of this experiment was to test the effectiveness of mass and stress reduction when using FGM in conjunction with TO, and compare results of this experiment with those of the single material TO tests done in section 4.5.

4.10.1 Model setup

The model set up used the same model set up as that of the FGM test without topology optimisation, as seen in section 4.9.3.

4.10.2 Solver setup

The solver set up in this experiment was identical to that in the single material topology optimisation tests, seen in section 4.5.2.

4.10.3 Results and conclusions

As expected, the mass of all material combinations reduced (and thus displacement increased) once TO was applied. The displacement and mass values of both the FGM parts without the TO and with TO are shown in table 4.11.

Table 4.11: FGM Results

Material	FGM		FGM + TO		
	Displacement [mm]	Mass [kg]	Displacement [mm]	% Material Remaining	Mass [kg]
Inc 625+Inc 718	0.108	1.658	0.242	35	0.58
Inc 625+SS 316L	0.109	1.638	0.246	35	0.573
Inc 625+Ti64	0.128	1.283	0.25	40	0.519
Inc 718+Inc 625	0.110	1.658	0.24	35	0.58
Inc 718+SS 316L	0.112	1.614	0.249	35	0.568
Inc 718+Ti64	0.132	1.258	0.248	40	0.512
SS 316L+Inc 625	0.112	1.638	0.244	35	0.573
SS 316L+Inc 718	0.114	1.614	0.25	35	0.565
SS 316L+Ti64	0.135	1.239	0.218	45	0.557
Ti64+Inc 625	0.156	1.283	0.234	45	0.577
Ti64+Inc 718	0.159	1.258	0.239	45	0.566
Ti64+SS 316L	0.161	1.239	0.243	45	0.557

The displacement and mass values of the FGM column are exactly the same as those shown in table 4.10 of section 4.9.5. They are shown here for reference purposes.

The FGM + TO column shows three pieces of information - the displacement of the part, the volume of material remaining at that displacement value, and the mass of the part when at that displacement value.

As mentioned in section 4.5.2, the TO solver removed material at 5% increments. For this reason, all values in the “% material remaining” column are divisible by five. The displacement values all sit on or just below the displacement constraint of 0.25 mm set out in section 4.2.3. The only exception to this is the “SS 316L+Ti64” result - it marginally failed the result when 40% material remained, but comfortably passed when 45% material remained, hence it’s displacement value being further from the constraint than other material combinations.

The mass values of the FGM+TO parts show significant reduction compared to the FGM parts, as expected. The results in this experiment when compared to the FGM tests without TO closely mimic the results comparison between the single material tests without and with TO, done in sections 4.4 and 4.5. From these results, it can be concluded that using FGM in conjunction with TO is an effective method for reducing the mass of a dual material part while keeping stresses to a minimum. The ability of FGM and TO to reduce stresses when compared to single material and TO will be discussed in section 4.11

4.11 Summary of preliminary test case results

A comparison of the test results is shown in table 4.12. The table shows the **masses** of all material combinations taken forward from the screening of materials first done in section 4.5.3 and further confirmed in sections 4.7 and 4.8. All the mass values are normalised to the mass of the robotic arm link made of Al6061-T6, and are shown in relative % terms. Those in red have positive percentage values, indicating they are heavier than the original Al6061 part. Those in green have negative percentage values, indicating they are lighter than the original Al6061 part.

Table 4.12: Summary of Test Results

Material	Single Material		Dual Material		
	Solid (%)	TO (%)	Distinct Segments (%)	FGM (%)	FGM + TO (%)
Inc 625	212.6	- 21.8	-		
Inc 625+Inc 718	-	-	207.9	203.1	6.0
Inc 625+SS 316L	-	-	204.3	199.5	4.8
Inc 625+Ti64	-	-	137.0	134.6	-5.1
Inc 718+Inc 625	-	-	208.0	203.1	6.0
Inc 718+SS 316L	-	-	199.8	195.0	3.8
Inc 718+Ti64	-	-	132.5	129.9	-6.4
SS 316L	196.3	- 11.2	-		
SS 316L+Inc 625	-	-	204.6	199.5	4.8
SS 316L+Inc 718	-	-	199.9	195.0	3.3
SS 316L+Ti64	-	-	129.0	126.5	1.8
Ti64	64.1	- 34.4	-		
Ti64+Inc 625	-	-	139.6	134.6	5.5
Ti64+Inc 718	-	-	134.9	129.9	3.5
Ti64+SS 316L	-	-	131.3	126.5	1.8

It is seen that topology optimisation reduces the mass of all the single material parts to below that of the original Al6061-T6 robotic arm. The same is also true with certain FGM combinations, but the performance of single material parts is greater. When comparing the single material results to the FGM+TO results, it is seen that the single material parts have lower masses than the FGM parts. The main reason for this is the specific stiffness value of the materials tested. Ti-6Al-4V has the highest specific stiffness of all the materials, and therefore creates the lightest arm link for

the constrained deflection. However it was proven in section 4.9 that FGM parts have consistently lower stresses than dual distinct material parts. That being said, these lower stresses in FGM parts, along with the desire to have multiple materials in a single part, show that FGMs are a viable research avenue.

4.12 Outcomes of preliminary test case

The outcome of the preliminary case study showed that the combination of FGM and TO was successful, reducing the stress concentrations in a part when compared to a part made of two distinct materials. The process is complex however, and creating the computer models took significant time. Because of this, the researcher decided it would be a valuable contribution to write a set of design guidelines to describe the process of creating lightweight FGM parts that incorporate TO.

Chapter 5

Design guidelines for FGM mechanical parts

5.1 Introduction

Chapter 4 summarised that a set of design guidelines for combining FGM and TO would be a valuable contribution to the field, a sentiment echoed in literature^[169]. Before the guidelines themselves are made, preliminary work must be done, including research into guideline-modelling and defining the focus of the guidelines.

5.1.1 Reasons for design guidelines

There are several reasons for creating a set of guidelines, some which have been previously mentioned, and others which have yet to be touched upon.

Firstly, it was noted in the preliminary test case that the process of applying FGM was complex to model on the computer. For this reason, having a set of guidelines would be useful to a researcher wanting to apply FGMs themselves.

The first reason leads to the second - having a document which covers the aspects of lightweight part design identified during the literature in Sections 2.1 - 2.5 would be a worthy contribution to the knowledge of creating lightweight FGM parts.

The last point leads on from the second - the preliminary test case was noted as complex, however, it focused on material choice and structural design only, it did not take into account form or manufacturing technique - the remaining two aspects of lightweight design identified during the literature review. Including these two elements increases complexity, and thus reinforces the argument for a set of design guidelines for the creation of lightweight parts which combine FGM and TO.

5.1.2 Design guidelines creation

This section will discuss the boundaries of the design guidelines in this thesis and adapt the structure from said well-known methodologies to create the basic layout of the design guidelines.

5.1.2.1 Design guidelines boundaries and layout

The design guidelines in this thesis will be created to allow the rigorous, repeatable creation of FGM and TO parts for robotic arm applications in harsh environments.

Since Pugh’s guidelines shared all the common similarities of the researched guidelines, they were chosen as the example to model the design guidelines around.

A simplified version of the design core from Pugh’s guidelines is shown in figure 5.1.

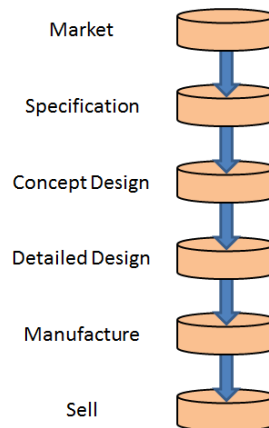


Figure 5.1: Simplified design core

The specification of the design guidelines is split into two sections. The first is a clarification of the specifications given in the design task. The second is a simplified list of options that the specification can choose from in each section of the design guidelines. The options are drawn from the literature findings for each of the four focus areas. An example of these specification options is shown in figure 5.2.

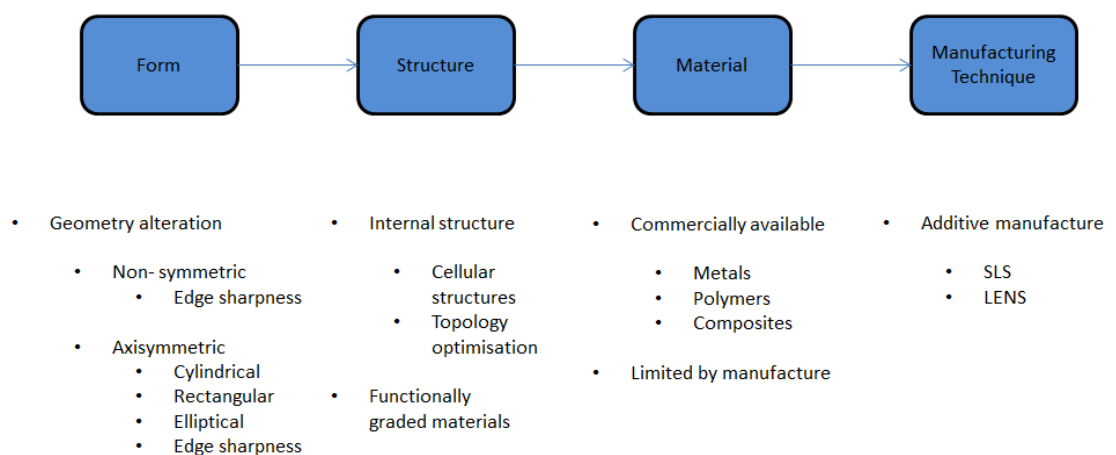


Figure 5.2: Conceptual design options

The next stages of the design guidelines are where most of the content is focused on.

After the specification is taken from the design task/model taken from the current part, the conceptual design and detailed design will occur hand-in-hand. Some steps in the guidelines will not move beyond conceptual, while others will detail exact processes required. As such, both conceptual design and detailed design will receive strong focus. The final stage of the methodology will discuss manufacture of the part. This will receive a light-moderate focus. The reason for this is due to the availability of manufacturing equipment - many additive manufacturing systems require a significant financial investment, and as a result, the end user of the methodology may have to use the equipment that is available to them, rather than the most appropriate system. Therefore, discussion of manufacture will cover general additive manufacture best practices, rather than in detail specifics of different technologies.

The guidelines in this thesis will finish at this stage. There will be no consideration given to commercial aspects of design. These alterations to Pugh’s design core result in the final layout of the guidelines, as seen in figure 5.3.

The “market” and “sell” stages are marked out of scope only in context of the design guidelines. The researcher understands that these two stages are critical for any commercial offering to be successful. However, the work contained within this thesis does not delve into market economics - instead focussing on the areas already highlighted in this section; chiefly design.

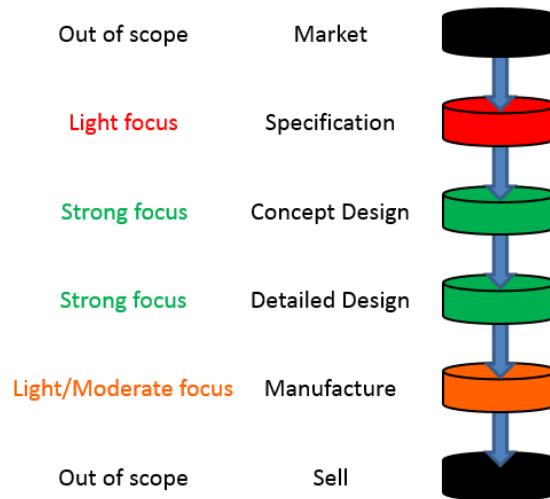


Figure 5.3: Final design core

5.1.3 Design guideline constraints

The following constraints are in place in the guidelines:

Cost As highlighted in the conclusion of Section 2.6, cost of additively manufactured components, especially those which contain functionally graded materials, will

be expensive. However, as this project is primarily conceptual, costs are omitted as a consideration.

Additive manufacturing rules The additive manufacturing restrictions in place are high-level only, designed to allow the guidelines to be AM agnostic. This way, an engineer can use the restrictions for a wider range of AM processes. Ideally, the guidelines should be stratified for each of the seven major AM categories.

Validation Due to the lack of physical testing, elements of these guidelines are unvalidated, especially the work surrounding measurement of residual stress after AM deposition. Any user of the guidelines should be aware of this restriction.

5.1.4 Defining the focus of the design guidelines

In section 5.1.2, the boundaries and layout of the design guidelines were defined. The depth of each phase was also briefly mentioned. In this section, the focus of the design guidelines will be defined. The layout of the guidelines will be linked to the four areas that have been discussed in Sections 2.1 - 2.5 (form, structure, material and manufacturing technique). **Due to space constraints, this thesis will be displaying the final version of the design guidelines, however, it should be noted that there were many iterations of the guidelines from original concept to what is shown in this thesis.**

5.1.4.1 Linking design guidelines to focus areas

To easier visualise the links between the design core and the focus areas of this thesis, the design guidelines will be re-oriented. Taking the boundaries of figure 5.3 and reorientating them gives figure 5.4.

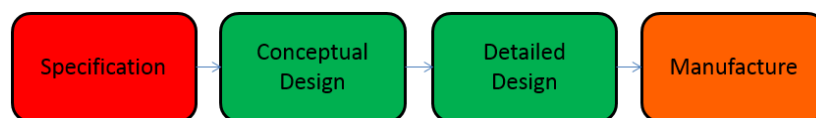


Figure 5.4: Reoriented design guidelines

Each of these areas must now be linked to the four areas of focus.

Specification As mentioned in section 5.1.2.1, specification will be based on the outcomes of the literature review. The specification options begin the thought processes over all aspects of the part, including what shape it will be/already is specified as, it's internal structure, the materials it will be created from and what manufacturing process will be used to produce it. These options do not require any decision to be

made. Instead, they merely show the designer the breadth of choice that will be given to them during the conceptual and detailed design phases, which is when the decisions will be made. Because it is linked to all four focus areas, the specification phase is connected to all four, even though the entire specification step will only receive light focus. Unlike Pugh’s guidelines where the specification is a deliverable, it will only be used as a reference for the researcher in these guidelines.

Conceptual design Section 5.1.2.1 highlighted that during the conceptual design phase and detailed design phase are intertwined. Many of the steps will contain iterative cycles - working from conceptual to detailed design. Since the conceptual design will be associated with every step in the design guidelines, it will by consequence be related to all four focus areas.

Detailed design The detailed design phase works in tandem with the conceptual design phase, giving greater specifics to certain areas of the design guidelines that are most important for creating a lightweight part. As such, this phase has the largest impact on the success of the design guidelines, as it has the biggest effect on the characteristics of the final part. Akin to the conceptual design phase, the detailed design phase is also connected to all four focus areas. The guidelines themselves will be explained in sections 5.2 to 5.6.

Manufacture The manufacture of the part is the last section of the design guidelines. As mentioned in section 5.1.2.1, this phase will describe manufacturing best practice, rather than give detailed descriptions of how the manufacture itself should be carried out. As such, it will place generalised best practice techniques and limitations into the guidelines in order to ensure that the part can be created once designed. These limitations and best practices impact all four focus areas, and for that reason, manufacture is linked to all four areas.

This figure can now be linked to the focus areas of the study in this thesis, as is shown in figure 5.5.

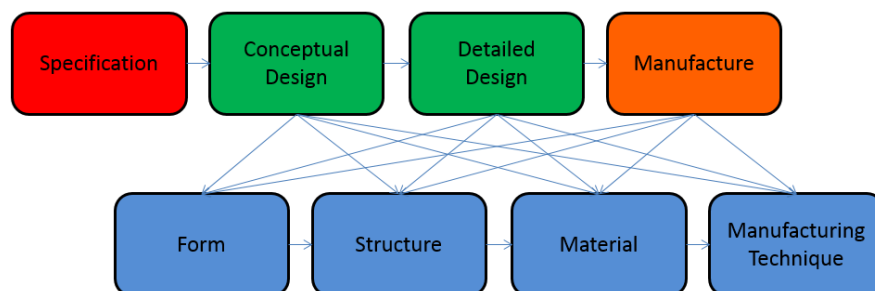


Figure 5.5: Design guideline stages linked to focus areas

As mentioned in section 5.1.2.1, both conceptual and detailed design happen hand in hand. The two will be amalgamated to give figure 5.6.

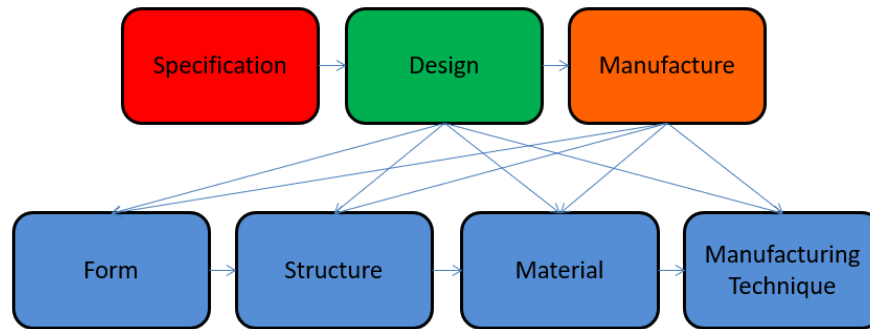


Figure 5.6: Design guideline stages linked to amalgamated focus areas

Sections 5.2 to 5.6 will describe each focus area in detail.

5.2 Form: Detailed description

5.2.1 Introduction

The form of the part describes its outer geometry on a macro level - the overall geometrical shape of the part. The form is important to the performance of the part because it can influence mechanical performance and alter stresses. When these stresses are reduced via re-arrangement of the outer geometry, the part can be reduced in mass. It should be noted that the use of non-axisymmetric cross sections is growing in use. However, the research required for such cross sections is complex and in-depth, and design of these forms will not be covered in these design guidelines due to time constraints.

5.2.2 STEP 1 - UNDERSTANDING DESIGN TASK

As first discussed in section 5.1.2, the design guidelines **assume that the design task is already in place**. This means that the designer already has a design for the part that is going to be made. The first step is therefore to extract information from the design task.

To better understand the design task, there are two stages required. The first is to draw out the design requirements from the design task. This will give the constraints for the design. The second stage is to validate the design to ensure it is feasible. This will be done using standard equations.

5.2.2.1 Elicit Design Requirements from Design Task

In order to know what features the part is going to need, the design requirements are needed. These can appear in one of two ways:

1. the requirements are directly listed in the design task, or
2. the requirements need to be inferred from other information given in the design task.

If the design requirements are not directly listed, they will need to be drawn from the design task. To do this, the design task must be read and interpreted. This is largely based on intuition of the engineer/designer. Requirements typically needed for the structural design of a robotic arm part could be, but are not limited to:

- dimensions
- construction materials
- loads on part

It is important at this stage to group the requirements as “primary” and “secondary”. Primary requirements are those which must remain fixed, and therefore act as constraints. Secondary requirements are those which can be altered by the designer.

Table 5.1: Organising design requirements

Primary Requirements	Secondary Requirements

To demonstrate this step, an example design task from a prospective designer/customer is shown in section [5.2.2.2](#).

5.2.2.2 Validate Design Task/Requirements

If possible, the design task should be validated at this early stage to ensure that the designer/customer’s requirements are feasible. This early validation step can be done manually using structural engineering equations. The equations used will depend on the part being designed. If it is found that the design is not feasible, the requirements must be altered. The protocol to follow to alter the design requirements is as follows:

1. Freeze any requirements which the designer/customer has deemed “primary”, as these are constraints.

2. Of the secondary requirements, alter that which causes greatest infeasibility.
3. Re-evaluate design using previous equations
4. Repeat steps 2 and 3 until the design is deemed feasible.

To demonstrate this step, the example from section 5.2.2.2 will be continued.

Example of design requirement elicitation This example is based on a robotic arm link, however, the process of requirement elicitation is the same when designing other robotic parts.

“I require two robotic arms to increase productivity on my car assembly line. The task for the arms will be to weld the frame of the car together. The two arms will do symmetric movements at various locations, each working on half of the frame. Each frame should take no longer than one and a half minutes to complete, of which one minute will be spent welding. It would be preferred if all cabling (electric, hydraulic) could be routed within the arms where possible. ”

From this design task, the following design requirements for a robotic arm link can be deduced:

Reach: The robot arm must be able to reach to all points along the length of a car, and up to half the width of the car. A standard car averages 4.8 m in length and 2 m in width. Assuming the arm is positioned centrally along the length of the vehicle, the maximum reach it would need is 2.6 m. Giving 400 mm of clearance next to the vehicle, **the arm reach will need to be 3 m.**

Material: No material was specified for the arm. The environment it is working in does not require any materials tailored for harsh environments - high temperature, high corrosion, etc. As a starting point, **the arm will be constructed from mild steel.**

Accuracy and Repeatability: A typical weld is 5 mm in width. To ensure the weld sufficiently contacts both surfaces being joined, **the deflection must be ± 1 mm.**

Payload: A welding tool typically weighs 10 kg. **The payload is therefore 10 kg.**

Velocity - Welds need to be made at various points over the frame of the vehicle. It is stipulated that the tool will need to travel 10 m in 30 seconds for every frame. Using these figures and assuming constant velocity, **$v = 0.33$ m/s**

Second moment of area - The arm will have to be hollow to allow cabling to be routed within. As a starting point, the design will use a **hollow circular cross section, with an outer diameter of 0.2 m and an inner diameter of 0.17 m.**

These design requirements can then be grouped as either “primary” or “secondary”.

Table 5.2: Example of organising design requirements

Primary Requirements	Secondary Requirements
Reach	Material
Deflection	Acceleration
Repeatability	Second moment of area
Payload	

Example of design task/requirement validation As mentioned, this is a continuation of the example in section 5.2.2.2. The requirements which need validation are:

- arm deflection given reach requirement
- arm dimensions given calculated deflection

Deflection The robot arms in this thesis are being treated as cantilever beams for static calculation purposes. For the deflection of a cantilever arm, the length of the arm, the payload, the acceleration, the material the arm is made from and the second moment of area are needed.

$x = \frac{FL^3}{3EI} = \frac{maL^3}{3EI}$, where x is the deflection, m is the payload, a is the acceleration, L is the reach, E is the Young’s modulus and I is the second moment of area.

$$x = \frac{10 * 9.80665 * 3^3}{3 * 2e^{11} * 0.0000375415} = 1.18e^{-4} \text{ m}$$

This deflection value is well within the 0.001 m tolerance specified in the design task. The design requirements are therefore feasible. In order to reduce the mass of the arm link, certain requirements can be relaxed.

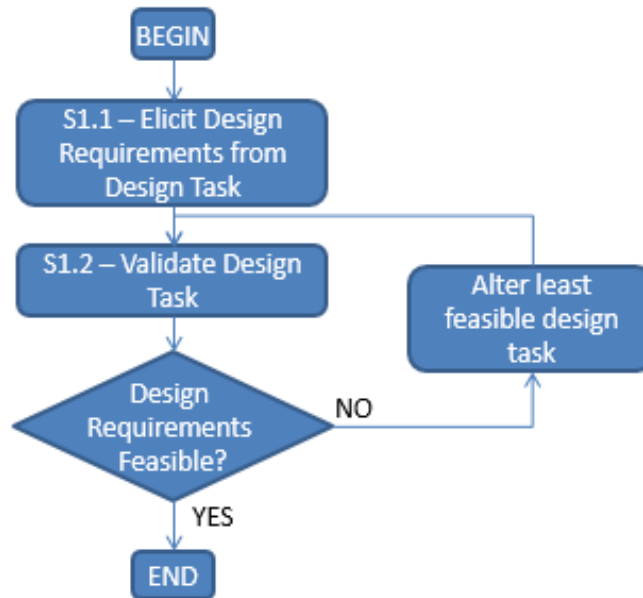


Figure 5.7: Validating the design task

5.2.2.3 Conclusion

Understanding the design task is paramount to successful design of a lightweight robotic arm link. The example given shows that the two stage elicitation followed by validation ensures that the design task given is fit for purpose. However, it requires specialist knowledge to ensure that all the requirements of the robotic arm link are captured. This is a potential shortcoming if the designer does not have the required knowledge. Further iterations of these guidelines should develop a method to ensure this does not happen.

5.2.3 STEP 2 - INFLUENCE OF FORM

Once the design task has been examined and validated, the form itself can be studied, and altered from the original form suggested in the design task, if need be.

5.2.3.1 Influence of Geometric Features

Any geometric feature on a part will increase stress when compared to a feature-barren part, for example, a simple cuboid. The value of stress increase is governed by the stress concentration factor, K_t , if applicable.

The maximum stress in a part is linked to the K_t value as follows:

$$\sigma_{\max} = K_t \sigma_{\text{ave}}$$

The geometry and location of a feature in respect to loading dictates the value of the K_t .

An example of a part with stress-concentrating features is shown in figure 5.8.

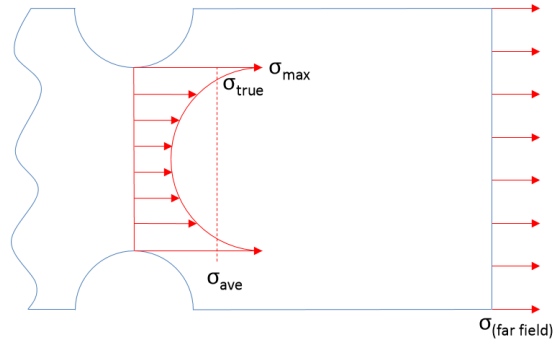


Figure 5.8: Description of stress concentration factor

In this case, the two notches increase the maximum stress within the part. The smaller the radius of curvature, the higher the stress concentration factor will be. This is seen in cracks, which have a very low radius of curvature. At the tip of a crack, the stress can be an order of magnitude higher than in the rest of the part. In order to arrest a crack, a hole can be drilled at the tip of the crack. This increases the radius of curvature and thus lowers the maximum stress in the part.

5.2.3.2 Conclusion

Due to the existence of stress concentration factors, the design guidelines suggest that no feature on the form of the part should be an acute angle.

Charts for calculating stress concentration factors are found in many engineering texts^[199;200].

5.2.3.3 Influence of material placement

As can be read in standard engineering texts^[199], the second moment of area shows that hollow cores outperform solid cores in stiffness terms when compared per unit mass. However, the placement of material about the centroid axis can further increase stiffness, as this increases “x” in the second moment of area equation.

If the designer has the freedom, the outer dimensions of the part should be made as large as possible. This allows the second moment of area to be as high as possible. However, in this circumstance, the wall thickness should be a minimum of 3 mm. This ensures that the part will not be obscenely large. In reality, there will often be constraints on the maximum outer dimensions meaning that the outer dimensions cannot be extremely large.

The absolute values of the part width and wall thickness must be monitored. If the part width/wall thickness ratio gets too high, local buckling of the part will occur. The bending factor (ϕ_B^e) is a measure of this ratio, and is the point when failure switches from yield buckling to local buckling. The maximum bending factor for a cross section is given by:

$$(\phi_B^e)_{\max} \approx 2.3 \left(\frac{E}{\sigma_f} \right)^{1/2}$$

where E is the Young's modulus of the material and σ_f is the yield strength of the material. Each cross section has its own ϕ_B^e value. These can be found in engineering texts, such as Ashby^[201].

5.2.3.3.1 Conclusion In order to maximise the second moment of area, the material should be placed as far from the centroid axis as possible. However, care must be taken to ensure local buckling does not occur. Alongside the distance from the centroid axis, the effect of orientation on the stiffness of parts is also important. This will be discussed in the next section.

5.2.3.4 Influence of Core Cross Section

The second moment of area is related to the cross section of a beam as well as the volume.

Figure 5.9 shows the same rectangular cross section in two orientations. The centroid axis is shown as a red-dotted line.

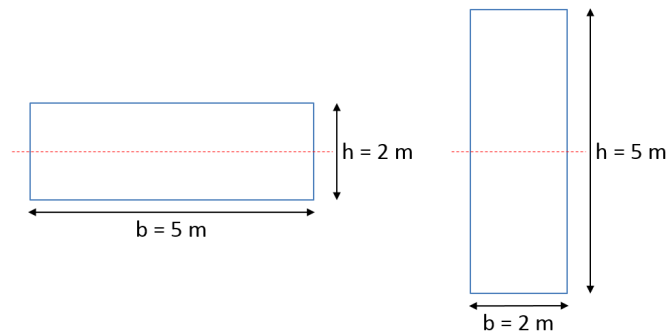


Figure 5.9: Altering the cross section

Calculating the second moment of area for both results in:

$$I = \frac{5 * 2^3}{12} = \frac{40}{12} = 3.333 \text{ m}^4$$

$$I = \frac{2 * 5^3}{12} = \frac{250}{12} = 20.833 \text{ m}^4$$

As seen, the second moment of area is 6.25 times higher in the example with material further away from the centroid.

5.2.3.4.1 Conclusion In order to increase the second moment of area, and thus the stiffness, material should be placed as far from the centroid axis as possible. This is also the reason for the greater “efficiency” seen in the hollow parts when compared to solid parts.

The example in figure 5.9 is the same cross section at two different orientations. The impact of altering the cross section on the second moment of area will next be investigated.

5.2.3.5 Influence of Breakeven Angle

The breakeven angle is defined as the angle at which cross sections equal one another in terms of stiffness (assuming each cross section has the same surface area). As most cross sections will be versions of either ellipses or rectangles (if not a circle), equations for these two cross sections are used as comparisons to the circle.

For an elliptical cross section, the breakeven equation to the circle is:

$$\alpha(I_{xx}) = \cos^{-1} \left(\sqrt{\frac{\frac{4I}{\pi bd} - b^2}{d^2 - b^2}} \right)$$

where I is the second moment of area of a circle with the same area, b is the HALF the breadth of the ellipse, and d is HALF the depth of the ellipse (as shown in Figure 5.10a). The ratio of b to d is called the “aspect ratio.”

For the rectangular cross section, the breakeven equation to the circle is:

$$\alpha(I_{xx}) = \cos^{-1} \left(\sqrt{\frac{\frac{12I}{bd} - b^2}{d^2 - b^2}} \right)$$

Again, I is the second moment of area of a circle with the same area. This time around, b represents the ENTIRE breadth of the rectangle, and d represents the ENTIRE depth of the rectangle (as shown in Figure 5.10b) The ratio of b to d is again called the aspect ratio.

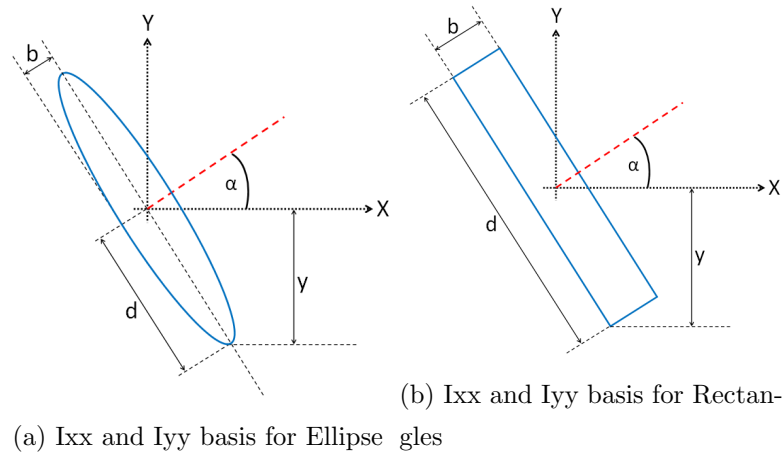


Figure 5.10: Description of “b” and “d”

As mentioned, using these equations allows the designer to find the angle at which the ellipse/rectangle has the same stiffness as a circle of the same area. Both these equations give the breakeven angle for I_{xx} . To find I_{yy} , the following equation is used:

$$\alpha(I_{yy}) = 90 - \alpha(I_{xx})$$

When the breakeven equations are solved for, it is seen that the aspect ratio has the largest effect on stiffness between the values of one and ten. Once over ten, the effect of increasing the aspect ratio does not bring about great increases in stiffness. This is seen in Table 5.3 and graphically in Figures 5.11 and 5.12.

Table 5.3: Breakeven angle values

Aspect Ratio	$\alpha(I_{xx})$ Breakeven Angle (°)	
	Ellipse	Rectangle
1.5	50.77	53.97
2	54.75	56.58
3	60	61.13
4	63.43	64.31
5	65.91	66.64
6	67.79	68.43
8	70.53	71.06
10	72.45	72.91
15	75.52	75.88
20	77.40	77.70

As can be seen, at an aspect of ratio of ten, the breakeven angle for both the elliptical

and rectangular cross sections is around 72°. This is a 72° rotation from the direction the payload is accelerating in (with gravity, if on Earth).

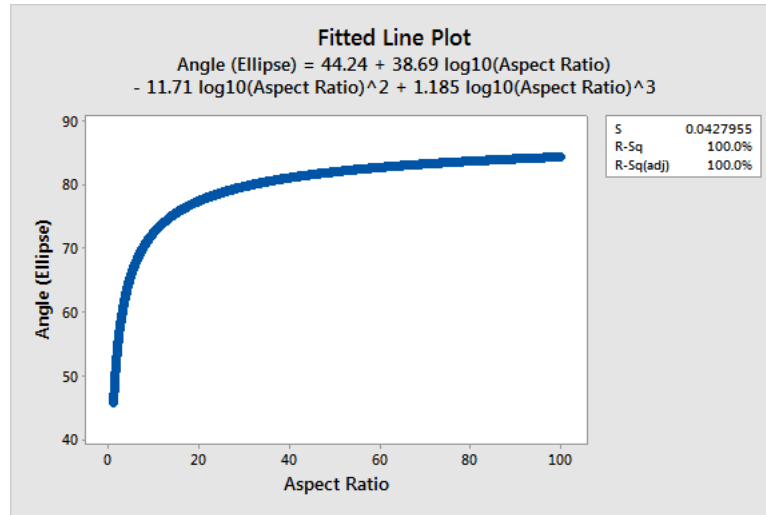


Figure 5.11: Regression Equation for Elliptical Aspect Ratio < 100

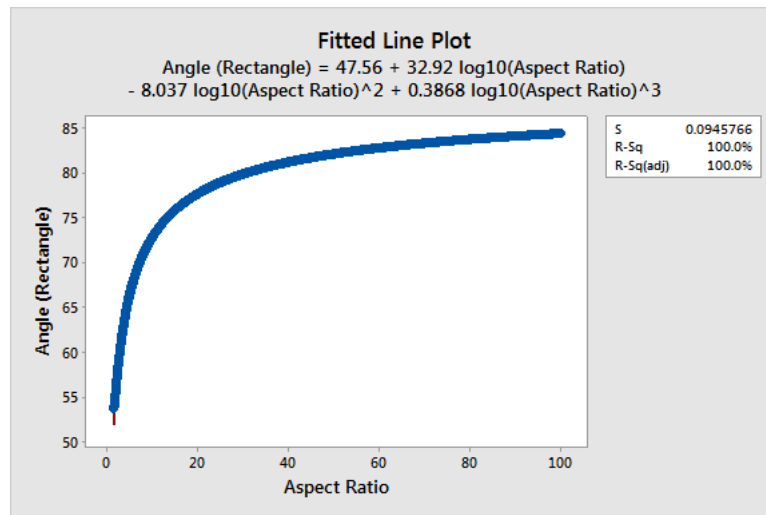
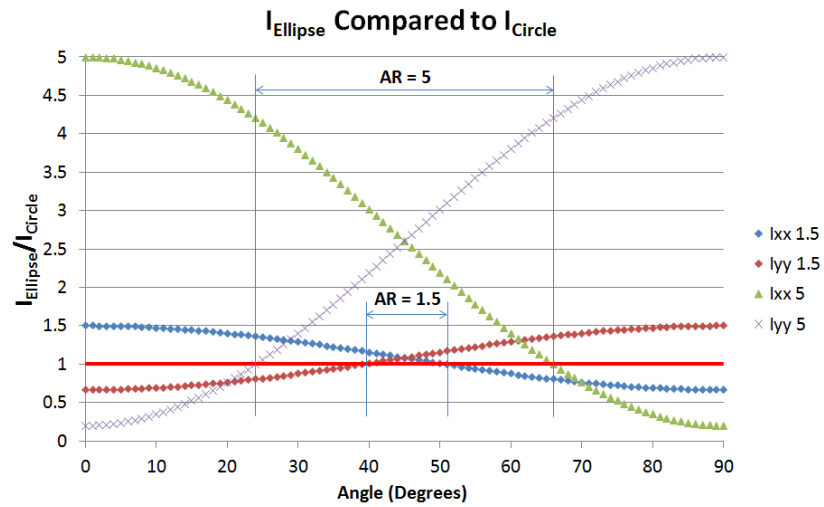


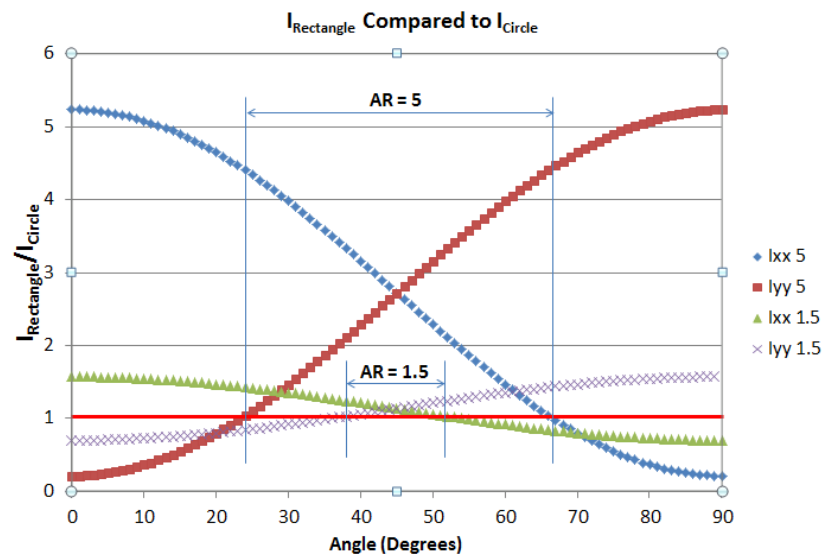
Figure 5.12: Regression Equation for Rectangular Aspect Ratio < 100

It can be seen that as the aspect ratio **increases** the range over which either cross section is stiffer than the circular cross section increases. However, the designer must keep in mind the manufacturability of components and the workspace that the robot will be operating in (the link can not be infinitely large). As mentioned, up to an aspect ratio of ten, the orientation angle increases more rapidly than once the aspect ratio exceeds ten. The theory that the increase of aspect ratio increases the range over which either the rectangular or elliptical cross section is stiffer than the circular one is also shown in figure 5.13. Each graph shows aspect ratios of 1.5 and 5. As can be seen, the aspect ratio of 5 has a wider range where the given cross section performs greater

than the circular cross section, when compared to the range of the aspect ratio set at 1.5.



(a) Influence of Ellipse Aspect Ratio



(b) Influence of Rectangle Aspect Ratio

Figure 5.13: Influence of Aspect Ratios

5.2.3.5.1 Conclusion As shown, the breakeven angle is directly linked to the aspect ratio. Up to an aspect ratio of 10, the breakeven angle quickly increases to a value of $\approx 72^\circ$. Above this, the breakeven angle does not increase as fast when compared to the aspect ratio. As such, a limit to the aspect ratio of 10 is put in place.

5.2.3.6 Influence of operating orientations

If the arm link is to move in both the x and y directions, both I_{xx} and I_{yy} need to be kept in mind. As I_{xx} increases, I_{yy} decreases, and vice versa. As mentioned, the maximum

I_{xx} breakeven angle is 72° , when the aspect ratio is 10. Above this angle (within the areas highlighted in Figure 5.14), the value of I_{xx} will increase when compared to a circle of the same area. However, the value of I_{yy} will become lower after the I_{yy} breakeven angle is reached ($\alpha(I_{yy}) = 90 - \alpha(I_{xx})$). This is of lesser importance than the I_{xx} angle though, as the arm link is not having to resist loads in I_{yy} - only I_{xx} is load bearing. This is due to the force of gravity through I_{xx} . Assuming gravity works along the y axis in Figure 5.14, the acceleration due to gravity will **constantly** work in this direction. The acceleration working along the x axis (which will relate to I_{yy}) will be dependent on the acceleration of the arm caused by actuation (decided by the designer in Chapter 5.2.2). It is very unlikely that a design will ask for an acceleration of the arm greater than 9.80665 m/s^2 , and therefore I_{xx} is of more importance than I_{yy} .

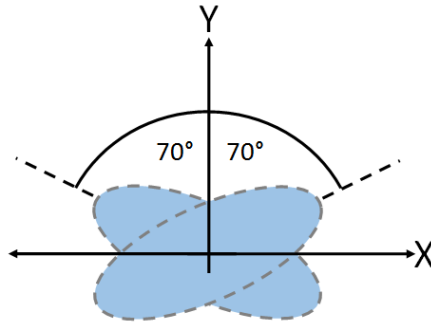


Figure 5.14: Range of elliptical or rectangular cross section with aspect ratio of 10

5.2.3.6.1 Conclusion During design, it is important to keep in mind not only I_{xx} , but also I_{yy} . The lower the acceleration value (from actuation), the lower I_{yy} can be without causing arm link failure. Therefore, the orientation range for a robotic arm link with two orders of rotational symmetry is from $\alpha(I_{xx})$ to $-\alpha(I_{xx})$, as highlighted in Figure 5.14.

5.2.3.7 Influence of Cross Section Alteration

5.2.3.7.1 Concept From section 5.2.3.4, it can be seen that the cross section used will have an effect on the second moment of area and therefore on the performance. This section will discuss the concept of how to alter the cross section of a rotationally-symmetric part. Although this methodology assumes the design task is already in place and therefore the form of the part already decided, an alteration of cross section in a rotationally-symmetric part is relatively easy, and can benefit the part's performance. As mentioned, due to the bespoke design and complexity of non-axisymmetric parts, these are not going to be focused on in the scope of this thesis.

Many arms have a cross section which is rotationally symmetric in at least four orientations (e.g, square or circular cross sections). These cross sections mean that the

arm link will have constant performance (in terms of stiffness) that is independent of orientation. Therefore, an arm link which is expected to perform across a wide range of orientations will *probably* benefit from a cross section that is rotationally symmetric around at least four orientations. An example of a circular cross section (with infinite orientations of rotational symmetry) is seen in Figure 5.15.

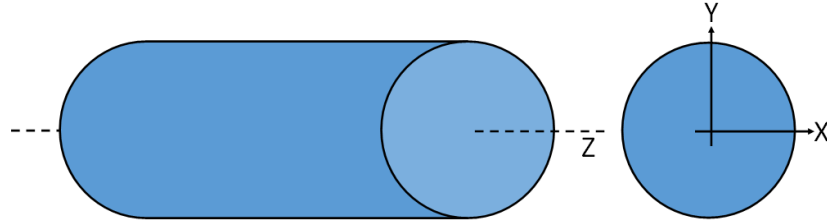


Figure 5.15: Circular Cross Section

Independent of loading direction, when rotated around the Z axis, the stiffness of the cross section in Figure 5.15 remains constant. This is in contradiction to the elliptical cross section shown in Figure 5.16.

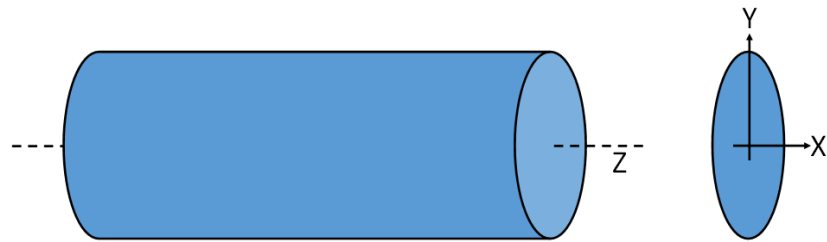


Figure 5.16: Elliptical Cross Section

This cross section has two orders of rotational symmetry. In certain orientations, the stiffness in the elliptical cross section will be lower than that of the circular cross section, while in other orientations, the stiffness will be higher. The stiffness performance will be discussed in section 5.2.3.7.2.

5.2.3.7.2 Theory In order to determine if the cross section of the part is suitable for the task or not, the steps in this section should be followed.

Define orientation range The orientation range **about the Z axis** that the robot arm link will be operating in is important to the design of the cross section. To help better define this range, see Figure 5.17. Once the range of the robot arm link is defined, the shape of the cross section can be chosen.

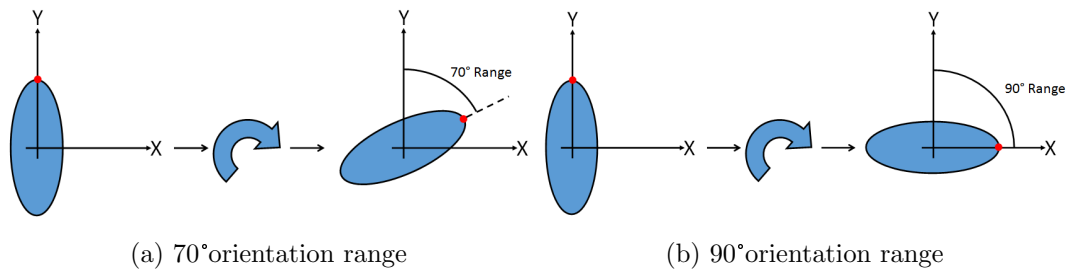


Figure 5.17: Defining orientation range

* Find “Breakeven” Angle

Finding the breakeven angle will give the maximum aspect ratio that the cross section can be set to, assuming there are no geometric constraints. Often geometric constraints will result in the part using an aspect ratio that is lower than the maximum value which the breakeven angle gives.

* List geometric constraints in the x and y planes

The geometric constraints in the x and y planes will limit any potential changes to the aspect ratio. Constraints in the x and y planes are typically caused by other parts of the robotic system, for example, additional arm links.

* Calculate area of current cross section

The aim of these design guidelines is to create a lightweight part. Therefore, a constraint put in place is to limit the area of any new cross section to be no higher than the current cross section being used.

* Alter cross section based on constraints

If the orientation range of the part is lower than the limit at which a circular cross section is the only option (above an aspect ratio of 5:1, at around 65°), the cross section could be altered, based on the following conditions:

1. If there is a MINIMUM diameter and a set wall thickness, a circular cross section should be used, as an ellipse would “become” a circle with these conditions
2. If there is a MINIMUM diameter and no set wall thickness, an ellipse/rectangle could be used, as it is potentially stiffer - the wall thickness will have to be monitored to ensure it does not fall below the ratio required for the minimum bending factor (section 5.2.3.3).
3. If there is no MINIMUM diameter, an ellipse/rectangle could be used, as there is a high chance either will be stiff enough, and have a lower cross mass than a circular cross section.

5.2.3.7.3 Conclusion

* Range above 70°

If the robot arm is working above $\approx 70^\circ$, the arm link cross section should have **at least** four orders of rotational symmetry. Therefore, if the current cross section in the design has at least four equidistant straight edges (regular tetragon, regular pentagon, regular hexagon, etc) or is spherical, it should be kept. However, if it has two or less orders of rotational symmetry, it should be changed for a cross section design with four or more orders of rotational symmetry.

If the orientation range needs to be above $\pm 70^\circ$ from the vertical axis, the cross section should have a least four orders of rotational symmetry.

* Range below 70°

If the orientation range of the robotic arm link is less than $\approx 70^\circ$, the designer can consider using a cross section with two or fewer orders of rotational symmetry. Therefore, if the current cross section in the design has two or fewer orders of rotational symmetry, it should be kept. However, if it has three or more order of rotational symmetry, it should be changed with a cross section design with two or fewer orders of rotational symmetry.

If the orientation range is less than $\pm 70^\circ$ from the vertical axis, the value for the range should be cross referenced against Figures 5.11 and 5.12, and an appropriate aspect ratio for the cross section can be chosen.

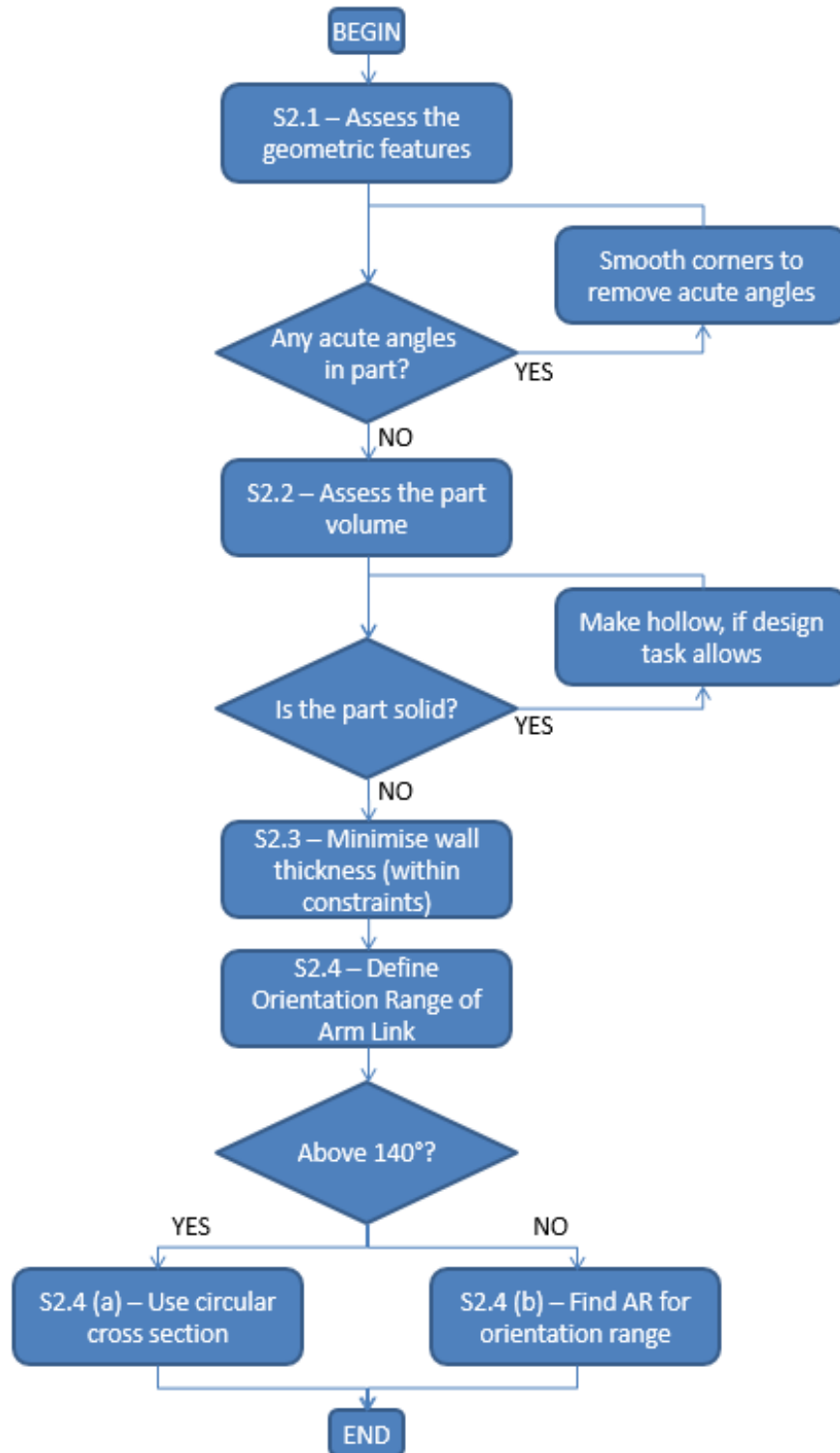


Figure 5.18: Assessing the influence of cross section orientation

5.2.3.8 Choosing core dimensions

Using the findings from section 5.2.3.7, the following steps can be created:

- If part is axisymmetric:

1. Find the orientation range of the part
 2. Find the aspect ratio which satisfies this orientation range
 3. Find the outer geometric constraint of the part.
 4. Design cross section of part with this maximum outer geometric constraint and aspect ratio
 5. Place material along surface of geometric constraint, and begin working inwards
 6. Working inwards towards the axis, add material to the part.
 7. Work inwards until sufficient material is present to satisfy the design requirements by the required factor of safety.
- If part is not axisymmetric:
 1. Core should be left unaltered from design given in design task.

The reason for these two different techniques is due to how different part shapes will be reduced in mass. These techniques will be discussed in section 5.3 and demonstrated in sections 5.5.2.1.2 and 5.5.2.10.1.

5.3 Structure: Detailed Description

5.3.1 Introduction

Structure describes the geometry at a smaller scale when compared to the form. The structure is important, as it impacts the stresses in the part, and the overall mass of the part.

The research into structure in these design guidelines focusses on two methods - topology optimisation and structured cells. As shown in figure 5.5, structure is not linked to the specification stage. This is because the structural optimisation work is not assumed to have been detailed in the specification, but instead will occur during the redesign done when these design guidelines are used.

5.3.2 Constraints on internal structure

Ideally, materials blend seamlessly in FGM parts. However, in reality, there is a minimum resolution which can be achieved by the AM process, and this resolution governs the gradation of materials/properties within FGMs. The thickness of each graded layer should be a multiple of the minimum resolution the AM equipment can perform. Each segment of unique material composition should be THREE layers thick AT LEAST (no maximum restriction on the number of layers). This will allow for uneven distribution

of material when in powder form. Therefore, no structural features in the design space should be smaller than this minimum resolution.

5.3.3 STEP 3 - CHOICE OF INTERNAL STRUCTURE TECHNIQUE

The designer must choose whether to use structured cells, topological optimisation or a mixture of both within the robotic arm link. This decision must be made here, as the outcome will affect the part modelling.

The descriptions of both structured cells and topology optimisation were given in depth during the literature review (section 2.3). Structured cells are defined in this methodology as any repeating cell structure. Examples of can be seen in the literature review (section 2.3.2).

The rules in this methodology aim to make sure that any situation not deemed appropriate for structured cells is deemed appropriate for topology optimisation. These situations are covered in the next three sections.

5.3.3.1 Structured cells in this thesis

All structured cell work in this thesis assumes that cells have the same form in any part. The cells can be of different size, but must alter only in size, and not geometric shape. The dimensions of trusses can increase in length, but cannot increase in diameter.

5.3.3.2 Geometry of part

5.3.3.2.1 Appropriate use of structured cells Since structured cells repeat themselves, they are best suited to geometries that are symmetric in as many axes as possible. For this methodology, that covers cross sections that have at least two orders of rotational symmetry. All structured cell work in this thesis assumes that cells have the same form in any part. The cells can be of different size, but must alter only in size, and not geometric shape. The dimensions of trusses can increase in length and diameter. **The minimum dimension of a structured cell is 3 mm in the perpendicular direction to the outer skin.** This constraint is put in for manufacturing reasons - any smaller than 3 mm, and the features of the structured cell become too small to manufacture due to resolution limits of the AM hardware.

5.3.3.2.2 Inappropriate use of structured cells/Conclusions Cross sections that have less than two orders of rotational symmetry will *probably* have features that are difficult to fit identically-shaped (but not necessarily on the same scale) structured cells of at least 3 mm into. Therefore, topological optimisation should be used in these cases.

5.3.3.3 Loading conditions on part

5.3.3.3.1 Appropriate use of structured cells Unless graded in size, structured cells are identical, and therefore each cell will deform identically if a uniform load is applied. Therefore, in these design guidelines, structured cells will only be applied when the loading conditions are “symmetric”. “Symmetric” loading relates to the orientation range in section 5.2.3.7. Independent of the loading directions on the arm link, symmetric loading only occurs if the orientation range is above 72° (if the arm link rotates around the z-axis by more than 72°).

Figure 5.19 illustrates symmetric loading. The red points and arrows show fictitious independent loading conditions, that will remain in those locations independent of the orientation range of the arm link about the z-axis. The orientation range is marked with the yellow arrows. If this orientation range of the arm is above 72° , then structured cells can be used.

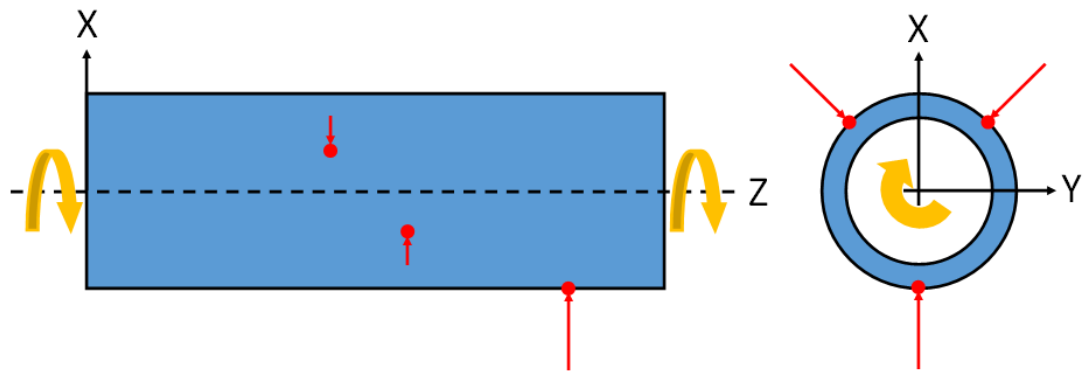


Figure 5.19: Descriptor of symmetric loading

5.3.3.3.2 Inappropriate use of structured cells/Conclusions If the orientation range is below 72° (referred to as non-symmetric loading conditions), topology optimisation should be used. As mentioned in section 5.3.3.3.1, all cells in any part must have the same form. Under non-symmetric loading conditions, the stiffness required of the cells in the directions of loading will mean that the cells not in the direction of loading will have a stiffness which is unnecessarily high. These stiffness-redundant cells will add unnecessary mass to the arm.

5.3.3.4 Number/size of structured cell layers

The dimensions of the structured cells will have an impact on multiple parameters of the part, including flexural rigidity, mass and vibration damping. In order to balance the many parameters, the number and size of structured cells must be managed.

5.3.3.4.1 Appropriate use of structured cells Number of layers. There is no upper limit to the number of layers of structured cells in a part, in either direction. As noted in Section 5.3.3.2.1, there can therefore be multiple layers of cells, each with different truss length and diameter, but the same overall form.

Size. The maximum size of the structured cell depends on the geometry of the cell itself. There is no maximum size of for the cells themselves.

5.3.3.4.2 Inappropriate use of structured cells/Conclusions Number of layers. The minimum size for structured cells is 3 mm, as discussed in Section 5.3.3.2.1. This is to allow for manufacturing constraints. If the wall thickness of the robotic arm is less than 3 mm, structured cells should not be used.

Size. Due to the periodic nature of the structured cells, the distance between the two outer skins of the arm link must be constant. If this distance is not constant, it will not be possible to fit in a structured cell of constant size and shape throughout the structure.

5.3.3.5 Summary of using structured cells

To use structured cells, ALL the following conditions must be met:

- Part must have at least two orders of rotational symmetry.
- Loading must be symmetric (orientation range above 72°).
- The distance between the two outer skins of the arm link must be constant, and above 3 mm.

If any of these conditions are not met, topology optimisation must be used.

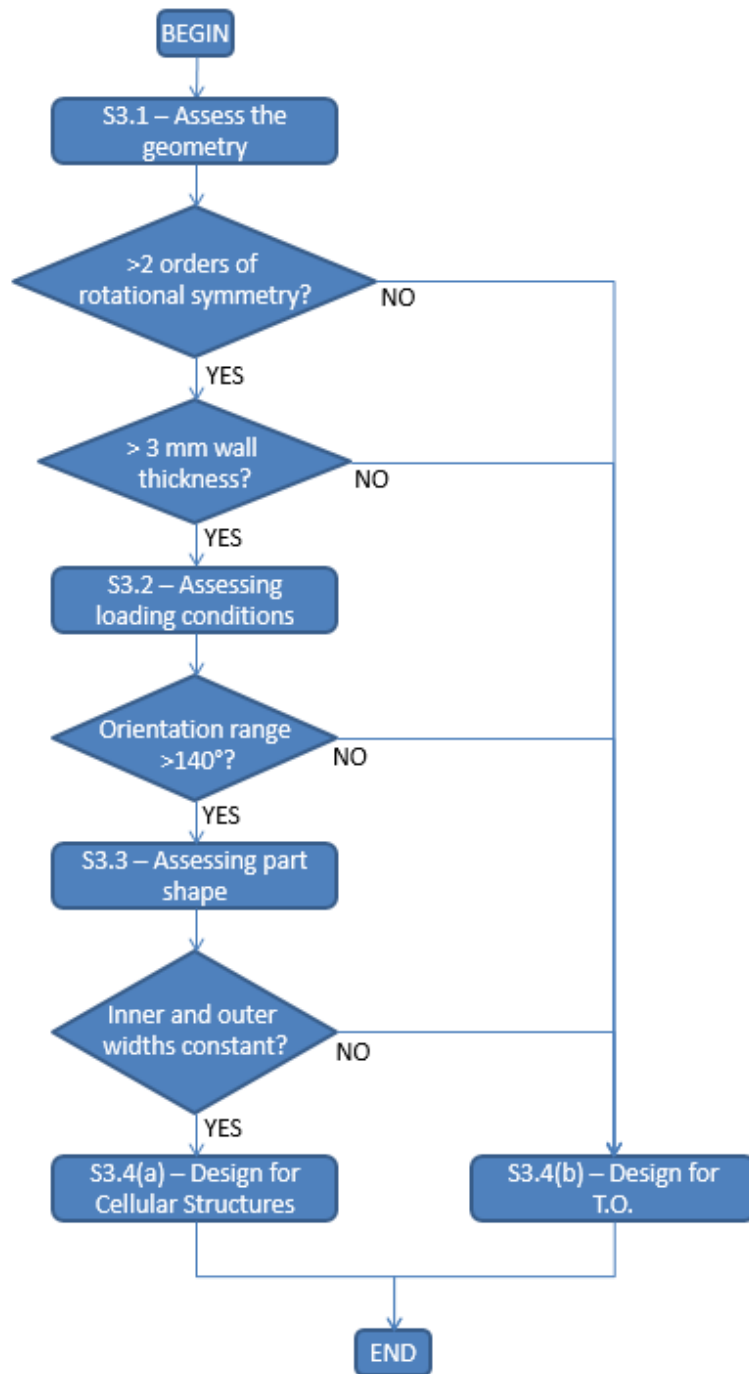


Figure 5.20: Choosing internal structure technique

5.4 Material: Detailed Description

5.4.1 Introduction

The material section discusses how to apply materials to the part. Irrespective of the structure, material application is the same. The material is important, as it is the

inherent properties of the materials which give many of the properties to the part. As highlighted in section 5.3.2, the physical limitations of AM hardware mean that material blending resolution has a finite limit. This limitation and how to design for it will be focussed on.

As stated in section assumptions, this thesis does not take into account interaction effects at material boundaries, as that is out with the scope of this thesis. Neither is it aimed at developing a new material. Rather, the aim is to use currently commercially-available materials while keeping in mind basic manufacturing constraints - melting temperature and coefficient of thermal expansion.

As shown in figure 5.5, material is not linked to the specification stage. This is because the material optimisation work is where the FGM ideas are detailed. The FGM work is a key reason for the existence of the design guidelines, and therefore it is assumed that the part will not currently contain FGMs, as otherwise there is little reason in using them.

5.4.2 STEP 4 - PART SEGMENTATION

5.4.2.1 AM layers vs FGM/SUMC layers

In this section of the design guidelines, two different layer terms will be used. While they are intertwined, it is important to differentiate each.

AM layers describe each layer which the AM hardware lays up. This is directly fixed to the layer thickness that the AM hardware is specified to deposit.

FGM layers are the layers of unique material composition. In this methodology they are referred to as **segments of unique material composition (SUMC)**. Because mixing is constrained to 0.5% increments, there can be, at most, 200 SUMC layers.

The thickness of each SUMC layer is dictated by the AM technology - it has been decided that there must be at least 3 AM deposition layers of any SUMC layer. Most AM technology has a minimum resolution of 0.1 mm, therefore most SUMC layers have a minimum thickness of 0.3 mm. However, **each SUMC layer can have many AM layers** - it is not limited to three. Indeed, many parts will have 30 or 40 AM layers within each SUMC layer. The number of AM layers within each SUMC layer is dependent on the size of the entire part - the larger the part, the more AM layers within each SUMC layer there will be.

5.4.2.2 Segmentation Constraints

The segmentation constraints are to ensure that the segmented part will be as close a representation as possible to the desired part, while adhering to manufacturing limits. The constraints, in order of importance, are:

1. **Each SUMC must be at least (AM minimum resolution x 3) thick.** As stipulated when investigating internal structure, the minimum feature size is equal to (AM minimum resolution x 3). The three layers allow the powder to spread evenly, ensuring each SUMC has an even distribution.
2. **Each SUMC must have an integer number of AM minimum resolution layers within.** To ensure the best dimensionally accuracy during the AM stage, each SUMC must have a thickness which is exactly divisible by the AM minimum resolution.
3. **There must be as many SUMCs as possible.** The greater the number of SUMCs, the smoother the blend will be. There is a practical limit, though. This will be covered in Section [5.4.3.1](#).

5.4.2.2.1 Conclusion The segmentation constraints use the manufacturing restrictions as a hard limitation, because if the AM hardware can not produce the part, there is little point in the proposed design. At present, the segmentation constraints are set for current state of the art AM hardware. As hardware improves, these segmentation constraints can be refined.

5.4.2.3 Segmentation technique

The FGM technique in these design guidelines differs from that in past work. To ensure manufacturability, grading/blending has a strict minimum constraint placed upon it. Once the part is segmented into SUMCs, all elements within each SUMC contain the same material properties (unlike previous FGM work whereby properties alter between, or in some cases, within, individual finite elements). The number of elements within the part is independent of the number of unique segments.

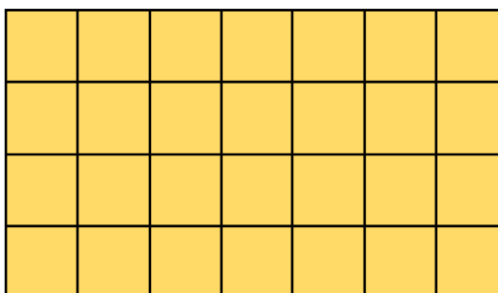


Figure 5.21: FGM Description

Figure 5.21 shows this idea. Each square in this image represents a different SUMC. Within each of these squares can be a varying number of finite elements, chosen by the user. However, all the finite elements within any one square will have the same material properties. Figure 12.0.1 of appendix A shows the code for calculating both the number and the thickness of each layer.

5.4.2.3.1 FGM extremity In these design guidelines, the FGM extremities are the edges/faces of the part that are chosen to begin and end the material blend at. This choice should be based upon the task the FGM part is being used for. For example, if the part is to work in a large temperature gradient, one FGM extremity should be the edge/face that is subjected to the high temperature, and the other extremity should be the edge/face that the heat should dissipate towards.

5.4.2.3.2 FGM extremity distance As the parts will be made using AM, consideration has to be taken for the orientation of the part during manufacture. This is due to the layer-wise deposition of AM. The orientation should be based upon the direction which the material alters over in the part. In these design guidelines, this distance is called the **FGM extremity distance**. This is the line which joins one FGM extremity (100% of material A, 0% of material B) to the other FGM extremity (0% A, 100% B). Examples of this distance are shown in Figure 5.27.

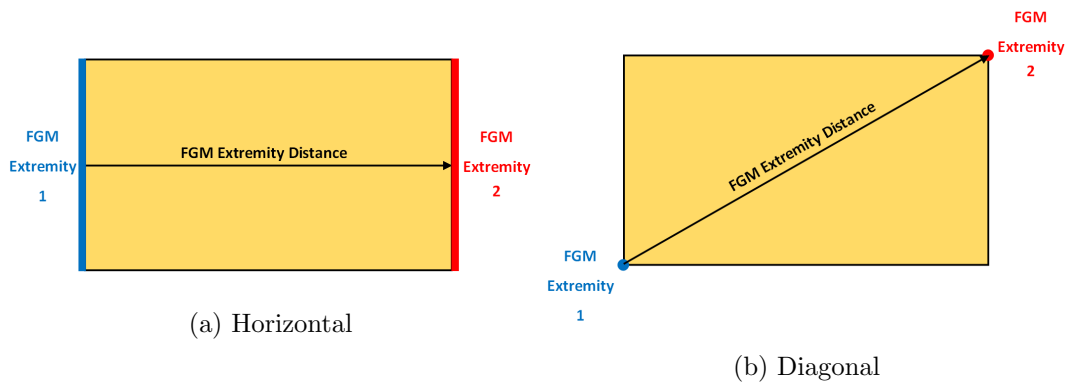


Figure 5.22: FGM Extremity

When being manufactured, the parts should be oriented such that each layer/slice is perpendicular to this FGM extremity line.

5.4.2.3.3 FGM extremity distance vs blending distance The orientation of FGM extremities relative to one another will have an impact on the placement of the FGM. This is due to the **blending distance**.

The blending distance is the span over which the FGMs will be altering. When the FGM extremities are parallel, the blending distance is the same as the FGM distance. This is the case in figures 5.22a and 5.22b. However, as the inclination angle between the two FGM surfaces increases, the ratio of the blending distance to the FGM distance decreases. This is the case in figure 5.23. The FGM distance is shown by the dotted line. Due to the inclination of the two FGM extremities, the entire FGM blend (the blending distance), has to happen between the arrows (region B). Region A is 100% material A, 0% material B, and region C is 0% material A and 100% material B.

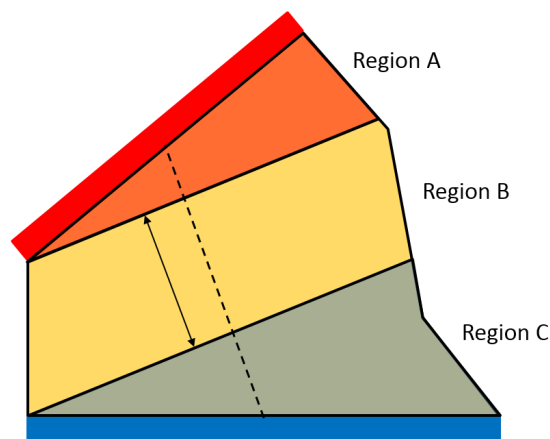


Figure 5.23: FGM extremity distance vs blending distance

The orientation of the FGM extremities will also affect the number of AM layers in

each SUMC.

If the FGM extremity edges are PARALLEL, then each SUMC layer will have a near equal amount of AM layers. Discrepancies in number of AM layers per SUMC will be due to differences in SUMC thickness, which will be covered in section 5.4.3.

However, if the FGM extremity edges are NOT parallel, the SUMCs outwith the blending distance will have many more AM layers than those within the blending distance. Figure 5.23 shows an example of these areas outwith the blending distance that will require many AM layers of the same composition.

These areas outwith the blending distance should still have layer thicknesses at the minimum resolution of the AM technology. A fast interior, accurate exterior AM strategy cannot be used as parts will have TO features which need the minimum resolution accuracy for manufacture.

5.4.2.3.4 Segmentation rules In order to ensure manufacture, rules for segmentation are needed. It is decided that parts should be segmented in two directions. This means that, if need be, the gradation of material can occur in two directions. When the part is being split into the SUMCs, there are two rules which must be followed:

1. **Segmentation orientation 1 perpendicular to “FGM extremity distance” line**
2. **Segmentation orientation 2 following the longest contour on the part which is not an FGM extremity contour**

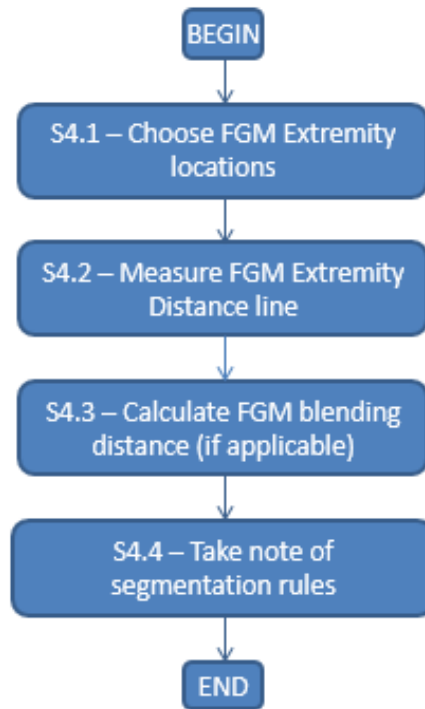


Figure 5.24: Following the segmentation rules

All steps and techniques up to this point are shown sequentially in figure 5.25. Figure 12.0.2 in appendix A shows the code for partitioning the part. Examples of implementing the part segmentation steps are done in section 5.4.3.5, at which point material percentages in each SUMC are also taken into account.

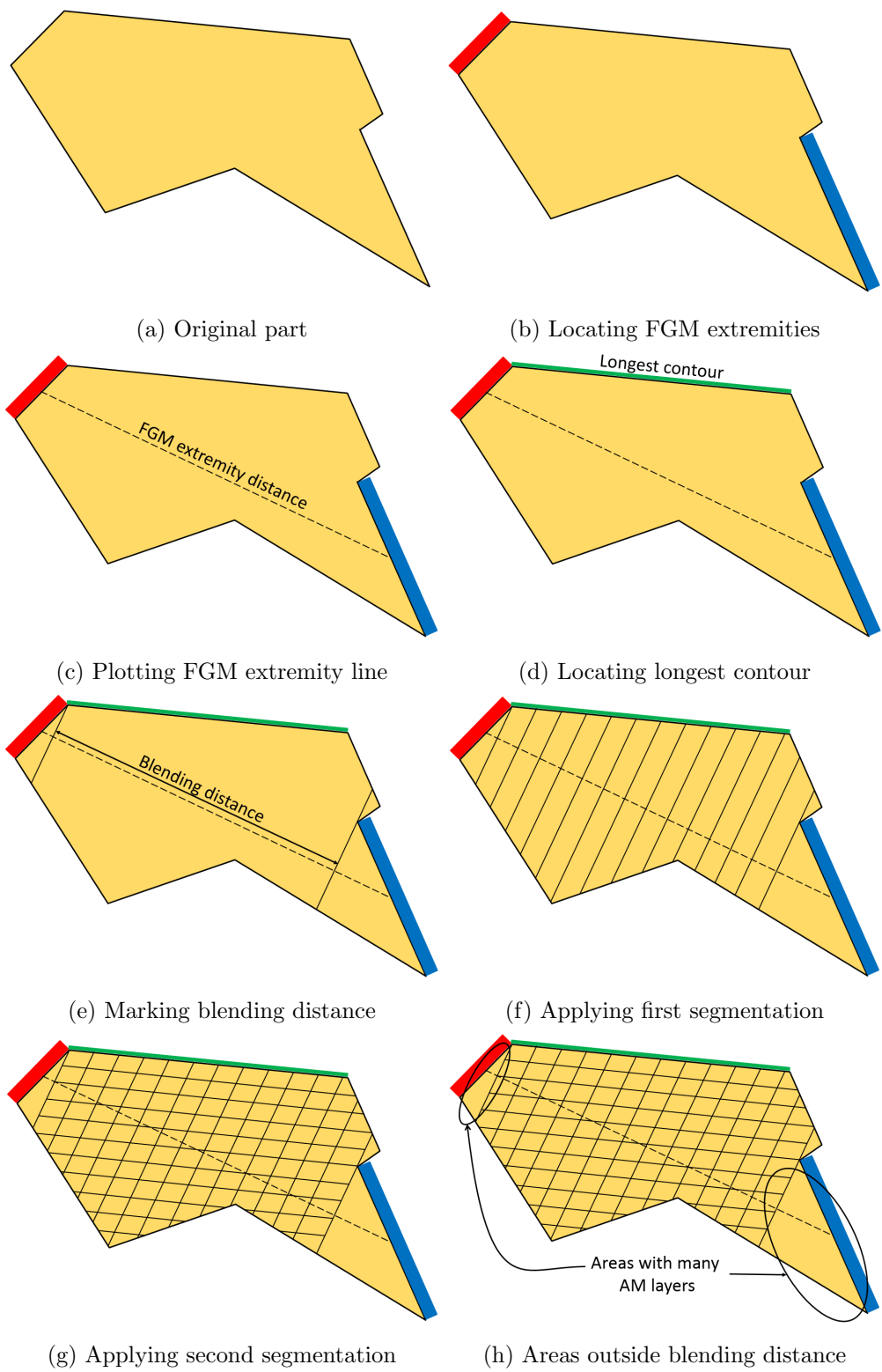


Figure 5.25: Description of applying SUMCs to part

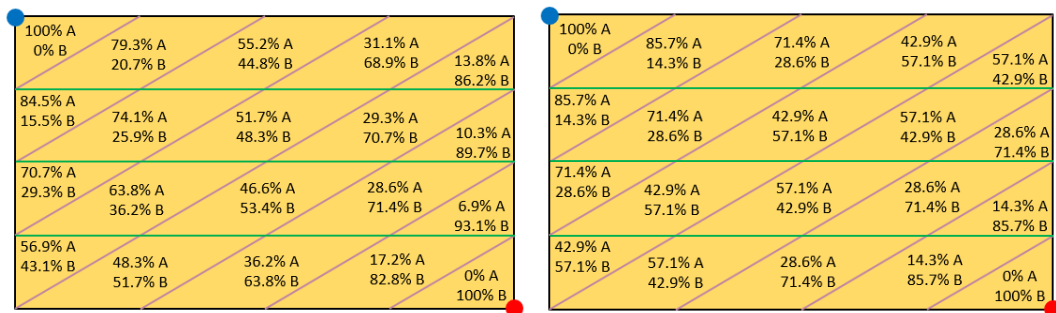
Discussion surrounding segmentation

The segmentation step in the design guidelines has been covered in section 5.4.2. This section discusses how the FGM are blended, the successful implementation of the blending, and some differing ideas which were also investigated.

Radial vs straight blending

As mentioned in Section 5.4.2.3.4, the SUMC constraints are set up to allow material to blend in two directions. These two directions allow “radial” blending to be used. Linear interpolation is used to calculate the composition in any SUMC when making a radial blend. This was done in the experiments in the preliminary tests (section 4).

An example of radial blending is shown in figure 5.26a. The lilac lines show the segmentation perpendicular to the FGM extremity distance. The green lines show the segmentation following the longest contour which is NOT a FGM extremity.



(a) Radial blending on a rectangular part (b) Straight blending on a rectangular part

Figure 5.26: Radial vs straight blending

The ability to alter material composition over two dimensions gives more flexibility to the process. However, the manufacturability of a radial blend part is difficult - there is no obvious layer wise direction for the AM hardware to follow. The hardware used must therefore have the fidelity to supply many material composition combinations at a high turn over rate.

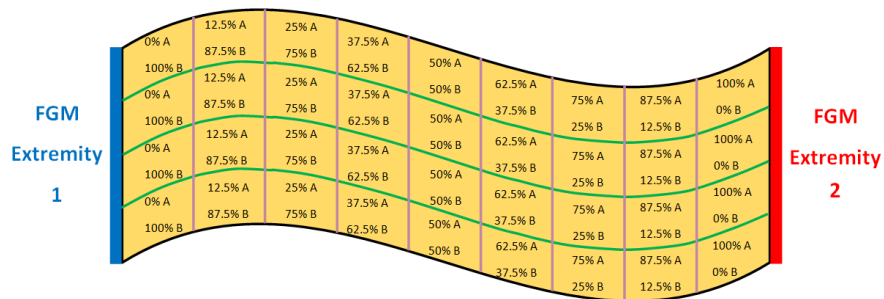
A “straight” blend can also be made using the created constraints. This means the material blends in one direction only. This can be seen when looking between any two lilac lines in figure 5.26b - the composition values are identical within each layer. The composition of each SUMC is based upon the number of SUMC layers in the part. The higher the number of SUMC layers, the lower the percentage change in material composition between each layer. However, there is a lower limit (set by geometry) and an upper limit (set by manufacturability) which will be outlined in section 5.4.3.

Figure 5.26b shows the same rectangular part, this time with straight blending.

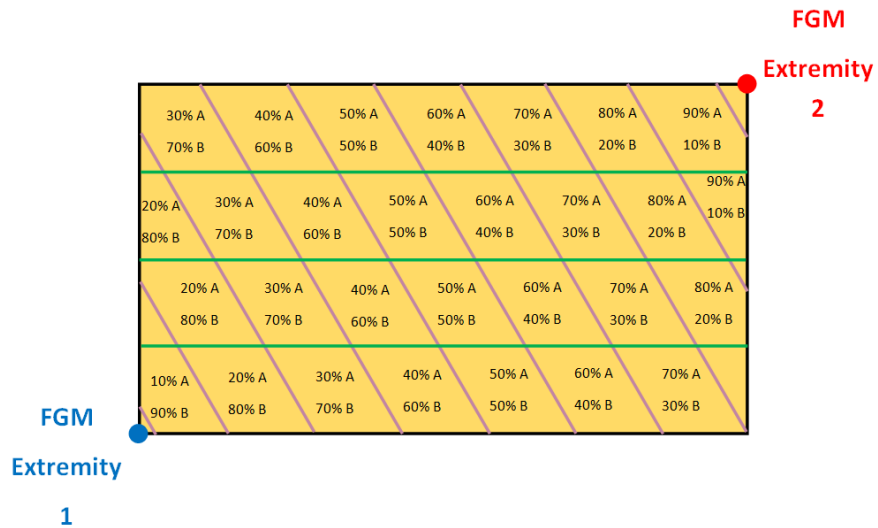
The straight blend is not as flexible as the radial blend. However, it does make manufacturing far easier compared to the radial blend. The material composition does not need to be altered as often, and the AM hardware therefore does not need to be as responsive to material composition alterations. For this reason, all tests in this thesis will use straight blending.

Successful implementation of segmentation constraints

This section shows some fictitious parts with straight blending and the two constraints created in Section 5.4.2.3.4 in place. These two constraints can be seen in the images in figure 5.27.



(a) Curved Edge/Horizontal FGM



(b) Straight Edge/Diagonal FGM

FGM Extremity 1	0% A	16.5% A	33.5% A	50% A	66.5% A	83.5% A	100% A	FGM Extremity 2
	100% B	83.5% B	66.5% B	50% B	33.5% B	16.5% B	0% B	
	0% A	16.5% A	33.5% A	50% A	66.5% A	83.5% A	100% A	
	100% B	83.5% B	66.5% B	50% B	33.5% B	16.5% B	0% B	
0% A	16.5% A	33.5% A	50% A	66.5% A	83.5% A	100% A		
100% B	83.5% B	66.5% B	50% B	33.5% B	16.5% B	0% B		
0% A	16.5% A	33.5% A	50% A	66.5% A	83.5% A	100% A		
100% B	83.5% B	66.5% B	50% B	33.5% B	16.5% B	0% B		

(c) Straight Edge/Horizontal FGM

Figure 5.27: Following Contours

Different segmentation ideas

This section describes different segmentation ideas that were tested, but not chosen for the design guidelines, due to reasons discussed.

5.4.2.3.5 Point-to-Point Rather than basing the 2nd segmentation on the orientation of the outer contour, another idea was to base it on a point-to-point method, done on a percentage-basis. Segmentation lines travel from a chosen percentage distance along one FGM extremity to the equal percentage distance along the other FGM extremity. Figure 5.28 shows this.

FGM Extremity 1	0% A	12.5% A	25% A	37.5% A	50% A	62.5% A	75% A	87.5% A	100% A	FGM Extremity 2
	100% B	87.5% B	75% B	62.5% B	50% B	37.5% B	25% B	12.5% B	0% B	
	0% A	12.5% A	25% A	37.5% A	50% A	62.5% A	75% A	87.5% A	100% A	
	100% B	87.5% B	75% B	62.5% B	50% B	37.5% B	25% B	12.5% B	0% B	
0% A	12.5% A	25% A	37.5% A	50% A	62.5% A	75% A	87.5% A	100% A		
100% B	87.5% B	75% B	62.5% B	50% B	37.5% B	25% B	12.5% B	0% B		
0% A	12.5% A	25% A	37.5% A	50% A	62.5% A	75% A	87.5% A	100% A		
100% B	87.5% B	75% B	62.5% B	50% B	37.5% B	25% B	12.5% B	0% B		

Figure 5.28: Non-Parallel Edges

Length of Extremity 1 = 6 cm

Length of Extremity 2 = 12 cm

Splitting the part into four sections, each segment should be $100/4 = 25\%$ of the entire length of each extremity.

⇒ Extremity 1 should be split into $6/4 = 1.5$ cm segments and extremity 2 should be split into $12/4 = 3$ cm segments.

This works adequately when FGM Extremity contours 1 and 2 are similar in length. However, when the two edges are vastly different in length, one of two things happens:

1. the unique segments on the large edge become extremely large (Figure 5.29a)
2. the unique segments on the shorter edge become too small to manufacture (Figure 5.29b)

This is shown in Figure 5.29.

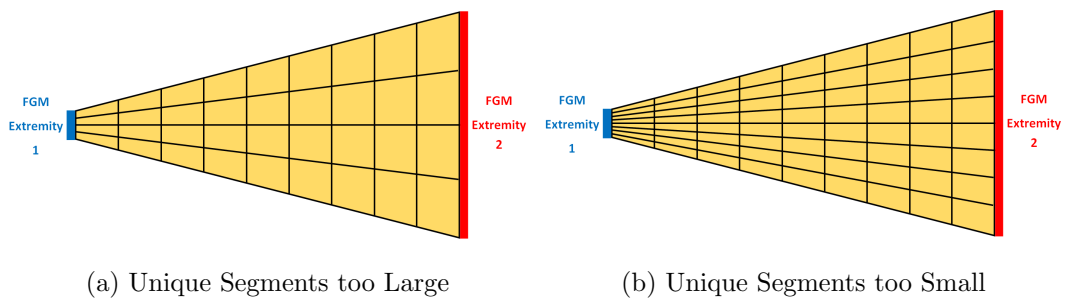


Figure 5.29: Point-to-Point Problems

5.4.2.4 Conclusions

This section introduced many of the concepts required for segmenting a lightweight robotic arm link. They are very similar to the sequential representation method^[83] and aim to minimise the angle difference between print orientation and material variation. The FGM extremities mark the surfaces/edges that the FGM blend should start and end at. The direct distance between these two features is noted as the “FGM extremity distance”. If the two extremity surfaces are not parallel to one another, the “FGM blending distance” must also be measured - this will be shorter than the “FGM extremity distance”. This blending distance is used to calculate the number and thickness of each FGM layer, called SUMC layers (Segment of Unique Material Composition). These SUMC layers are laid out as per the segmentation rules.

This current version of the part segmentation is the result of many iterations. Some previous ideas are shown in the later parts of this section, along with discussion as to why they have not been used. Currently, this is deemed the most appropriate segmentation technique. However, there is a chance it could be refined further after physical testing occurs and unforeseen matters arise.

5.4.3 STEP 5 - THEORETICAL MATERIAL MIXING

Theoretical material mixing relates to how the idealised blending will take place in the AM hardware. It begins with the constraints that are needed to be put in place for manufacture, and then shows how material will blend, depending on whether composites are present, or not. These constraints work in line with the segmentation constraints from section 5.4.2.2.

5.4.3.1 Mixing Constraints

The mixing constraints are to ensure that the theoretical blending will be as close a match to the physical blending as possible. The constraints, in order of importance, are:

1. **Mixing must be to the nearest 0.5%.** The part should be segmented such that material mixing in each SUMC is rounded to the nearest 0.5%. This value is chosen such that any modern dry mixing apparatus can achieve this constraint. As shown in literature, using a P.I controller to regulate the powder flows of both constituent materials allows 0.5% material mixing targets to easily be met^[202].
2. **Materials must mix from relative 100% of the first material, to relative 100% of the second material.** Regardless of the composition of materials at either FGM extremity, the FGM should blend from a relative 100% of the material composition at one FGM extremity to a relative 100% of the material composition at the other FGM extremity. This is illustrated in Figure 5.30.
3. **There can be a maximum of 200 mixtures.** Assuming materials are graded from 100% of the first material to 100% of the second material, this material mixing constraint means that any FGM part, independent of size, can have a maximum of 200 SUMC in any one direction ($100/0.5 = 200$). However, the primary constraint that each SUMC must be **at least** (AM minimum resolution x 3) thick, means that, in certain situations, there are less than 200 SUMC in the FGM blending distance.

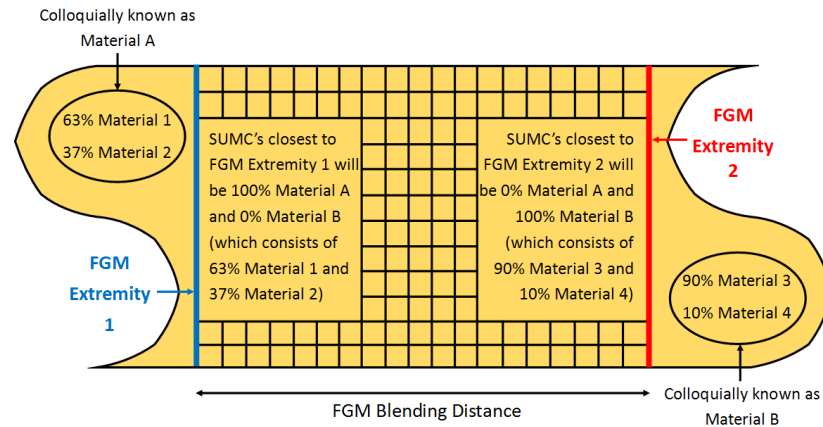


Figure 5.30: Relative Blending Description

5.4.3.1.1 Conclusion Akin to the segmentation constraints, the mixing constraints have a hard limit from current state of the art AM hardware - the mixing percentage limit of 0.5%. This percentage may be reduced in the future as control of particle flow is better understood and managed. The second constraint is intrinsic of any FGM part, but the researcher felt it should be made a constraint to avoid ambiguity.

5.4.3.2 Definitions

Some definitions need to be explained before this stage of the design guidelines is discussed:

- **“Complete FGM” distance** The complete FGM distance is distance needed to blend from 100% of material A to 100% of material B, at the minimum resolution allowed. As discussed in the constraints of section 5.4.3.1, there can be a maximum of 200 SUMCs, and each SUMC must have a minimum of three AM layers within. If the AM minimum resolution is 0.1 mm, the complete FGM distance will be $(0.1 \times 3) \times 200 = 60$ mm.

- **Homogeneous blending** Homogeneous blending describes blending of material when non using binder-matrix composites in addition to another material. When not using binder-matrix composites, the materials can be pre-mixed before deposition (or as deposition occurs) and thus each SUMC will have a homogeneous material mix through it.

- **Non-homogeneous blending** Non-homogeneous blending describes blending of material when using binder-matrix composites in addition to another material. The

presence of the binder-matrix means that this material must be deposited separately to the additional material in the FGM. This results in each SUMC being non-homogeneous.

- **Number SUMC Alterations** The number of SUMC alterations is the number of times the material changes within the FGM part.

- **Number of SUMC Layers** The number of SUMC layers is the number of unique material layers within the FGM part. This is always equal to the one greater than the number of SUMC alterations, as there has to be a 100%/0% layer at both ends of the part.

5.4.3.3 Homogeneous Blending (Not using Composites)

Ideally, each segment of unique material composition needs to have a homogeneous material within that segment. For example, if it is 25% material A and 75% material B, it would be best to mix the two constituent materials before dispensing them, rather than depositing 25% pure material A followed by 75% pure material B.

If not using composites, the methodology is straight forward - materials are blended homogeneously for each segment of unique material composition before being deposited. Instead of using a composite along with another constituent material to form the FGM, the chopped carbon fibres can be mixed through the metallic powder or through the polymer powder to create an MMC (metal matrix composite) or a PMC (polymer matrix composite). If a powder-based AM technique is used, the carbon fibre may need to be made into a powder before deposition as part of either a PMC or MMC. This can be done using planetary ball milling, as shown to work in literature^[203]. Rather than transitioning from 100% carbon fibre at one end, the part would need to mix to a maximum fibre saturation point - the maximum fibre ratio. In composites, this is generally regarded as 50% - 65%^[204]. Therefore, the maximum percentage of composite fibres in any MMC or PMC in the part at the “fibre rich” end would be 50% - 65%. A maximum fibre percentage of 60% is set for these parts. Therefore, FGM parts with fibres as one constituent will reach a maximum of 60% fibre at the fibre-rich FGM extremity. Figure 5.31 visualises this. The black figures show the FGM blending percentages, the red figures show the constituent material percentages.

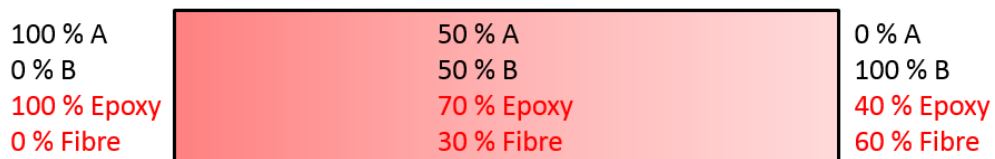


Figure 5.31: Maximum fibre percentage of 60% in FGM parts

5.4.3.3.1 Conclusions Homogeneous blending is assumed as the default blending mechanism in these guidelines. As noted in literature, assuming the material properties at any point as being a combination of the properties of the two constituent materials is valid^[83], assuming constituent material compatibility. As shown, the materials have been split into three distinct groups based on their melting temperature. The deposition temperature will be set as the higher melting temperature of the two constituent materials, however, as they material combinations have similar melting temperatures. it is hoped that both will fully melt, but neither will be damaged by over-heating. Any chemical instabilities from different blends have not been taken into account, as noted in the assumptions. Care has to be taken if using a fibre in the part, as there is a maximum volume fraction of fibres that can be supported by a matrix.

5.4.3.4 Non-Homogeneous Blending (Using Composites)

As discussed, non homogeneous blending is difficult to accomplish due to the multiple deposition stages that would be needed on every SUMC. It is included in the design guidelines as an option, however, all work in this thesis will focus on homogeneous blending. There are two avenues described when working with non-homogeneous blending - the first is to use current manufacturing methods, and the second is to postulate on future technology advances.

5.4.3.4.1 Using Current Technology If current technology is to be used, the composite material and the other constituent material must be kept separate, creating a part with distinct material boundaries throughout. This is not ideal, as there will be many stress concentration areas at the boundaries between the two materials (the composite and the other material). A decision how to mix the two materials is required. The priority is to keep the number of distinct material boundaries to a minimum, therefore, within each segment of unique material composition, there should only be **ONE** material boundary - when the material changes from the composite to the other constituent material.

Figure 5.32 shows three options available that abide to this constraint. Figure 5.32a puts material B on the right hand side of each segment of unique material composition. Figure 5.32b puts material B on the left hand side of each segment of unique material composition. Finally, Figure 5.32c puts material B in the centre of each segment of unique material composition.



(a) On RHS

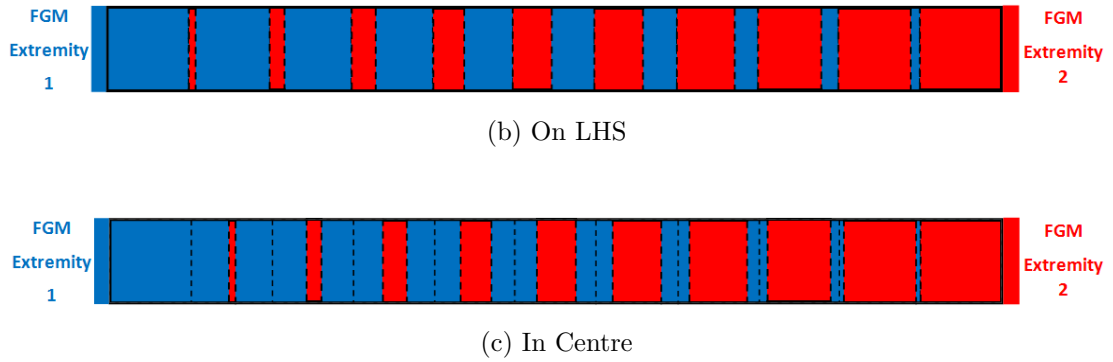


Figure 5.32: Distinct Material Locations

The decision of which configuration to use should be based on the number of stress-concentration boundaries. In figure 5.32, material appending to the RHS (figure 5.32a) of each SUMC has the fewest stress concentration boundaries. This is due to the direction of blending considering the materials at either extremity. The two materials should be arranged in each SUMC such that each is closest to its FGM as possible. This is the case in figure 5.32a, and hence why it has fewer material boundaries than the other two options.

5.4.3.4.2 Preliminary work for Future Technology The second option is to postulate that in future, technology will exist that has the ability to produce intricate parts using two or more dissimilar materials simultaneously. The materials are dissimilar when compared by material properties. Under this assumption, the composite could be mixed with the powder of the the other constituent material in the FGM before deposition to create a homogeneous material. This material could then be deposited.

5.4.3.4.3 Conclusions If the constituent materials must be kept apart, non-homogeneous blending should be used. This is not optimal, as each part has many stress concentrations at each material interface (see figure 5.32). Work in the future may devise a way to combine non-homogeneous materials into homogeneous materials, at which point the use of conventional ceramic composites (CFRP) within FGMs will be realisable.

5.4.3.5 Examples of Homogeneous Material Blending

This example will show two options - when blending above the complete FGM distance, and when blending below it. The examples will assume SLS technology is being used.

5.4.3.5.1 Constraints

1. There have to be 3 layers minimum to give certainty that each SUMC layer has been produced. The minimum resolution is 0.1 mm. Therefore, the minimum

thickness for each SUMC = $3 \times 0.1 = \mathbf{0.3 \text{ mm}}$.

2. Mixing is limited to 0.5% and must mix from 100% of first material, to 100% of second material. Therefore, the maximum number of segments of unique material composition = $100/0.5 = \mathbf{200 \text{ segments}}$.
3. Each SUMC must have an **integer number** of AM layers within.

Using the values from these constraints, the complete FGM distance for this example = $200 \times 0.3 = \mathbf{60 \text{ mm}}$.

5.4.3.5.2 Blending above “Complete FGM” Distance An additional constraint in section 5.4.3.1 stated that each SUMC must have an integer number of AM layers within. Due to this constraint, it is expected that not all of the 200 SUMC layers will be the same thickness. Interpolation must be used to find the different thicknesses required.

Example 1) FGM blending distance = 464 mm

Finding SUMC Thickness:

$$\begin{aligned} \text{SUMC Thickness} &= \frac{\text{FGM blending distance}}{\text{Number of SUMC Alterations}} \\ \Rightarrow \text{SUMC Thickness} &= \frac{464}{200} = 2.32 \text{ mm per SUMC} \end{aligned}$$

This thickness has a greater resolution than that allowed by the constraints (it is not exactly divisible by the minimum resolution of the AM hardware). Therefore, interpolation must be used to find the two thickness values.

Finding interpolation limits:

$$\frac{\text{SUMC Thickness}}{\text{AM Minimum Resolution}} = \frac{2.32}{0.1} = 23.2$$

$$\Rightarrow \text{Lower Limit} = 2.32 \times 23 = 2.3 \text{ mm}$$

$$\Rightarrow \text{Upper Limit} = 2.32 \times 24 = 2.4 \text{ mm}$$

Interpolate between limits:

$$\frac{\text{SUMC Thickness} - \text{Lower Limit}}{\text{AM Minimum Resolution}} = \frac{2.32 - 2.3}{0.1} = 0.2$$

Finding SUMC Percentages:

$0.2 \times 100\% = 20\%$ of SUMC's will be 2.4 mm thick and the remaining 80% will be 2.3 mm thick.

Finding Split of SUMCs:

SUMC Percentage x Total Number of SUMCs

$\Rightarrow 20\% \times 200 = 40$ SUMCs at 2.4 mm

$\Rightarrow 80\% \times 200 = 160$ SUMCs at 2.3 mm

Confirmation:

Composition of FGM = (No. SUMC 1 x SUMC Thickness 1) + (No. SUMC 2 x SUMC Thickness 2) = $(40 \times 2.4) + (160 \times 2.3) = 464$ mm

Example 2) FGM blending distance = 173 mm

Finding SUMC Thickness:

$$\text{SUMC Thickness} = \frac{\text{FGM blending distance}}{\text{Number of SUMC Alterations}}$$

$$\Rightarrow \text{SUMC Thickness} = \frac{173}{200} = 0.865 \text{ mm per SUMC}$$

Finding interpolation limits:

$$\frac{\text{SUMC Thickness}}{\text{AM Minimum Resolution}} = \frac{0.865}{0.1} = 8.65$$

\Rightarrow Lower Limit = $0.1 \times 8 = 0.8$ mm

\Rightarrow Upper Limit = $0.1 \times 9 = 0.9$ mm

Interpolate between limits:

$$\frac{\text{SUMC Thickness} - \text{Lower Limit}}{\text{AM Minimum Resolution}} = \frac{0.865 - 0.8}{0.1} = 0.65$$

Finding SUMC Percentages:

$0.65 \times 100\% = 65\%$ of SUMC's will be 0.9 mm thick and the remaining 35% will be 0.8 mm thick.

Finding Split of SUMCs:

SUMC Percentage x Total Number of SUMCs

$$\Rightarrow 35\% \times 200 = 70 \text{ SUMCs at } 0.8 \text{ mm}$$

$$\Rightarrow 65\% \times 200 = 130 \text{ SUMCs at } 0.9 \text{ mm}$$

Confirmation:

Composition of FGM = (No. SUMC 1 x SUMC Thickness 1) + (No. SUMC 2 x SUMC Thickness 2) = (70 x 0.8) + (130 x 0.9) = **173 mm**

5.4.3.5.3 Blending below “Complete FGM” Distance When below the “complete FGM” distance, the constraints dictate that the total number of SUMCs will be below 200. Therefore, the material mixing percentage change between each SUMC will be greater than 0.5%. Interpolation must be used to find this material mixing percentage change, to the nearest 0.5%.

Example 1) FGM blending distance = 22 mm.

$$\text{Number of SUMC Alterations} = \frac{\text{FGM blending distance}}{(\text{AM Minimum Resolution} \times 3)}$$

$$\text{Number of SUMC Layers} = \text{Number of SUMC Alterations} + 1$$

The number of SUMC layers is 1 larger than the number of SUMC alterations, as the first SUMC layer has 0% of the material B in it (it is 100% material A).

$$\mathbf{X} = \text{Percentage change between each segment} = \frac{\text{Blending Percentage}}{\text{Number of SUMC Alterations}}$$

X must be interpolated, so that segment values to the nearest 0.5% can be obtained.

Finding number of SUMC alterations:

$$\frac{22}{0.1 \times 3} = 73.3 \text{ SUMC alterations}$$

Finding interpolation limits:

$$\frac{100}{73} = 1.36\% \text{ increase per subsequent SUMC layer}$$

Interpolate between limits:

Interpolate 1.36% between 1.0% and 1.5% (closest values within 0.5%).

$$1.36 - 1.0 = 0.36$$

Finding SUMC Percentages:

$$\frac{0.36}{0.5} = 0.73 \Rightarrow 73\% \text{ of blend should use 1.5\% segment.}$$

Finding Split of SUMCs:

$$73.3 \times 0.73 = 53 \text{ SUMC alterations.}$$

$$53 \times 1.5\% = 80\%.$$

$$73 - 53 = 20 \text{ SUMC alterations.}$$

$$20 \times 1\% = 20\%$$

Confirmation:

$$80\% + 20\% = 100\% \text{ blending.}$$

Example 2) FGM blending distance = 40 mm.

Finding number of SUMC alterations:

$$\frac{40}{0.1 \times 3} = 133 \text{ SUMC alterations}$$

Finding interpolation limits:

$$\frac{100}{133} = 0.75\% \text{ increase per subsequent SUMC layer}$$

Interpolate between limits:

Interpolate 0.75% between 0.5% and 1.0% (closest values within 0.5%).

$$0.75 - 0.5 = 0.25$$

Finding SUMC Percentages:

$$\frac{0.25}{0.5} = 0.5 \Rightarrow 50\% \text{ of blend should use } 1\% \text{ segment.}$$

Finding Split of SUMCs:

$$133 \times 0.5 = 66.5 \text{ SUMC alterations.}$$

$$66 \times 1\% = 66\%.$$

$$133.5 - 66.5 = 66.5 \text{ SUMC alterations.}$$

$$66.5 \times 0.5\% = 33\%$$

Confirmation:

$$66\% + 33\% \approx 100\% \text{ blending.}$$

5.4.3.5.4 Conclusion As stated, homogeneous blending is the default technique that will be used in this project. The calculations developed for calculating the material percentages of each SUMC are proved to be robust - working both above and below the “complete FGM” distance. The researcher is confident that these equations will function as expected when the guidelines are used to make physical parts.

Figure 12.0.3 of appendix A shows the code used to create the materials, including interpolating the material properties

5.4.3.6 Examples of Non-Homogeneous Material Blending

Practically, keeping the materials distinct makes the parts far larger. Adhering to constraints from Step 2, the materials must be mixed to the nearest 0.5% and the minimum thickness of any layer is the (AM minimum resolution x 3).

Rather than the homogeneous blended parts where the minimum thickness of each SUMC layer is (AM minimum resolution x 3), the minimum thickness now applies to

both materials in **EACH** SUMC layer of the non-homogeneous material mix.

To calculate blending distances needed when incorporating composites, the following equations are needed:

$$A = \frac{100}{\text{Desired \% Increase between subsequent SUMC layers}} \quad (5.1)$$

A is the number of SUMCs that will be made throughout the part.

$$B = A \times (\text{AM Minimum Resolution} \times 3) \quad (5.2)$$

B is the thickness that each SUMC layer will be.

$$B \times A = \text{Blending Distance} \quad (5.3)$$

5.4.3.6.1 Blending above “Complete FGM” Distance Using SLS with a minimum resolution = 0.1 mm,

Complete FGM Distance:

$$A = \frac{100}{0.5} = 200$$

$$\Rightarrow B = 199 \times 0.3 = 59.7$$

$$\Rightarrow \text{Complete FGM Distance} = 60 \times (200) = \mathbf{1200 \text{ mm}} = 12 \text{ m}$$

Since the complete FGM blending distance is 12 metres, no calculations will be done for blending when above the complete FGM distance, as it is envisaged that no parts will ever be that large.

5.4.3.6.2 Blending below “Complete FGM” Distance The point of FGMs is that the materials (and thus, material properties) GRADUALLY blend from one material to another. The lower constraint of blending is 0.5%, as otherwise, manufacture becomes impossible. However, once the blending percentage between subsequent SUMC layers becomes too high, the benefits of FGMs are lost. Table 5.4 shows the overall blending distances needed for non-homogeneous blends of various percentage changes between subsequent SUMC layers.

Table 5.4: Non-Homogeneous Blending Distances

% Change Between Subsequent SUMC Layers (%)	Overall Blending Distance (mm)
50	1.8
25	6
20	9
10	33
5	5
2	765
1.5	1360
1	3030
0.5	12060

As can be seen, once the % change between subsequent SUMC layers becomes acceptable for FGM parts ($< 2\%$), the overall blending distance is becoming very large (upwards of 1 metre). For this reason, no calculations will be done for non-homogeneous parts with a blending distance below the complete FGM distance, either.

5.4.3.6.3 Conclusion The non-homogeneous blending calculations work correctly, however, the results show that the parts are either far too large for practical purposes, or the change of material percentage between layers is so high that the benefits of gradual blending are rendered useless.

5.4.3.7 Layer stacking rule

Once the complete FGM distance and thicknesses of each SUMC layer/percentage alterations between SUMC layers has been calculated, their position in the part must be set. In these design guidelines, the SUMC layers with the larger thicknesses or larger percentage difference between each SUMC layer are placed in the centre of the part. The number of SUMC layers at the lower thickness or smaller percentage change between layers is halved. The first half of these layers is positioned, followed by all the thicker/larger percentage change layers, and finished with the remaining half of the thinner/lower percentage difference layers.

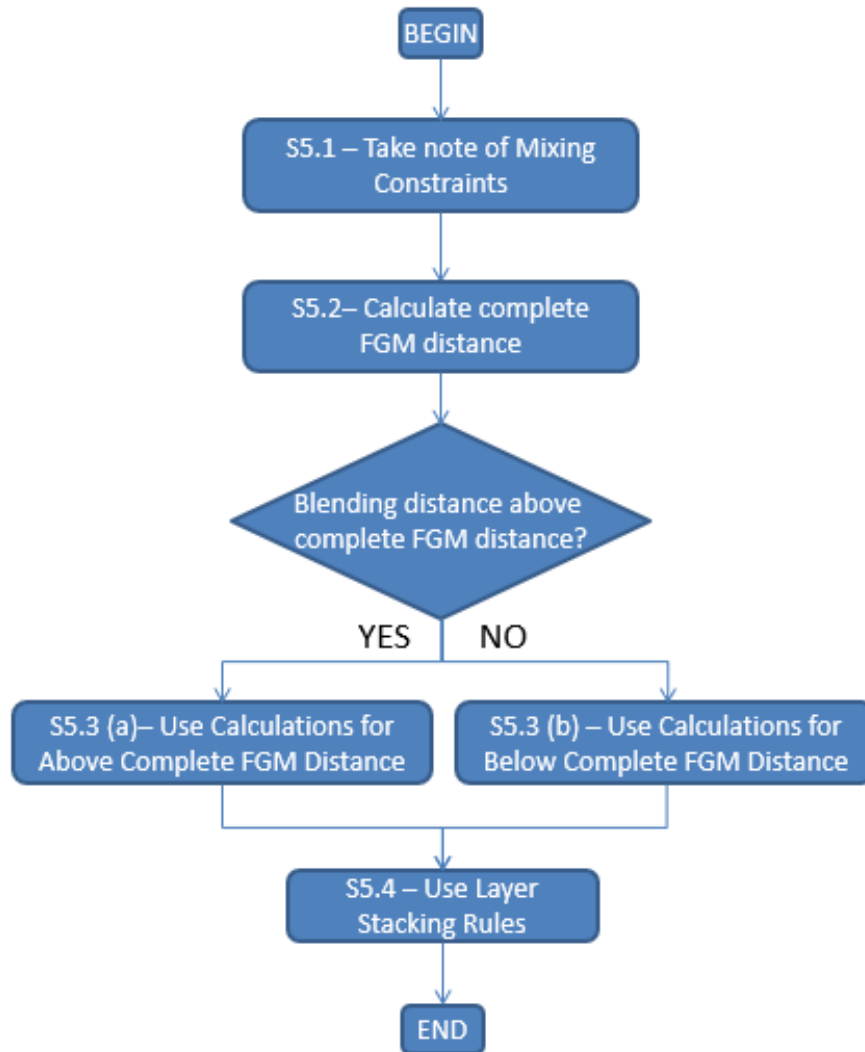


Figure 5.33: Position the materials as per the layer stacking rule

5.4.3.7.1 Conclusion The difference in dimension between the thicker SUMCs and thinner SUMCs within a part is envisaged to be very small. That being said, placing the thicker slices in the centre is considered by the researcher as the best solution, as it means that parts can be simulated with a greater degree of accuracy compared to random distribution of the thicker SUMCs.

5.4.4 STEP 6 - MATERIAL CHOICE

The first step in choosing materials is to list the possible candidate materials which could be chosen from.

5.4.4.1 Finding suitable materials

All commercially-available materials are potential candidates for a lightweight robotic arm. The materials are separated into three groups, based on their melting temperature - in any one group, all materials can be melted at the higher materials melting temperature without damaging the material with the lower melting temperature.

There will be three different material groups, roughly grouped as “high temperature metals”, “low temperature metals” and “polymers”. These are the same groups used in the preliminary tests in section 4. Each group will contain carbon fibres and glass fibres. If used, the fibres must be chopped, rather than left in long lengths. Short fibres do not have all the advantageous material properties of long, oriented fibres. However, since the fibres are being mixed with other materials (the secondary constituent material in the FGM), long fibres cannot be used.

Once the list of available materials is known, selection of materials for the specific task can begin. This is a three stage process:

1. Material choice is dependent on the task of the arm. The first step is therefore to translate the design requirements from Step 5.2.3 into material properties.
2. It is possible that the material properties specified in the design requirements can be altered in order to reduce the mass of the part. Therefore, once the material properties are known, the second step is to see if the design requirement values can be optimised.
3. With the optimised material property values, the materials themselves can be chosen. In order to do this, a combination of the constituent material properties is done to find approximate values for the material properties of the FGM materials. As noted in literature, this is a valid assumption for simulation at the macro-level^[83].

5.4.4.1.1 Conclusion In order to limit the number of materials, a list of currently commercially-available will be used to select from. This is a further hard constraint from the manufacturing technique - there is no point in choosing materials which can not be manufactured using AM hardware. The choice of material is a three stage process, and will be discussed in the following sections.

5.4.4.2 Stage 1 - Translating Design Requirements into Material Properties

The requirements given in the design task are often not in the form of material properties and therefore must be translated in order to choose materials. Some example design requirements and the material properties which describe them are shown in Table 5.5.

Table 5.5: Linking Design Requirements and Material Properties

Design Requirement	Material Property
Absolute Temperature Gradient	Glass Transition Temperature/Melt Temperature
Cyclic Thermal Heating	Coefficient of Thermal Expansion
Acceleration	Poissons ratio, density, Young's Modulus
Accuracy	Poissons ratio, density, Young's Modulus
Repeatability	Poissons ratio, density, Young's Modulus
Vibration	Poissons ratio, density, Young's Modulus
Reach	Poissons ratio, density, Young's Modulus
Payload	Stiffness, Young's Modulus

5.4.4.2.1 Conclusion This is the first of three steps towards choosing materials for a lightweight robotic arm link. This stage requires engineering intuition to correctly link design requirements from the design task to material properties. In future iterations of the design task, this information could be placed into a database to remove the need for said intuition, as there is the current possibility that design requirements will not be correctly linked to equivalent material properties.

5.4.4.3 Stage 2 - Optimising Design Requirement Values

As mentioned in Section 5.2.2.2, certain parameters stated in the design requirements can often be relaxed. The decision to alter is based upon what has previously been done. For example, if form has already been optimised for orientation range in section 5.2.3, the second moment of area will not be altered at this stage. The degree to which they can be relaxed is based upon the equation which was first used in Section 5.2.2.2. This equation brings together the accuracy, payload, acceleration, reach, Young's modulus and second moment of area of the arm.

Conclusion

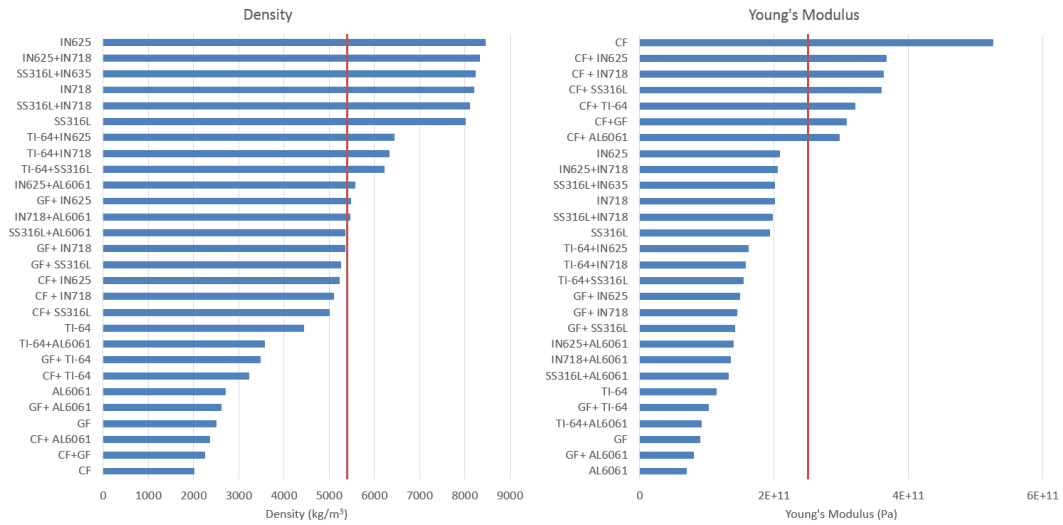
The second of three steps is to optimise the design requirement values. Depending on the outcome of this during testing, future work may aim at breaking this step down

into a series of smaller steps, as geometry can make optimising the design requirement values an intricate step. The next step is to choose the materials themselves.

5.4.4.4 Stage 3 - Combine Material Properties

By this stage of the design guidelines, the user already knows the dimensions and layout of material in the part. In order to aid choosing materials, it is possible to get a simplified idea of material performance by combining individual material properties. This combination can be done by interpolating the material properties. As one of the constraints in Step 5.4.3 states, all material must mix from a relative 100% of material A to 100% of material B. Assuming the FGM extremities are parallel to one another and therefore the first and final SUMC layers do not have many additional AM layers when compared to the rest of the part, the **GLOBAL** material properties of the part can be assumed as a combination of 50% material A and 50% material B. If the FGM extremities are not parallel, this percentage split will need to be altered to represent the percentage (by volume) of each constituent material.

The following two charts in figure 5.34 show the combined material values of density and Young's modulus of the "high temperature metals" materials used in the preliminary tests (section 4). As mentioned above, the values in these charts are 50/50 combinations of the two constituent materials, based on the assumption that the part is a combination of 50% material A and 50% material B. If the actual part uses different composition values, the charts can be altered to said composition values. For completeness, the virgin materials are also on each chart. An arbitrary constraint mark is put on each chart as an indicator for if the material combination should be accepted or rejected. This constraint is project-dependent. As already stated, the maximum service temperature is not interpolated - it is set as the value for the higher of the two constituent materials - the materials have been grouped based on their similar melting temperatures, and therefore both constituents should fully melt, without either being damaged.



(a) Combined density chart

(b) Combined Young's modulus chart

Figure 5.34: Combined material property charts

5.4.4.4.1 Conclusion The final of three steps is to combine the materials onto charts. As stated in Zhang et al. [83], the assumption that the material properties at any point in an FGM is the combination of the constituent materials at that point is valid on the macro level. Future work should include consideration of chemical compatibility in the resultant alloys, as instability could be an issue.

5.4.4.5 Screen materials based on design constraints

Multiple material properties can also be placed on one graph. This is useful if multiple properties are of importance to the project. An example chart is shown in Figure 5.35. This plots average Young's modulus values against average density values.

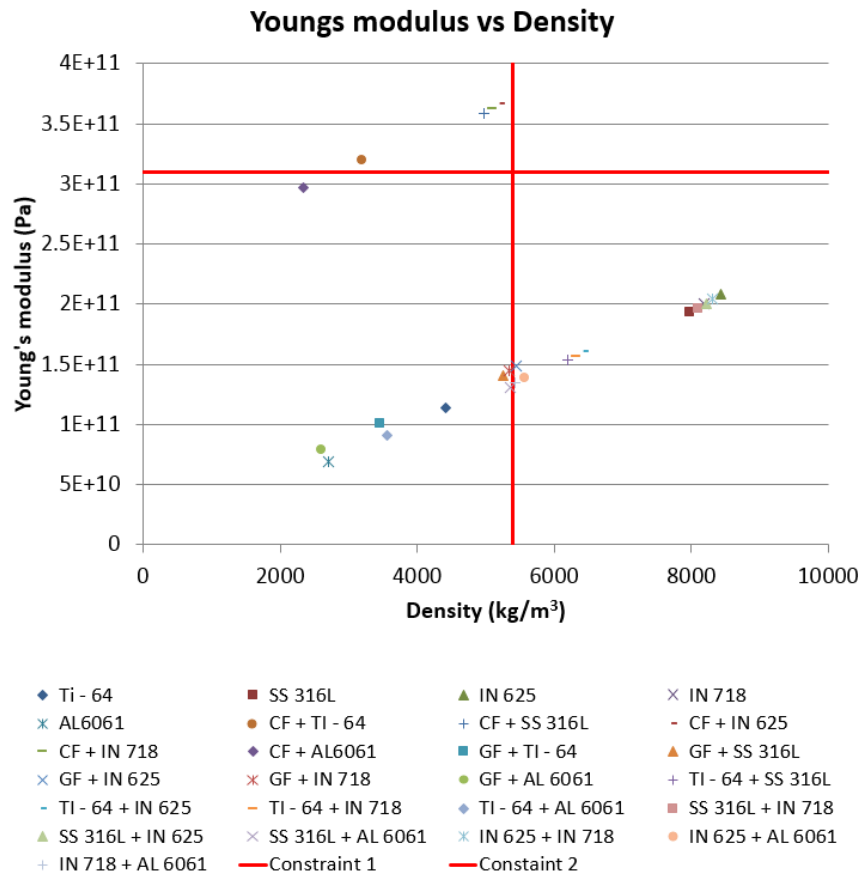


Figure 5.35: A combined Young's modulus vs density chart

Two constraint values are placed on this graph - a Young's modulus value of 3.1×10^{11} and a density value of 5400 kg/m^3 . If this was the case, it can be seen that only four possible material combinations would be suitable:

- carbon fibre and Ti-6Al-4V
- carbon fibre and stainless steel 316L
- carbon fibre and Inconel 625
- carbon fibre and Inconel 718

5.4.4.5.1 Conclusion The screening removes any material that does not satisfy the original constraints. As the combined material properties are assumed, a material combination should still be excluded if it lies on one of the constraints. As stated in the assumptions, material interactions during the additive manufacture process are not in the scope of this project, and therefore the three stage process shown here will be used for all upcoming testing of the design guidelines.

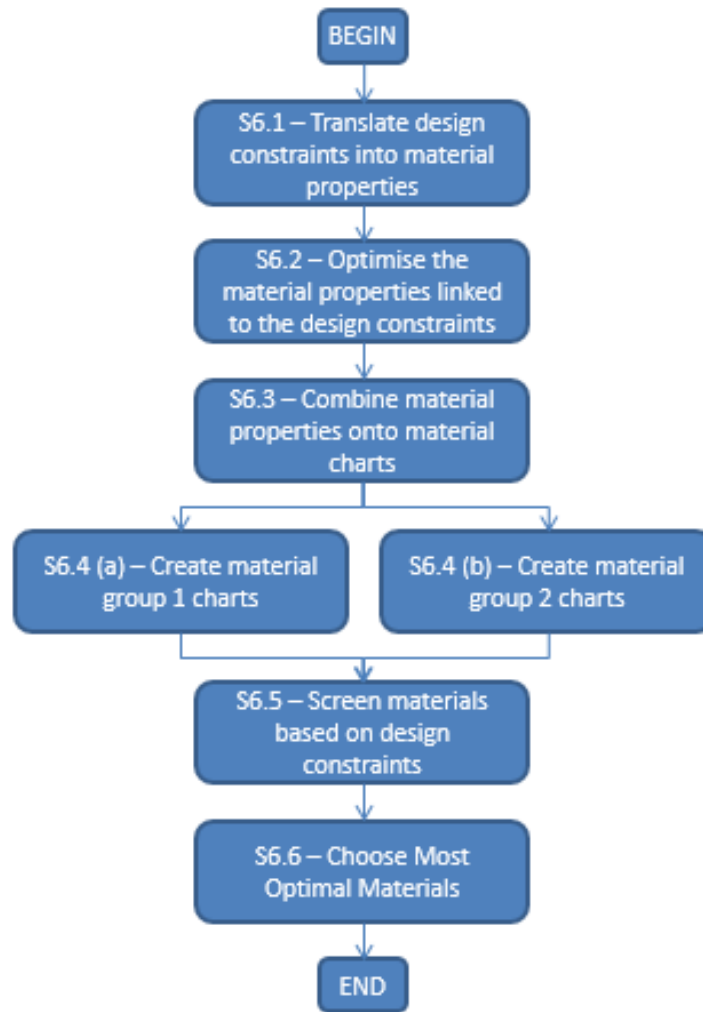


Figure 5.36: Choose the most optimal materials

The final stage is to choose the materials. This should be straight forward, as the screening process will have limited the available options. At this stage, all materials are viable options, and the choice of which material(s) to choose may depend on additional factors not directly linked to any of the original design requirements; for example, cost.

5.5 Computational Testing: Detailed Description

5.5.1 Introduction

By this stage in the design guidelines, the chosen form, materials and structure of the part should be known. With this information, it is possible to create an FE model and computationally test the design. This stage describes the functions used in the FE package. There are three stages to the FE tests: pre-processing, processing and post-processing. Most of the engineers work is spent in the pre-processor, so this will

be the main focus in these design guidelines.

5.5.2 STEP 7 - COMPUTATIONAL TESTING: PRE-PROCESSOR

5.5.2.1 Model definition

The first stage in the computational test is to create the model. At this point in the design guidelines, it is known whether the part will use structured cells or TO. This section describes how to design for both possibilities.

5.5.2.1.1 Structured cells In these design guidelines, parts created with structured cells are built bottom-up. That is, the repeating cell is first created, and then replicated many times (with modification to truss lengths, if necessary) until the final part is finished. The procedure for creating structured cells is explained in section [5.5.2.1.2](#).

5.5.2.1.2 How to apply structured cells If the arm link passes all the conditions highlighted in section [5.3.3.5](#), the structured cells can be used. Before the design steps, two pre-design steps must be made:

1. Calculate the distance between the inner and outer surfaces. This distance will determine how many structured cells should be fitted between the two surfaces.
2. Decide on the form of structured cell. This is based upon the decision of:
 - (a) Loading on the part
 - (b) How many cells should be placed between the inner and outer surfaces
 - (c) How many cells should be fitted radially

Both of these decisions can easily be altered via the scripts created for these design guidelines. It is advisable to iterate through a combination of the number of cells between the inner and outer surfaces and the number of cells radially, until a design that is satisfactory is found.

Once these two decisions are made, the design steps can be made:

1. Make a solid spatial envelope representation of each structured cell in the radial direction. No matter the design, the chosen cell shape will have an outer spatial envelope. The shape will increase in size in the radial direction. The first step of design is to create solid models of each of these. In Abaqus, this is done using the CAD tools under the “part” tree.

2. Partition the solid model into radial SUMC layers. While solid, the model should be partitioned into radial SUMC layers, if applicable. If radial blending is not being undertaken, this step is not necessary.
3. Shell the solid spatial representation. The third step is to shell the solid model. This will leave a wireframe representation of the cell. The wireframe will be used to build the elements around. The “Create Wire: From selected edges” command in Abaqus is found under the “part” tree.
4. Create additional wires. The wireframe will be used as the building frame for the elements. Depending upon the design of the structured cell, additional wires may be required in addition to those which are created during the shell process. The “Create Wire: Point to Point” command in Abaqus is found under the “part” tree.
5. Create the nodes on the wireframe. In order to build the elements, nodes must first be made. The node positions depend on the design of the structured cell. The number of nodes around the wires and the distance that each node sits from the wires can be altered. In Abaqus, nodes are placed manually using the “Mesh → Edit Mesh → Node” command found under the “mesh” tree. Nodes must be placed to allow pre-defined element shapes (for example, wedge or quadrilateral) to match up to the nodes.
6. Connect the nodes to create elements. The nodes have been intelligently placed to allow pre-defined elements to fit between the nodes. The elements are placed using the “Mesh → Edit Mesh → Element” command found under the “mesh” tree in Abaqus.
7. Draw the outer walls onto the outermost structured cell. This will be patterned to ensure the outer wall surrounds all the structured cells.
8. Assemble all individual structured cells and outer wall. Creating the assembly of one “slice” of the part is the pre-cursor to using a pattern to create the entire part. The assembled instances are created using the “Create Instance” command under the “assembly” tree in Abaqus. Positioning the instances is done using position translation and constraint commands. There are various commands available - the choice of which depends on the shape and features of the structured cells.
9. Use a linear pattern array to replicate the structured cells in the z axis, so as they are the length of the arm link. In Abaqus, the linear pattern tool is found under the “assembly” tree.

10. Use the pattern feature to complete array in the x-y plane. The type of array depends on the cross sectional shape of the part:

- a circular array for circular cross sections
- a linear array for tetragon cross sections

Both array tools are found under the “assembly” tree in Abaqus.

5.5.2.1.3 Topology optimisation Unlike the design for structured cells which requires the repeating cell to be built first and the part then to be created via replication of the cell, topology optimisation requires the entire part to be in place to begin with. Designing for topology optimisation is not as in depth as structured cells, since the TO solver is carried out by the computer.

The design space should be left as full as possible. When this is done, the solver will have the greatest chance of finding the best topologically-optimised solution. If the form of the part is too greatly constrained when creating a topologically optimised part, the solver will not have sufficient material within the design space in order to find the best solution, or worse, may never converge on a solution. For example, if the robotic arm is to be a square box cross section with no internal cabling, only the **maximum allowable** cross section dimensions, length and any fixing points should be constrained. The rest of the design space should be left full for the optimisation solver to use as necessary.

5.5.2.1.4 Conclusion Defining the model refers to it’s initial creation in the FE software. This is linked to the decisions made during the “structure” chapter in the guidelines, and focusses on either building structured cells, or setting up for topology optimisation. The instructions given for both structured cells and topology optimisation will be tested at later stages in this thesis to ensure they are robust.

5.5.2.2 Section Definition

Every SUMC needs its own section definition in order to apply the unique material - a unique identifier for every segmented volume in the part. This is easiest to do in the python script.

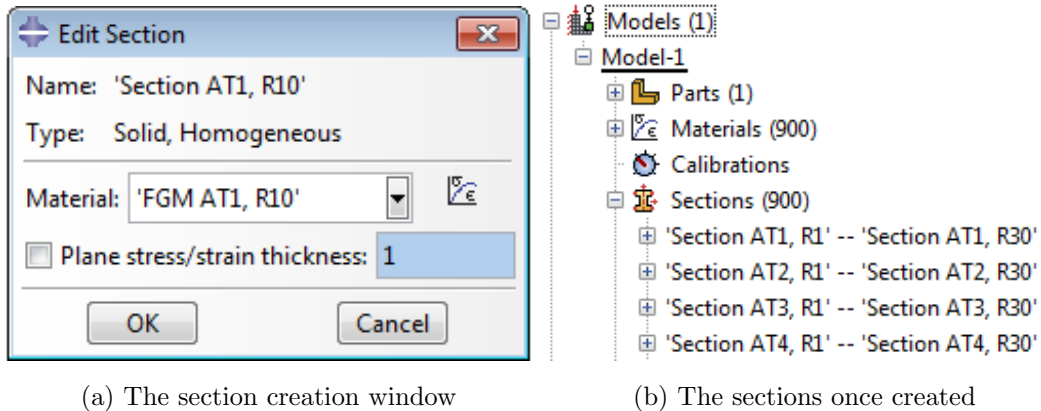


Figure 5.37: Creating the sections and applying the materials

5.5.2.3 Surface/Edge/Node Definition

Surfaces/edges/nodes are put in place to artificially alter the part. This is necessary to do if the arm link has various loads, materials, mesh shapes/sizes or boundary conditions to be put in place. On occasion, features of the part may need partitioned and/or datum planes/axes may need created in order to define the surfaces/edges/nodes of interest. These definitions are given an identifier which can be called upon at later stages.

5.5.2.4 Material definition

All materials that will be used in the FEA must be defined. As highlighted when converting the design requirements into material properties in section 5.4.4, the modulus of elasticity, density and Poisson's ratio are needed for the mechanical testing of the arm link. If creating an FGM, each material mix must be given an associated material definition at this stage. As set out in section 5.4.3, these design guidelines assume that when the two materials are mixed, the resultant material property values lie between those of the two constituent materials, except material melt temperature, which is set as the higher melt temperature of the two constituent materials, otherwise the higher temperature material would not fully melt.

5.5.2.4.1 How to apply functionally graded materials The application of functionally graded materials requires several steps either side of the actual material allocation itself. Before the material is allocated, the following steps are necessary:

1. Carry out calculations. The calculations described in section 5.4.3 must be worked out. These include:
 - (a) The FGM distance

- (b) The interpolation limits
 - (c) The SUMC percentages
 - (d) The two layer thicknesses required
 - (e) The two material percentage blends needed (if FGM blending distance is BELOW complete FGM distance)
2. Partition the part. The FGM blending distance area of the part should be partitioned. The distance between the partitions is found from the calculations. The partition is visual only, so the layers of the model remain bonded to one another. The partitions represent layers of material. It is therefore easiest to partition using datum planes. There are multiple options to create planes in Abaqus, depending on the geometry. The “create datum plane” options can be found under the “part” tree.

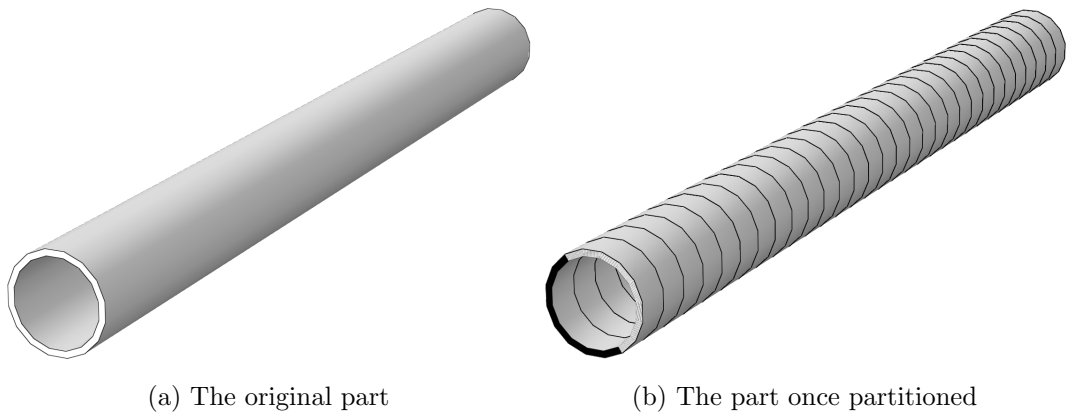
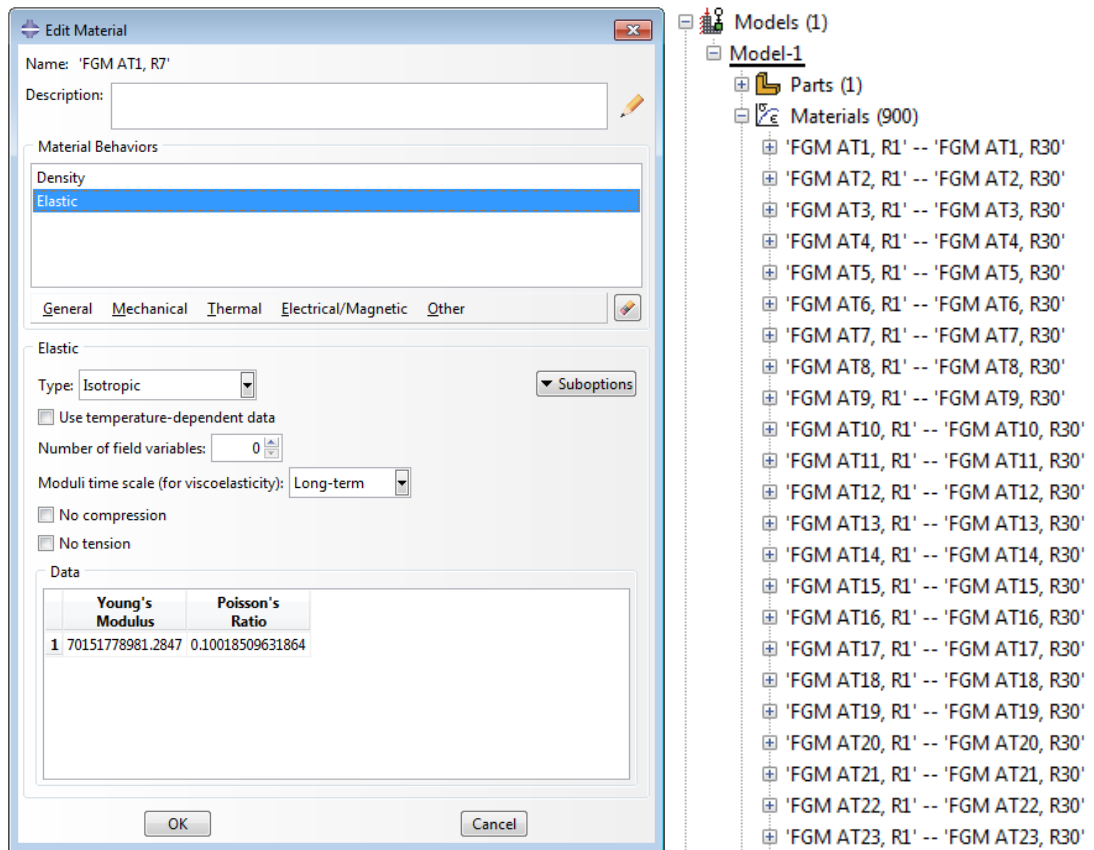


Figure 5.38: Partitioning the part

Once these steps are complete, the FGMs can be applied. For this, the following steps are required:

1. Creating the materials. The materials must first be created. This is done using the “Create Material” command under the “property” tree on Abaqus. A unique material must be created for each SUMC layer in the part - shown in figure 5.39. As discussed, all material properties bar the melt temperature are an interpolation value of the two constituent materials in the part. The values used for the interpolation are found from the calculations.
2. Apply the materials. The materials are applied to the sections created during the section definition (5.5.2.2). Each material is applied to its specific section.
3. Assign the sections. Each section must be assigned to a specific SUMC layer of the part, as shown in figure 5.41. Multiple areas of the part can be assigned to

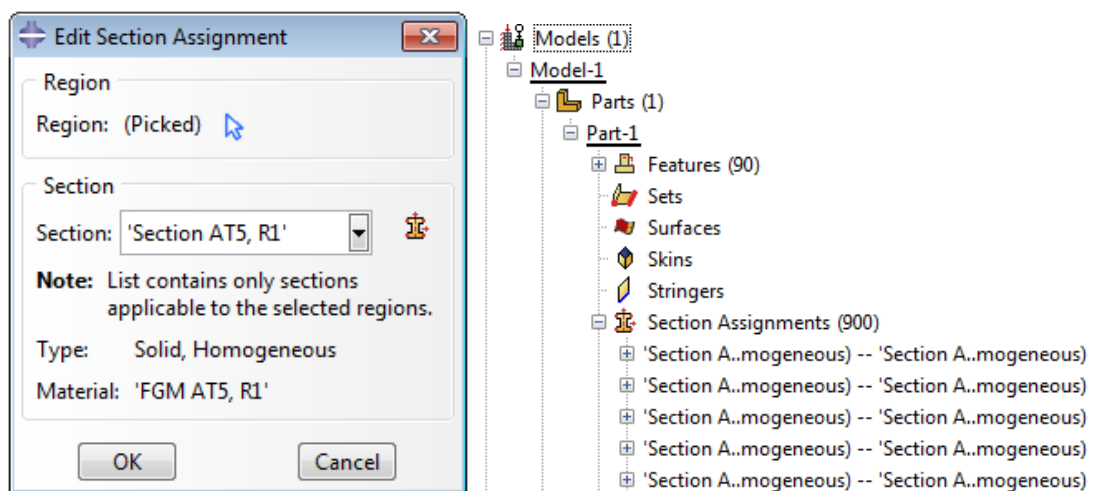


(a) The material creation window

(b) The materials once created

Figure 5.39: Creating the materials

the same section. This allows the areas outside the FGM blending distance to have the same material applied as the SUMC closest to them.



(a) The section assignment window

(b) The sections once assigned

Figure 5.40: Assigning the sections

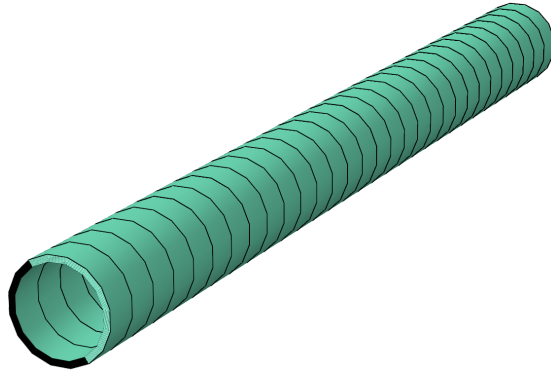


Figure 5.41: The part with sections assigned

5.5.2.4.2 Conclusion This technique for creating and applying FGMs has already been tested in the preliminary test case, and shown to reduce stress concentrations. As already stated, the assumption made to create the FGMs in this way (assuming perfect bonding at material interfaces) is valid on the macro scale^[83]. For these two reasons combined, it will be used for the remaining duration of this thesis, when FGMs are applied.

5.5.2.5 Step Definition

Steps are required in the pre-processor. They are used to assign different loads and boundary conditions that occur during the simulation to replicate the dependence/independence/ order of actions, as they would be in reality. The step itself does not hold any analysis information. For example, the arm link would have its permanent fixed faces present from the outset of the test (the initial step), and the force resembling the loading due to actuation and payload present from a second step.

5.5.2.6 Interaction/Constraint Definition

In certain situations, interactions and/or constraints are needed between points in the pre-processor model. Able to imitate a wide range of scenarios, common uses include contact between objects (interaction), or how one point/part moves in relation to another (constraint). With respect to a robotic arm link, interactions/constraints can be used to model the influence of joints and links not currently present in the solver, but that would exist in reality. These joints and links would be represented as points in space, and an interaction/constraint between said points and the FE model would be made.

5.5.2.7 Boundary Condition Definition

Boundary conditions are limitations on what the part can do. They are used to mimic the limitations seen on the actual part. In the case of the arm link, all boundary conditions will be geometric restrictions. They will be both axial (displacement) and torsional (rotation) limitations. Each boundary condition will be assigned to both a pre-defined section/surface/edge/node and a pre-defined step. Boundary conditions can also be used to simplify an FE model via symmetry. In the case of an arm link it is possible that only a portion of the arm link need be modelled, if the loading conditions are such that symmetry is possible. This will reduce computational times.

5.5.2.8 Load Definition

Different from a boundary condition which arrests movement, a load is any force which acts to move the arm link. For the arm link, loads include torsional loads and axial loads. Each load will be assigned to both a pre-defined section/surface/edge/node and a pre-defined step.

5.5.2.9 Mesh Definition

The size and shape of the mesh make a large difference on the outcome of the analysis. The robotic arm link will not be undergoing large displacements/deformations, therefore adaptive meshes are not necessary. The model may well contain complex geometric features, so may need element shapes that are not as computationally-accurate as others in order to fit into the complex geometries. Sections can be used to artificially segment areas of the arm link. This will allow different element sizes and shapes to be used, useful if the mesh needs refined in certain areas. Smaller mesh sizes require greater computational power to process when compared to larger mesh sizes. The smaller the mesh gets, the closer the representation to reality it gives. As stipulated in the design guidelines, the thickness of any FGM material layer must be at least three times the value of the AM minimum resolution. As such, the minimum feature size must also be three times the value of the AM minimum resolution. It is known that for more realistic results, there should be multiple finite elements in every direction of any feature. The mesh size should therefore be set to the AM minimum resolution size too, meaning there will be at least three finite elements for any feature. Because of this small mesh size, symmetry boundary conditions will be used where possible to reduce the overall size of the test volume.

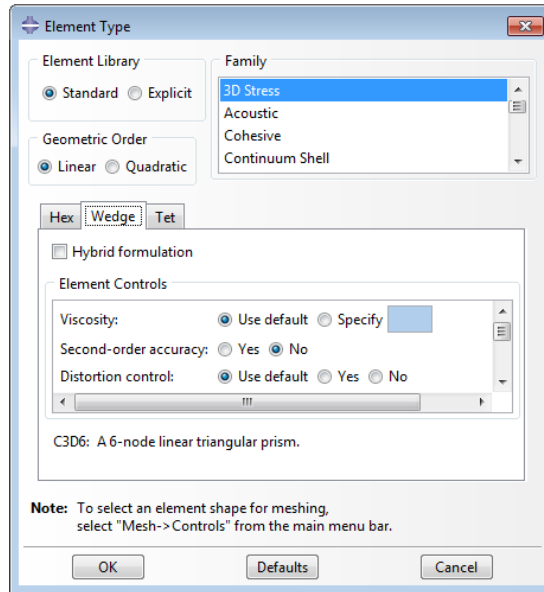


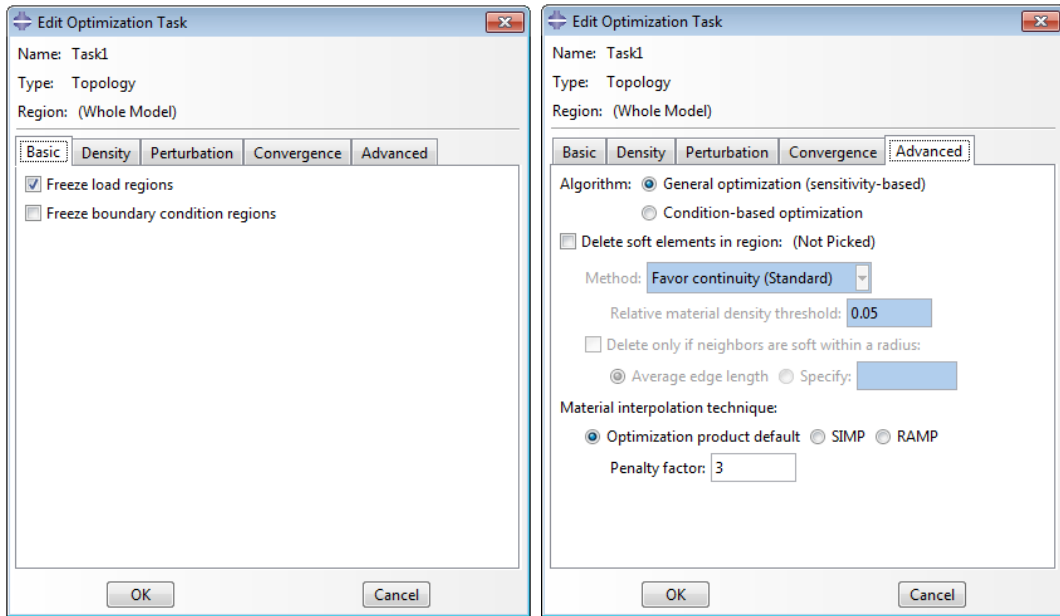
Figure 5.42: The choice of element type

5.5.2.10 Optimisation Definition

Topology optimisation is applied once the part is created. All testing parameters must be applied (loading forces, materials, boundary conditions, etc) beforehand, as in sections 5.5.2.1 to 5.5.2.9.

5.5.2.10.1 How to apply topology optimisation The procedure to set up the TO solver is as follows:

1. The optimisation task is created. Decisions at this stage include:
 - (a) Freezing load and boundary condition regions. The load and boundary condition regions can be frozen, or left in the optimisation volume.
 - (b) Solver algorithm. Generally, the stiffness algorithm should be used for strain energy - volume problems, as it is more efficient than the general optimisation routine. However, the stiffness algorithm cannot handle multiple materials, and therefore the general optimisation routine must be used for all parts in these design guidelines (as it was for the preliminary tests in section 4).
 - (c) Material interpolation technique. By default, the SIMP technique is used (described in section 2.3.3.2). The RAMP technique, developed for tests using pressure loads, gives higher accuracy when load or boundary condition regions are altered during the optimisation.



(a) Freezing regions

(b) Algorithm and interpolation technique

Figure 5.43: Optimisation task options

2. The design responses are chosen. Decisions at this stage include:

- (a) Choice of design response. The design responses are the variables in the optimisation routine. The available options will be limited to the solver algorithm chosen in the optimisation task.

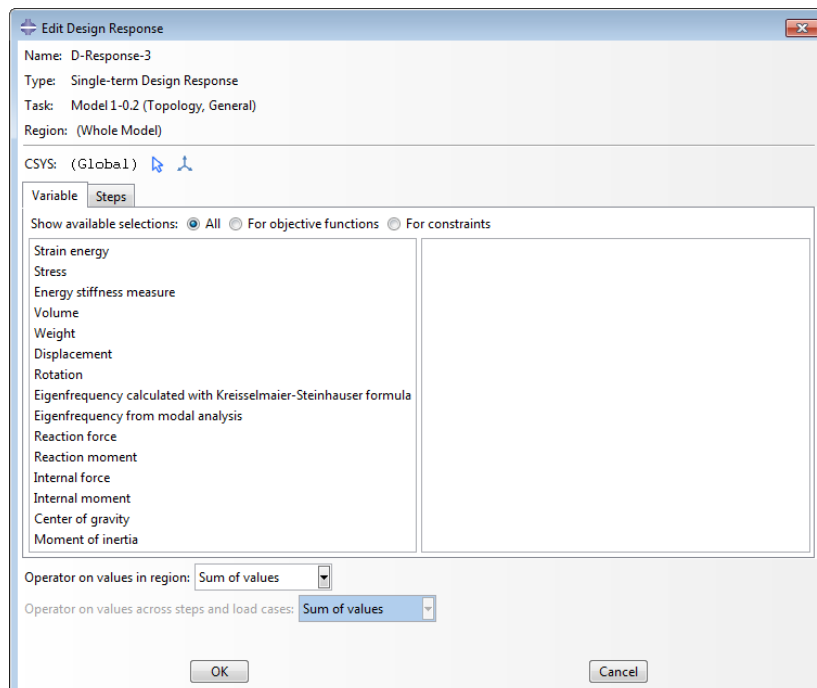
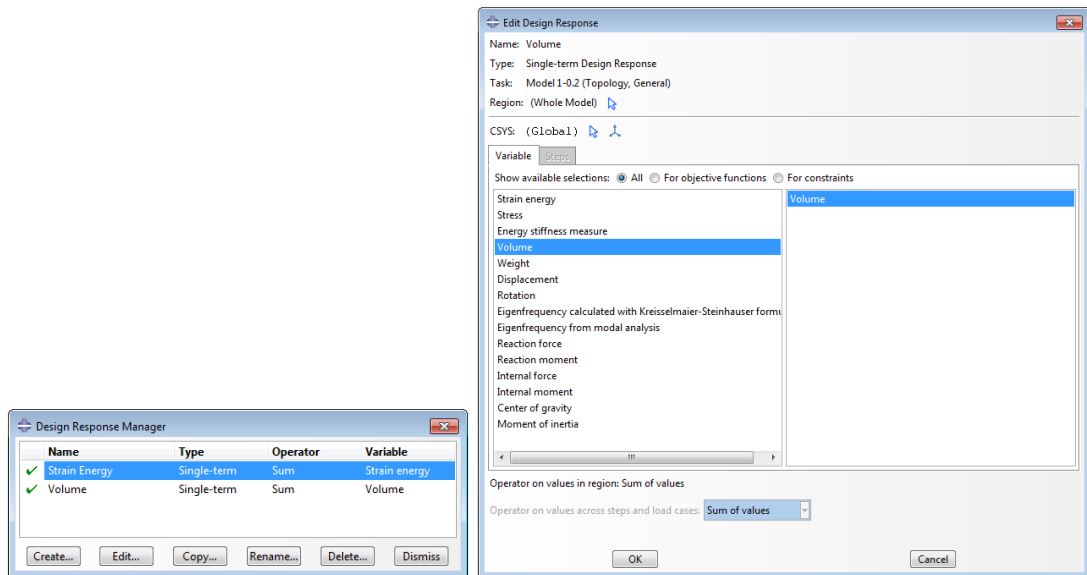


Figure 5.44: The possible choice of design response

- (b) The focus region. The focus region for each design response must be chosen. It can either be the entire model, or specific regions. Ideally, the region should be kept as small as possible to decrease external factors influencing the optimisation routine.
- (c) Direction of design response. It must be ensured that the design response is aligned in the correct direction on the part, or the optimisation routine will not solve the problem as desired.
- (d) Activation of design response. By default, the design response will be optimised for during all steps of the simulation. However, if multiple simulation steps have been created, the design responses must be set to activate and deactivate as necessary during the optimisation routine.



(a) The design response manager (b) Setting volume as a design response

Figure 5.45: Design responses for strain energy/volume

3. Set the objective function. Decisions at this stage include:

- (a) The target of the objective function. The objective function can be set to minimize, maximise or minimise the maximum design response values. When solving for structural optimisation problems, minimising the strain energy while keeping the volume constrained is the most straightforward approach.
- (b) Weighting within objective functions. If multiple design responses are needed to be combined into one hybrid design response, it is done by creating an objective function with multiple design responses within. Each individual design response must be given a weighted average.

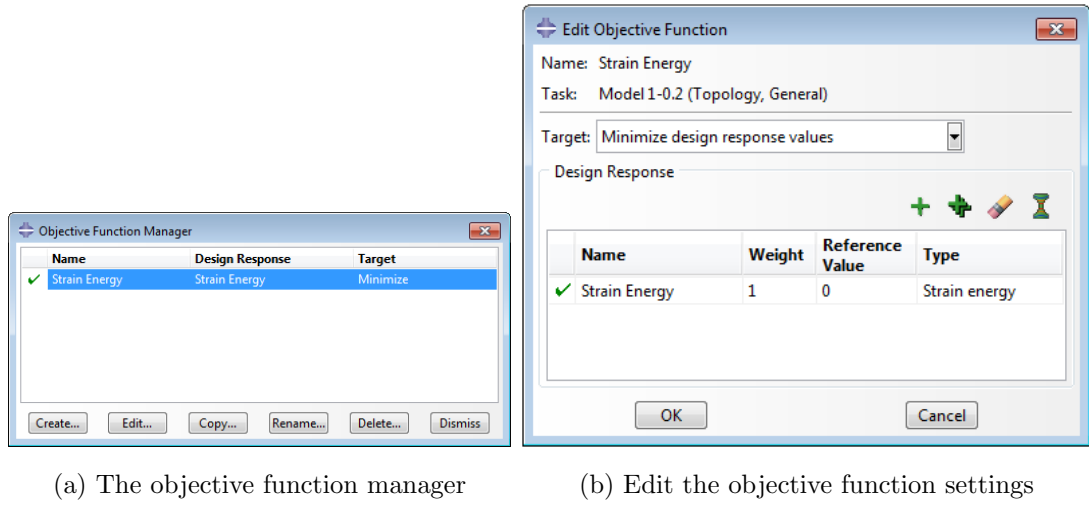


Figure 5.46: Creating the objective functions

4. Creating the constraints for the test. Decisions at this stage include:
- (a) The number of constraints. Multiple constraints can be placed on the model, for example moment of inertia, reaction forces and displacement. However, the greater the number of constraints, the more difficult the solver will find it to converge on a solution. When solving for stiffness problems, a single volume constraint is often used.
 - (b) Limits of constraints. The constraints take priority over solving the objective function. If the limits of the constraints are not feasible, the task will not be solved.

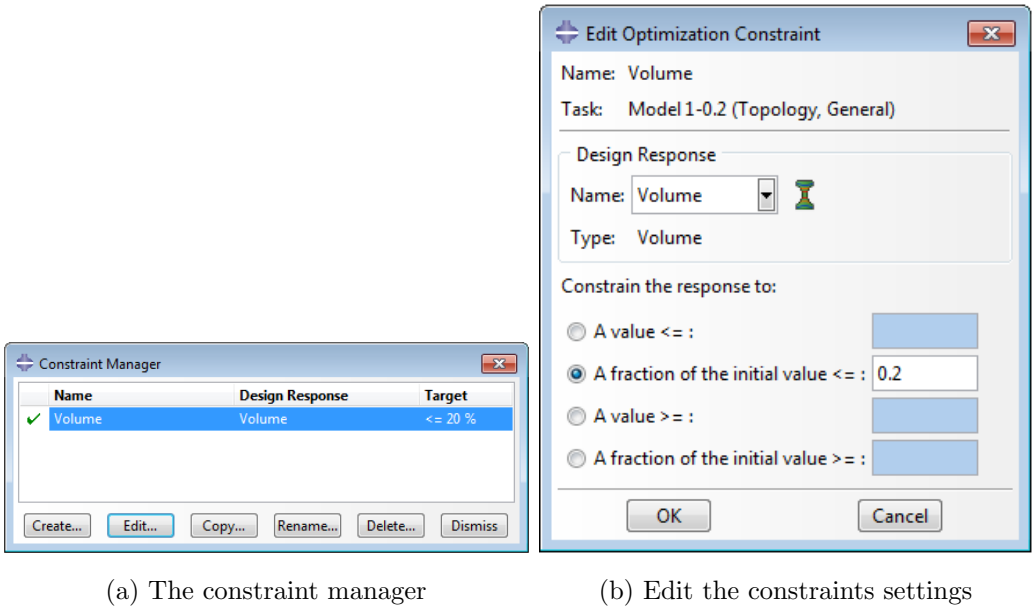


Figure 5.47: Creating the constraints

5. State the geometric restrictions. Decisions at this stage include:
- (a) Member size. If the part is to be additively manufactured, there will be a limited feature size that can be created. This value must be greater than twice the average size of the elements, otherwise the result will be dependent on the mesh size.
 - (b) Gap between members. If a minimum gap size between members is needed, this can also be specified.
 - (c) Frozen areas. Areas of the part to be excluded from the topology optimisation are set here. These may include fixing points or loading areas.
 - (d) Symmetry. Symmetrical designs can be created in the part. Cyclic, rotational and planar symmetrical designs can all be achieved.

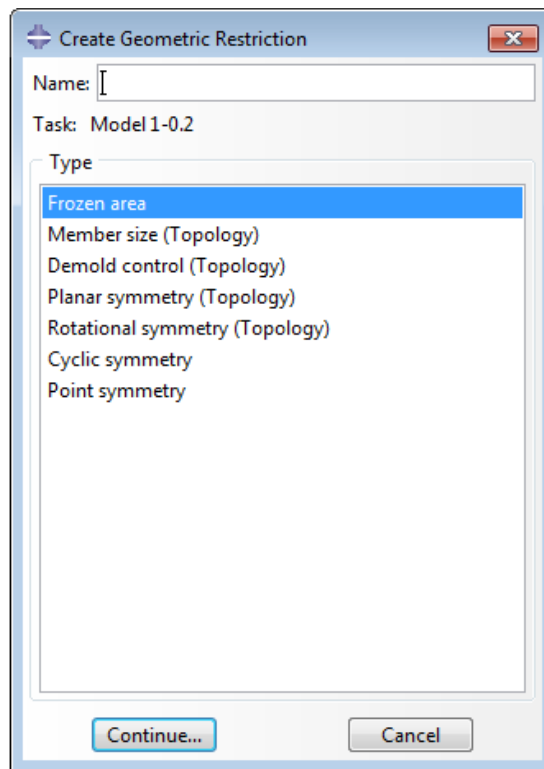
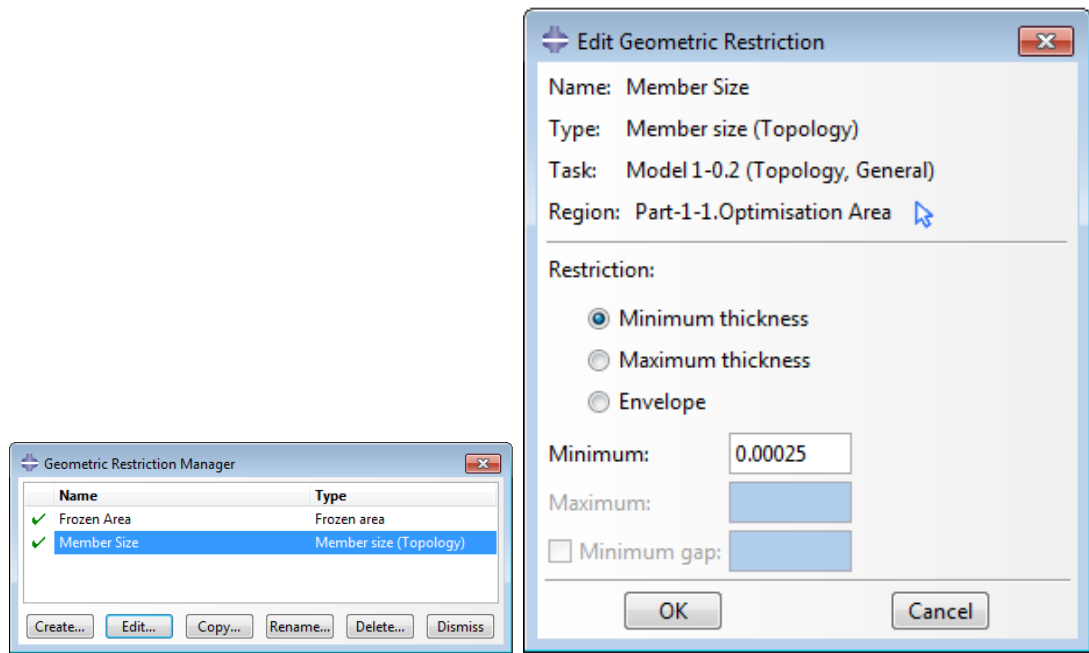


Figure 5.48: The possible choice of geometric restriction



(a) The constraint manager

(b) Edit the constraints settings

Figure 5.49: Creating the geometric restrictions

These steps can be found in greater detail in the Abaqus/CAE User's Guide (section 18 of guide version 6.14).

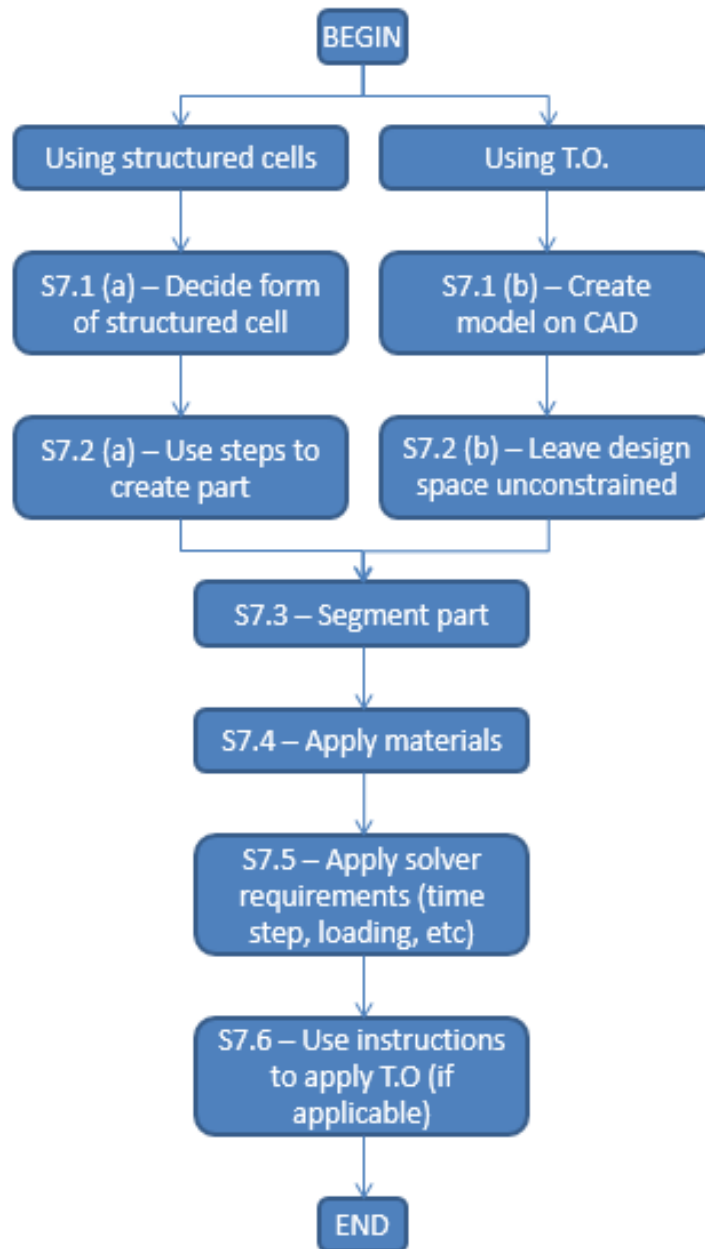


Figure 5.50: Use instructions to apply T.O. (if applicable)

5.5.2.10.2 Conclusion Applying topology optimisation is fairly straightforward. Engineering knowledge is required to choose the correct design responses. At present, there is no option to pick “packages” of design responses in order to solve for a specific task - for example, strain energy and volume to solve for minimum mass. A future iteration could be to code these predefined “packages” in order to make topology optimisation within this software easier for those without the engineering knowledge.

5.5.3 STEP 8 - COMPUTATIONAL TESTING: PROCESSOR

5.5.3.1 Data Check

Before the processor is run, a **data check should be carried out**. using the software. This allows the users to see if any obvious errors have been made during the pre-processing stage.

The data check will take all inputs and run them through an input file processor. If any inconsistencies were made during the inputs, the input file processor will flag these, and the model can not be run. The data check only ensures that all information is present, it does not indicate whether the processor will be able to converge on a solution, or not.

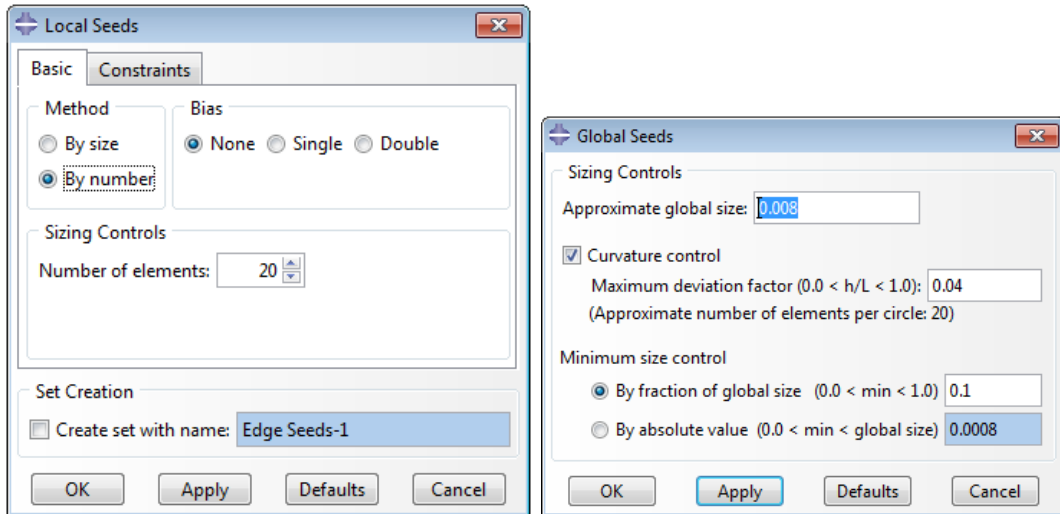
Once the data check has been passed, the processing may begin. This process differs depending on whether structured cells or topology optimisation is being used.

5.5.3.1.1 Conclusion The data check is important to ensure that no errors have been made during the pre-processor set up. Currently, the diagnostic tool on the FE software is not very intuitive. While not something which can easily be altered by the researcher, it should still be noted that future work from software developers could improve the user experience of problem solving the data check outputs.

5.5.3.2 Using structured cells

The first sub step when using structured cells is to run an elementary FE analysis.

5.5.3.2.1 FEA Elementary Processing The processing is carried out by the FE code. This stage requires minimal user interaction. If all information has been correctly entered during pre-processing, the processing stage will successfully run. The time required is dependent on the model set up and the computational power available. This elementary test is to assess if the inputs during pre-processing are realistic, or not. This allows the user to discover any glaring mistakes made during the pre-processor stage which do not fail the input data check, but do lead to erroneous results. The only difference at this stage compared to the detailed testing stage is the mesh size used. A larger mesh will be used here, as it requires less computation. If the results are as expected, the process can continue. If the results are far from what was expected, and assuming the model was correctly set up, then the structured cell needs altered. This can be done by altering the thickness of struts on the part. If altering the thickness of the struts does not solve the cell, the form of the cell (chosen in section [5.5.2.1.2](#)) can be altered.



(a) Assigning local seeds

(b) Assigning global seeds

Figure 5.51: Creating the geometric restrictions

5.5.3.2.2 FEA Detailed Processing The second processing test is a detailed test, and only occurs if the outputs from the elementary test were promising. **The mesh size is reduced to the size of minimum resolution of the AM technique being used.**

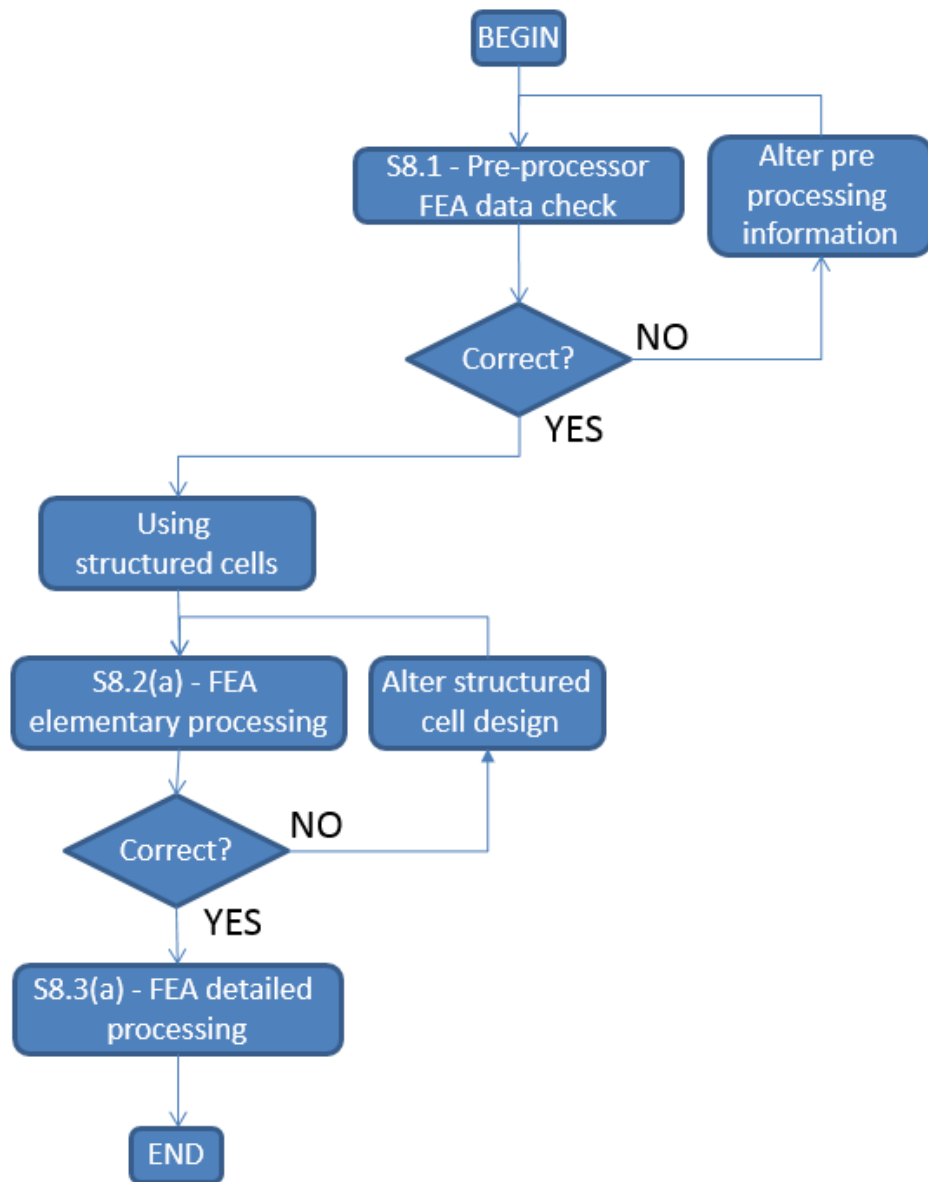


Figure 5.52: Undertake a data check on the T.O. pre-processor information

5.5.3.2.3 Conclusion This stage simply alters the mesh size, as the majority of work for structured cells is carried out during the model definition in the pre-processing stage (section 5.5.2.1.1). Simple alterations to the form of the structured cell may be required, but this is a straightforward process, assuming the build steps in section 5.5.2.1.2 are followed.

5.5.3.3 Using T.O.

There is an additional step when using topology optimisation when compared to using structured cells.

5.5.3.3.1 FEA elementary processing This is identical to the elementary processing done when using structured cells. Again, the mesh size is set to a large size in order to reduce computational time. If the results from this test are as expected, then the T.O. can be implemented in the model. There is no need to do TO on the coarse mesh model - the outputs from the unaltered/original part are sufficient to see if the behaviour is as expected, or not.

5.5.3.3.2 T.O. data check Using T.O. requires another input of variables. These must be checked, akin to the normal variables in section [5.5.3.1](#).

5.5.3.3.3 FEA + TO detailed processing This test is identical to the detailed processing done when using structured cells. Again, the mesh size is reduced to the size of the minimum resolution of the AM technique being used. This process takes significant time. as it must also run the TO solver.

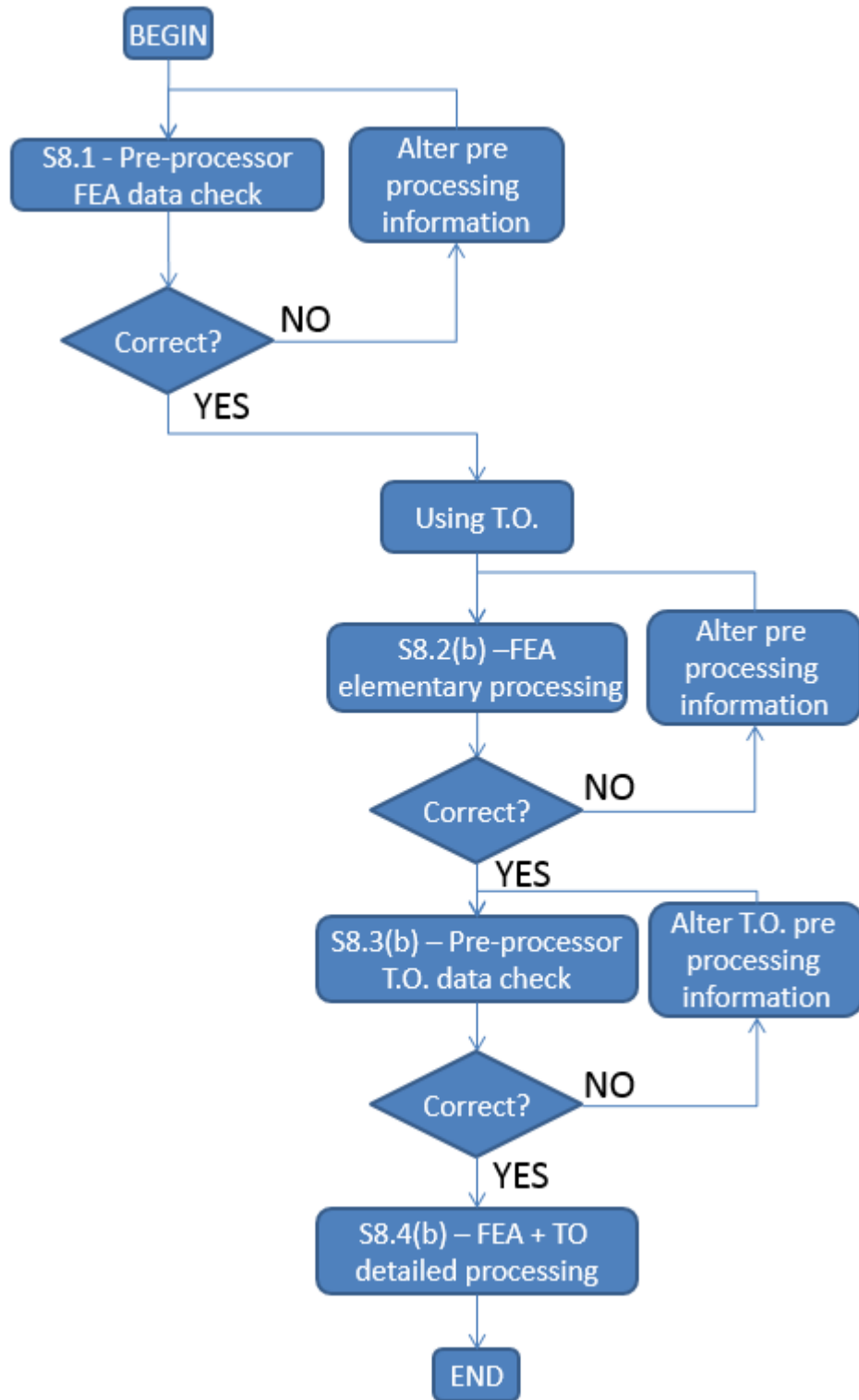


Figure 5.53: Undertake a detailed FEA test

5.5.3.3.4 Conclusion This stage also simply alters the mesh size after a coarse mesh has validated that there are no issues in the pre-processor. The task of altering the T.O pre-processing information is extremely simple, if required. Simply follow the

commands given in section 5.5.2.10.1.

5.5.4 STEP 9 - COMPUTATIONAL TESTING: POST-PROCESSOR

5.5.4.1 Part smoothing (TO only)

Once the topology optimisation solver has completed, the surface mesh of the model requires smoothing. To do this, select **optimisation**→**extract**.

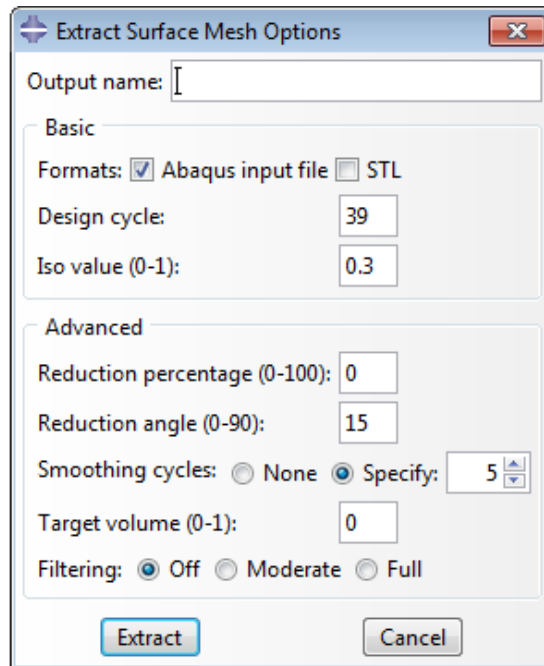


Figure 5.54: Settings for mesh smoothing

The options which can be set are:

1. File type. The extracted mesh can either be an STL file (for use with AM hardware), an Abaqus .inp file (to allow further work/validation), or both.
2. The ISO value. The ISO value dictates at which point within the surface elements the new, smooth surface should be created. Increasing the ISO value means the nodes for the new surface will be further “within” the each surface element, and thus the overall volume of the model will decrease
3. Reduction percentage. The reduction percentage aims at reducing the number of faces on the surface of the part, making it smoother. It is linked to the reduction angle, which is a value controlling the allowable angle between faces. When set to 100, the reduction percentage will remove as many faces as possible. When set to 0, it will not remove any faces.

4. Reduction angle. As mentioned, the reduction angle controls the allowable angle between faces. The higher the reduction angle, the more faces will be removed.
5. Smoothing cycles. The higher the number of smoothing cycles, the smoother the model will be. However, too many cycles may affect the structural performance of thin regions.
6. Target volume. The target volume of a part is the ratio of the the smoothed mesh volume and the original post TO volume. If a value is set, the ISO value set above is ignored. Care must be taken not to set the target volume too high/low, as the smoothing will fail if the target is outwith the ISO value limits of 0 - 1.

5.5.4.2 Validation

In order to ensure the design is valid, a further simulation is required. If possible, the part should be assembled along with other components of the arm which have not been altered by these design guidelines, but do come together to make the entire robotic arm (additional joints, links, etc).

The validation should test the parameters that were designed for. A static simulation is sufficient. Ideally, the deflection of the entire system will be within acceptable limits, and the mass will have reduced when compared to the original design, due to the lightweight design techniques used in these design guidelines.

5.5.4.2.1 Conclusion Post processing of the TO computational testing is very straightforward using the built in extraction tool described in section 5.5.4.1. There are additional software tools available with greater flexibility that can give more options for smoothing. If the user decides to use these, they should export the STL without running the inbuilt smoothing algorithm. The results of the inbuilt smoothing algorithm will be checked in the later test cases in this thesis.

5.5.5 Introduction

This stage of the design guidelines is related to the physical manufacture of parts, including material mixing strategies, processing parameters during AM production, and pos-processing techniques often required after the AM process has been completed in order to clean up parts and enhance their properties.

5.6 Manufacturing Technique: Detailed Description

5.6.1 STEP 10 - ACTUAL MATERIAL MIXING

5.6.1.1 Mixture definitions

Mixtures can be broadly categorised as ordered, random or adhesive/interactive.

5.6.1.1.1 Ordered Ordered mixtures are only possible theoretically, as they describe a situation where powders of both constituents form a perfect homogeneous mixture. Figure 5.55a shows an ordered mixture.

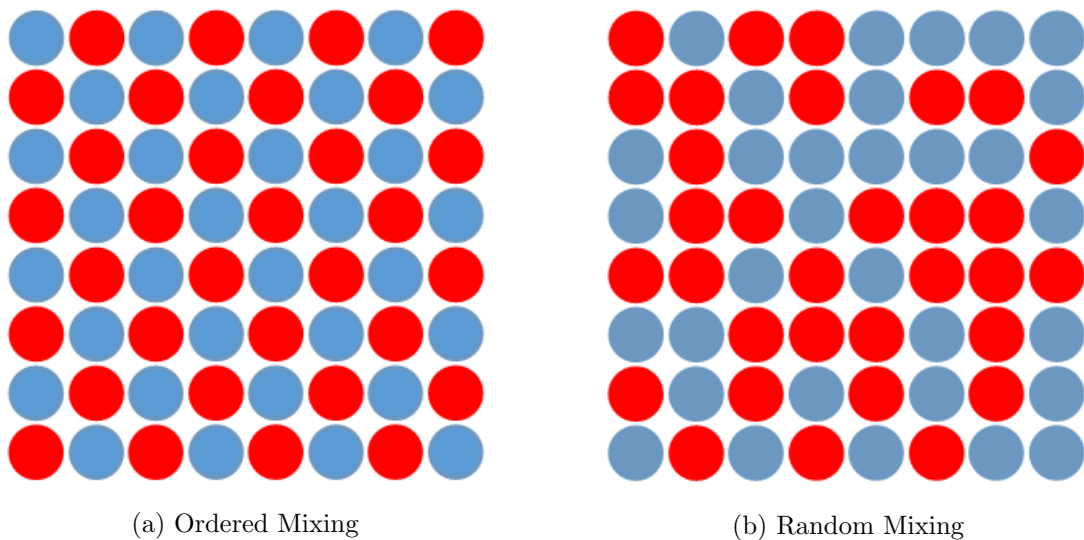


Figure 5.55: Mixing Descriptions

5.6.1.1.2 Random Random mixtures occur between two free flowing powders. The powder particles have to be non-cohesive, and all of similar size, shape and density. Figure 5.55b shows random mixing. If the powders do not fulfil the latter three requirements, segmentation will occur, whereby the materials disassociate from one another, with the lighter, larger particles sitting above the smaller, heavier particles. The mixing duration dictates the homogeneity level of the mixture.

5.6.1.1.3 Adhesive/interactive Adhesive/interactive mixtures occur when cohesive and non-cohesive powders are mixed. In order to be completely mixed, no particles of the cohesive powder can remain upon mixing completion. To avoid segregation, it is best if the two constituent materials have particles of the same size, however, this is not obligatory. Often seen in practice is a pairing of interactive and random mixtures, whereby loose non-cohesive particles exist in amongst an interactive mixture.

5.6.1.1.4 Conclusion The material mixing will be random, as this is an inherent feature of dry powder mixtures. Assuming that the powder feed control is sufficiently accurate (as advertised on the AM hardware), the random mixing will still be well distributed - there will be no clumps of single material.

5.6.1.2 Staged vs Continuous mixing

Staged mixing is done using an independent material system. Continuous mixing is done in-process while the AM hardware is depositing material.

5.6.1.2.1 Staged Staged mixing describes mixing via independent mixing systems. Powders are weighed and added to the mixing system. As such, the mixing percentage is better controlled, and blends are better proportioned. However, there are complications when using staged mixing. The first is segregation of material - mixing must be done in close proximity as possible to the AM hardware as possible, as any transportation will agitate the mixture. The second complication is related to contamination issues - at the beginning of every new SUMC layer, the AM hardware would need cleaned. This is both expensive and time consuming. As such, staged mixing is not recommended, unless a multi-material machine is not available.

5.6.1.2.2 Continuous Continuous blending describes mixing in-process while the AM hardware is depositing material. The hardware must have at least two hoppers. Rather than being weighed as with staged mixing, material proportions in continuous mixing are controlled via flow rates of the two materials. As such, the mixing percentage is not as accurate as staged mixing, due to inherent flow rate control issues. However, there is no need for expensive and time consuming cleaning. The design of the hoppers has a large influence on the flow rate of particles. These design guidelines recommend the user follows the instructions from the AM hardware manufacturer to find best practice for creating a homogeneous solid-solid particle mix.

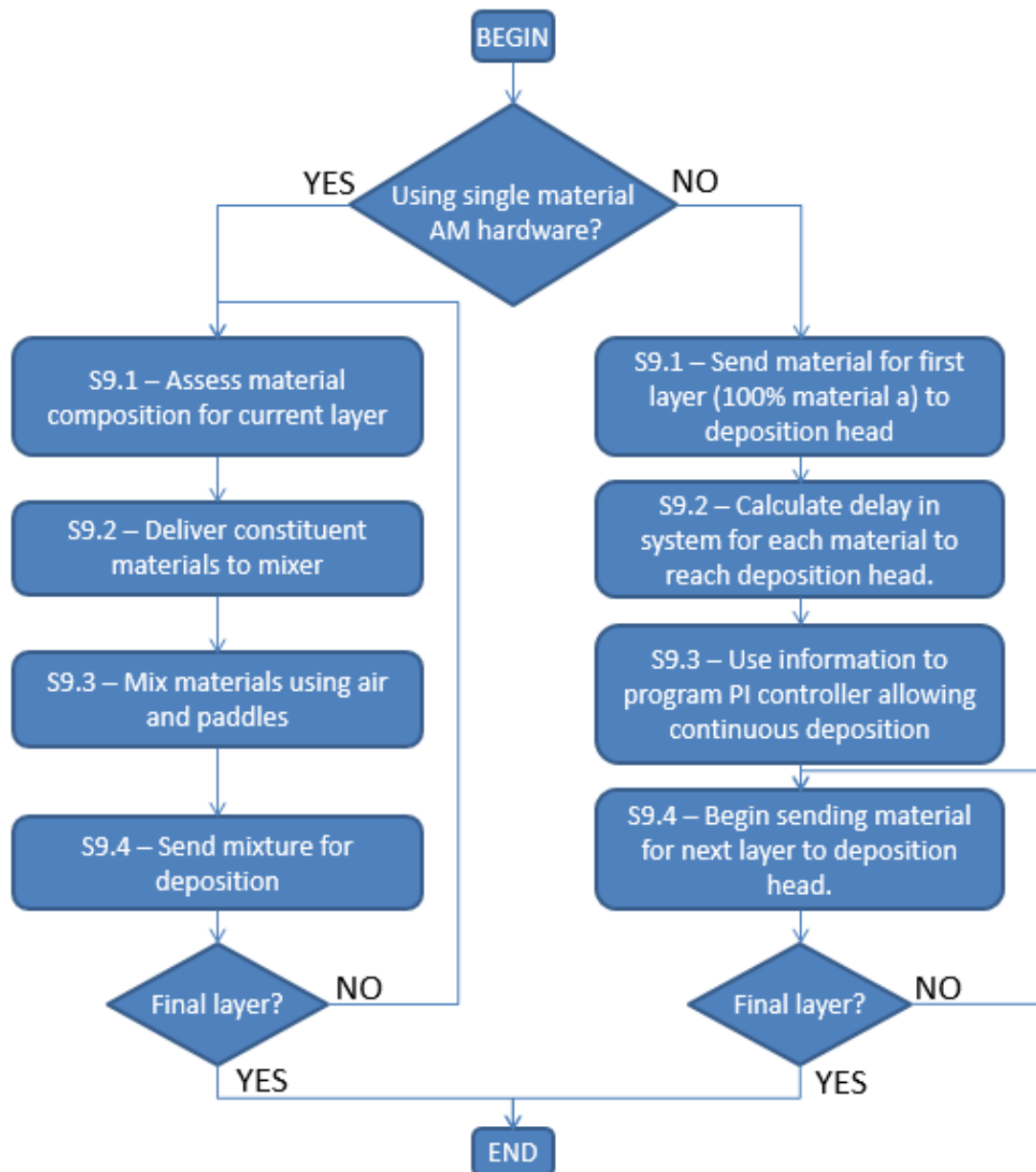


Figure 5.56: Continuous mixing for multi material AM hardware

5.6.1.3 Conclusion

One of the constraints put in place was ensuring constituent materials were always mixed at 0.5% increments to ensure production by the AM hardware. Staged mixing is more accurate than continuous mixing, as it does not require any in-process alterations via P.I controllers. However, as shown by Muller et al.^[205], P.I-controlled continuous mixing can achieve the 0.5% increments required by the constraints. As such, the material mixing technique chosen depends ultimately on the equipment available. If possible, continuous mixing should be used, due to the speed and cost of use compared

to staged mixing.

5.6.2 STEP 11 - MANUFACTURING: PROCESSING

5.6.2.1 Choosing AM Technology

The choice of AM hardware to use is based upon two main factors:

1. The minimum feature size of the part
2. The materials that the part is going to be made from

Ideally, these two factors are decided based upon the design requirements. However, much of the current AM hardware on the market requires significant financial investment, and therefore in reality, these two factors may be limited by the availability of AM hardware.

5.6.2.2 Processing Parameters

Setting the process parameters (laser power, scan speed, etc) is one of the most difficult aspects of creating FGM parts. The AM hardware must fully consolidate both the powder materials, but not damage (e.g, overheat) either of them. For this reason, the materials were put into three groups during the preliminary tests in section 4. The process parameters will be set as follows:

- The power from the energy source (laser, electron beam, etc) will be set to a constant value - that required to fully consolidate the material with the higher melt temperature.
- The scan speed will be altered, based upon the composition of the FGM at every SUMC. It will increase as the percentage of lower melt temperature material increases. As such, the higher melt temperature material will have a slower scan speed, and thus more time under the energy source to consolidate. This is illustrated in figure 5.57.

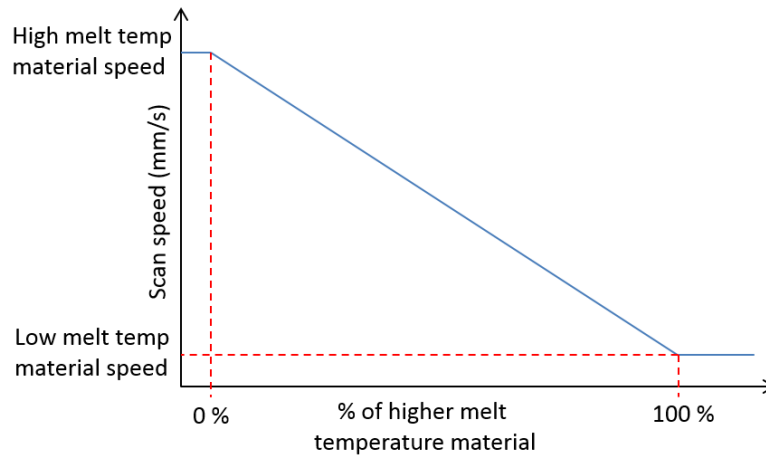


Figure 5.57: Altering the scan speed with material melt temperature

5.6.2.2.1 Conclusion Altering the scan speed is easier than altering the intensity of the energy source, hence the decision to keep the energy source constant, and change the scan speed. Once physical manufacturing has been tested, it may become apparent that there may be more processing parameters which need controlling.

5.6.2.3 Scanning Strategies

5.6.2.3.1 Between SUMC layers The scanning strategy has a large influence on the mechanical properties and heat profiles of the FGM part. When working with FGMs, the scanning strategy must follow the gradation of material blending. This can be described mathematically, looking at Figure 5.58 below:

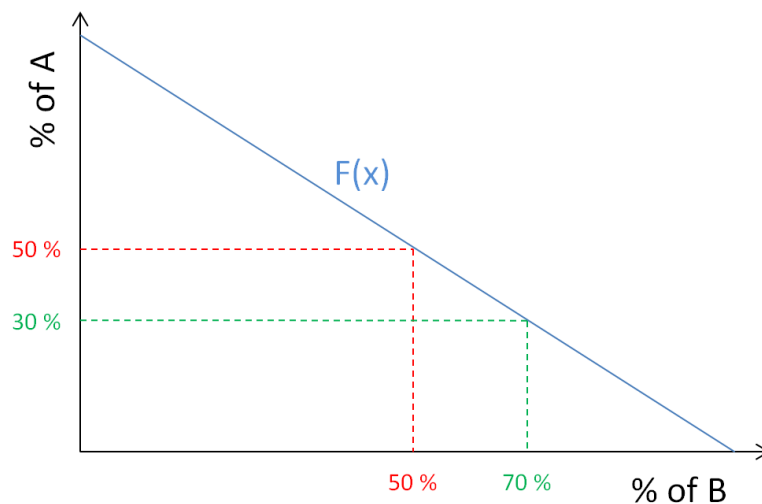


Figure 5.58: Ideal FGM Function

This graph shows the relationship between two materials - material A (on the vertical axis) and material B (on the horizontal axis). The blue line is the mixture of the two

materials, and can be represented by a function, $F(x)$. As seen, this line is linear with a constant gradient. The red and green lines are examples of materials A and B grading into one another - the red being 50% of material A and material B, the green being 30% of material A and 70% of material B.

The reason for the scanning strategy following the gradation of material blending is two fold:

- Firstly, it will keep the number of process parameter changes to a minimum, and thus the part build can be more easily controlled.
- Secondly, it reduces the number of material changes. This is important when using either staged or continuous mixing, as the material deposition can be more tightly controlled, and thus the scanning strategy has a better chance of achieving the desired material gradation, shown by $F(x)$ in figure 5.58.

5.6.2.3.2 Within SUMC layers It has been established that the scanning strategy should follow the material gradation **between** SUMC layers, however, thought must be given to scan paths **within** each layer also. As mentioned, thermal gradients are heavily influenced by the scanning strategy. As a general rule, the smaller the area that the energy source works on for a given time, the lower the thermal gradient on the part. For this reason, many scanning strategies segment up the entire deposition surface into smaller consolidation areas to avoid the large thermal gradients seen over the surface when the surface is unsegmented. These smaller areas are typically raster scans.

Figure 5.59 shows three different scanning strategies that can be used.

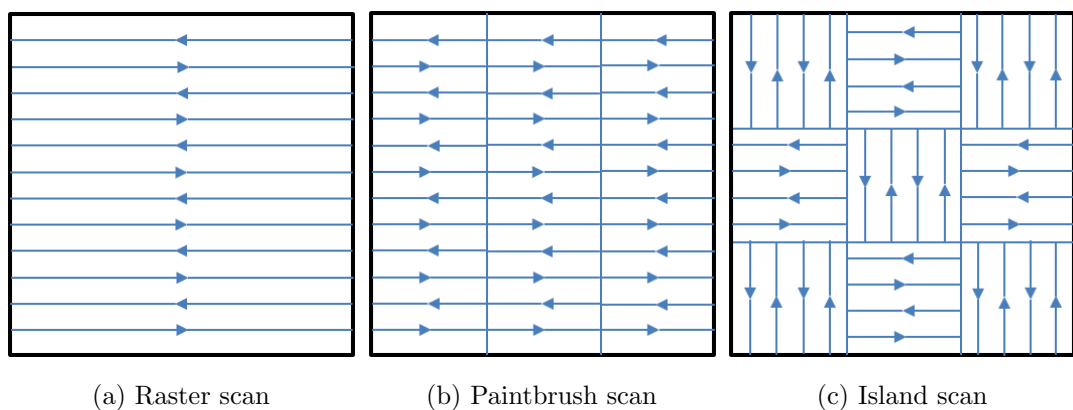


Figure 5.59: Scanning strategies

The simple raster scan (figure 5.59a) is easy to implement. However, thermal gradients on the surface of the part make this strategy undesirable. An option to reduce the

thermal gradient is to increase the scanning speed, and make multiple passes with the energy source, until the part is fully consolidated.

The paintbrush scan (figure 5.59b) segments the raster scan up into smaller areas. Doing this reduces the thermal gradient when compared to the raster scan, as mentioned. The island scan (figure 5.59c) further segments the surface (into “islands”). The segments are scanned at different orientations to one another to homogenise the temperature values. There is no specific order in which to deposit each island; indeed, research has shown that randomising the deposition order decreases the thermal gradient of the part^[206].

5.6.2.3.3 Conclusion In reality, the scanning strategy will not be able to produce a perfectly smooth transition from one material to the other, as depicted by $F(x)$ in figure 5.58. The aim is to have a scanning strategy which can follow that transition as closely as possible. This is also related to the material mixing (section 5.6.1) and processing parameters (section 5.6.2.2). Within each SUMC layer, the scanning strategy that will be chosen is dependent on the geometry - although certain strategies produce better results than others under testing, they are only possibilities if they can fit. As such, the main decider for the scanning strategy within the SUMCs should be the geometry of the part.

5.6.2.4 Thermal impact of AM hardware

The thermal gradient within the part is also affected by the AM hardware used. Technology which uses an electron beam creates lower thermal gradients, as the print bed can be preheated in the vacuum to a much higher temperature compared to that which uses a laser. Again, this may be a moot point as the realistic availability of AM hardware could be the deciding factor.

5.6.2.5 Grain Size

Grains of material should be as small as possible to increase the theoretical density of the part. As part density increases, so does UTS, another benefit of smaller grain size. The grain size also minimises the staircase effect, the phenomenon seen in Section 2.5.2.4. However, there is a practical limitation to the grain size – once too small, cohesive forces impede grain flow. Grains cluster as they do not have enough mass to transport across the surface, and surface finish decreases.

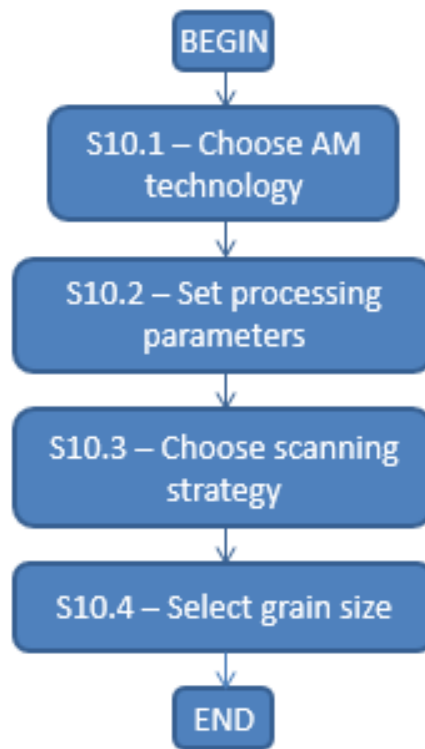


Figure 5.60: Selecting the grain size

5.6.2.6 Support Structures

Support structures are required when overhangs in parts are created during manufacture. Several studies have concluded that the critical angle for support structures is around 45° . Above this angle, support structures are required^[151;207;208]. Since the deposition direction is always perpendicular to the FGM extremity distance, there will be situations when the part is being created at an angle which will require external support structures. This is also the case with internal features - at times, support structures will be required. It is hoped that the user of the design guidelines will be able to incorporate work from^[209]. This work has created an algorithm to ensure that internal structures of a part require no support structures, as it forbids any features being placed at angles greater than 45° . This work is currently **not** incorporated into the design guidelines, however.

5.6.2.7 File Format

If possible, the part should be saved in the X3D format, to aid model slicing when the part is created using the AM hardware. However, many AM hardware manufacturers and FE software developers still use the STL file format, and as such, it may need to be used.

5.6.3 STEP 12 - MANUFACTURING: POST-PROCESSING

Post processing occurs after the AM deposition stage. It is required for three main reasons, each important for ensuring the part functions as expected:

1. Remove support structures that were required during part building.
2. Further consolidate part (increase the relative density of the part)
3. Improve the surface finish

5.6.3.1 Removing support structures

Depending on the technology used and the angle of inclination during deposition, support structures will need to be removed. Removal processes depend on the geometry of the arm link and/or the materials used for support. For example, some polymer supports are soluble in solutions that the primary materials are inert towards. Others will first require mechanical removal before the surface can be improved. Loose powder from the deposition may also remain, and also needs to be removed. Systems that both rotate and vibrate the part, collecting any loose powder for future use are common.

5.6.3.2 Further consolidating the part

Post processing consolidation can be done using isostatic pressing. Pressure (up to 200 MPa) and heat (up to 2000°C) on the part increases the relative density by eliminating pores and removing defects in the part. This in turn improves the material and mechanical properties. Although the process is isotropic, care must be taken not to damage complex features of parts, such as would be seen on the arm link.

5.6.3.2.1 Conclusion Although many AM processes now produce parts with density $\geq 99\%$, consolidation is often recommended, as any non-dense areas could be at critical (structural) locations in the part which could lead to unexpected failure of the lightweight robotic arm link.

5.6.3.3 Improving the surface finish

5.6.3.3.1 Isostatic pressing Surface finish can be improved using numerous methods, the most basic being sanding and polishing. Chemical treatments can be used for certain materials (polymers), but care must be taken that they do not weaken the arm link. Isostatic pressing, at a lower pressure than that used for increasing the density, is also used to improve surface finish.

5.6.3.3.2 Tumbling Tumbling is an established method for improving surface finish. The most common technique is to tumble the part at a low speed for a long time in a bath of small abrasive particles. Other techniques use lubricants (including water) instead of, or in addition to, the abrasive particles.

5.6.3.3.3 Blasting Blasting uses a pressurised fluid (dry or wet) to fire abrasive particles onto the part. Depending on the material of the part, the type of fluid and abrasive particle will be altered.

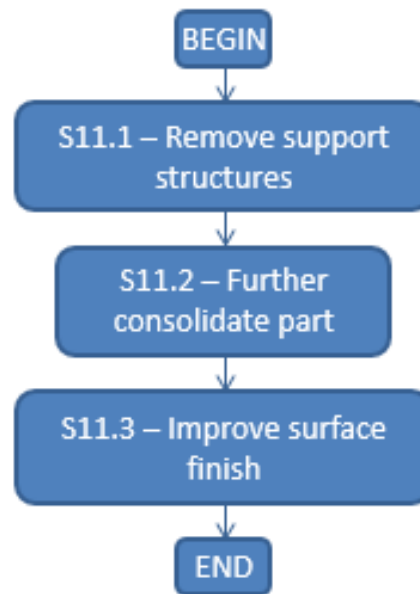


Figure 5.61: Improving the surface finish

5.6.3.3.4 Conclusion The three techniques for improving the surface finish have all been used on additively manufactured parts. Isostatic pressing is recommended for the work in this thesis, as it is the only technique of the three which can give effective results on areas that can not be easily seen/accessed - both tumbling and blasting require unhindered view and easy access of the part features.

5.7 Diagram of complete design guidelines

Linking all four areas of the design guidelines into a flowchart gives the design seen in figure 5.62. As seen, there is no feedback between steps, as each step must be completed before the subsequent can begin. Feedback is modelled within many of the steps.



Figure 5.62: Diagram of complete design guidelines

Enhancing this diagram to include the inputs and outputs of each step gives figure 5.63

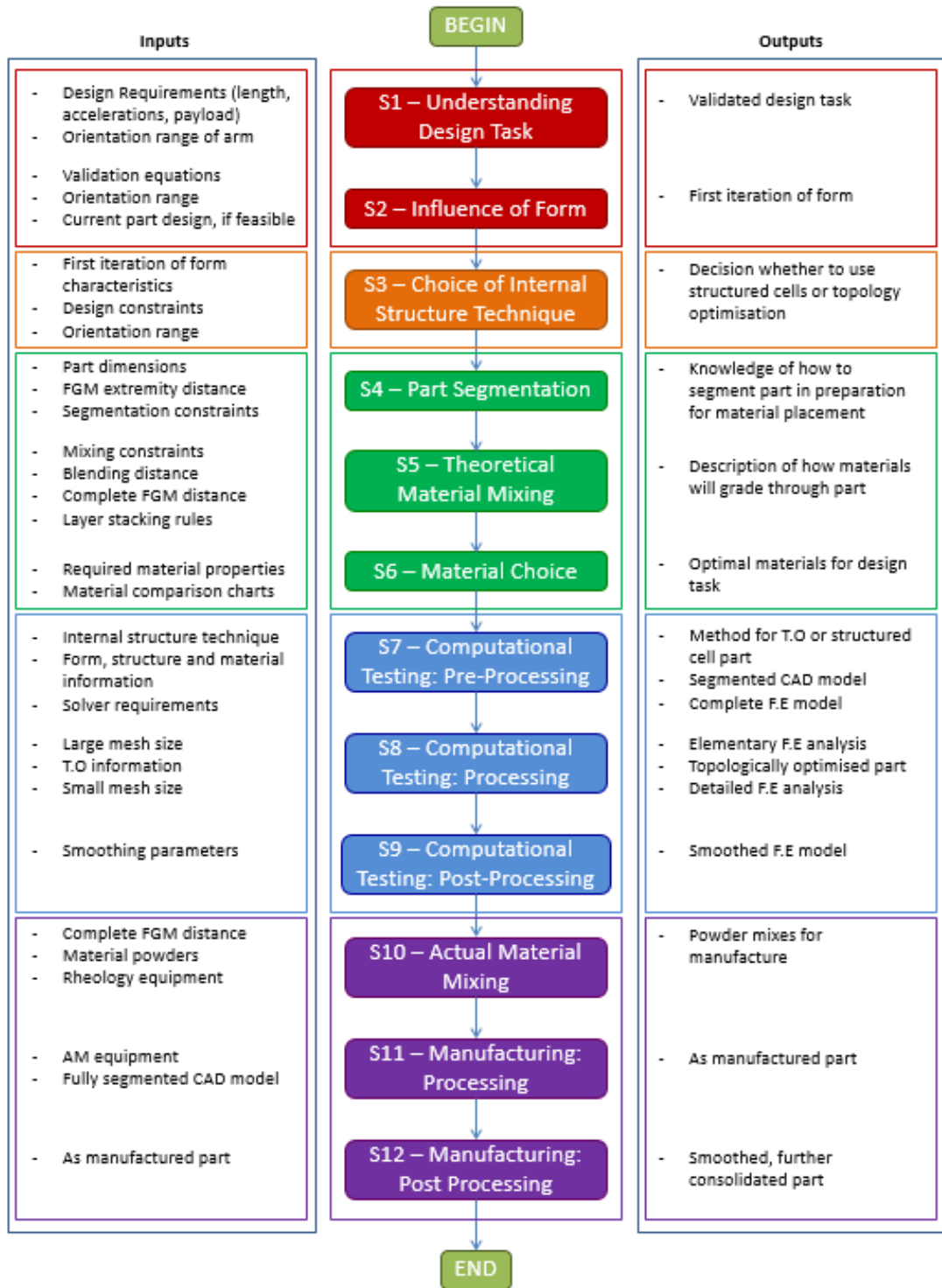


Figure 5.63: Diagram of complete design guidelines, including inputs and outputs

5.7.1 Conclusion

All four focus areas of the design guidelines have been addressed. Using the guidelines, it is postulated that the researcher will be able to design a lightweight part. Validation

of the guidelines must be done in order to ensure the information contained within is viable. Rather than testing the entire design guidelines, to begin with, only the most important steps will be evaluated. The first test case will evaluate the computational testing steps (steps 7 and 8). These steps use many aspects of the of earlier steps (from step 3 to step 6), however, the test itself will only use steps 7 and 8.

Chapter 6

Test case 2 - verification of Computational testing segments of design guidelines

The design guidelines were introduced in section 5. The computational testing steps contain many of the untested concepts in the guidelines. For this reason, it was decided that this section should first be tested independently. A test case was needed in order to do this. The researcher is affiliated with the AFRC, and therefore a test case was chosen from there due to practicality reasons. At first, the researcher wanted to test a robotic arm link, as this is what the design guidelines had been written for. However, as the eventual aim was to make a physical part and experimentally test it, the decision was made to test a fixture of a robotic arm instead, as it was deemed too much of a risk by the owners of the robotic arm to disassemble it and fit an after market part. Due to this, the test case chosen was one of a pair of identical grippers used at the end of a robotic arm which picks and places components into and out of a forging cell at 950 °C.

As already said, the aim of this test case is to run the computational stage of the design guidelines. Even though the guidelines will make this pair of grippers lighter, it should be noted that, in reality, the function of this robot will not benefit to any significant degree from having a lighter pair of grippers.

The high temperature that these grippers work at will be both a benefit and a challenge for the guidelines. On the one hand, it will mean that FGMs will be very viable, as a material with a high melt temperature can be used at the contact surface, and a material with a lower melt temperature can be used at the point the gripper connects to the arm. However, the challenge will be to find two AM-ready materials which can be used in production, one which has a melt temperature above 950 °C. Of further significance for this gripper is that it will be ideal for physical testing, as a direct comparison of both the original part and the part resulting from these tests can be done.

The test case will test the computational testing: pre-processor stage (step 7), the computational testing: processor stage (step 8) and the computational testing: post-processor stage (step 9).

6.1 COMPUTATIONAL TESTING: PRE-PROCESSOR

The aim of the section is to evaluate the **pre-processor** computational testing segments of the guidelines. A copy of “Step 7 - Computational Testing: Pre-Processor” is shown in Figure 6.1. However, since this is steps 7, 8 and 9, there are additional steps which are required before and during computational testing. They are as follows:

1. Model definition - a model of the robotic arm gripper is needed before any of step 7 can be done.
2. Choosing internal structure technique - this choice is made during “step 3: choice of internal structure technique”, and merely implemented during the computational pre-processor stage. This decision must be made once the form of the robotic arm gripper is seen.
3. Part segmentation - the part segmentation process (S7.3) is done on the computer in the pre-processor, hence why “segment part” is in Figure 6.1. However, the process itself is used for creating FGMs, and therefore described in detail during “step 4: part segmentation” found in the material stage of the design guidelines.
4. Theoretical material mixing - the thickness of each segment must be calculated before materials can be applied. This is described in detail in “step 5: theoretical material mixing”, also located in the material stage of the design guidelines.

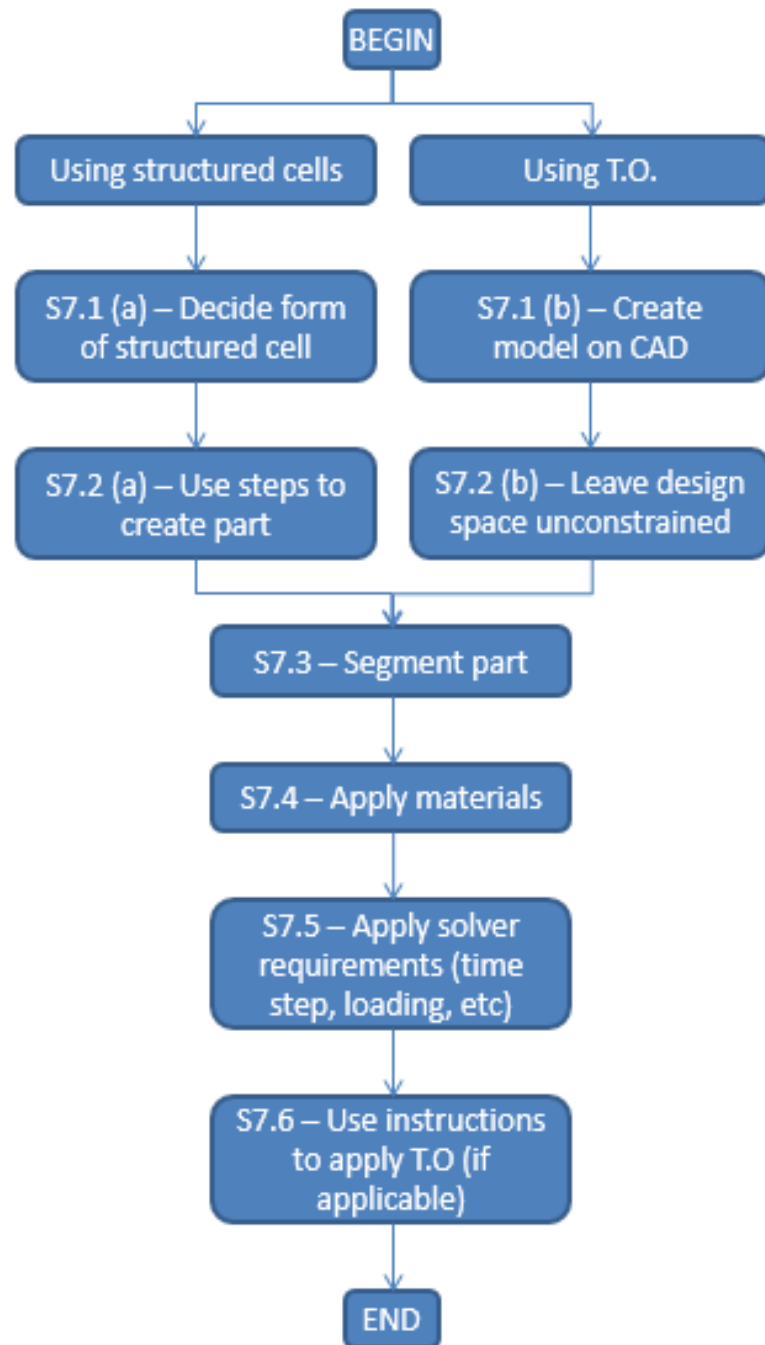


Figure 6.1: Computational testing: pre-processor guidelines

6.1.1 Model Definition

The first step of the design guidelines is to create the model, in this case a model of the gripper. The gripper was supplied to the researcher as seen in Figure 6.2.



Figure 6.2: Gripper, as taken from hot forging cell robot arm

No 3D model of the part could be obtained, so it was decided to 3D scan the part. An ATOS 3D GOM scanner was used for this, which produces a point cloud of surfaces measurements. In preparation for scanning, the part had to be coated in a titanium oxide spray to dull the surface, and a series of stickers. The stickers are a precisely chosen diameter, and are used as reference points for the scanning cameras. The as-scanned gripper is shown in Figure 6.3.

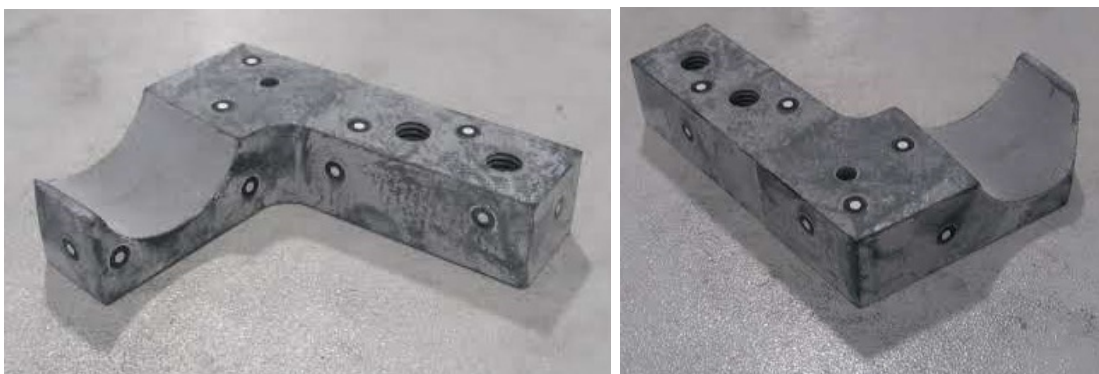


Figure 6.3: Gripper, prepared for ATOS GOM scan

The analysis software measured many parameters. The scan itself is shown in Figure 6.4. The researcher was advised by the original designer that all radii and surfaces were originally smooth. Any deviation from smooth surfaces was therefore deemed a result of the gripper going into and out of the furnace at 950 °C. Important radii are shown in Figure 6.5 - the fact the fitted green cylinders do not fit perfectly onto the curved faces shows that they must not be completely smooth. The flatness of the bottom surface and top surface are shown in figures 6.6 and 6.7, respectively. The key dimensions are shown on the CAD model of the part in Figure 6.8.

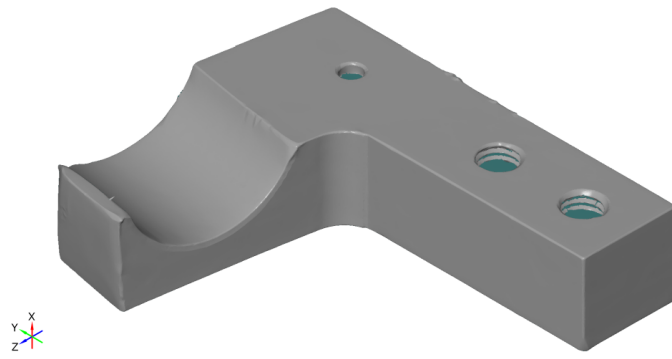


Figure 6.4: The scanned part

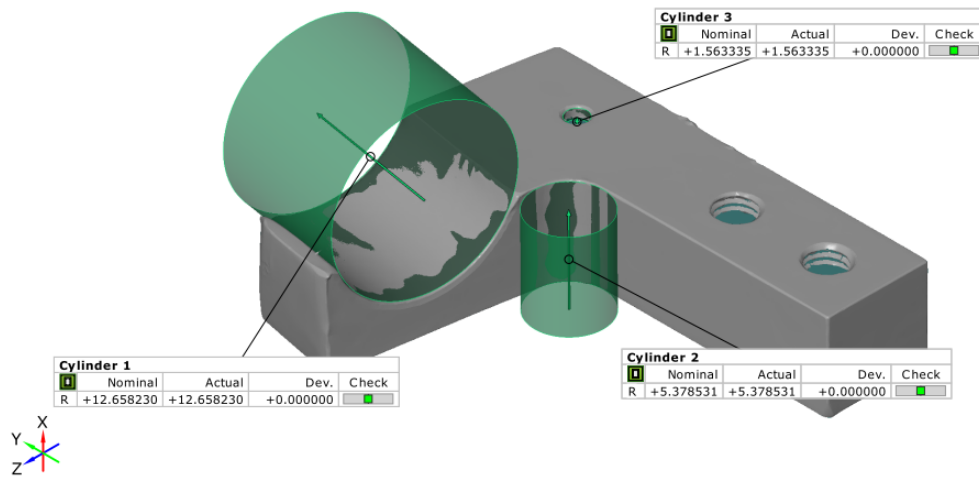


Figure 6.5: Finding radii of gripper features

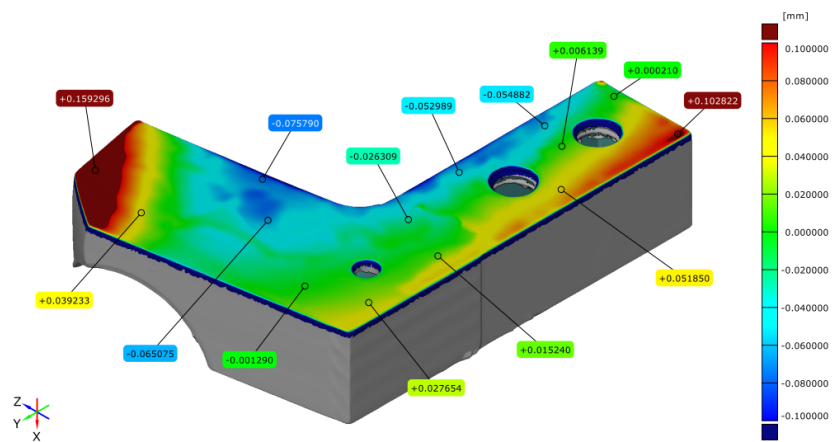


Figure 6.6: Deviation of the bottom face from a fitted plane

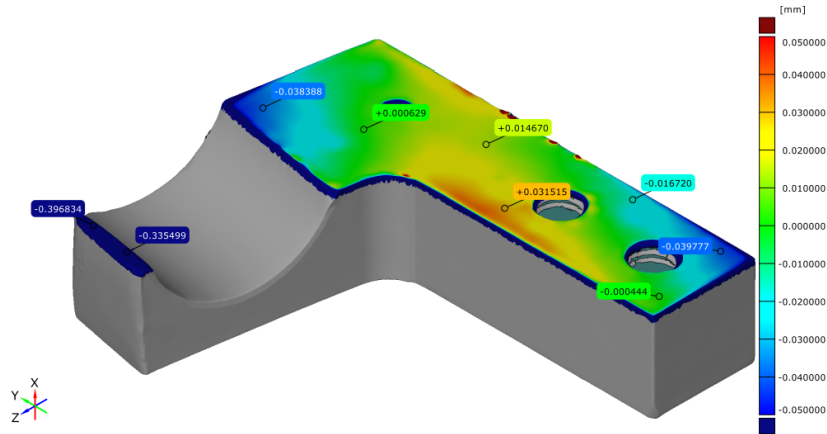


Figure 6.7: Deviation of the top face from a fitted plane

The scan output is a surface mesh. In order to undertake the steps in the design guidelines, a solid model is needed. To convert the surface .stl mesh into a solid, the Abaqus to “Create geometry from mesh” plug-in, created by Simulia Benelux, is used. Upon discussion with the operatives of the robotic arm which the gripper belongs to, it was learnt that a corner of the gripper had been removed for a different project. A third hole (not a fixing point) had also been made for the same project. These had to be corrected on the model if the gripper was to be used on the hot forging robotic arm. Once the surfaces damaged due to heat were flattened, the corner re-built, and the hole filled, the model had become that seen in Figure 6.8.

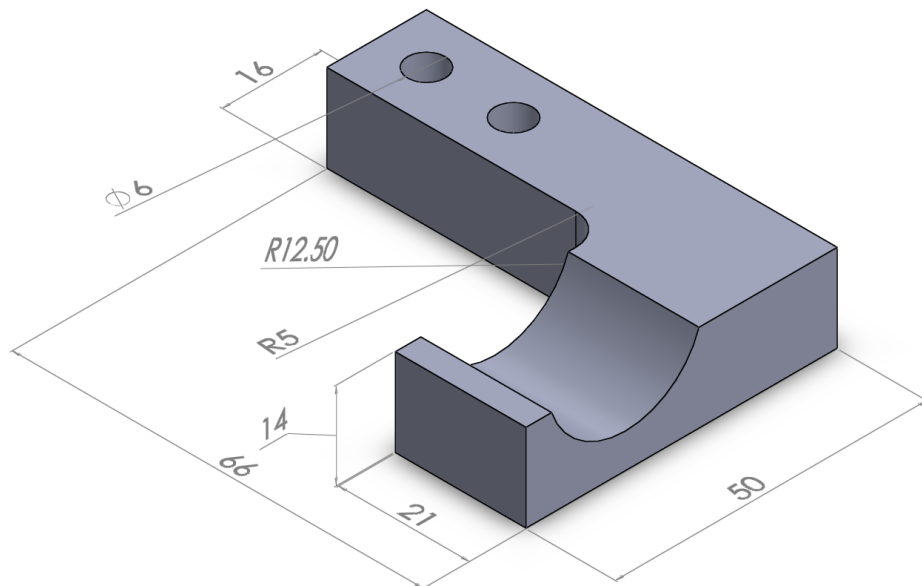


Figure 6.8: Isometric view of the gripper used in validation tests

6.1.2 Structured cells vs TO

The decision whether structured cells vs TO will be used is based on a decision made during “step 3: choice of internal structure technique” in the structure stage of the design guidelines.

The next stage of the guidelines requires steps 4 and 5 from the “material” design guidelines - rules for part segmentation, and theoretical material mixing. When the design guidelines are being used in their entirety, these steps will be done in sequence. However, as this test case is only running steps 7, 8 and 9 of the guidelines, steps 4 and 5 must be recalled.

6.1.3 Part Segmentation (from STEP 4: PART SEGMENTATION)

Segmenting the model requires the process described in step 4: part segmentation. A copy of this step is shown in Figure 6.9.

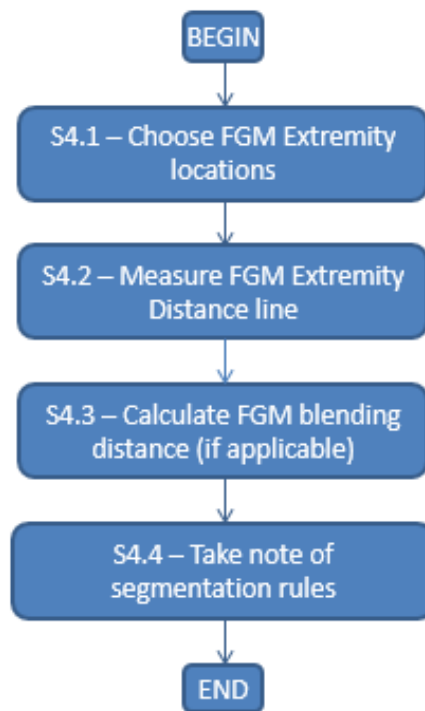


Figure 6.9: Process from Step 4: Part Segmentation

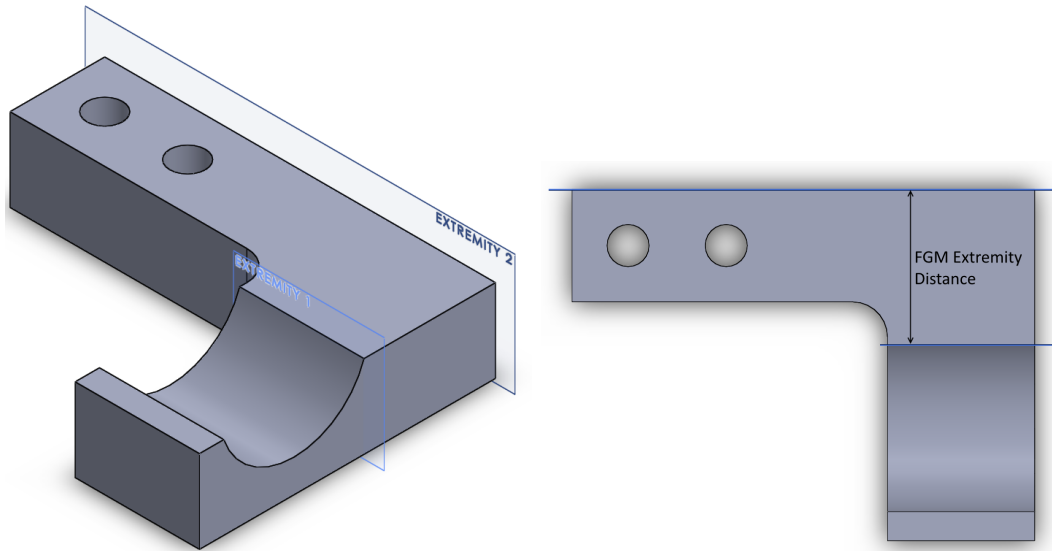
6.1.3.1 Choose FGM Extremity locations

As discussed in the guidelines, the placement of the extremities depends on the function of the part being made. In this case, the gripper picks up a part from a hot forge. The hemispherical face is the one which contacts the hot part. Therefore, one FGM extremity should be next to that face. The other extremity will be the face parallel to

the first extremity. Figure 6.10a shows where the FGM extremities are.

6.1.3.2 Measure FGM Extremity Distance line

The FGM extremity distance line must be plotted. Its distance dictates how many FGM layers there will be. The line is seen in Figure 6.10b.



(a) Highlighting the FGM extremity planes (b) Plotting FGM Extremity Distance Line

Figure 6.10: Identifying the FGM extremity locations

As the two FGM extremities are parallel to one another, there is no need to plot the FGM blending distance, as it is the same as the FGM extremity distance in this case.

6.1.3.3 Calculate FGM blending distance

In this case, the length of the blending distance line is 22.2 mm. Assuming the part is to be physically manufactured, the next stage is to identify the hardware that will be used.

6.1.3.4 Take note of segmentation rules

The segmentation rules must be checked at this stage to keep in mind what is segmentation is possible and to understand how the segmenting will look. This knowledge is needed to work out the thickness of each SUMC (segment of unique material composition).

Taken from Section 5.4.2.3.4, the two segmentation rules are as follows:

1. **Segmentation orientation 1 perpendicular to “FGM extremity distance” line**

2. Segmentation orientation 2 following the longest contour on the part which is not an FGM extremity contour

Looking at Figure 6.10b, the first segmentation rule will place many slices in parallel with the two extremities, and in parallel with them. The second segmentation rule will make segmentation lines perpendicular to the first rule. In this instance blending will not occur in both directions as this test case aims to assess the computational testing guidelines, and one direction will be sufficient for this.

This concludes step 4. The next action is to implement step 5 - theoretical material mixing.

6.1.4 Theoretical material mixing (from STEP 5: THEORETICAL MATERIAL MIXING)

The theoretical material mixing step is used to calculate the thickness of each SUMC, using geometry-dependent calculations. A copy of step 5: theoretical material mixing is shown in Figure 6.11.

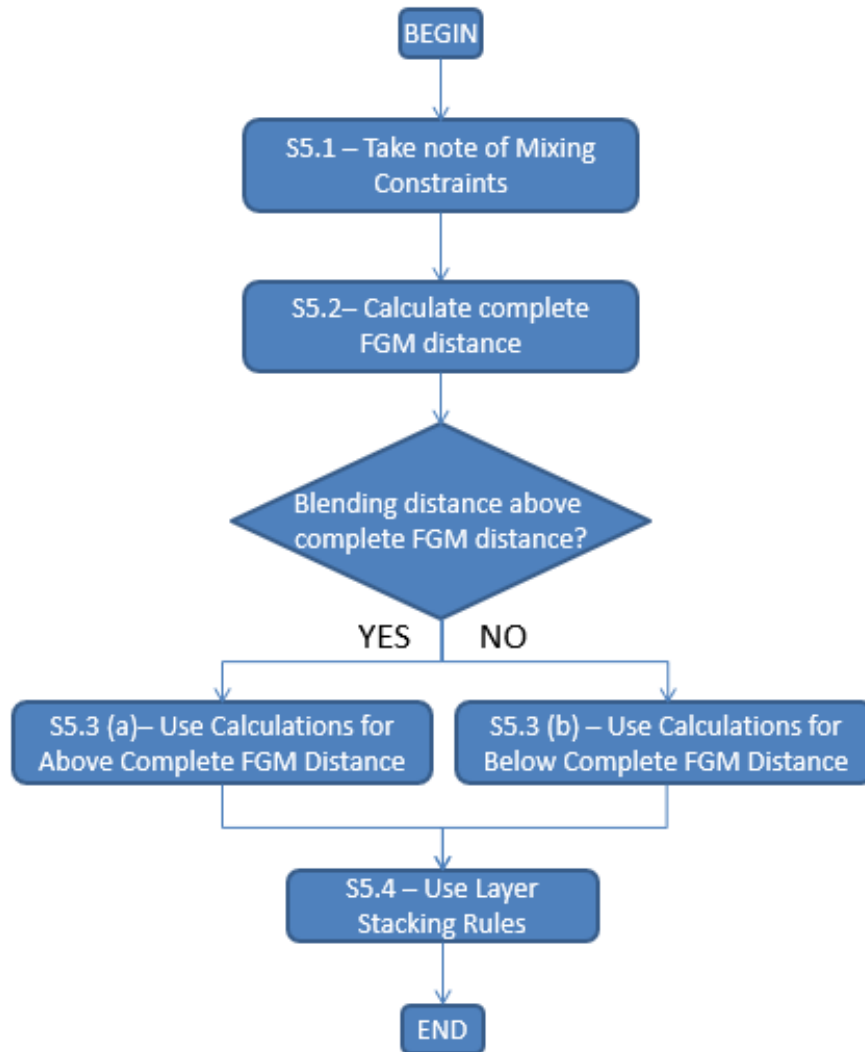


Figure 6.11: Process from step 5: theoretical material mixing

6.1.4.1 Noting mixing constraints

The hardware used to produce the part will dictate the number of SUMC layers due to its minimum resolution. Either LENS or EBM will be used to manufacture the part, as it will need to be metallic in order to work in the elevated temperature of the forge.

6.1.4.2 Calculate the complete FGM distance

The complete FGM distance is the minimum distance required to gradate from 100% material A to 100% material B at 0.5% increments, with each increment having 3 layers of material at the minimum resolution of the AM hardware.

In this case, the complete FGM distance is therefore:

$$\frac{100 \times (0.1 \times 3)}{0.5} = 60 \text{ mm}$$

Since the blending distance is below the complete FGM distance, the calculations for below the complete FGM distance must be used.

6.1.4.3 Calculations for below complete FGM distance

Finding number of SUMC alterations:

$$\frac{22.2}{0.1 \times 3} = 74 \text{ SUMC alterations}$$

Finding interpolation limits:

$$\frac{100}{74} = 1.35\% \text{ increase per subsequent SUMC layer}$$

Interpolate between limits:

Interpolate 1.35% between 1.0% and 1.5% (closest values within 0.5%).

$$1.35 - 1.0 = 0.35$$

Finding SUMC Percentages:

$$\frac{0.35}{0.5} = 0.7 \Rightarrow 70\% \text{ of blend should use 1.5\% segment.}$$

Finding Split of SUMCs:

$$74 \times 0.7 = 52 \text{ SUMC alterations.}$$

52 SUMC alterations should be at 1.5%.

$$74 - 52 = 22 \text{ SUMC alterations.}$$

The remaining 22 SUMC alterations should be at 1%.

6.1.4.4 Use layer stacking rules

Since the FGM blending distance is below the complete FGM distance, all layers are the same thickness, but not all layers have the same percentage change of materials

across them. In this case, there are 74 SUMCs - 52 at 1.5% and 22 at 1%. The layer stacking rules dictate that there should therefore be 11 1% SUMCs, followed by the 52 1.5% SUMCs, and finished with the remaining 11 1% SUMCs.

The part can now be segmented using the segmentation rules as guidance. In this test, only the first rule will be used. This means the material will only blend in one direction - along the FGM blending distance line.

Figure 6.12 shows the gripper once segmented into 74 SUMCs.

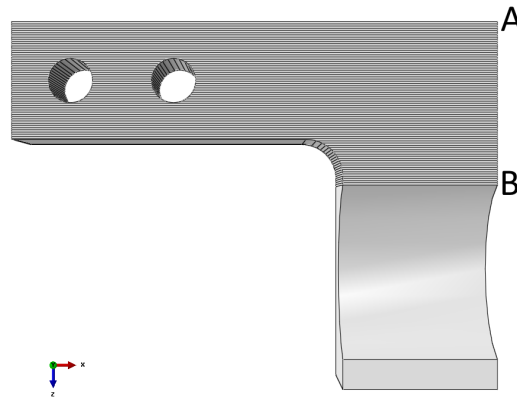


Figure 6.12: The gripper once segmented

Now that the part has been segmented, the next step of the computational testing guidelines can proceed - applying materials.

6.1.5 Apply materials

The gripper does not satisfy the requirements for structured cells laid out in section 5.3.3.5, therefore topology optimisation will be used to reduce the mass. The design space must therefore be left as unconstrained as possible. The only constraints that shall be put in place are frozen area constraints to ensure the gripper retains the contact surface and the fixture holes.

This test case is a purely theoretical demonstration of the computational stage of the design guidelines; it is not evaluating the material choice step of the design guidelines - this will be done in the latter stages of the thesis. As such, materials will be chosen based solely on their melt temperature characteristics (due to the information that the gripper works in a hot environment), and nothing else. Stainless steel 316L and Ti-6Al-4V will be used due to their high melt temperatures.

The titanium will be used on the contact surface area and begin blending from 100% at point B. The stainless steel will begin blending from 100% at point A.

As found in the preliminary test (section 4), the material with the lower Young's modulus should always be placed further from the fixing points to reduce deflection in the

part. Therefore, the Ti-6Al-4V will be used on the contact surface area and begin blending from 100% at point B; further from the fixing points. The stainless steel will begin blending from 100% at point A; closer to the fixing points.

6.1.6 Apply solver requirements

A section is needed for each SUMC layer. As there are 74 SUMC layers, there need to be 74 sections. The contact surface area will be included in the same section as the first SUMC layer at point B (100% titanium).

6.1.6.1 Interaction/Constraint Definition

This solver requires no interactions, however it does require a constraint. The constraint couples the centre of the fixing holes to the internal surface of each hole.

6.1.6.2 Boundary conditions Definition

The two fixing holes need bound. They will be “pinned”, eliminating translations, but allowing rotations.

6.1.6.3 Load Definition

There are two loads required in this part:

1. A moment around the fixing holes caused by the mass of the part being moved, calculated using $M = F \times r$. Both F, the force exerted, and r, the length of the moment arm, are needed. The r value is measured from the centre of the contact face of the gripper, to the centre of the closer fixing hole.

Calculating F:

- Force due to gravity is given by $F = m \times a$, where $a = 9.80665 \text{ m/s}^2$.
- Including a factor of safety, the mass of the part is taken as 1 kg.
- $\Rightarrow F = 1 \times 9.80665 = 9.80665 \text{ N}$

Calculating r:

- Using Pythagorean theory, $r^2 = X^2 + Z^2$
- $\Rightarrow r = \sqrt{33.5^2 + 26^2} = 42.2\text{mm} = 0.0424 \text{ m}$

The moment about the Y axis of the fixing hole caused by the mass of the part being moved is therefore: $M = F \times r = 9.80665 \times 0.0424 = 0.416 \text{ N/m}$.

2. The pressure force on the contact face needed to arrest the part being moved, calculated using $P = F/A$. Both F, the force due to friction arresting the part, and A, the area of the contact face, are needed. Calculating F:

- Friction force is given by $F_F = \mu_s \times F_N$.
- Both the part being moved and the contact face are made from titanium. The coefficient of friction, μ_s between two titanium faces is 0.35.
- The normal force, F_N is equal to the gravity force, calculated previously as 9.80665 N.
- $\Rightarrow F_F = 0.35 \times 9.80665 = 3.43$ N

Calculating A:

- The area of the contact face is $654 \text{ mm}^2 = 0.000654 \text{ m}^2$

The pressure force on the contact face needed to arrest the part being moved is therefore: $P = F/A = 3.43/2 \times 0.000634 = 2622$ Pa. A factor of safety was included in the original mass of the part the gripper is moving, therefore one will not be added here.

6.1.6.4 Mesh Definition

If possible, the part should be meshed with as many quadrilateral elements as possible, due to the larger number of calculation points within each when compared to a tetrahedral element. The part is sectioned into smaller volumes in order to achieve this.

6.1.7 Use instructions to apply topology optimisation

The last step of the computational testing: pre-processor guidelines in Figure 6.1 is to apply T.O, if applicable. T.O. will be used to reduce the mass of the part. The steps in section 5.5.2.10.1 will be followed.

6.1.7.1 Creating the optimisation task

It was decided at this stage to:

- Freeze both the load and boundary condition regions, as the load region contains the contact face which needs to remain intact, and the boundary condition regions contain the fixing holes, which are needed to hold the gripper in the robotic arm.
- Use the SIMP solver technique, as the pressure load seen in this problem will not deform the load or boundary condition regions.

6.1.7.2 Setting the design responses

The following choices were made at this stage:

- Two design responses were set - strain energy and volume
- The focus region for both design responses was set as the entire volume of the model
- The design responses both used the global coordinates of the model
- Both design responses were set to be active during the entire optimisation routine, as there is only one additional step to the initial one in the model.

6.1.7.3 Setting the objective function

The objective function is chosen to be the strain energy. It's target is to minimise the design response value. As there is only one objective function, weighting of the objective functions is not required.

6.1.7.4 Setting constraints

The sole constraint set is a minimum value on the volume of the part which must remain once testing is complete. Generally, several optimisation tests are run, each one setting the constraint to a different value. The trade off between part displacement and mass will be measured for each test, and a choice of which volume percentage to use will be made. Three values are tested:

1. 15% volume remaining
2. 22.5% volume remaining
3. 30% volume remaining
4. 37.5% volume remaining
5. 45% volume remaining

These five values will hopefully show a range of responses from the part. If all five volume fractions return deflections which are unacceptably large, the percentages can be altered. The lowest percentage is expected to fail (deform too much) and the highest percentage is expected to pass (deform within tolerance). The expectation of the mid percentage tests is difficult to predict.

6.1.7.5 Setting the geometric restrictions

The following geometric restrictions are made:

- The minimum member size must be double the size of the elements. The average element is 0.45 mm, therefore the minimum member size is set to 0.9 mm.
- No additional frozen areas are needed, as they are constrained in the load and boundary condition freezing during optimisation task creation.
- There is no symmetry in the part, hence the solver can not be simplified.

6.1.8 Conclusion

Testing of the computational pre-processing step has successfully set up the gripper in preparation for running the computational tests. It successfully chose which structural technique to use based on the number of degrees of rotational symmetry, set the various FGM distances and segmented the part, and led the designer through the necessary steps to Abaqus FE set up steps. One note of the guidelines is that they are not basic enough - the designer still needs background knowledge of Abaqus in order to complete the computational pre-processor stage. The researcher had chosen the current depth of description in order to indicate what should be done, but still leave the designer with scope to choose specific settings. Future work may include an in-depth lead-through of the Abaqus FE software in the context of these guidelines, in order to aid those unfamiliar with the software.

6.2 COMPUTATIONAL TESTING: PROCESSOR

The aim of this section is to evaluate the **processor** computational testing segments of the guidelines. This leads off from the pre-processing stages in section 6.1. A copy of the steps in the processing stage are shown in Figure 6.13.

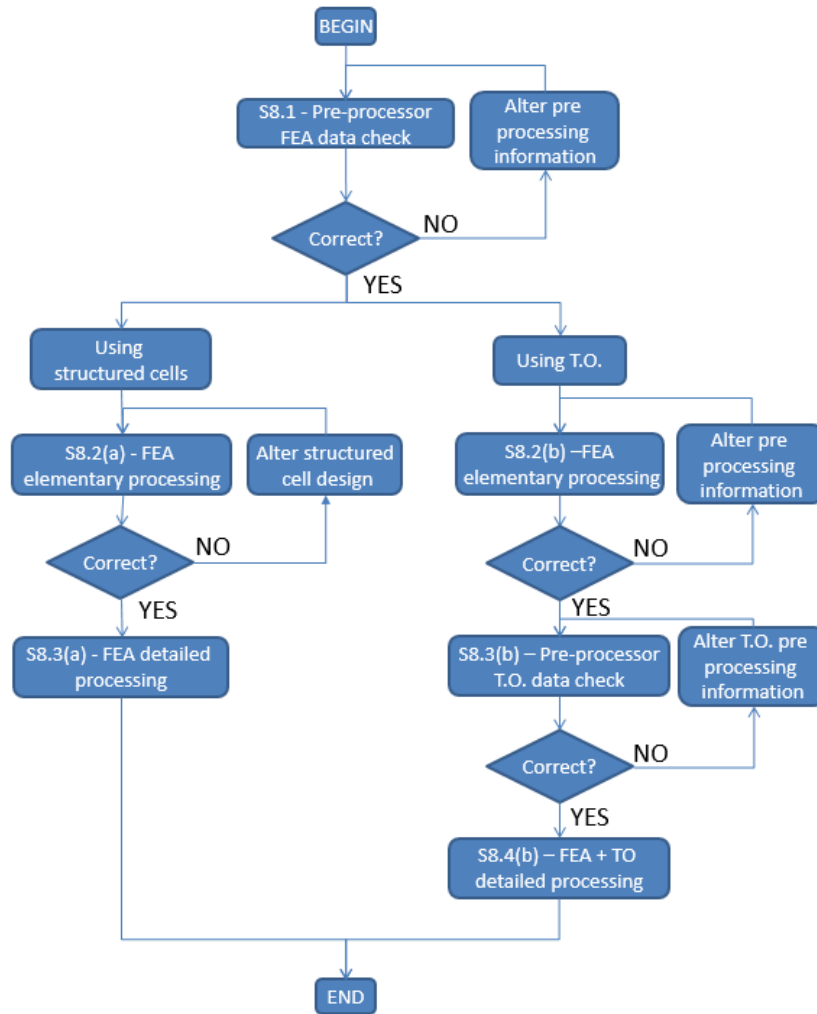


Figure 6.13: Computational testing: processor stage

6.2.1 Pre-processor FEA data check

A data check of the FEA pre-processor allows any errors to be found. There were no issues with inputs to the pre-processor on this model, and thus it passed.

6.2.2 FEA elementary processing

The pre-processor data check is done on a coarse mesh of the gripper, as seen in Figure 6.14a.

This gives an approximation to the performance of the part. If any values are not expected, the pre-processor can be altered. In this case, the deformation is of interest. The values and locations of deformations are seen in Figure 6.14b.

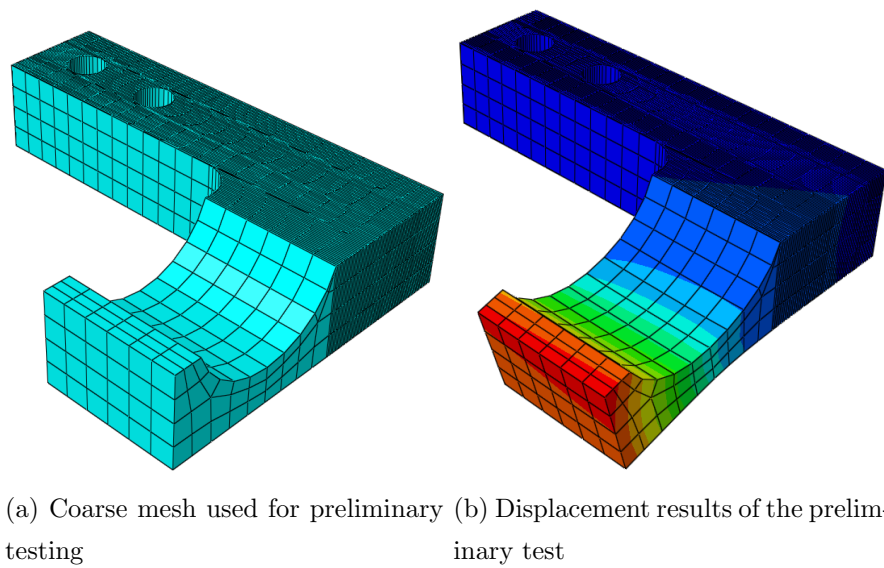


Figure 6.14: Preliminary testing of the gripper

The deformation value is about 0.12 mm in the base of the contact surface. This is as expected, and within realistic tolerances. Ti-6Al-4V is less dense than the original H13 steel, and thus greater deformations are expected when compared to the original part. T.O is being used, so the next step is to do a pre-processor T.O check.

6.2.3 Pre-processor T.O data check

The T.O data check returned successful. The final step of the processor stage is to run the detailed FEA test with TO.

6.2.4 FEA and TO detailed processing

This is largely similar to the FEA preliminary processing. The mesh is reduced in size, T.O is applied. The mesh used is shown in Figure 6.15.

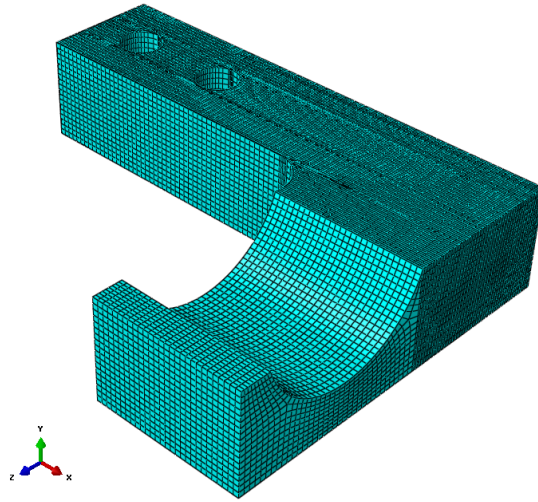


Figure 6.15: A fine mesh used for the detailed testing

The finer mesh reduces the deformation of the part slightly, from 0.12 mm to 0.116 mm. This is a result of smoother displacement when more elements are present. As mentioned, the topology optimisation will be run at five different volume fractions - 15%, 22.5%, 30%, 37.5% and 45%. Three of the pre-smoothed parts are shown in figures 6.16, 6.17, and 6.18.

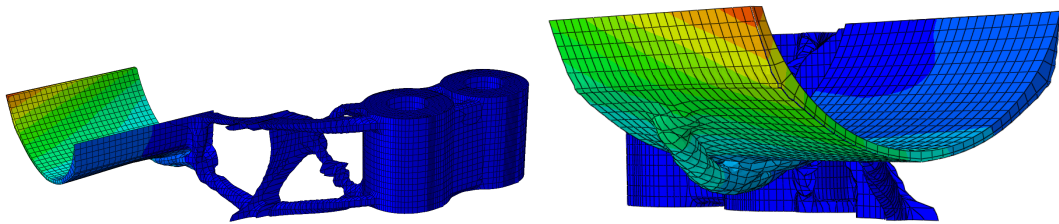


Figure 6.16: The gripper, at a volume fraction of 15%

The maximum deformation at 15% is 7.94 mm. In the centre of the contact surface (U_{CSC}) it is approximately 5.82 mm. This is above the deflection constraint given to the researcher, and therefore the volume fraction must be increased. The reason for the failure is due to the available remaining volume fraction once the frozen areas are taken into account. The fixing holes need to have enough material around them to allow the holes to be tapped, and the contact surface needs to be sufficiently stiff to hold the component being moved. These two areas combine to 12% of the volume of the entire part, meaning that the TO solver only has the equivalent of 3% of the volume to move around. This is not enough to ensure the gripper is stiff enough to adhere to the deflection constraint.

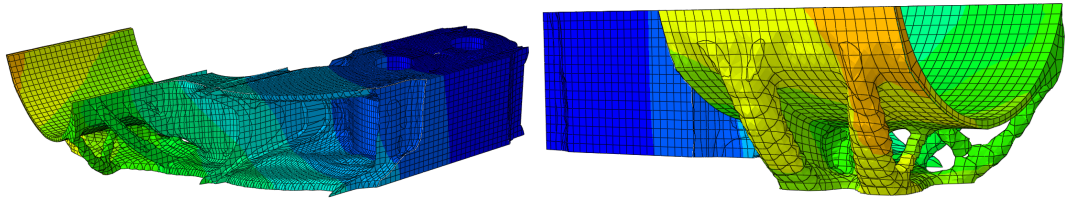


Figure 6.17: The gripper, at a volume fraction of 30%

The deflection at the centre of the gripper's contact surface with 30% of its volume remaining is approximately 0.4 mm. This is still above the tolerance of 0.25 mm given to the researcher, though much closer to the constraint than the model with 15% of its volume remaining.

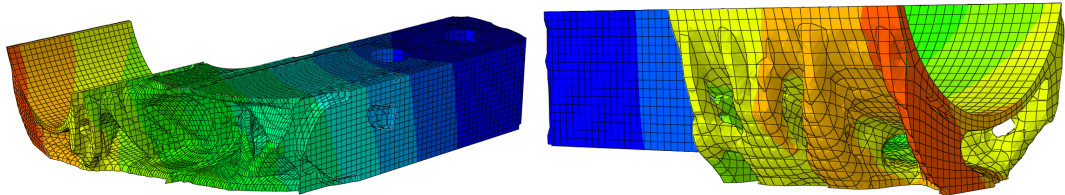


Figure 6.18: The gripper, at a volume fraction of 45%

The deflection of the 45% volume fraction gripper is roughly 0.2 mm at the centre of the contact surface. This is within the 0.25 mm constraint. Though not pictured, the deflection at the centre of the gripper's contact surface with 37.5% of its volume remaining is approximately 0.23 mm. This is within the tolerance of 0.25 mm given to the researcher. However, once smoothing has been done in the post-processor, the gripper could then fail the constraint, as it is currently very close.

6.2.5 Conclusion

The processing step of the computational testing design guidelines is written to ensure that mistakes are caught as early as possible. In this case, all data checks and preliminary tests passed first time with credible results, and therefore no alteration to the model was needed.

6.3 Results

The results will discuss the mass vs displacement performance of the gripper, as this was the main aim of the design guidelines. There will then be a brief discussion regarding the thermal performance of the gripper, given it's task of moving parts in and out of a hot forge.

6.3.1 Mass

The main aim of the design guidelines is to reduce the mass of a part using functionally graded materials and alterations to the form and structure of a part. The results of the mass reduction compared to the displacement using the five volume fractions are shown in Table 6.1. A comparison to the mass vs displacement of a un-altered gripper is also shown in the table.

Table 6.1: Mass vs displacement results from testing the computational section of the design guidelines

Volume Fraction	U_{\max} (mm)	U_{CSC} (mm)	S_{\max} (MPa)
15%	7.94	5.82	4.972
22.5%	2.58	1.27	1.246
30%	1.63	0.43	1.251
37.5%	0.72	0.23	1.235
45%	0.46	0.2	1.234
100%	0.19	0.12	1.221

U_{\max} is the maximum displacement seen on the gripper, always at the tip furthest from the fixing holes. U_{CSC} is the displacement at the centre of the contact surface. S_{\max} is the maximum Von Mises stress in the part. Maximum stress is always seen at the fixing holes, showing that the FGMs are successfully working to reduce stresses at the material interfaces.

As seen, the volume fraction (mass) of the parts drops significantly when compared to the displacement, demonstrated by the graph in Figure 6.19. The use of FGMs and T.O is therefore seen viable to reduce the mass of parts while ensuring the desired materials are located only where necessary.

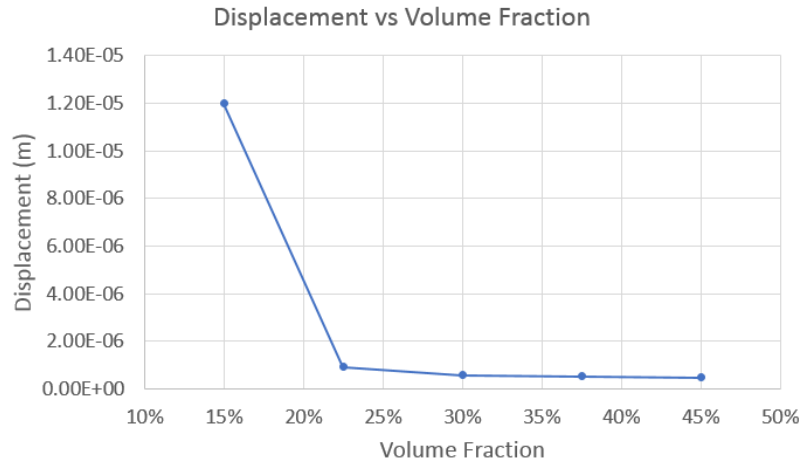


Figure 6.19: The displacement vs volume fraction results, showing a sharp drop in volume fraction compared to displacement

6.3.2 Thermal

This gripper is to be used in a hot environment and transport parts at elevated temperatures. It's thermal properties, especially thermal conductivity, are therefore important. The lower the thermal conductivity of the gripper, the closer the actual temperature of the part being picked up will be to the desired temperature.

The original gripper was constructed from H13 tool steel. As mentioned, this gripper was constructed from a mix of Ti-6Al-4V and stainless steel 316L. The area containing the contact surface of the gripper was constructed from Ti-6Al-4V - the primary reason for this decisions was mechanical (as mentioned in section 6.1.5), and the secondary reason was the lower thermal conductivity of Ti-6Al-4V when compared to stainless steel 316L or H13 tool steel. Thermal conductivity values of the three materials are shown in Table 6.2.

Table 6.2: Thermal conductivities of gripper materials

Material	Thermal Conductivity (W/m.K)
H13 tool steel	28.6
Ti-6Al-4V	6.7
Stainless steel 316L	16.5

As shown, the thermal conductivity of the H13 tool steel is far higher than that of the Ti-6Al-4V or stainless steel 316L. Therefore, the part being moved will cool quicker if

the gripper is made from H13 tool steel than if it is made from a mixture of Ti-6Al-4V/stainless steel 316L. This is undesirable, as the forge temperatures are specifically chosen in order to instil certain mechanical properties in the part. Any alterations to the part temperature will tamper with the desired mechanical properties.

The design guidelines were not written to monitor the temperature of the part when in use. However, the researcher is aware that the temperature during manufacture of the part can have a large impact on the mechanical properties of the part. Inclusion of temperature monitoring during manufacture would be advantageous to the design guidelines.

6.4 COMPUTATIONAL TESTING: POST-PROCESSOR

Computational post-processing should always include validation in order to ensure the outputs are expected. Since this test case uses topology optimisation, part smoothing can also be done to improve the surface roughness of the part.

6.4.1 Part smoothing

Of the five volume fractions tested, the part with 45% of its volume remaining was one of two which passed the displacement constraint, and the only one which passed it comfortably. For this reason, it will be smoothed in preparation for deposition and consequent physical experimentation. Smoothing is done in two cycles - the first reduces the angularity of the topologically-optimised model seen in Figure 6.18. The second smoothing cycle removes any sharp edges and points from the first smoothing cycle. Views of the first cycle are shown in Figure 6.20.

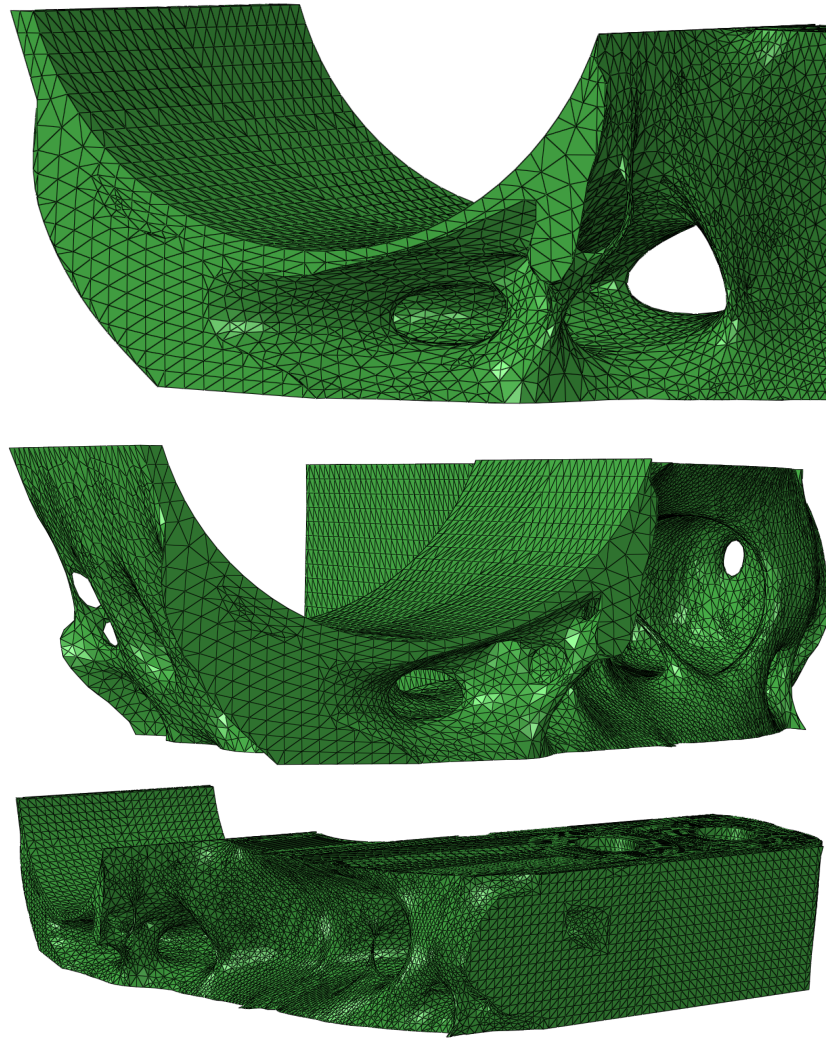


Figure 6.20: The gripper, once smoothed

6.4.2 Validation

To validate the smoothed model, it must be simulated using the same static structural analysis parameters that were used when the part was ran through the topology optimisation algorithm.

Figure 6.21 shows the displacement of the part once the second smoothing cycle has been done. As can be seen, the sharp edges from the model in Figure 6.20 have been removed.

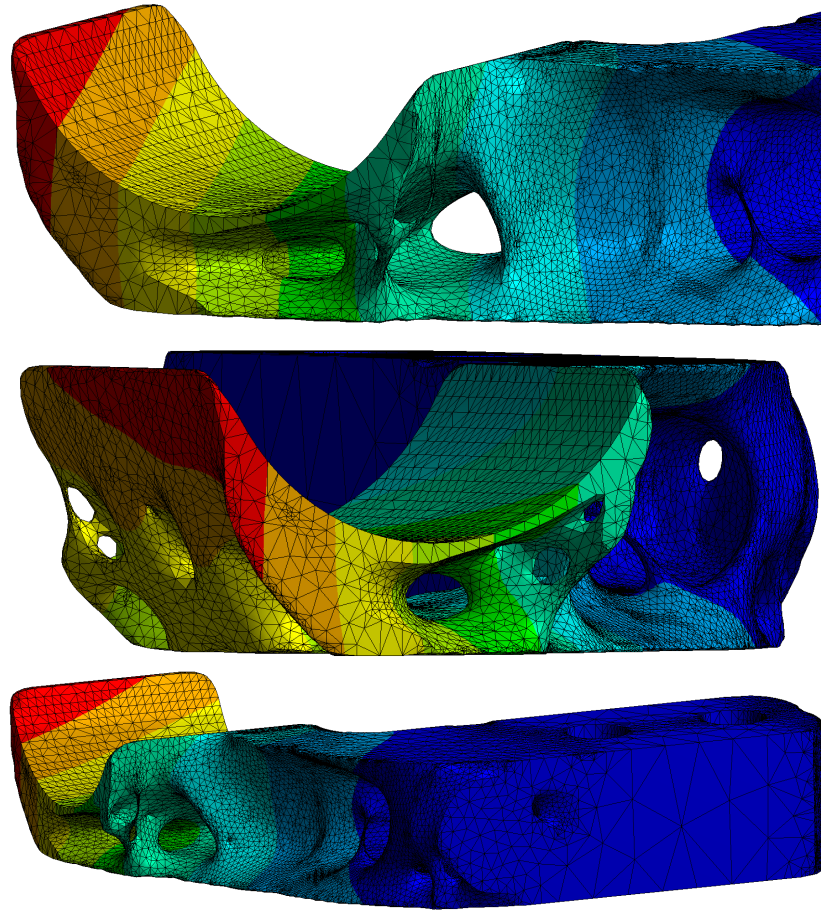


Figure 6.21: The gripper, once smoothed

This smoothed gripper has a volume fraction of 46.2% and a displacement value at the contact surface centre of 0.21 mm. The smoothing has therefore increased the volume (and thus mass) of the part and increased the displacement, a non-ideal result. The displacement is still comfortably within the 0.25 mm constraint set, though. The increase in displacement during smoothing is the reason that the model with a 37.5% volume fraction was not chosen - there is a good chance it would have failed the displacement constraint after smoothing. This volume and displacement increase is a consequence of the iso surface created during smoothing. The smoothing process is not “smart” - it cannot distinguish between elements which are bearing the greatest loads, and which are not. The iso surface will have done a combination of changes to the model:

- elements which are bearing loads could have material removed from them to increase local smoothness.
- elements could have been added to increase local smoothness but not increase the rigidity of the part - instead they increase the compliance because they are “dead weight”.

Despite the increase in compliance, this smoothed, topologically optimised part has passed the validation as it is still within the displacement constraint. The next step would be to physically manufacture the part, however, this will not be done due to financial limitations on the researcher.

6.5 Conclusions

This test case has shown that the guidelines can successfully computationally-test a robotic arm gripper. The shape of the part was not axisymmetric around at least two axes, and therefore the guidelines led the designer to use topology optimisation. The optimised structure reduced the mass significantly, while keeping the displacement within tolerable limits. The materials chosen for the part reduced the thermal conductivity of the part, important for ensuring the temperature change of the item being transported would be minimised. This benefit is an advantage of using FGMs - thermal conductive “channels” can be deposited in parts if required. As noted, the temperature during manufacture of the FGM part would be beneficial to ensure the part would perform as expected. Unfortunately, physical experimentation of this part will no longer occur despite the small dimensions of the part, as previously unknown financial restrictions have rendered the manufacture of the part impossible.

Chapter 7

Heat flow guidelines

7.1 Introduction

In the previous chapter, the computational testing sections of the guidelines were successfully tested. The displacement of the part when compared to its mass showed a marked improvement over the original design. However, the researcher noted in the literature review that the additive manufacturing process itself has a large influence on the residual stress and mechanical properties of the part due to effects including warping and temperature hot spots (section 2.5.2). Therefore, the processes during manufacturing which affect the mechanical properties should be taken into account. The most notable of these is the heat flow. This chapter will lay out and explain the steps required in a code for monitoring heat flow.

7.2 Code

As before, a computer code is needed to implement the heat flow in the design guidelines. The code will be written in Python and implemented on Abaqus. Abaqus is chosen for continuity as it had already been used during the design guidelines. Any researcher wanting to use the guidelines would therefore require only one piece of software, thus limiting investment requirements. Microsoft visual studio will also be used to apply the moving heat source.

7.2.1 Aspects to be modelled

In order to replicate the additive manufacture processes seen in the literature review in section 2.5, the following needs to be modelled, in addition to the part itself:

- The scanning path of the heat source, including speed, and power of energy source;
- The energy source itself;
- The print bed of the additive manufacturing hardware.

7.2.2 Assumptions for model

In order to ensure this chapter does not become extremely complex, assumptions need to be made to bound it. The assumptions made for the heat flow code were:

- Chemical reactivity/incompatibility between materials at elevated temperatures. It is realised that some material combinations may not be stable when combined. The research boundary for “material interaction” has been set at rejecting combinations with dissimilar melting temperatures.
- Thermal conductivity is isotropic. No attempt has been made to investigate thermal conductivity changes that may occur between AM deposition layers
- Thermal resistance is not taken into account. Thermal resistance between the part and print bed is not taken into account. Heat transfer elements are used in all of the model, and the print bed and part are “tied” together.
- Perfect bonding. As previously discussed, the assumption of perfect bonding between multiple materials is valid on the macro scale^[83]. This assumption will remain in place.
- Emissivity values. Similar to the other material properties in this thesis, the emissivity values are also an interpolation of the total hemispherical emissivity values **in air** for the two materials. Where available, values for non-polished surfaces are chosen, as these will more closely represent the surface finish of the AM processes. It is acknowledged that the interpolation of emissivity values is a simplification.

7.2.3 Variables used in simulation

The simulation requires multiple variables in order to predict the heat flow through the parts with accuracy and model all aspects mentioned in section 7.2.1. Since FGMs are a possible option in the design guidelines, the heat flow simulation must be able to incorporate this - something which increases the complexity of the work. The chosen variables are shown in table 7.1.

Table 7.1: Variables required for the heat flow simulation

Variable	Unit
Print base temperature	K
Print base thermal conductivity	W/m.K
Print base heat capacity	J/kg/K
Print base density	Kg/m ³
Print deposit heat transfer coefficient	W/m ² K
Print deposit emissivity	N/A
Print deposit temperature	K
Nozzle velocity	m/s
Ambient temperature	K
Part cool down time	s

7.2.4 Graphical user interface

A graphical user interface has been created. The rationale behind the GUI is two fold:

1. Firstly, it gives an easy to use input for designers who may not be confident working with the lower level code. If wanted, the designer does not have to interact with Abaqus during the pre-processing stage.
2. Secondly, it streamlines the process of setting up the experiment. Instead of having to alter and save a python code, open Abaqus, and then import the code, once the GUI is populated and ran, all the Abaqus processes are done automatically.

The GUI was designed using Python's tkinter package. The layout is designed to increase ease of use, as it is separated into four broad categories: part/geometry information, print base information, heat flow information and temperature information. When the GUI is ran, the inputs are saved to a text document. The GUI also launches Abaqus, and tells Abaqus to read the text document in order to find the inputs for the simulation. The GUI is shown in figure 7.1.

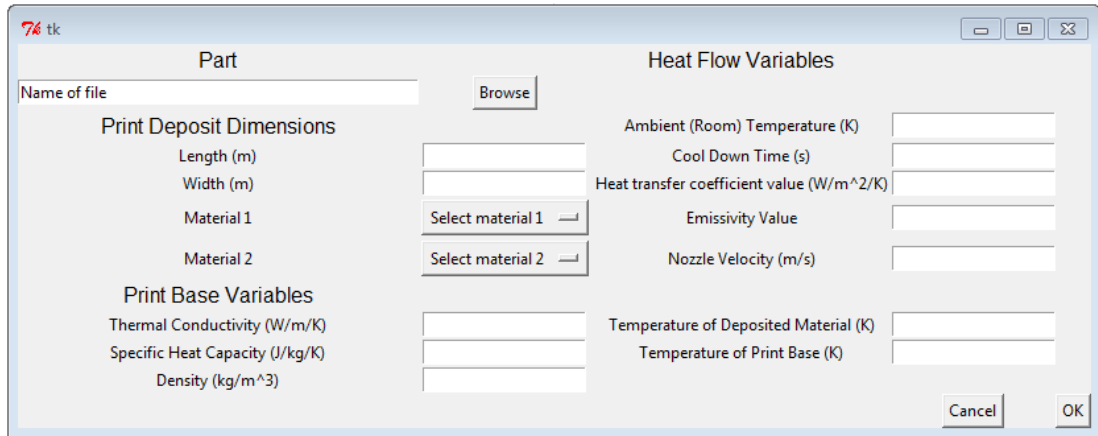


Figure 7.1: Graphical user interface for heat flow simulations

Using the GUI, the first step is to browse for the part. If the part has been made on other solid modelling software, this will be searched for. If the part is to be created in Abaqus, it should be done so, and then saved beforehand. Alternatively, if the part is very simple (cube or rectangle), the required dimensions can be input in the GUI without a part file needed.

The next step is to choose the two materials that the part will be constructed from using the two drop down menus. The drop down menus are populated with the commercially-available materials identified in section 2.4. If the part is to be constructed from one material, the two drop down menus should be set to the same material. The remaining entries are required for the variables listed in table 7.1.

7.2.5 Conclusion

The only practical way to include heat flow into the work is to using computer coding. The code that is required to run heat flow tests on FGM parts will be complex. It will require many inputs to ensure that the outputs represent reality. Abaqus is being used as the backbone of the code, however, functionality above that which Abaqus provides will be required. Microsoft visual studio (running Fortran), will be used for this purpose. In order to reduce the complexity for users, the researcher has created a GUI for front-end interaction. The GUI can be updated in future with enhanced part building tools.

7.3 Steps in code

The idea in this code is to segment the part into many small volumes that can realistically represent beads of deposited material. These will then be “activated” in the same

order as the scanning path of the deposition head. Constraints between each segment will be introduced to ensure that the heat flows between each as expected. The first step is to segment the part.

7.3.1 Segmenting the part

The code begins similar to that written for section 6. The part is first segmented. **Each segment represents a single volume of deposited material.** However, unlike section 6 that only requires the FGM blending distance to be segmented, this code requires the entire part to be segmented. This is because the whole part needs to be deposited, and as stated, each segment represents a single volume of deposited material. The thickness of each segment **must** be set to the same as that of each SUMC layer. The length and width can be chosen by the user. For this reason, choosing a length and width which fit an integer number of times into the part is advisable. The smaller each segment, the more accurate the heat flow simulation will be, at the trade-off of increased computation time.

7.3.2 Applying FGMs

The FGMs are applied using the same process used in section 6. For this test, the density, thermal conductivity and specific heat capacity of each material are needed. They are inserted into each material definition.

7.3.3 Creating the print bed and meshing the part

Once the part is segmented and materials are applied, the print bed must be created. It is important to simulate the print bed, as the temperature and material of it have a large impact on the heat flow in the part. The thickness of the print bed is user-defined. The length and width of the print bed is automatically scaled to be 50% longer and 50% wider than the part being made. The print bed is coupled to the part.

Figure 12.0.4 of appendix A shows the code building the print base with dimensions proportioned to the part.

At this stage, both the print bed and the deposition segments are meshed. Combined heat transfer - displacement elements are used. These elements can be used for both pure heat transfer analysis, and heat transfer analysis coupled with displacement tests. The print bed is meshed such that the areas in contact with and surrounding the part are an order of magnitude finer than the area at the edges of the print base.

Appendix A shows the code for seeding and meshing both the print bed and deposition segments.

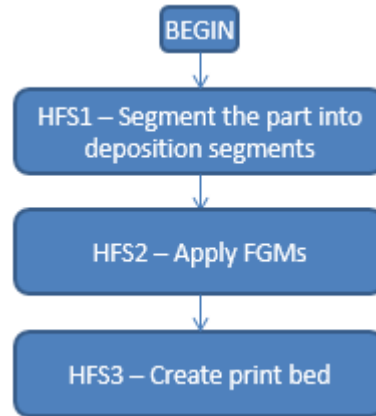


Figure 7.2: Heat flow steps 1 - 3

7.3.4 Creating the tool path

The tool path for the deposition is chosen by the user to ensure that the desired tool path is used, rather than being decided by a piece of software. As noted in section 5.6.2.3, there are numerous tool paths to choose from. The tool path itself has a large impact on the heat flow within the part, and therefore careful consideration and choice should be made. A common technique is to choose a tool path which mimics the over-riding shape of the part - for example, a circular tool path, if the part is cylindrical. In order to set the desired tool path, the centre of each deposition segment needs to be calculated. With the centre of each segment, a mathematical description of the tool path can be written which links the segment centres. The coordinates of each central point are written to a .txt file, giving a list that describes the tool path.

Figure 12.0.6 of appendix A gives the code for how the raster scan of the tool path is written into a file to be read later.

7.3.5 Deactivating deposition segments

As mentioned, the basis of this code is the deactivation/activation of the deposition segments. Once the part has been segmented and the tool path written, the deposition segments need to be deactivated. All deposition segments are placed into a set. Using this set, all segments are deactivated in a single step.

At this stage, only the print bed is “active” and the simulation resembles the additive manufacturing hardware just before deposition begins - only the print bed can be seen. Figure 12.0.7 of appendix A shows the code for “turning off” the print deposits prior to heating.

7.3.6 Creating the heat transfer conditions

In order to resemble reality as closely as possible, conduction, radiation and convection are all present in the simulation.

7.3.6.1 Conduction

Since both the part and the the air about the part are near-stationary, conduction is the predominant heat transfer mode. For this reason, it is important to model the conductivity. It is simulated within the part and between the part and the print bed using the thermal conductivity and specific heat capacity of the interpolated constituent materials - both controlled via the GUI. These properties influence the cooling rate within the part and thus alter the residual stresses in the part. The constraints between each segment and between the print bed and the part ensure that the heat conducts.

7.3.6.2 Radiation

Surface radiation from the part also influences the cooling rate. This is controlled by the emissivity of the material^[210-212], which is set in the GUI. The model is set to radiate heat uniformly from the surface of the part down to the ambient temperature, also controlled via the GUI. It is applied to the front face of the print bed and all external surfaces of the part.

7.3.6.3 Convection

As mentioned, conduction is the primary heat transfer mode due to the low convective currents that will be present. That aside, convection is also simulated, as it too influences the cooling rate of the part. Natural convection to the ambient temperature is used, as this is the convection characteristic in additive manufacturing hardware. It too is applied to the front face of the print bed and all external surfaces of the part.

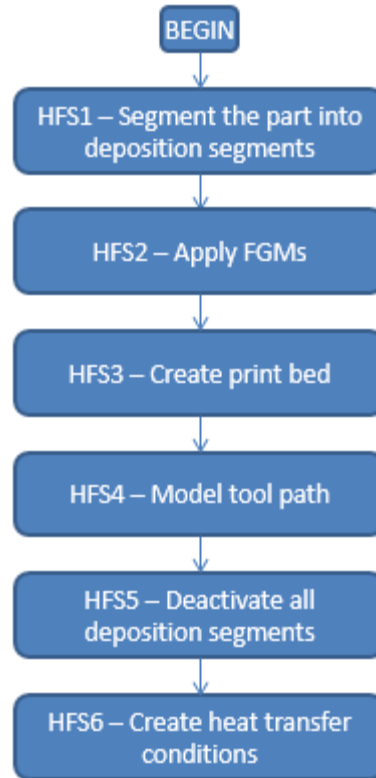


Figure 7.3: Heat flow steps 1 - 6

Figure 12.0.8 of appendix A shows the code for creating all three heat transfer conditions.

7.3.7 Heating the material

The material must be heated to the deposition temperature. As stated, this will be the higher melting temperature of the two constituent materials, and therefore, will not be interpolated unlike the other material properties in the FGMs.

7.3.8 Reactivating deposition segments

All deposition segments have now been deactivated and heated. The next step is to “reactivate” each segment to mimic the material deposition as it will be done by the additive manufacturing hardware. A heat transfer step is used to reactivate each deposition segment. The time between each reactivation is based on the nozzle velocity.

7.3.8.1 Controlling the nozzle velocity

The nozzle velocity is set via the GUI. However, the time it takes to “complete” a deposition segment depends on the relative volume of material in said deposition segment. This time - volume relationship is described mathematically:

$$t = \frac{V_c}{V_d} \times \frac{L}{s}$$

where t is the time to complete a deposition segment (s), V_c is the material volume of the current deposition segment (m^3), V_d is the total volume of the current deposition segment (m^3), L is the length of the deposition segment (m) and s is the velocity of the deposition head (m/s).

The segment appears at the beginning of the calculated time period, and cools over the time period until the beginning of the next time period, at which point the subsequent segment appears. With this relationship, the less material there is in the current deposition segment, the shorter the deposition time will be. Additionally, the smaller the deposition segments, the lower the “ t ” value will be. The “ t ” value for each segment is appended to the line of the .txt file that contains the central point coordinates of that segment.

7.3.8.2 Modelling the heat flow

In order to define the moving heat source, a DFLUX subroutine must be written in Fortran, compiled using Microsoft Visual Studio, and incorporated into the Abaqus simulation. This subroutine must be used during every single heat transfer step - once for every deposition segment, as it has to update the current position of the deposition head. A Gaussian distribution is used to model the heat source, as follows:

$$Q(r) = \frac{Q_L}{\pi r_o^2} e^{(1 - \frac{r^2}{r_o^2})}$$

where $Q(r)$ is the heat flux in terms of radial distance from the centre of the laser beam, r is the current position of the laser spot, Q_L is the laser power and r_o is the radius of the laser beam.

The position r is calculated using the coordinates of each central point written into the .txt file during step 4 (HFS4 - Section 7.3.4), as follows:

$$r^2 = x^2 + y^2 + z^2$$

The Gaussian distribution controls which deposition segments are heated, and which are not. Any deposition segment whose centre falls within the radius of the laser spot will be heated during the current heat transfer step. All other deposition segments will not be heated. The parameters and influence of segment size are shown in Figure 7.4.

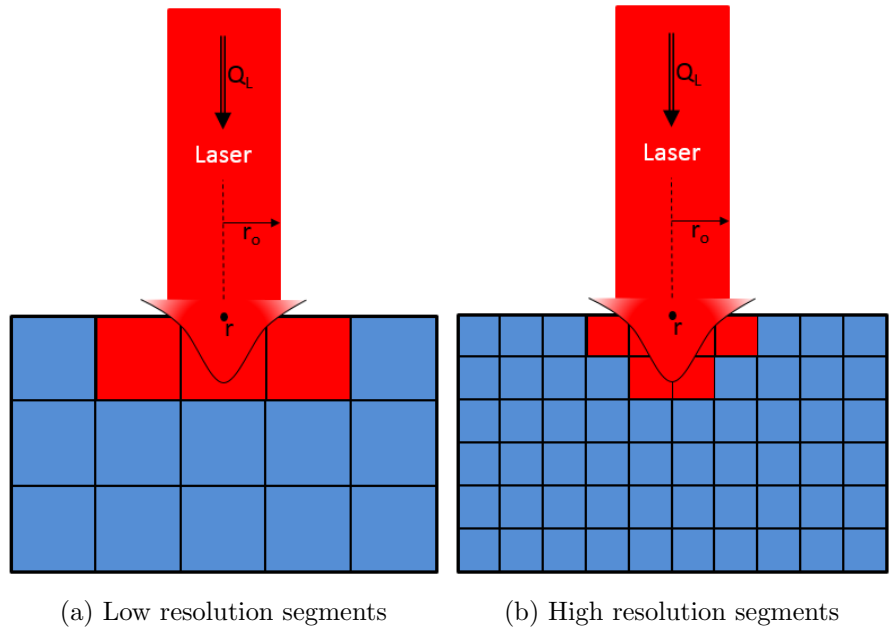


Figure 7.4: Heat flux parameters and influence of segment resolution

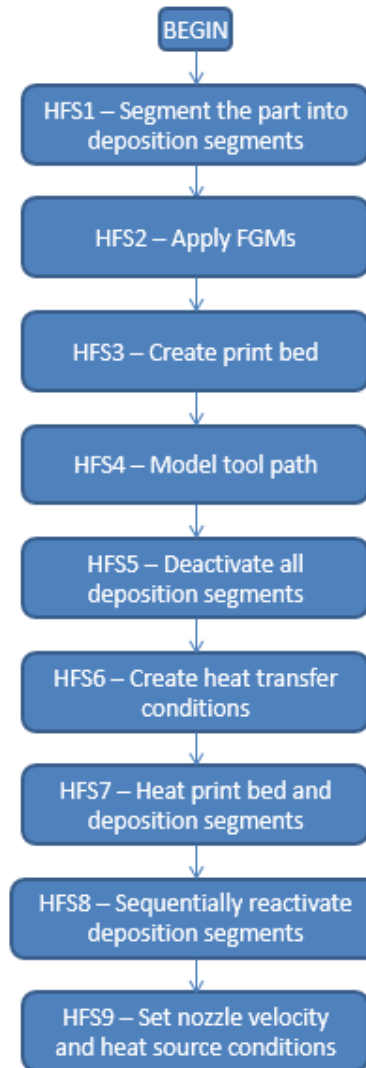


Figure 7.5: Heat flow steps 1 - 9

7.3.9 Applying a radiative surface heat flux

Any surface with line of sight to the deposition head experiences a radiative heat flux. As such, all external surfaces have radiative heat flux applied.

7.3.9.1 Cooling the part

Part cooling is also important, as the cooling rate has a large effect on the residual stresses in the part. A heat transfer step to cool the part is included. The rate of cooling is user defined, and can be set in the GUI.

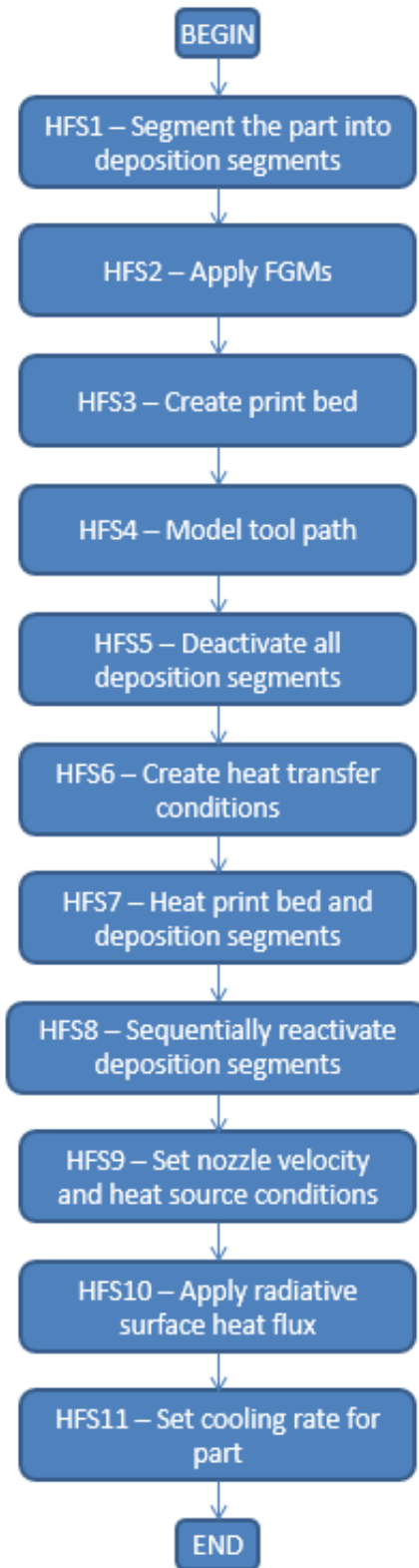


Figure 7.6: All heat flow steps

Figure 12.0.9 of appendix A is the code used to heat, deposit and cool the deposition segments.

7.3.10 Conclusion

The simulation of the additive manufacturing process is still in relative infancy compared to simulation of other manufacturing processes, and therefore this technique has been devised.

Attempts have been made to ensure that both constituent materials in the FGM will fully consolidate by grouping materials based on their similar melting temperatures. This is deemed a reasonable compromise for this thesis, as it does not aim to research details of materials science. Future work may be required in the chemical stability of the proposed combinations however, as some of the resulting alloys may be volatile.

Chapter 8

Test case 3 - Implementing the heat flow guidelines

8.1 Using guidelines

The guidelines are tested on the robotic arm gripper - identical to that in figure 6.8, used in section 6. The set up of the heat flow tests on the robotic arm gripper show various stages of the developed code.

8.1.1 Step 1 - Segmenting the part

The FGM extremities and blending distance are set to the same as used in figure 6.8 of section 6. In order to reduce computation time, the blending distance is segmented into 7 segments only, meaning each SUMC layer is far thicker than it was in section 6. When being used as part of the design guidelines, the researcher recommends reducing this layer thickness in order to improve the realism of the simulation. The layer stacking rule described in section 5.4.3.7 is used, as not all layers are the same thickness. The area beyond the blending distance (including the contact face) is also segmented into deposition segments. This was not necessary in section 6, as segmentation was made for material placement only. The resulting segmented gripper is shown in figure 8.1.

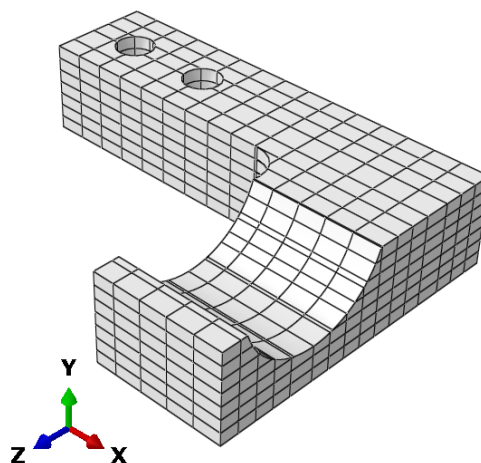


Figure 8.1: Segmenting the part for heat flow calculations

8.1.2 Step 2 - Applying the FGMs

Materials are altered from the tests in section 6 to Inconel 625 and stainless steel 316L. This choice was made for two reasons - firstly, these materials are closer in thermal properties than the Ti-6Al-4V/stainless steel 316L combination used in section 6 and secondly, using different materials will test the rigour of the code. Additionally, very similar materials have been successfully deposited on one another using LENS in previous studies^[213]. As mentioned, all material values for this test, bar the melting temperature, are interpolated from the material values of the constituent materials, as done in section 4.

8.1.3 Step 3 - Creating and attaching the print bed

As described in section 7.3.3, the print bed is created after the part is segmented and the materials applied. The code successfully created, partitioned and attached the print bed, as seen in figure 8.2.

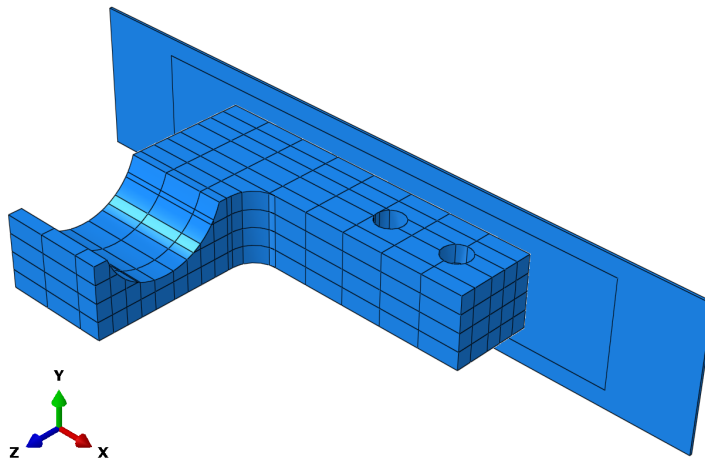


Figure 8.2: Creating, partitioning and attaching the print bed

8.1.4 Step 4 - Creating the tool path

A raster scan tool path is chosen, as it is quickest to program. A triple nested loop is used to create the tool path, working as follows:

1. Beginning in the third level, X direction loop, a bounding box checks if the current cell contains solid geometry. If it does not, it moves to the next cell in the X direction, and checks for solid geometry.
2. If solid geometry does exist in the cell, it applies a material and a section.
3. Once the counter in the third level (X direction) loop reaches it's final value, the second level (Y direction) loop increments by one.

4. The Y increment increase flips a counter switch from zero to one (or vice versa).
5. The X direction loop cycles again, this time in reverse from the previous loop, due to the Y direction counter switching.
6. Once the second level (Y direction) loop reaches it's final value, the first level (Z direction) loop increments by one.
7. The Z increment increase flips a counter switch from zero to one (or vice versa).
8. The Y direction loop cycles in the reverse direction compared to the previous Z layer, due to the Z direction counter switching.
9. All three loops continue until all cells are checked.
10. The coordinates of the centre of each solid geometry cell are recorded in a .txt file.

8.1.5 Step 5 - Deactivating the deposition segments

Once the tool path is created and the materials applied, the code deactivates all the segments. The FEA solver at this stage shows only the print bed, as seen in figure 8.3.

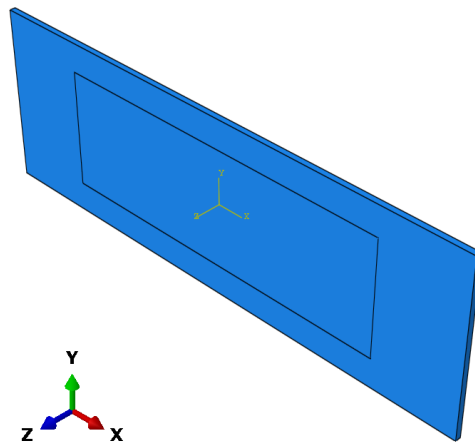


Figure 8.3: Deactivating the deposition segments, leaving the print bed

8.1.6 Step 6 - Heat transfer conditions

Conduction occurs in the model if the thermal conductivity and specific heat capacity of the materials are set, heat transfer-compatible elements are used, and a thermal conductance interaction property is set at the interface between the part and the print bed. These thermal property values for the FGM layers also interpolate between the values of the two constituent materials, as was done for the mechanical properties in section 6.

The conductance interaction property is set to mimic perfect conduction - at a distance of zero it is set to 10000 W/m/K.

For radiation, emissivity is set as an average of the emissivity values of the two constituent materials. In this case, emissivity was set at 0.64, averaged from the emissivities of stainless steel 316 and Inconel 625^[214].

Convective surface cooling is set on both the print bed surface and the surface of each deposition segment as it is deposited. The convection film coefficient is calculated as 8.5 W/m²K, using calculations for a horizontal flat plate with natural convection. For the radiative and convective cooling, 293 K is set as the ambient temperature.

8.1.7 Step 7 - Heat print bed and deposition segments

The print bed is heated to 493 K. Figure 8.4 shows the preheated print bed. The entire print bed is at the same temperature, and thus the same colour. All entries in the legend are the same value.

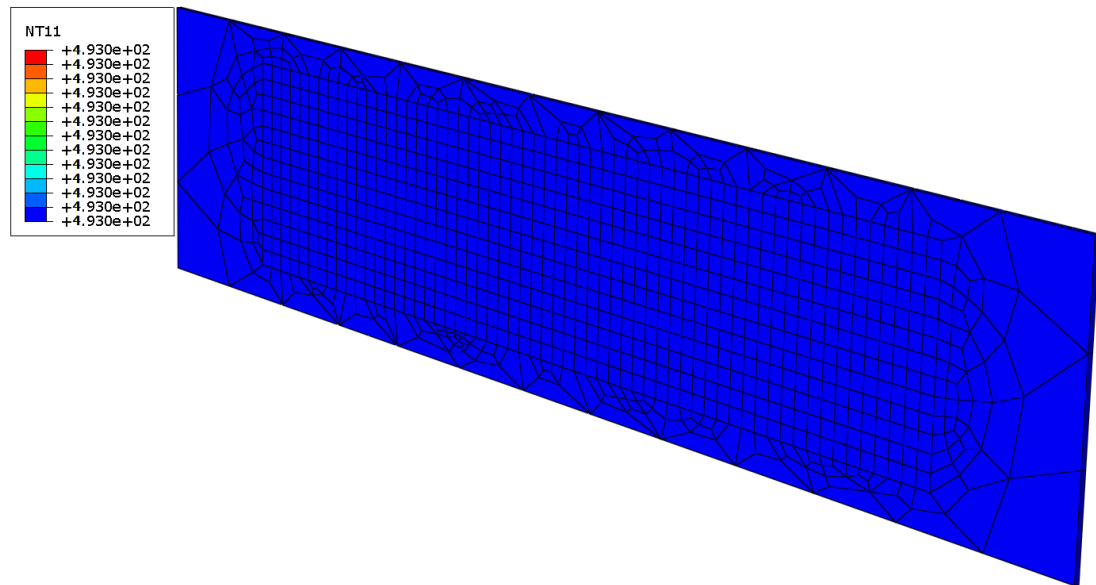


Figure 8.4: The temperature after heating the print bed

The deposition segments are heated to the melting temperature of the Inconel 625 (1650 K), as it has a higher melting temperature than the stainless steel. The reactivation of the print deposits causes the print bed to heat above its preheated temperature, due to conduction.

8.1.8 Step 8 - Sequentially reactivate the deposition segments

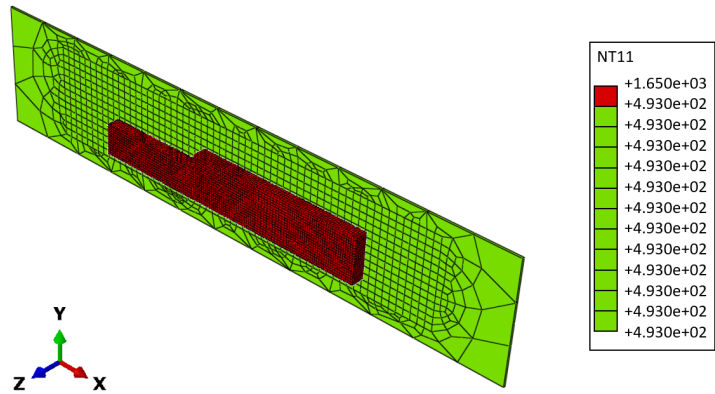
Using the order of the entries in the .txt file written during the tool path creation, a step is created for each deposition segment. In each step, the segment appended to

that step is reactivated. The deposition segments are reactivated as per the order they are ordered in the .txt file.

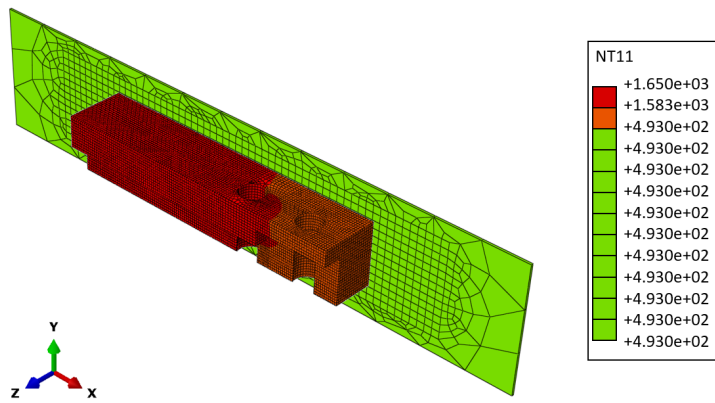
8.1.9 Step 9 - Set nozzle velocity and heat source conditions

Using the calculations in section 7.3.8.1, the heating time that each deposition segment requires is calculated. This time is used as the time interval for each step created in section 8.1.8, and appended to each line of the .txt file created in section 8.1.4. The equation in section 7.3.8.2 moves the heat source at the beginning of each step to the coordinates of the current deposition segment (read from the .txt file), and keeps it there for the time interval associated with the deposition segment, also read from the .txt file. As mentioned, if the distance from the current heat source location to the centre of the deposition segment is less than the heat source radius, the deposition segment will be heated. This applies to all deposition segments during every step, not just the deposition segment associated with the current step. From literature, laser power required for depositing Inconel 625 is 1200 W^[215;216]. The laser spot size is set at 5 mm. This gives a laser intensity of $\frac{1200}{0.005} = 240000 \text{ W/m}^2$. The nozzle velocity is set at 1.5 mm/s. The laser has to raster a distance of roughly 3000 mm, therefore, it will take approximately 2000 seconds to deposit with the current number of deposition segments.

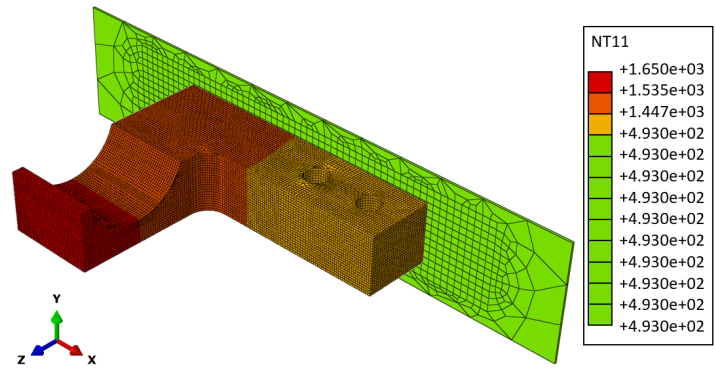
Figure 8.5 shows the reactivation and nozzle velocity influence at various stages. The heat flow can be seen progressing through the part.



(a) Early in the reactivation process - all deposits at high temperature



(b) Mid way through reactivation - certain deposits can be seen cooling



(c) Reactivation complete - cooling now seen clearly through the part

Figure 8.5: Reactivating the deposition segments

Three consecutive elements will be looked at to demonstrate the nozzle velocity and deposition segment volume relationship. The timings are calculated using the equation written in section 7.3.8.1.

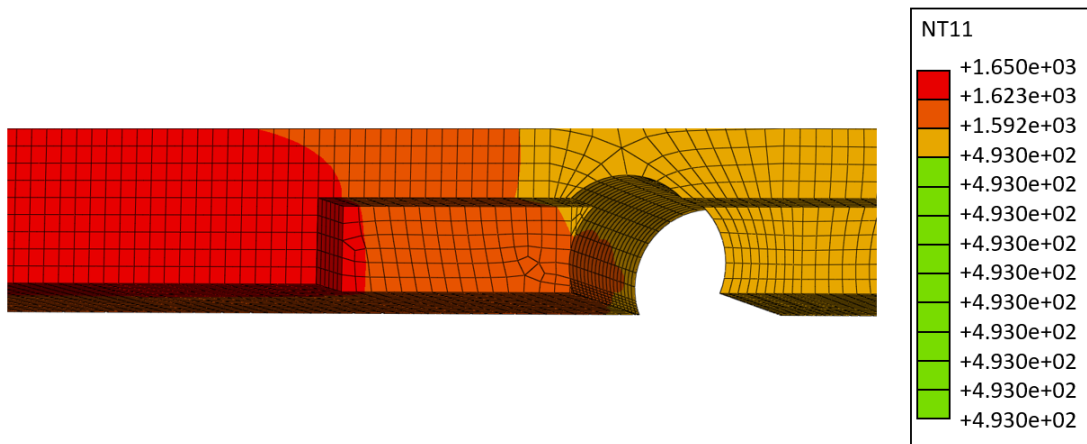
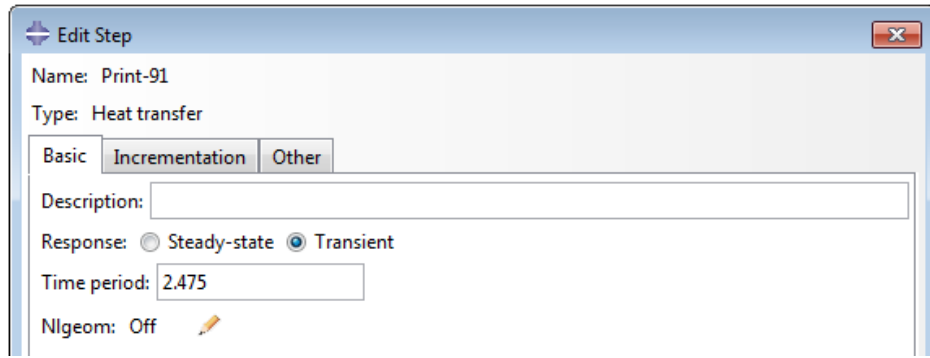


Figure 8.6: Timing and deposition of the 91st print deposit

Figure 8.6 shows the deposition area after the 91st segment has been laid, which is seen to take 2.475 seconds.

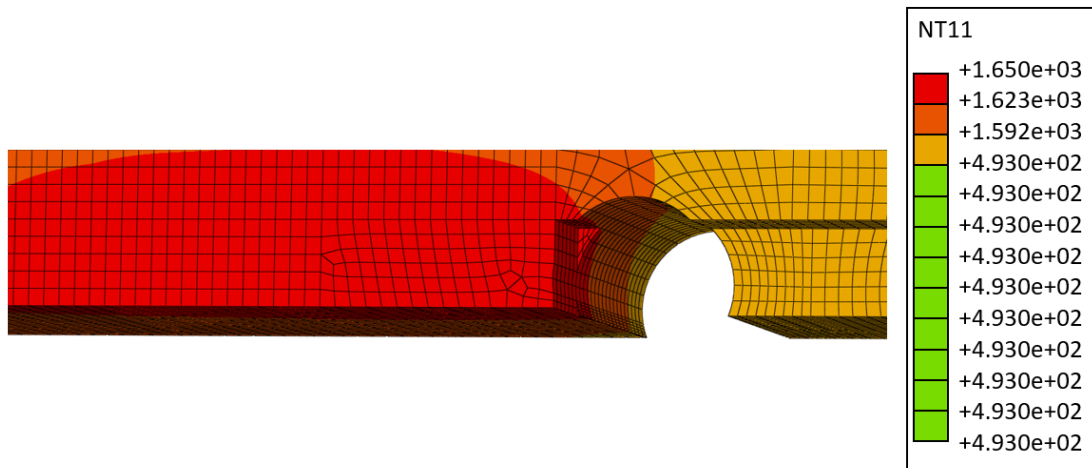
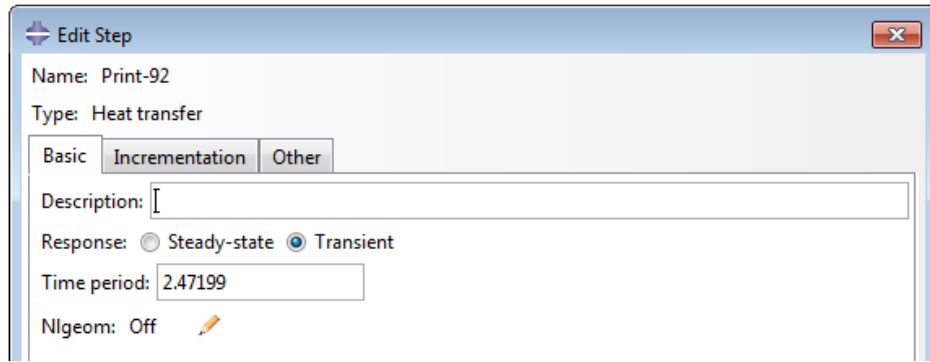


Figure 8.7: Timing and deposition of the 92nd print deposit

Figure 8.7 shows the 92nd deposition segment in position. The time step for this segment is 2.47199 seconds - slightly less than the previous segment. This is due to the upcoming hole in the part - this has removed a fraction of the 92nd deposition segment, as can be seen upon careful inspection.

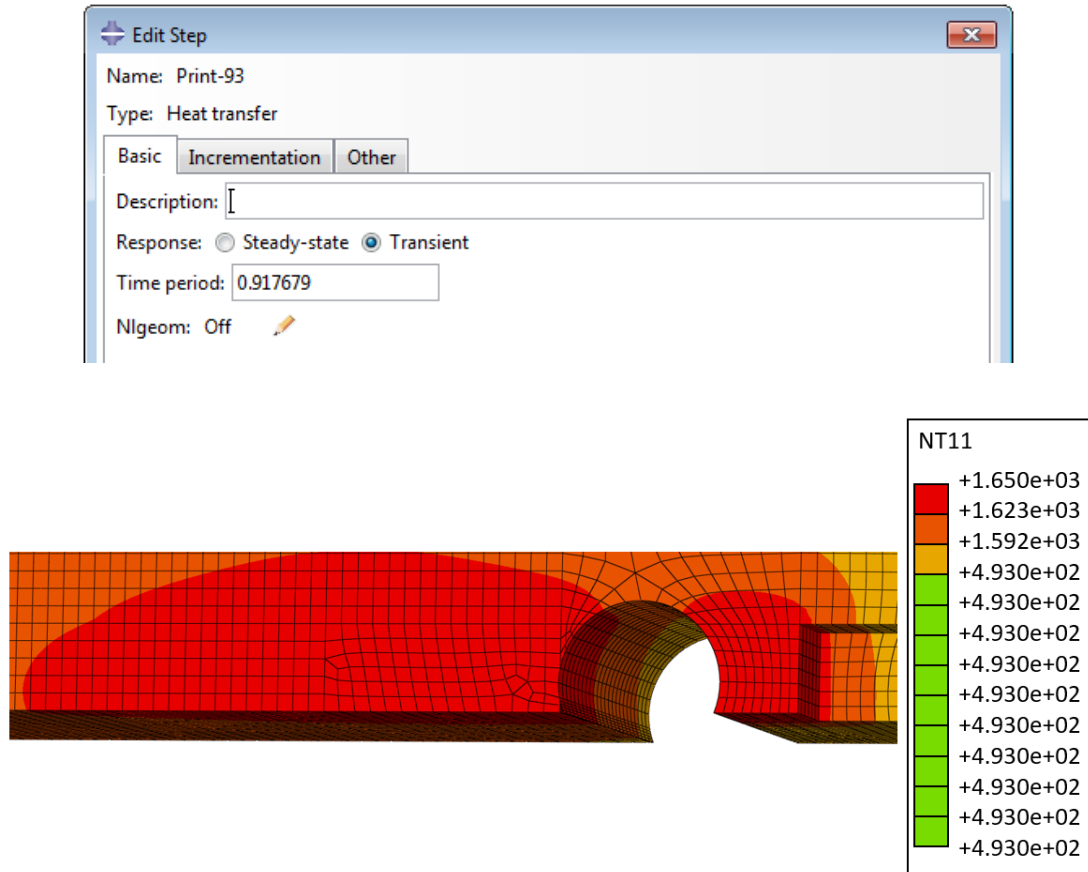


Figure 8.8: Timing and deposition of the 93rd print deposit

Figure 8.8 shows the 93rd deposition segment in position. The time step for this segment is far lower than the previous two segments, due to the hole in the centre of the segment. The nozzle velocity vs volume relationship can therefore be said to work correctly, as deposition segments with different volumes take varying durations to print.

8.1.10 Step 10 - Apply radiative surface heat flux

The radiative heat flux is called, as this initiates the DFLUX subroutine at each step. The magnitude of the heat flux is set as 1 W/m^2 - chosen as a value is needed at this point to satisfy the mandatory field in the model set up. The first time the DFLUX subroutine is called (and every subsequent time), the heat flux will be set at 240 kW/m^2 , as calculated in section 8.1.9. The fact it is set initially as a positive value tells Abaqus™ the heat flux is into the surface, not out of it.

8.1.11 Step 11 - Set cooling rate for part

The cooling rate for the part will impart different mechanical properties. Natural air cooling to the ambient temperature is chosen for this test. A time step of 300 seconds is set - the temperature 300 seconds after the final deposition segment had been printed would be seen. This is shown in figure 8.9.

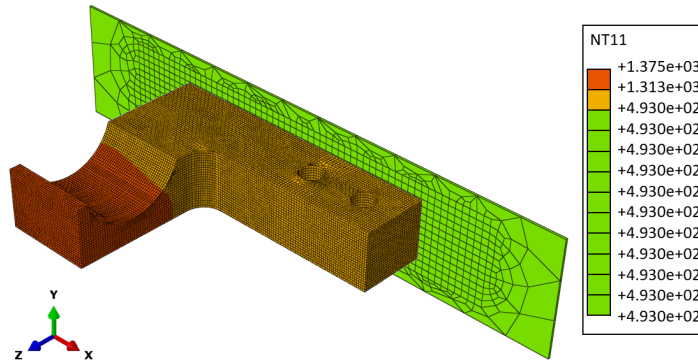


Figure 8.9: The temperature profile after cooling for 300 seconds

8.1.12 Conclusion

By this stage, applying the FGMs is well established, and the method works robustly on any shape.

Attaching the print bed to the part is done using a contact constraint to ensure conduction between the parts. A high value of conductance will be set at the zero distance to ensure that the model does not limit thermal conductivity between the part and the print bed.

This test used a raster scan path, as it was quick. Future work could experiment with different paths, and possibly incorporate a selection of different paths into the GUI, so the designer does not have to code their own, unless they need a bespoke path.

The process of deactivating and then sequentially reactivating cells is deemed by the researcher to be a fair representation of the AM process. If the temperature profile of the part does not follow the scan path written, then work will be done to alter this technique.

8.2 Addition of residual stress

Residual stress has not been reported in these results, though is important for assessing the behaviour of the part. Attempts will be made to predict the residual stress in these parts, although, it must be noted that these predictions are based on the heat flow code which has yet to be validated via physical experiments. For that reason, the researcher

does not recommend use of the residual stress values by any prospective user of this work until they can validate the heat flow steps outlined above.

In order to find the residual stress, two changes need to be made to the steps in section 7.3:

1. The thermal expansion coefficient, elastic modulus and Poisson's ratio is needed for each material in addition to the properties set for the heat flow test
2. The heat transfer steps must be altered to coupled thermal-displacement steps

8.3 Fitting heat flow into design guidelines

The heat flow guidelines simulate the deposition of the material and the residual stress in the part. As such, they should be placed before manufacture, but after computational testing. The outcome of the heat flow test will have a possible impact on the design of the part. If the residual stresses are too high in the part, the materials and possibly the design will need altered. The updated design guidelines need to show this. A breakdown of images showing the inclusion of the heat flow testing into the design guidelines are shown in the following images.

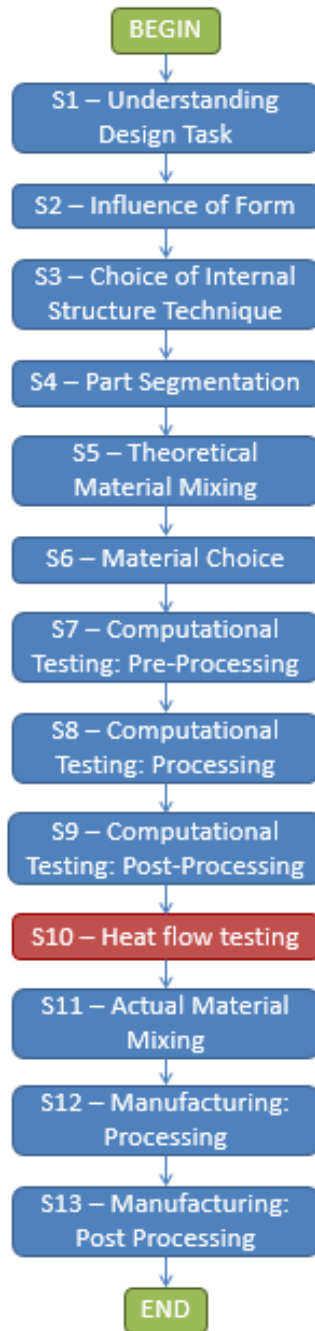


Figure 8.10: Where the heat flow testing fits in the design guidelines

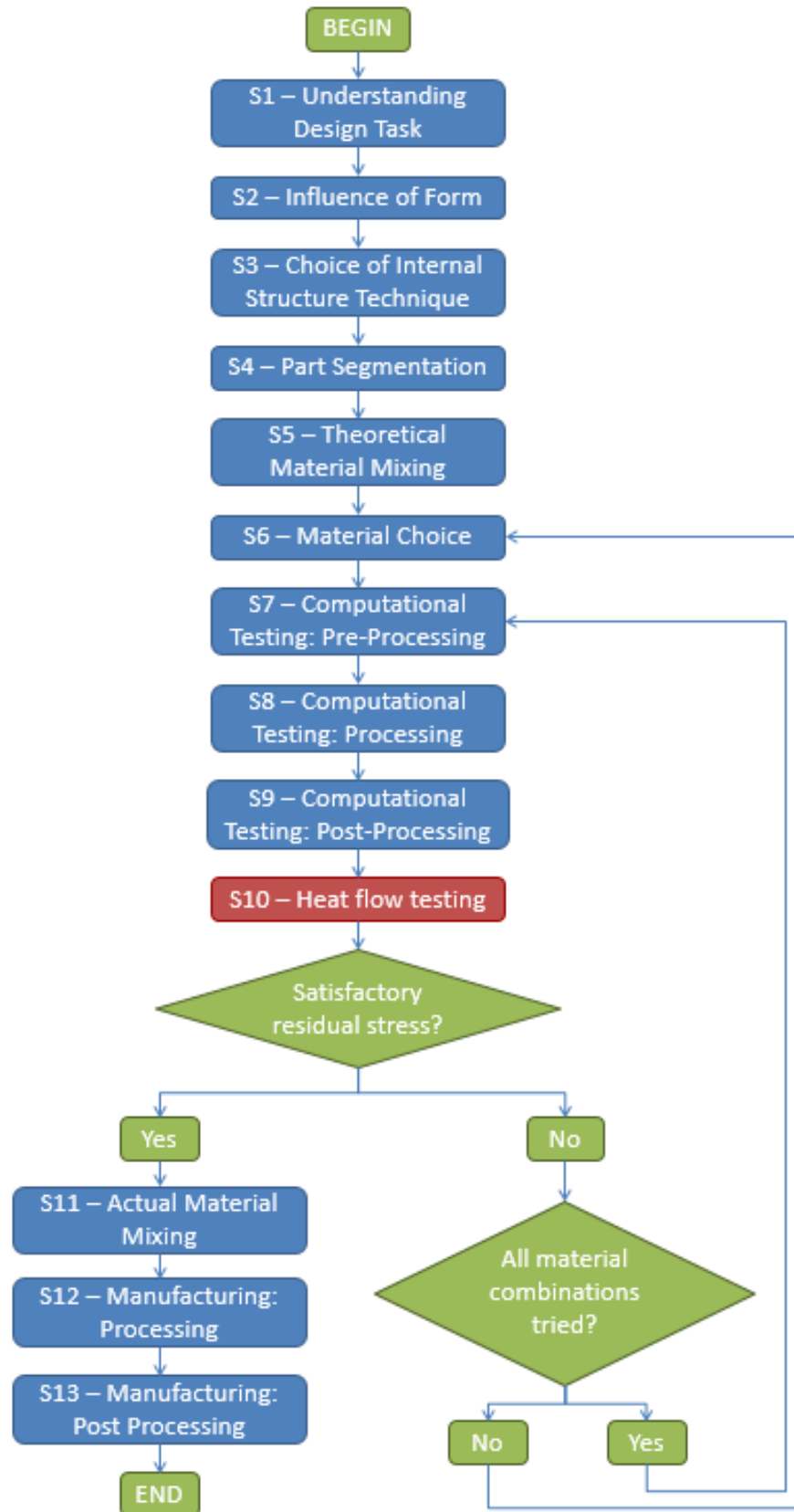


Figure 8.11: The influence the heat flow testing has on the guidelines

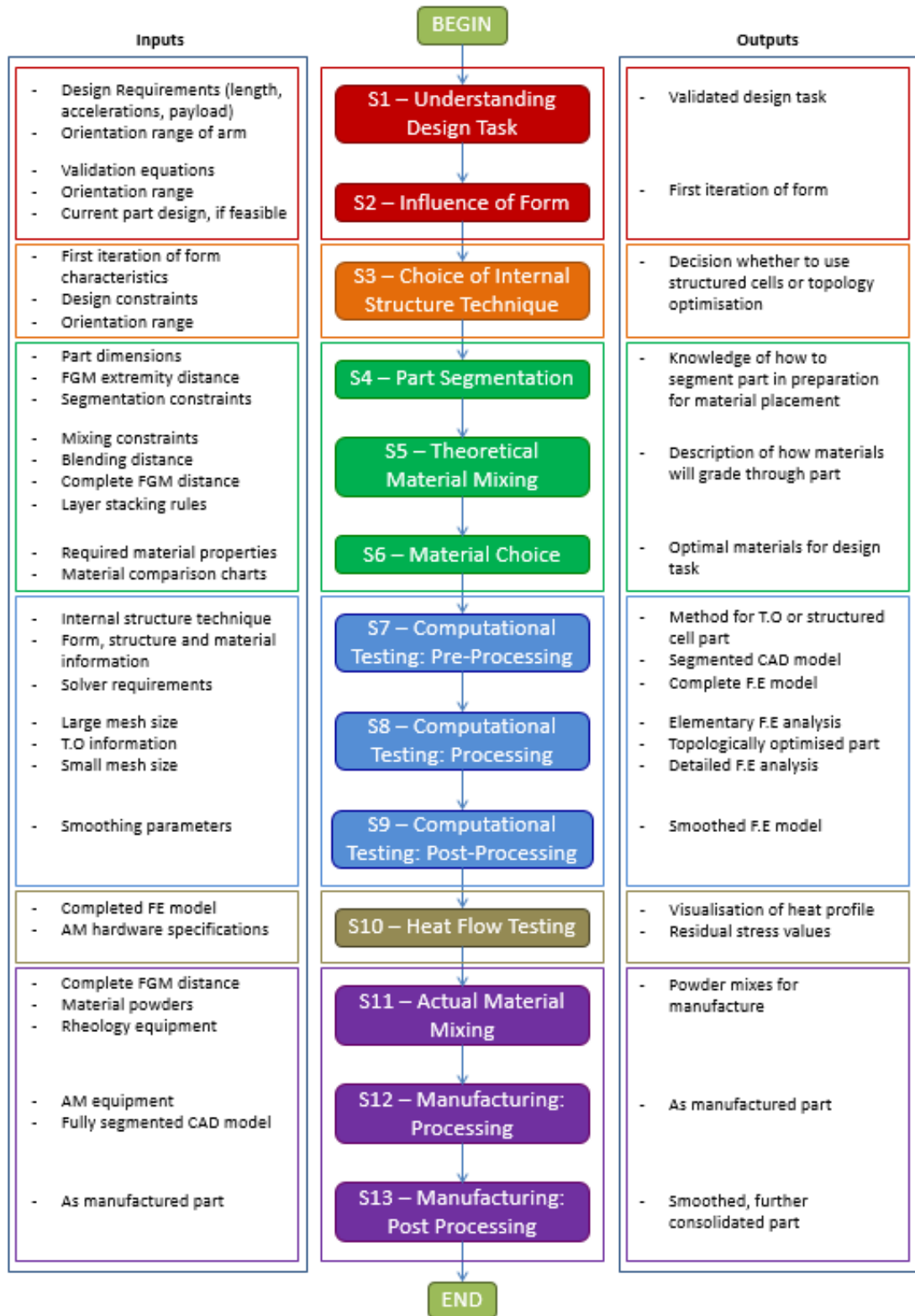


Figure 8.12: The heat flow testing included in the overall methodology

8.4 Conclusion

The deposition path successfully follows the deposition path that was set and the heat flow trends are expected based on heat transfer mechanics. However, without validation from a physical experiment, it is impossible to assess the heat flow code for its ability to mimic the actual manufacturing process. Temperatures are broadly as expected - up to the set deposition temperature, and cooling towards ambient temperature once the heat source is removed. The model of the heat source itself is deemed robust as it uses a Gaussian profile to mimic the laser spot. This is widely regarded in literature as an acceptable profile to model a point heat source. The model also takes into account all three heat transfer conditions (conduction, convection and radiation), however, once again it is impossible to know how well these are modelled due to the lack of physical data to validate. It was seen that altering these heat transfer conditions had a stark effect on the heat profile of the part, and therefore it assumed that these would need tweaking to give a closer representation to any physical experiments. Since this test case did not have the physical experiment values in order to fine tune the parameters; it can only claim to show that the concept would work. Since the concept did work, this additional step will be added to the design guidelines. However, as stated, it must be remembered that it is not validated.

The final step of the heat flow guidelines which are not in this test case is the measurement of residual stress. This will be in the final test case of the thesis.

Chapter 9

Testing the entire design guidelines

9.1 Introduction

The second test case tested the computational testing steps of the design guidelines. The third test case created and tested a method for monitoring heat flow through an FGM part while being manufactured. This test case aims to test the design guidelines in their entirety, from the first step, to the last. However, due to the unforeseen financial constraints mentioned in section 6.5, the final manufacturing steps cannot be tested, and therefore testing will conclude at the end of the computational testing stage.

9.2 Model

The original model from the preliminary first test case is chosen. This will allow the design guidelines to be tested on a familiar part, giving the researcher a more accurate information of how effective the design guidelines are. The original model is shown in figure 9.1.

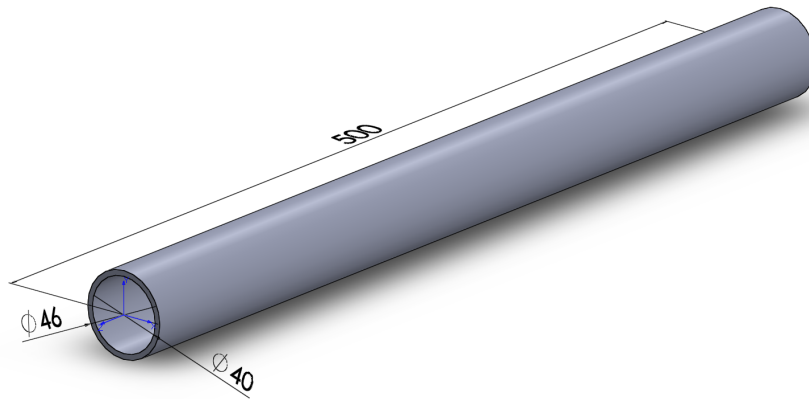


Figure 9.1: Original model of robot arm used in preliminary tests

The first step of the design guidelines is “understanding the design task”.

9.3 Step 1 - Understanding Design Task

The substeps of the first step are shown in figure 9.2.

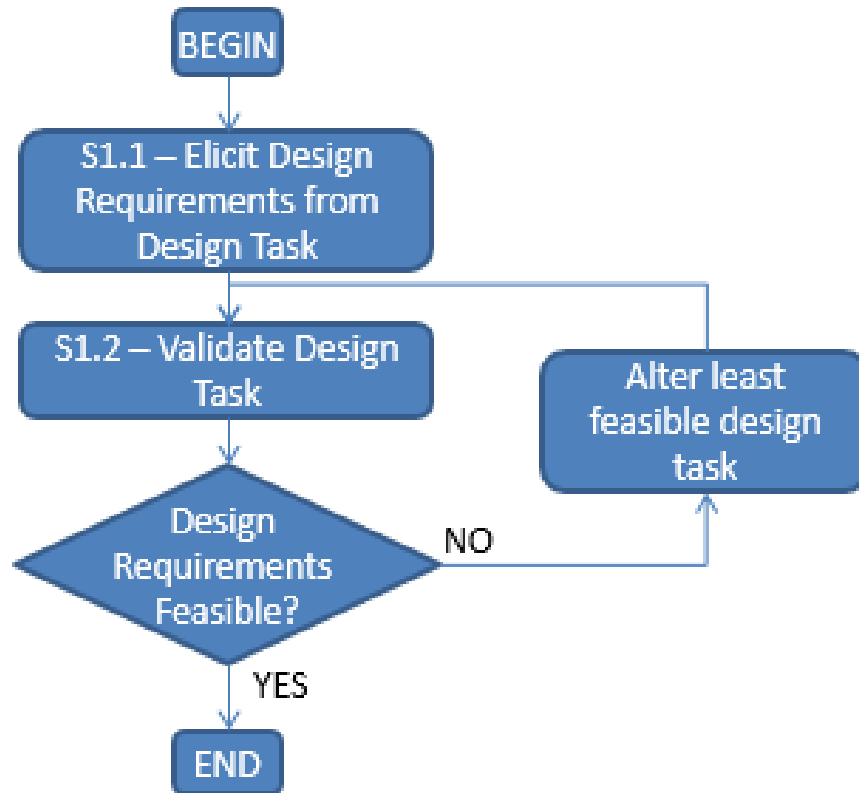


Figure 9.2: Step 1: Understanding the design task

9.3.1 Elicit design requirements from design task

Most of the design requirements for this design task were directly listed in the specification from the research laboratory. These are listed in table 9.1.

Table 9.1: Design requirements for test case

Parameter	Value
Material	Al 6061
Mass	0.547 kg
Length	0.5 m
Cross section	Circular
Internal Diameter	0.04 m
External Diameter	0.046 m
Maximum Displacement	0.00025 m

The design requirements must be organised as either primary or secondary. This is shown in table 9.2.

Table 9.2: Organising design requirements

Primary Requirements	Secondary Requirements
Length	Material
Maximum Displacement	Mass
Internal Diameter	Cross Section
	External Diameter
	Orientation Range

9.3.2 Validate design task/requirements

Of the primary requirements, the displacement is the only one which needs in depth verification. The length and internal diameter can easily be verified using a distance measuring device (calipers, ruler, etc).

9.3.2.1 Displacement

In order to calculate the displacement, the forces on the arm are first needed. A free body diagram of the entire arm is shown in figure 9.3. Values for the variables are given in table 9.3.

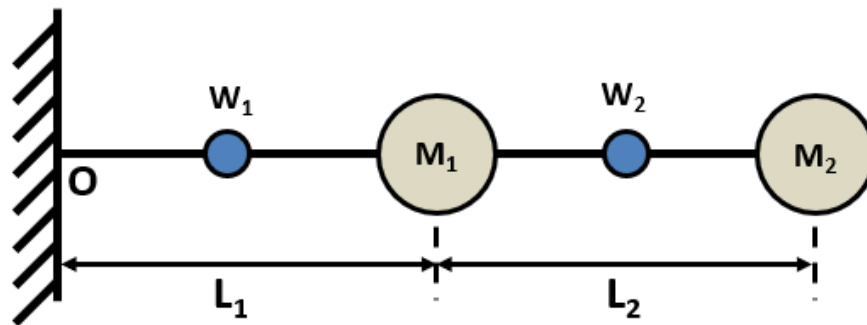


Figure 9.3: Free body diagram of entire arm

Table 9.3: Variables for robotic arm

Variable	Value
L_1	0.5 m
L_2	0.5 m
M_1	1.5 kg
M_2	0.8 kg
W_1	0.75 kg
W_2	0.6 kg

A bending moment diagram based on information in Table 9.3 with calculated moments is shown in Figure 9.4.

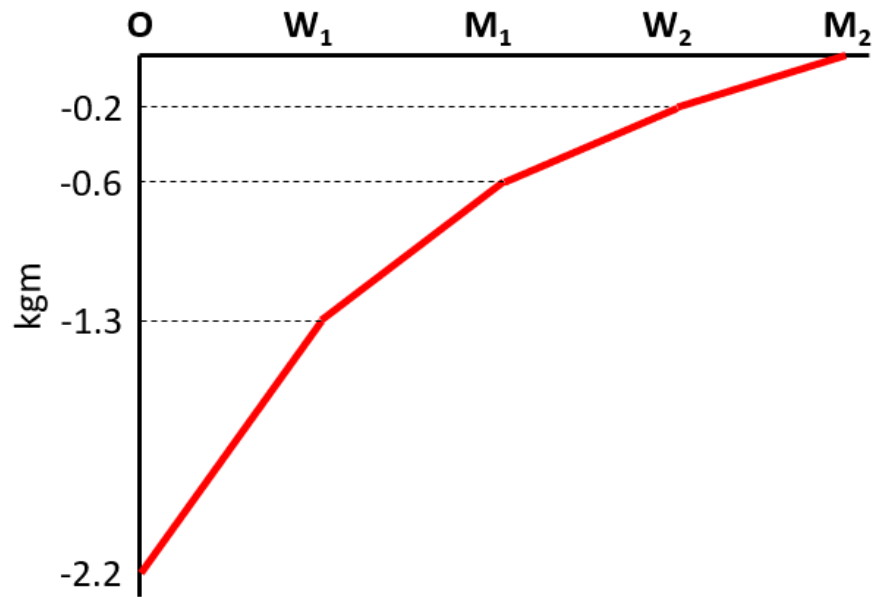


Figure 9.4: Bending moment diagram of entire arm

This example aims to reduce the mass of the first arm link, represented by W_1 . The free body diagram in Figure 9.3 is redrawn, as shown in Figure 9.5, T_1 represents the bending moment caused by the remaining arm components.

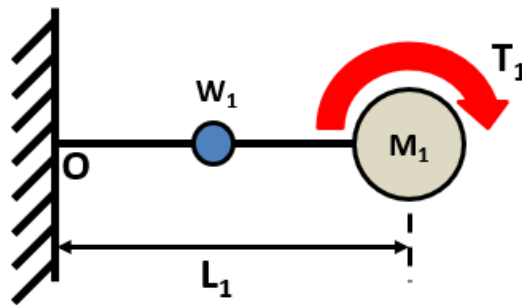


Figure 9.5: Free body diagram of the first arm link

This diagram is subdivided into two sections, as shown in Figure 9.6.

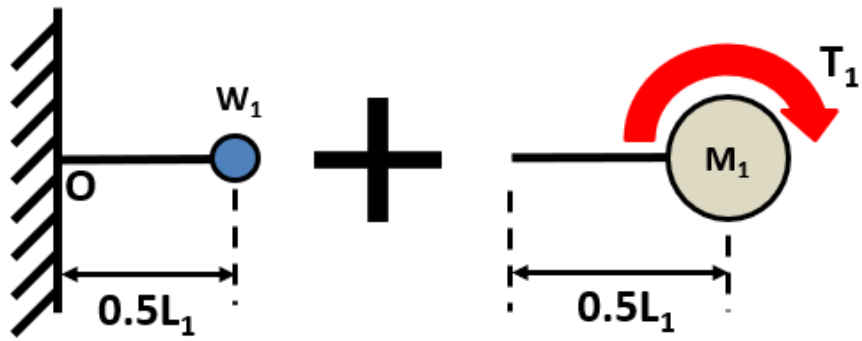


Figure 9.6: Free body diagram of the two parts of the first arm link

Using the moment area method, the deflection at W_1 and M_1 can be found. This uses the angles between tangents to points O , W_1 and M_1 , as demonstrated in Figure 9.7.

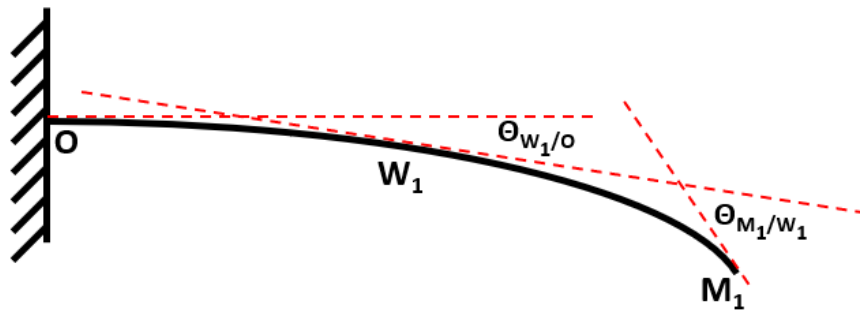


Figure 9.7: Demonstration of angles between tangents to points O , W_1 and M_1

Using the first and second moments of area, the vertical displacements (t) between points O , W_1 and M_1 can then be found, as demonstrated in Figure 9.8.

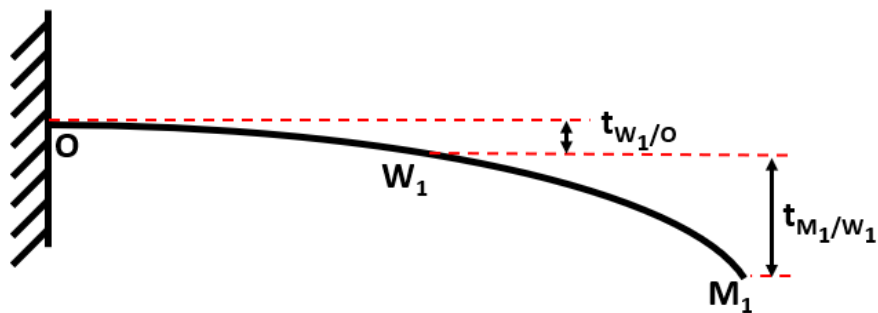


Figure 9.8: Demonstration of vertical displacements between points O , W_1 and M_1

The vertical displacement values are:

$$t_{W_1/O} = 0.006 \text{ mm}$$

$$t_{M_1/W_1} = 0.05 \text{ mm}$$

The resultant total displacement is thus 0.056 mm.

This value of displacement is below the constraint, **giving a safety factor of $0.25/0.056 = 4.5$.**

9.3.3 Conclusion

The design requirements are elicited from the design task and successfully categorised as primary or secondary. As stated in the conclusion of section 5.2.2, the designer requires engineering knowledge to elicit the design requirements. Future iterations of these guidelines should develop a technique to eliminate/limit this. The displacement constraint is satisfied. Since it is the only constraint which requires in-depth verification, the design requirements are feasible, and step one of the design guidelines is complete. The next step is the “influence of form”.

9.4 Step 2 - Influence of form

9.4.1 Influence of geometric features

The part is currently circular, meaning there are no acute angle features currently on the part. As such, the process can continue.

9.4.2 Influence of Core Volume

The part is already hollow, and therefore it's flexural rigidity per unit length is higher than it would be if made from a solid cylinder. One constraint of the part was that it must be hollow to allow transmission and power systems to be fitted within the part, also.

9.4.3 Influence of cross section alteration

The cross section of this part is currently circular. As such, it may be possible to alter the cross section to improve part stiffness.

9.4.3.1 Define orientation range

The one design requirement that is not directly listed is the orientation range of the arm link. Reading the specification of the arm link and understanding how it interacts with other components of the robotic system, it can be seen that the arm link does not have to rotate around its Z axis, nor do any of the components dependent on the arm link. As such, it has a orientation range of 0°.

9.4.3.2 List geometric constraints in the X and Y directions

X direction There is a geometric constraint in the X direction, caused by the location of the second arm link. This can be seen in figure 9.9.

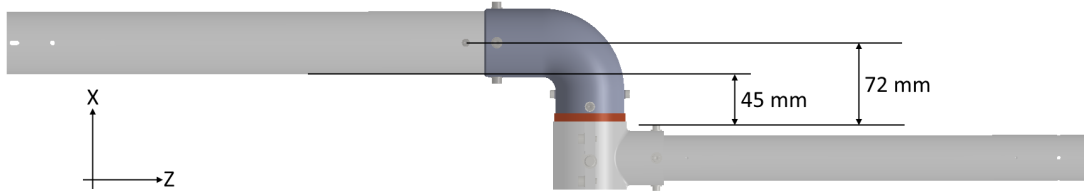


Figure 9.9: Entire robot arm, showing constraint in X direction

The maximum radius of a part can be 72 mm, as this is the distance from the centre of the arm link, to the supporting bolt which holds the second (dependent) arm link of the robotic system.

Y direction In the Y direction, there is no geometric constraint.

Wall thickness There is no wall thickness constraint, so long as the internal diameter does not go below 40 mm to allow internal cabling.

9.4.3.3 Calculate area of current cross section

In order to ensure the arm does not gain any mass, the cross section of the current arm must be calculated. For this hollow circular cross section,

$$\begin{aligned} A &= \pi(r^2 - r_i^2) \\ &= \pi(0.025^2 - 0.02^2) \\ &= 7.069e^{-4} \text{ m}^2. \end{aligned}$$

9.4.3.4 Alter cross section based on constraints

The internal diameter is a primary constraint, so must stay at 40 mm.

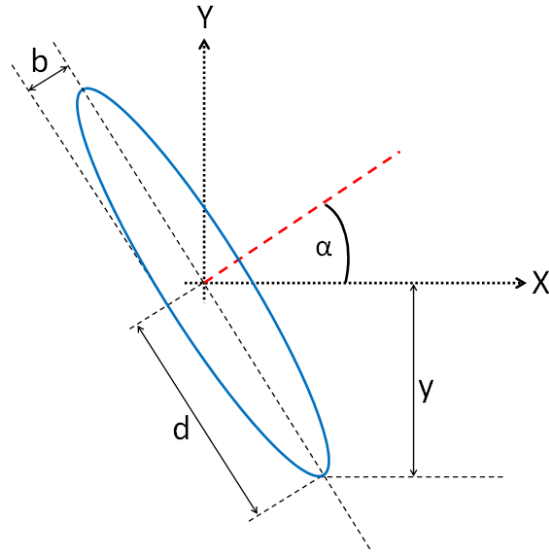


Figure 9.10: Variables needed to calculate area of ellipse

The area of an ellipse is given by $A = \pi \times b \times d$, where b and d are seen in figure 9.10.

For a hollow ellipse, $A = \pi \times (b_2 \times d_2 - b_1 \times d_1)$

b_1 is set at 20 mm. The wall thickness is set at 3 mm. Therefore, $b_2 = b_1 + 0.003$.

The values of d_1 and d_2 unknown, but due to the wall thickness constraint, $d_2 = d_1 + 0.003$. With this information, the unknown values can be solved for.

$$\begin{aligned}
 A &= \pi \times (b_2 \times d_2 - b_1 \times d_1) \\
 &= \pi \times ((b_1 + 0.003) \times (d_1 + 0.003) - 0.02 \times d_1) \\
 &= \pi \times ((0.02 + 0.003) \times (d_1 + 0.003) - 0.02 \times d_1) \\
 &= \pi \times (0.023 \times (d_1 + 0.003) - 0.02 \times d_1) \\
 &= \pi \times (0.023 \times d_1 + 6.9e^{-5} - 0.02 \times d_1) \\
 7.069e^{-4} &= \pi \times (0.03 \times d_1 + 6.9e^{-5}) \\
 \frac{7.069e^{-4}}{\pi} &= 0.03 \times d_1 + 6.9e^{-5} \\
 \frac{7.069e^{-4}}{\pi} - 6.9e^{-5} &= 0.03 \times d_1 \\
 \left(\frac{7.069e^{-4}}{\pi} - 6.9e^{-5}\right) \div 0.03 &= d_1 \\
 \Rightarrow d_1 &= 0.052\text{m} \\
 \Rightarrow d_2 &= 0.055\text{m}
 \end{aligned}$$

The new geometry is seen in figure 9.11.

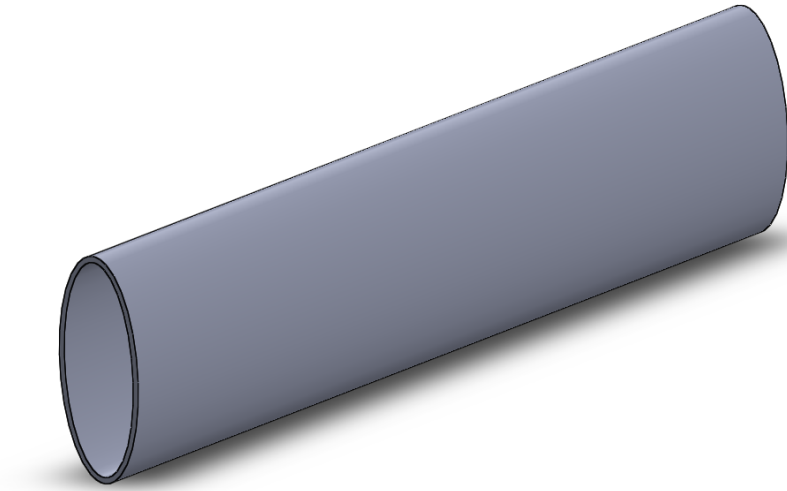


Figure 9.11: The arm link once redesigned

9.4.4 Influence of material placement

The internal diameter is fixed at 40 mm at the narrowest point. The redesigned arm above has the internal diameter fixed at 40 mm at its narrowest point, and a constant wall thickness of 3 mm. The wall internal diameter increases to 104 mm at its widest point, within the geometric limit of 144 mm highlighted in figure 9.9.

The maximum bending factor should be calculated at this point to ensure the part will not locally buckle.

$$(\phi_B^e)_{\max} \approx 2.3 \left(\frac{E}{\sigma_f} \right)^{1/2}$$

For aluminium the maximum bending factor, $(\phi_B^e)_{\max} \approx 2.3 \left(\frac{69e^9}{95e^6} \right)^{1/2} = 61.986$.

The bending factor is given by the ratio of the part width to the wall thickness. This is done at the narrowest point, which is 40 mm diameter, plus a 3 mm wall thickness. The max bending factor in this model is therefore $46/3 = 15.3$. This is far below the maximum bending factor value, and therefore the part will not locally buckle.

9.4.5 Conclusion

This step is very useful because it does several simple checks early on to the current model to ensure that no obvious alterations should be made. Geometry and core volume are checked to ensure no obvious angles or volumes should be altered. The test for local buckling ensures that the wall thickness is not too low - something which can easily be overlooked. Through investigation of the orientation range, the cross section is altered to increase the second moment of area. It must be noted that this alteration of cross section will not suit many robotic arm configurations, due to the instantaneous dynamic

loading which can act in any of an infinite number of directions, as originally described in section 2.1.

9.5 Step 3 - Choice of Internal Structure Technique

With the updated form, the choice of internal structure technique can be made. A copy of the the third step guidelines is shown in Figure 9.12.

9.5.1 Assessing the geometry

The first sub step is to assess the geometry. There are two questions which need to be answered:

1. Are there at least two orders of rotational symmetry?
2. Is the wall at least 3 mm thick?

The updated form has a 3 mm wall thickness, and has two orders of rotational symmetry. Therefore, the next sub step, assessing the loading conditions, will be done.

9.5.2 Assessing the loading conditions

There is only one question associated with the loading conditions, which regards the orientation range. The orientation range for this part is 0° , therefore the guidelines can progress to the next substep, assessing the part shape.

9.5.3 Assessing part shape

In these guidelines, the inner and outer walls of a part must be at a constant distance from one another when viewing the cross section if structured cells are to be used. The inner and outer walls in the updated form are at a constant distance of 3 mm from one another, and therefore the part passes this condition.

9.5.4 Conclusion

The updated form passes all the conditions set, and therefore cellular structures will be used in its internal structure. However, future work should make this step more dynamic - for example, the 3 mm wall thickness should not be a blanket rule; instead, the wall thickness should be related to structured cell shapes and the task of the arm - certain situation will allow a lower wall thickness, while other situations may need it to be higher. The next step is to segment the part in preparation for material placement - the first phase of the “material” focus area.

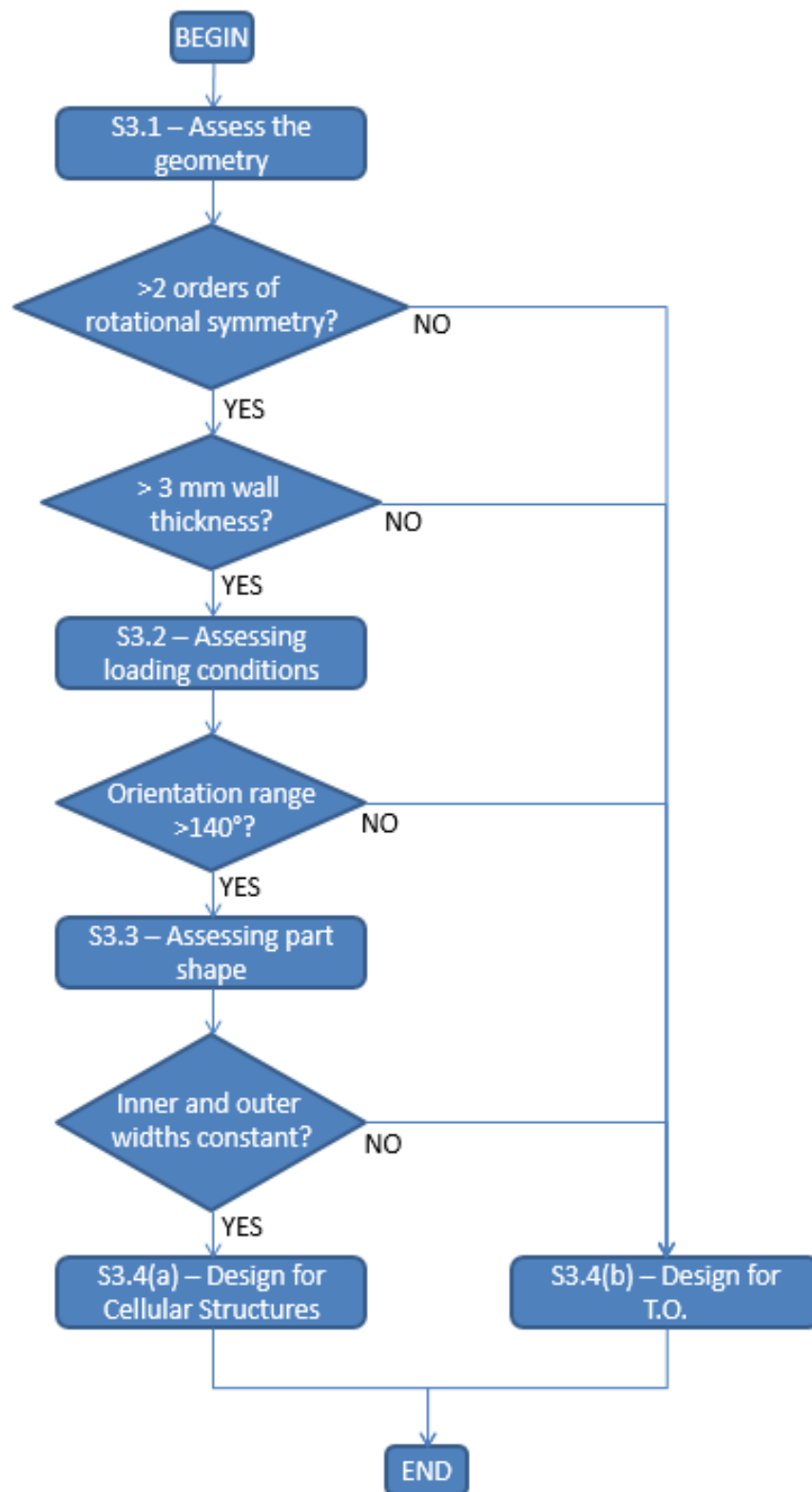


Figure 9.12: How to choose the internal structure technique

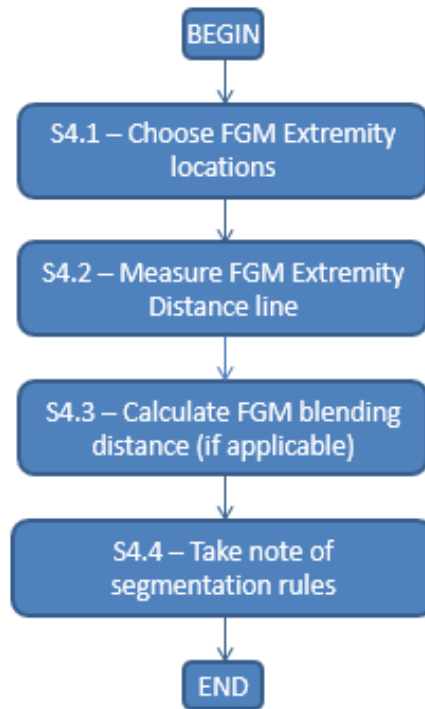


Figure 9.13: How to segment the part in preparation for material allocation

9.6 Step 4 - Part Segmentation

The first phase of the material focus area is to segment the part. Instructions for segmentation are seen in figure 9.13.

9.6.1 Choose FGM Extremity locations

The extremity locations for this project are the two ends of the part. These are chosen in order to fully test the ability of the segmentation controls, rather than for the performance of the arm link in its intended environment.

9.6.2 Measure FGM Extremity Distance line

As the two FGM extremity planes are parallel to one another and at the ends of the arm link, the FGM extremity distance is the same as the length of the entire part, 500 mm. The line can be seen in figure 9.15.

9.6.3 Calculate FGM blending distance

As the FGM extremities are parallel to one another, the FGM blending distance is the same as the FGM extremity distance in this test case, 500 mm.

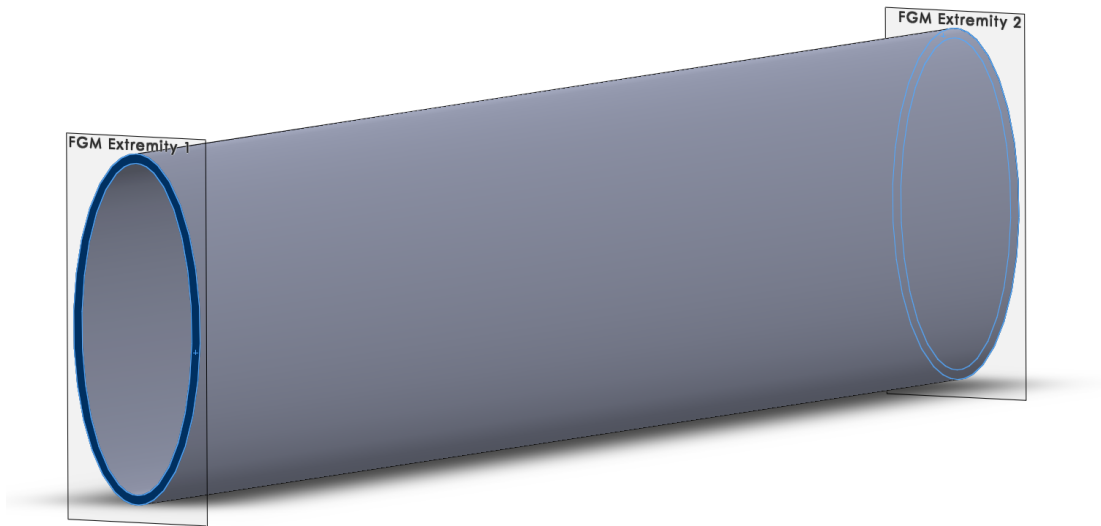


Figure 9.14: Choosing the FGM extremity locations

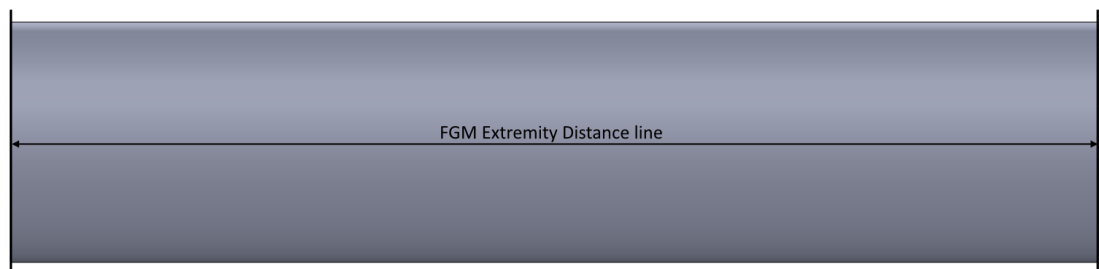


Figure 9.15: Plotting and measuring the FGM Extremity Distance line

9.6.4 Take note of segmentation rules

The segmentation rules dictate which direction(s) the segmentation will occur. In this case, the first rule will segment the part into many slices, parallel to the FGM extremity plane. The second rule would slice the part radially around the wall thickness. However, this will not be done, as the wall thickness value is very small compared to the length of the part and therefore will have negligible influence.

9.6.5 Conclusion

This step of the design guidelines is well established in this thesis and works robustly. The FGM extremities have been drawn and the blending distance calculated successfully. The researcher does not see any need to alter this step in the future.

9.7 Step 5 - Theoretical Material Mixing

Theoretical material mixing is split into four sub steps. These steps are shown in figure [9.16](#).

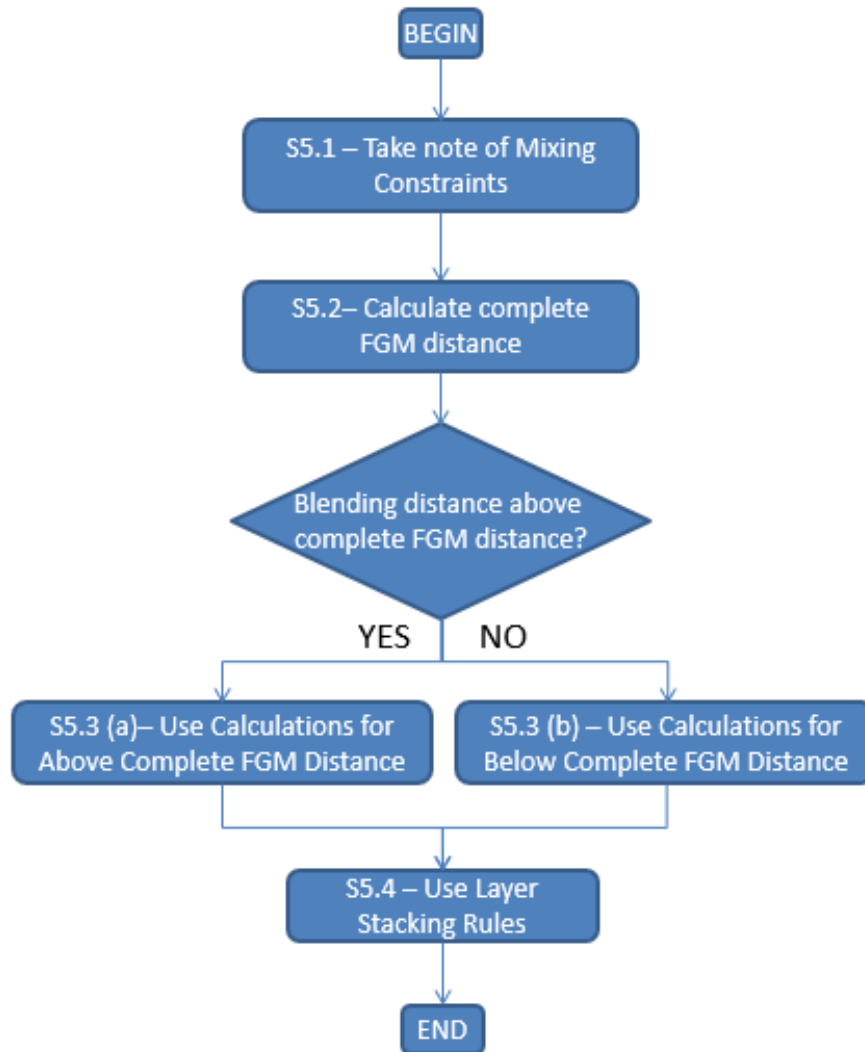


Figure 9.16: How to theoretically mix the functionally graded materials

9.7.1 Take note of mixing constraints

The mixing constraints ensure that the theoretical material mix will be as close as match to the physical mix as possible. The materials must mix in 0.5% increments, and blend from a relative 100% of the first material mix, to a relative 100% of the second material mix. The relative mixes account for situations where the material mix at either FGM extremity does not constitute a single material, but multiple materials, and therefore have negligible influence.

9.7.2 Calculate complete FGM distance

The complete FGM distance is that required to mix from 100% of the first material mix to 100% of the second material mix at the minimum deposition resolution of the AM hardware. The AM hardware available to the researcher has a minimum resolution

of 0.1 mm, and therefore this value will be used. As stated, the material must mix in 0.5% increments, from 100% of the first material, to 100% of the second material. This means that there can be no more than $100/0.5 = 200$ SUMC layers.

The first constraint of section 5.4.2.2 was to ensure that each SUMC had at least 3 layers at minimum AM resolution within. As there are a maximum of 200 layers, and each layer can be a minimum of 0.1×3 thick, **the complete FGM distance will be $(0.1 \times 3) \times 200 = 60$ mm.**

The complete FGM distance of 60 mm is well below the blending distance of 500 mm, therefore calculations for **above** the complete FGM distance will be used in the next sup step.

9.7.3 Use calculations for above complete FGM distance

Depending on the SUMC thickness and AM minimum resolution, there can be up to five sub steps needed to calculate the SUMC layer thickness for above the complete FGM distance. The calculations for this test case are as follows:

1) Finding SUMC Thickness:

$$\begin{aligned} \text{SUMC Thickness} &= \frac{\text{FGM blending distance}}{\text{Number of SUMC Alterations}} \\ \Rightarrow \text{SUMC Thickness} &= \frac{500}{200} = 2.5 \text{ mm per SUMC} \end{aligned}$$

An integer value is returned when dividing this thickness by the AM minimum resolution. As such, there is only one SUMC layer thickness value, and no interpolation to find the thickness of two SUMC layers is required. The five sub steps simplify to the one sub step already carried out above.

Confirmation:

$$\begin{aligned} \text{Composition of FGM} &= (\text{No. SUMC 1} \times \text{SUMC Thickness 1}) + (\text{No. SUMC 2} \times \text{SUMC} \\ \text{Thickness 2}) &= (200 \times 2.5) + (0 \times 0) = \mathbf{500 \text{ mm}} \end{aligned}$$

9.7.4 Use layer stacking rules

When using two different SUMC layer thickness values, stacking rules are required to place each SUMC layer. However, layer stacking rules are not required in this test case, as the layers are all of one thickness.

9.7.5 Conclusion

Likewise with the previous step, this step too is robust. The mixing constraints are set for current state of the art AM hardware. In the future, these constraints may change to lower values as hardware ability improves. The calculations for the thickness of FGM layers to ensure an integer number of complete layers perform as expected.

9.8 Step 6 - Material Choice

Material choice is split into six sub steps, as seen in figure 9.17.

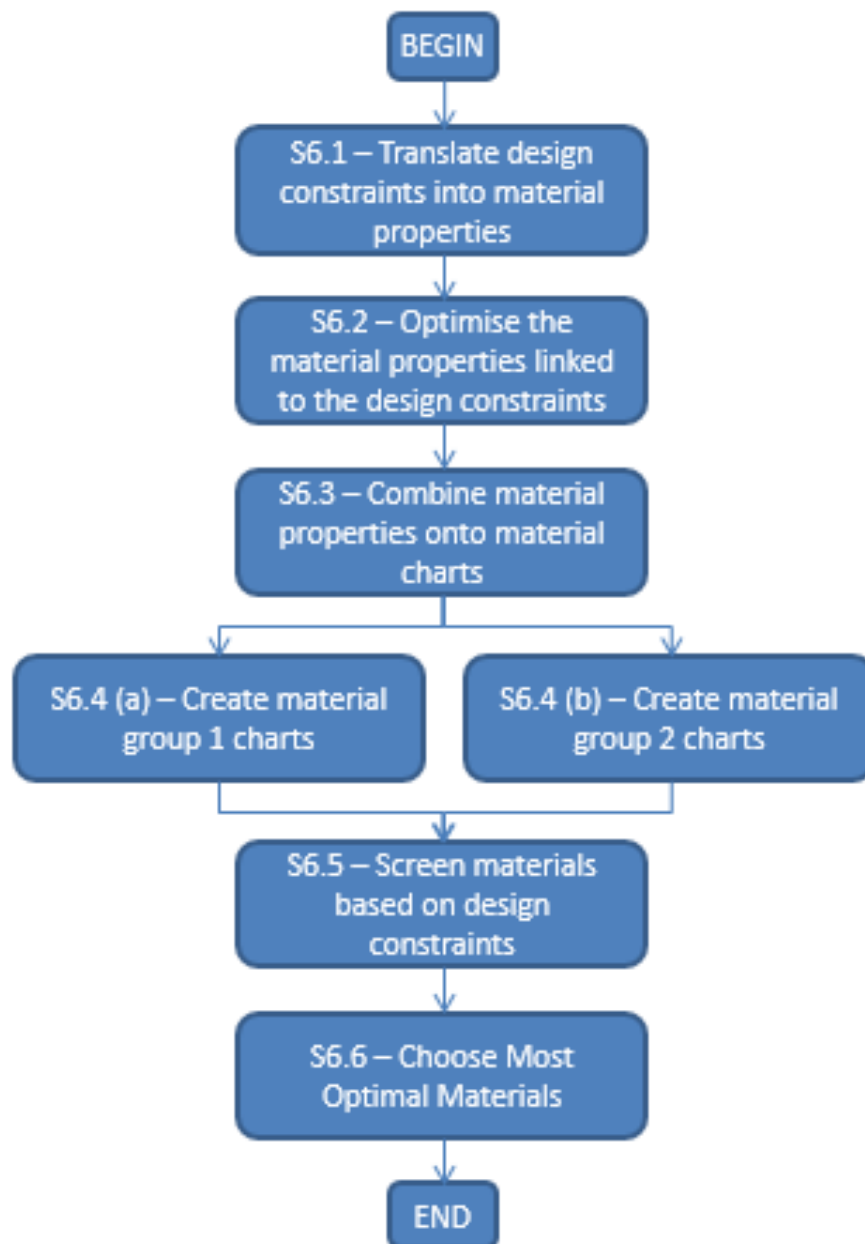


Figure 9.17: How to choose materials for the part

9.8.1 Translate design constraints into material properties

Depending on the design constraint, this sub step may require intuition on behalf of the designer.

The primary design constraint given in this test case is to maximise the stiffness. This is done through minimising the displacement of the arm.

The equation for displacement, seen in section 9.3.2, is:

$$\text{Displacement} = \frac{maL^3}{3EI}$$

The material properties are Young's modulus, and, by extension, second moment of area.

9.8.2 Optimise material properties linked to design constraints

9.8.2.1 Displacement

The design has already been altered to a new form in Section 9.4.3. Therefore, it will not be altered a second time, and thus the second moment of area will remain unchanged.

Rearranging the displacement constraint equation in terms of Young's modulus gives:

$$E = \frac{maL^3}{3Ix}$$

Plugging in the values for each variable gives = $\frac{4.375 * 9.81 * 0.5^3}{3 * 7.9676e^{-7} * 0.00025} = 8.978e^9$ Pa

This shows that, with the updated form, the Young's modulus of the part can be reduced from that of aluminium ($69 e^9$) to $8.978 e^9$.

9.8.3 Combine material properties onto material charts

This new Young's modulus value can be plotted on a graph with the combined Young's modulus values. As there are no restrictions in the specification denying the use of polymers, both metallic and polymer materials are investigated. Figure 9.18 shows the metallic materials, figure 9.19 shows the polymer materials. Materials which are not possible are omitted - two fibres without any matrix to bind them and fibres on their own. As described in section 5.4.3.3, **the properties for all combinations containing either CF or GF are calculated at 30% fibre volume fraction**, e.g, 30% CF reinforcement and 70% ABS matrix. This volume fraction was chosen based on literature^[204] to ensure that the fibre-rich end of the part had a fibre volume fraction of 60%. This limit of 60% was set to ensure that fibre-dryness does not occur - a phenomenon that occurs when there is not sufficient matrix to bond the fibres

together, thus leading to increased fibre pull out and poor material properties of the composite. Figure 5.31 in section 5.4.3.3 illustrates the composite material blend.

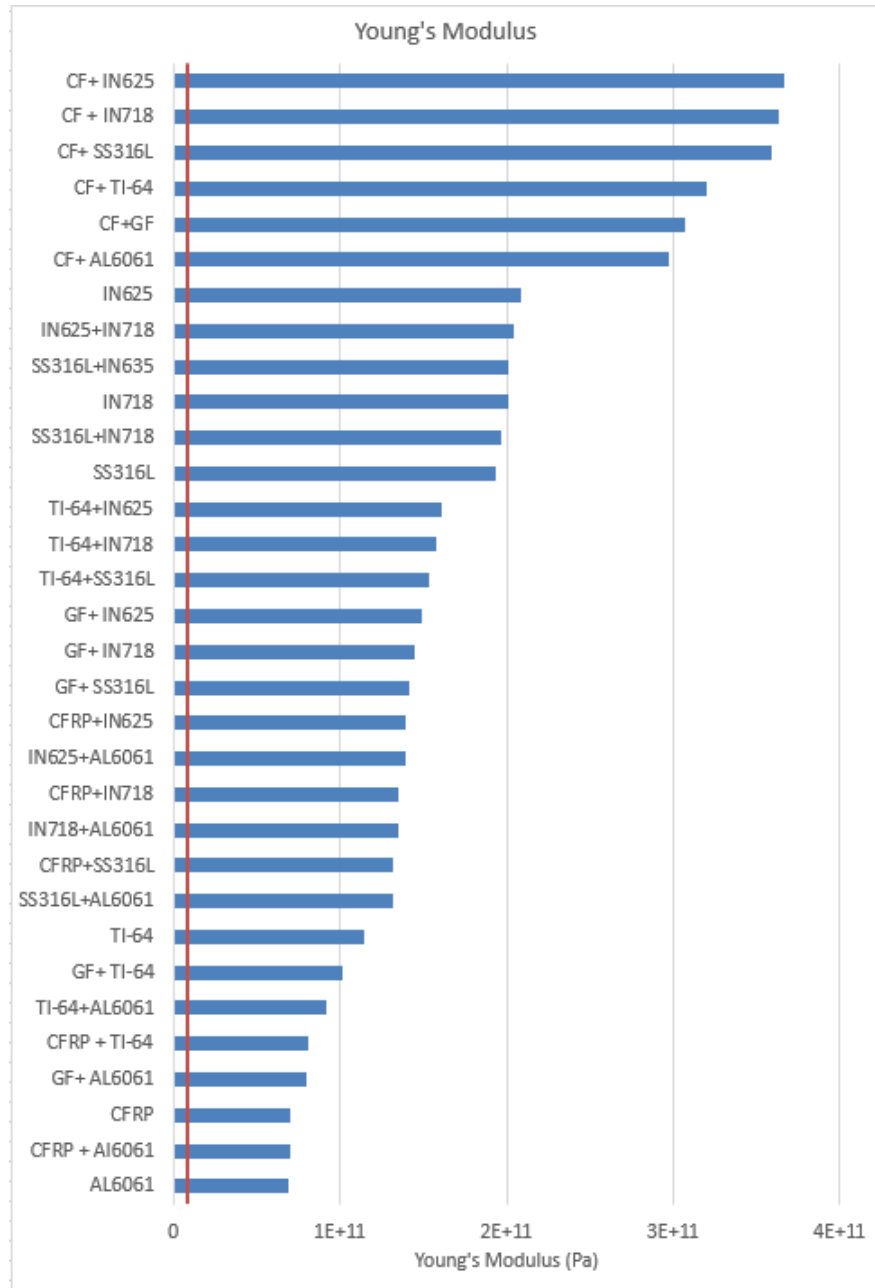


Figure 9.18: Combined Young's modulus values for metallic materials

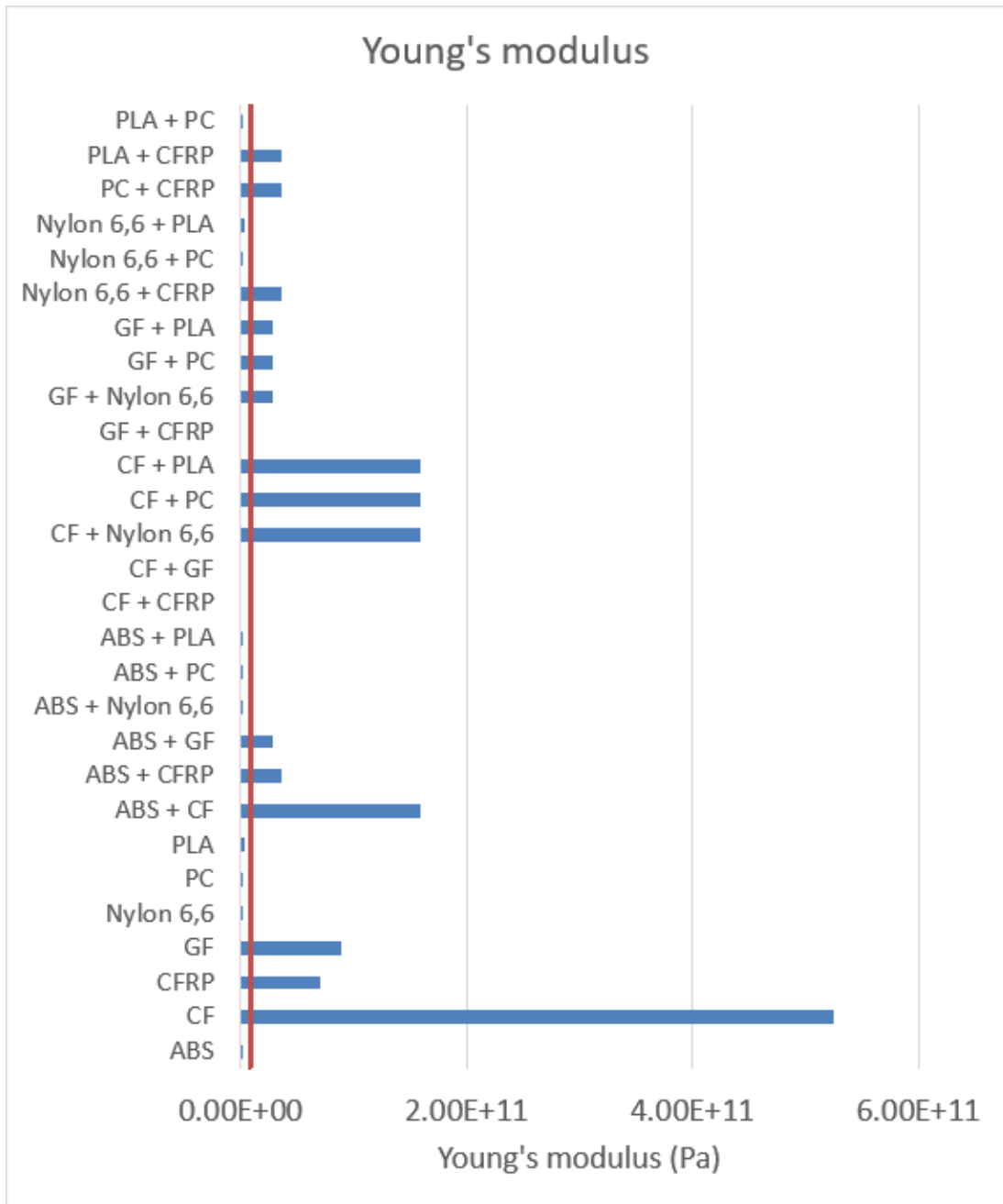


Figure 9.19: Combined Young's modulus values for polymer materials

9.8.4 Create material group charts

As seen, all metallic materials pass the Young's modulus constraint in figure 9.18. Figure 9.19 shows that none of the virgin polymers pass the Young's modulus constraint. However, many of the polymer - fibre materials do pass the constraint. Rather than the fibres being set in a epoxy matrix (as is the case with most composites), a different polymer is used. The values from figure 9.19 (omitting CF and GF, as neither can be used without a matrix) are plotted against their density. This is shown in figure 9.20.

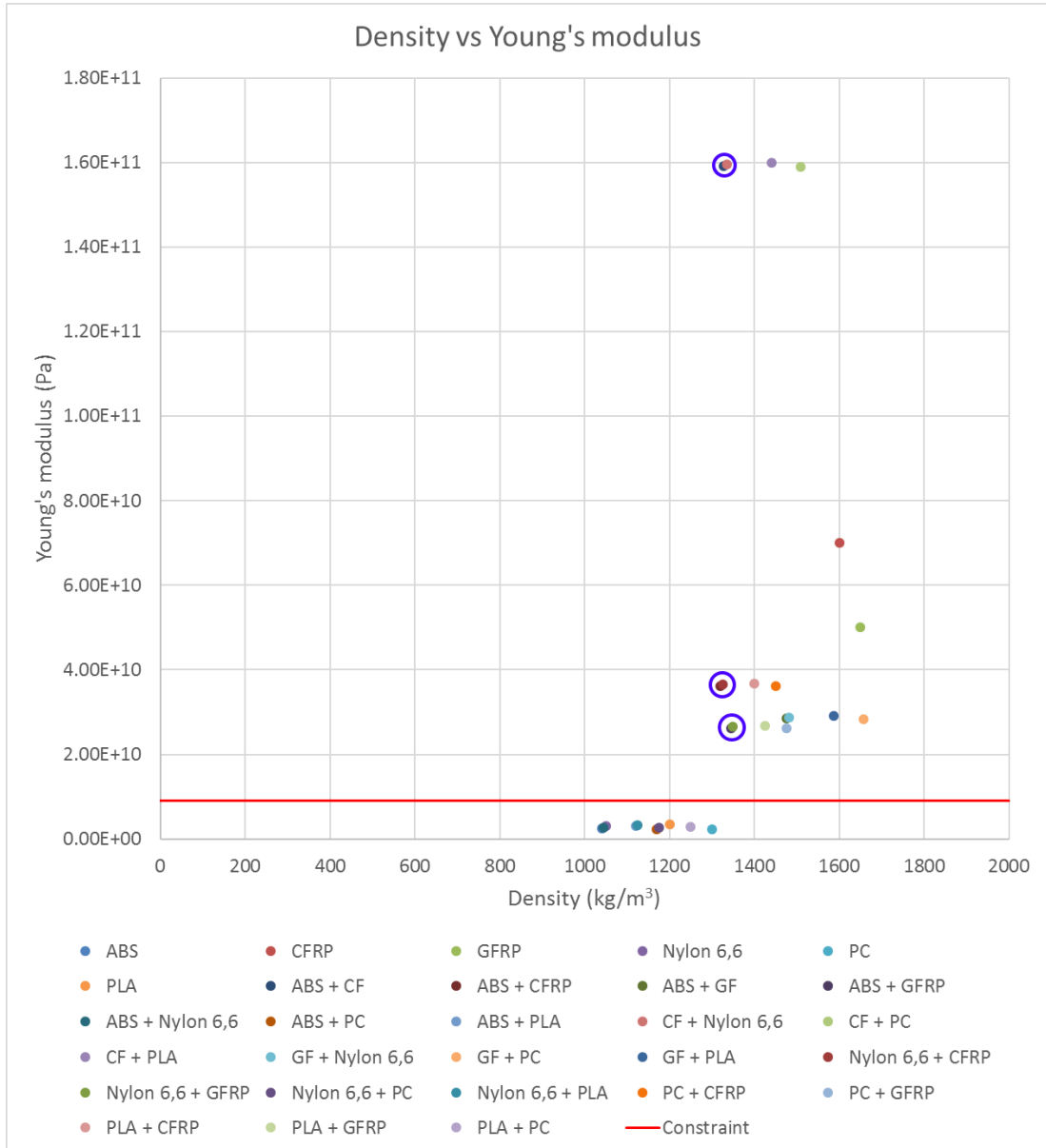


Figure 9.20: Combined density against Young's modulus values for polymer materials

9.8.5 Screen materials based on design constraints

The arm link is aimed to be as light as possible. Therefore, materials with a lower density are preferred. Four materials are circled from figure 9.20 (two in each circle). They are, from top to bottom:

- Nylon 6,6 and CF
- ABS and CF
- Nylon 6,6 and CFRP
- ABS and CFRP

9.8.6 Choose most optimal materials

As shown in sections 5.4.3.7 and 5.4.3.6.2, the dimensions required to fit two distinct materials (such as a composite plus polymer) into an FGM part are far higher than those of the arm link in this test case. For that reason, all the combinations containing CFRP are ignored. This leaves two options - Nylon 6,6, CF and ABS, CF. Both are far above the Young's modulus constraint. Therefore, the combination with the lower density will be chosen. **ABS - CF is thus chosen as the material of choice.**

9.8.7 Conclusion

Akin to eliciting the design requirements in step 9.3, converting the design requirements into material properties requires engineering knowledge. In future iterations of the guidelines, a database of design requirement-material property relations would be useful. Nonetheless, the current process correctly identifies the relationship between design constraints and material properties

Altering the form in step 9.4 allows the materials to be altered at this stage. Combining material properties is verified in literature as a valid technique for FGMs on the macro scale^[83]. Overall, this is a simple technique which can shed further mass from the part. Future work could make a GUI to aid the material selection process.

9.9 Step 7 - Computational Testing: Pre-Processing

There are six sub steps required for the computational pre-processor, shown in figure 9.21.

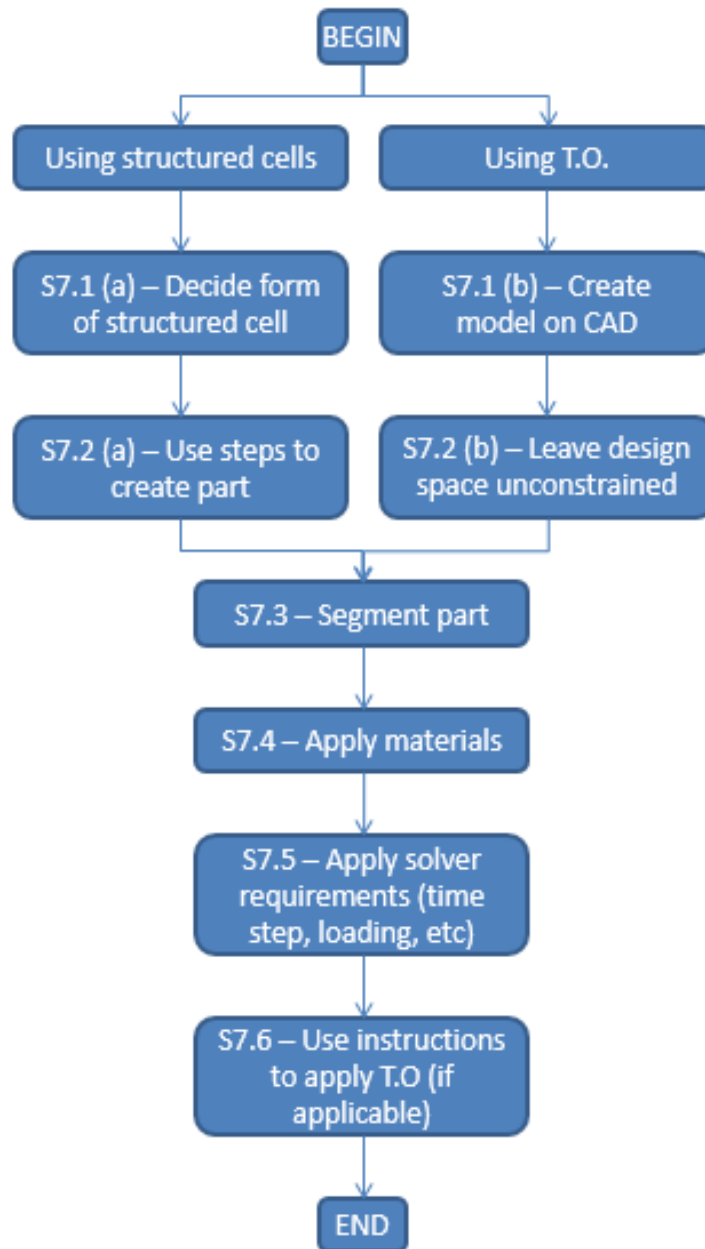


Figure 9.21: The steps required to set up the computational pre-processor

9.9.1 Decide form of structured cell

Section 9.5 concluded that structured cells would be used for this part. The first step is to decide the form of the structured cell. This depends on the loads on the part and space available. Axial loading in the direction of gravity is the greatest loading on this test case. The orientation of the second robotic link will apply a low torsional load to the test case, also. There is 3 mm available to fit the structured cell, so form must fit within this and provide the required stiffness. As such, an ‘X’ shaped cell is chosen, as it has been proven to resist loading from multiple dimensions effectively^[25]. The

researcher decided to make the cells have an aspect ratio as close to 1 as possible, as the loading is from multiple dimensions.

9.9.2 Use steps to create part

The steps required to create the part and demonstrated in section 5.5.2.1.1. There is only one cell in the radial direction, shown in figure 9.22.

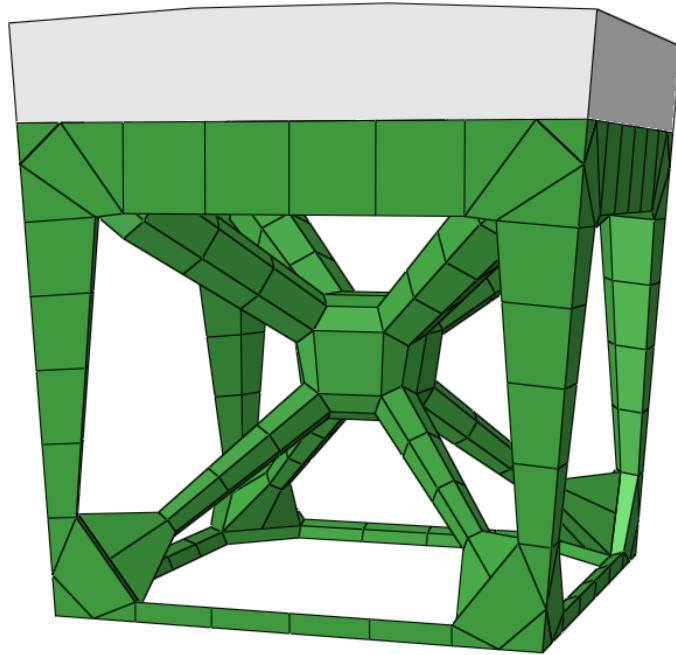


Figure 9.22: The structured cell with outer skin used in the test case

Once placed together, the inner surface is that seen in figure 9.23.

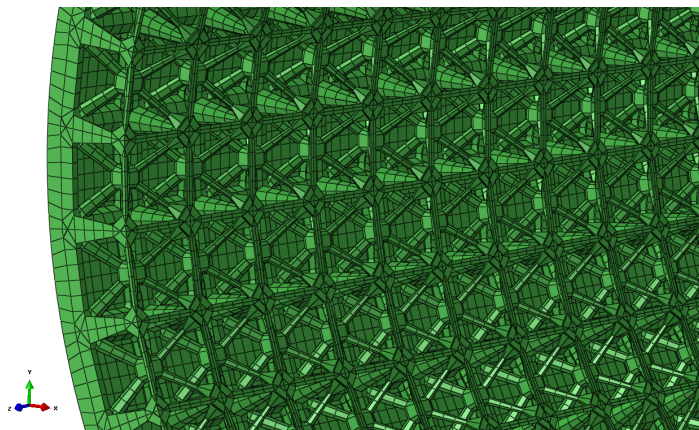


Figure 9.23: The inner surface of the test case

9.9.3 Segment part

The part is segmented at the interface between each layer of structured cells. Each layer is 2.5 mm thick, as calculated in section 9.7.3. This distance was chosen as it was convenient to segment at each structured cell interface; though the distance could have easily been reduced to segment each structured cell multiple times.

9.9.4 Apply materials

A layer-unique material is applied to every SUMC. To do this, a set for each layer of cells is created, and then called when the unique material is applied. There are 200 layers, and thus 200 materials.

9.9.5 Apply solver requirements

There are four solver requirement inputs required for this test case.

1. **Coupling constraint** A coupling constraint is created at the free end of the arm to link the geometric centre (around the axis of rotation) to the various features.
2. **Step** A time step is created to simulate the loading due to payload on the arm.
3. **Boundary conditions** One end of the arm is fully fixed to mimic the base plate of the robot arm.
4. **Load** The load calculated in section 9.3.2.1 is applied to the geometric centre linked to the coupling constraint.

9.9.6 Conclusion

This step tests the functionality of using structured cells during the pre-processor of the computational testing step, as compared to section 6 which tested the use of T.O. As shown, the step successfully creates a structured cell design for the part. However, future work may include a substep for testing various structured cells before applying them, as this would ensure that cells do not need to be altered if they fail during the processing stage

9.10 Step 8 - Computational Testing: Processing

The sub steps required for the processing stage of the computational testing are shown in figure 9.24.

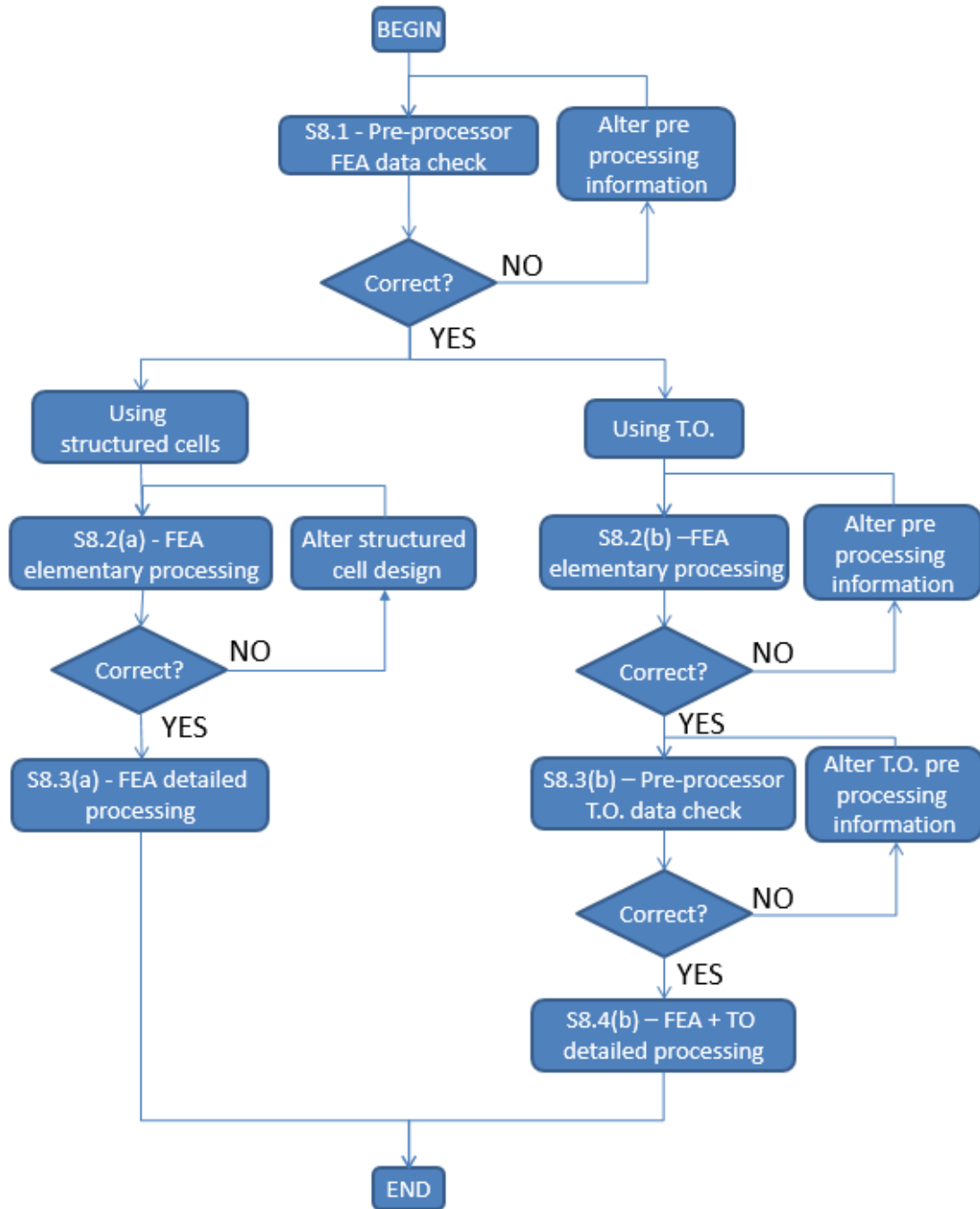


Figure 9.24: The steps required to set up the computational processor

9.10.1 Pre-processor FEA data check

The pre-processor data check ensures that all information input during the creation of the simulation is correct. The test case passed the data check, and therefore elementary processing could begin.

9.10.2 FEA elementary processing

The length of the test case will be altered, rather than the mesh size. This is to ensure the form of the cells remains unchanged, as altering the element mesh size alters the overall form of the structured cell (due to construction techniques used).

The length of the test case will be reduced from 500 mm to 100 mm. This will increase the 4.375 kg mass at the end of the arm as follows:

$$4.375 \times 500/100 = 21.875 \text{ kg}$$

Because the arm is shorter, the material percentage change between each SUMC will increase from 0.5% to 2.5%.

The maximum displacement is 0.25 mm. However, the current design (seen in figure 9.22) fails this constraint with a displacement of 0.58 mm, as seen in figure 9.25.

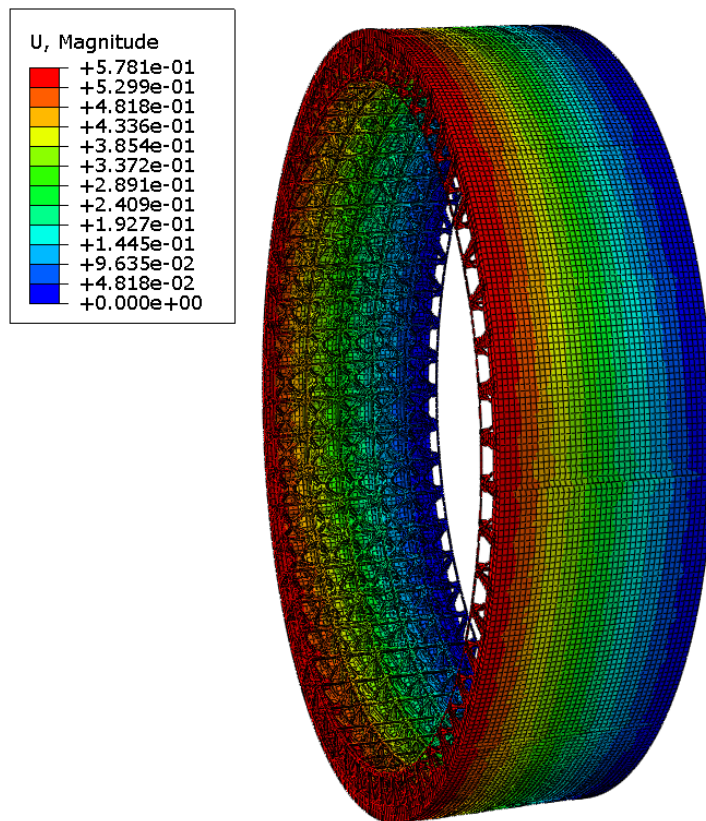


Figure 9.25: Evidence that the original structured cell is too flexible

The steps of the computational process in figure 9.24 show that if the FEA elementary processing is not correct, the cell design must be altered. The script written to create

the structured cells allows the dimensions of the struts to be changed. The struts are increased in thickness to that seen in figure 9.26.

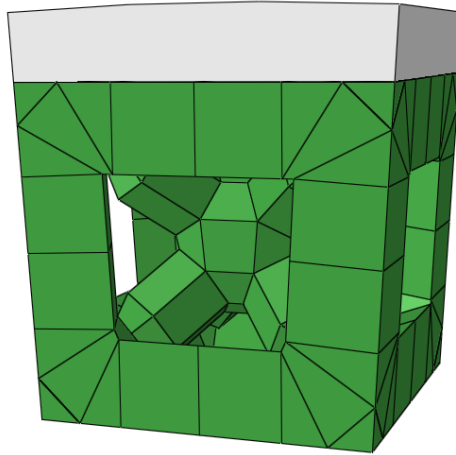


Figure 9.26: Increasing the strut thickness in the structured cell

This higher density cell reduces the maximum displacement to 0.24 mm, as seen in figure 9.27).

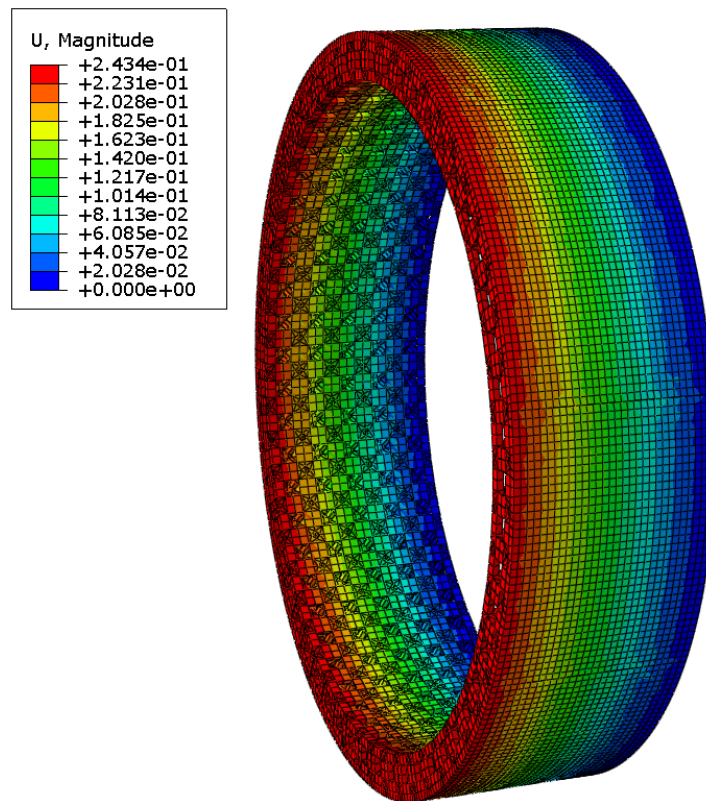


Figure 9.27: The results showing the displacement with the larger structured cells

The elementary processing is thus passed. The next sub step of the computational

processing stage is the detailed processing phase.

9.10.3 FEA detailed processing

The final step is to undertake the detailed processing. The arm link is altered to its correct length of 500 mm. This allows 200 2.5 mm SUMCs to be placed, and thus the material percentage change between each SUMC drops back to 0.5% from 2.5% used in the elementary tests. The mass at the end of the arm is altered to the correct value of 4.375 kg.

The deflection magnitude increases from by 0.15% from 0.2434 mm to 0.2437 mm. This increase is negligible, and assumed due to rounded errors while interpolating the material properties for each SUMC from the properties of the two constituent materials.

As expected, the stresses in the part drop between the elementary test and the detailed test, due to the lower material percentage change between each SUMC. This has been seen in the the preliminary test case in section 4 and the computational testing stage test case in section 6.

9.10.4 Conclusion

This step tests the processing stage of computational testing when using structured cells. The elementary FEA processing shows that the displacement is too high, and therefore the cell design has to be altered. This is successfully done to reduce the displacement within the constraint value. As mentioned in the conclusion of section 9.9, rather than having to alter the structured cell design, future iterations of the design guidelines could include a design and testing stage of the structured cell, in order to produce the most optimal form possible.

9.11 Step 9 - Computational Testing: Post-Processing

Smoothing of the part is not required, as topology optimisation was not used. As the part is not being altered (via smoothing), no validation of the part is required either, as it would be a direct repeat of the FEA detailed processing test done in section 9.10.3.

9.12 Step 10 - Heat Flow Testing

The final step is to simulate the heat flow during deposition, to ensure that the residual stresses will not be greater than the yield stresses of the constituent materials. As is the case with single-material additive manufacture, it is hypothesised that the highest

stresses will be at the interface between the print base and the part, and at any features with small cross sectional areas.

The steps described in 7.3 and shown in figure 7.6 were used in this test. As noted in the conclusion of Section 8, while the researcher is confident of the heat transfer mechanics built into the heat flow guidelines, the heat flow model itself is not yet validated with physical experiments, and therefore any user should use the ideas as a template for their work only.

9.12.1 Step 1 - Segmenting the part

As this is a continuation of testing the entire guidelines, the part is already segmented.

9.12.2 Step 2 - Applying the FGMs

In order to find the residual stresses the materials must be given thermal expansion, Young's modulus and Poisson's ratio values in addition to the parameters they already have, as described in section 8.2. Once these parameters are included, the FGMs are applied automatically using the written code.

9.12.3 Step 3 - Creating and attaching the print bed

Akin to section 8.1.3, the print bed is sized automatically to be 50% wider and 50% taller than the part. The centre of the part is aligned with the centre of the print bed.

The print bed itself is modelled as glass.

9.12.4 Step 4 - Creating the tool path

As the part is elliptical, a layer-wise elliptical tool path was chosen. This is done with a double nested loop, which steps around the circumference of all the cells within the layer, before moving to the next layer and repeating the process. The positions of the centre of each structured cell are written to a .txt file for later use.

9.12.5 Step 5 - Deactivating the deposition deposition segments

All the structured cells are deactivated to leave the print bed itself, as done in section 8.1.5 during the third test case.

9.12.6 Step 6 - Heat transfer conditions

Similar to step 6 in section 8.1.6, the emissivity value for radiative heat transfer is calculated as an average of the emissivities of the two constituent materials. The value

is 0.948. Convective surface cooling was set on the print bed surface and the external surfaces of each structured cell, with a film coefficient of $8.5 \text{ W/m}^2\text{K}$. The ambient temperature was set as 293 K.

9.12.7 Step 7 - Heat print bed and deposition segments

The print bed was heated to 373 K. The carbon fibres are not melted, as this would both remove the mechanical benefits of the fibre and require extreme temperatures. The ABS only requires melting before deposition. A value of 523 K is chosen for this.

9.12.8 Step 8 - Sequentially reactive the deposition segments

The structured cells are reactivated in the order they were set during the tool path creation, using the .txt file written during the tool path creation. In this case, a coupled thermal-displacement step is used, to allow the residual stress in the part to be measured.

9.12.9 Step 9 - Set nozzle velocity and heat source conditions

The creation of the nozzle velocity follows the same method described in section 8.1.9. From literature, the laser power required to deposit ABS is 100 W. The laser spot size was set at 5 mm, giving a laser intensity of $\frac{100}{0.005} = 20000 \text{ W/m}^2$. The nozzle velocity was set at 0.1 mm/s. As a result, the part would take roughly 5000 seconds to deposit.

9.12.10 Step 10 - Apply radiative surface heat flux

The surface heat flux is initially set at 1 W/m^2 , for the same reason as explained in section 8.1.10. This time it will be altered to 20 kW/m^2 , as this is the calculated laser intensity for this case study.

9.12.11 Step 11 - Set cooling rate for part

The part is set to cool from deposition temperature (573 K) to ambient temperature (293 K), giving a ΔT of 280 K. The time required to cool is set at 500 seconds, giving an average cooling rate of 0.56 K/s.

Once cooled, the part has stress concentrations at the interface with the print bed and the features with small cross sectional areas. As can be seen in figure 9.28, the stress concentration is seen only at the interface between the print bed and the part, as this is the point in the model where the materials in the model are most dissimilar. The FGM principle ensures that the residual stresses between the layers of the part are low.

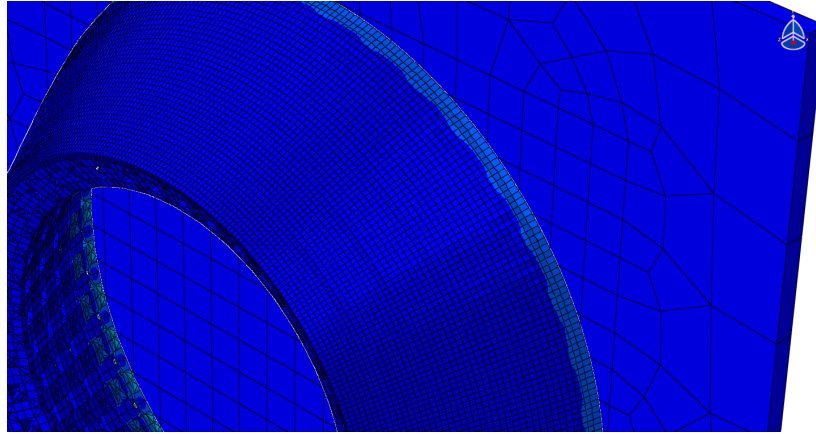


Figure 9.28: The stress concentration at the interface between the print bed and the part

Focusing on the internal cell structure at the interface between the print bed and the part shows the highest stress concentration, as seen in figure 9.29.

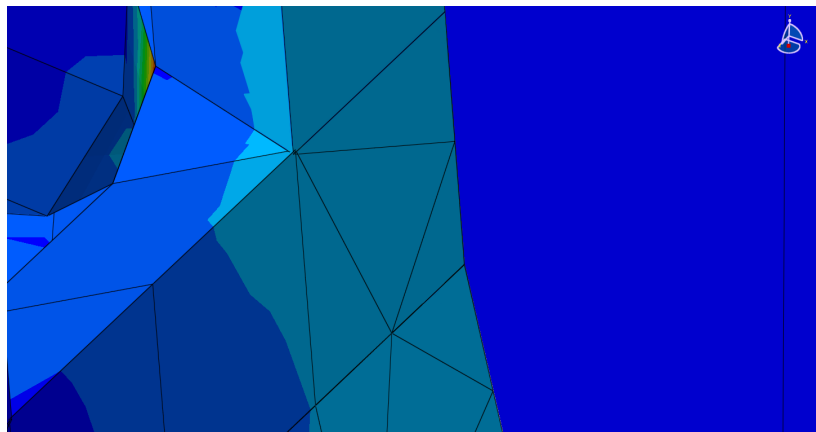


Figure 9.29: The stress concentration at the features with the smallest cross sectional area

The success of the FGM in keeping residual stresses low is seen in this example. To further demonstrate this, the material properties of the central layer in the part are altered. The result is seen in figure 9.30.

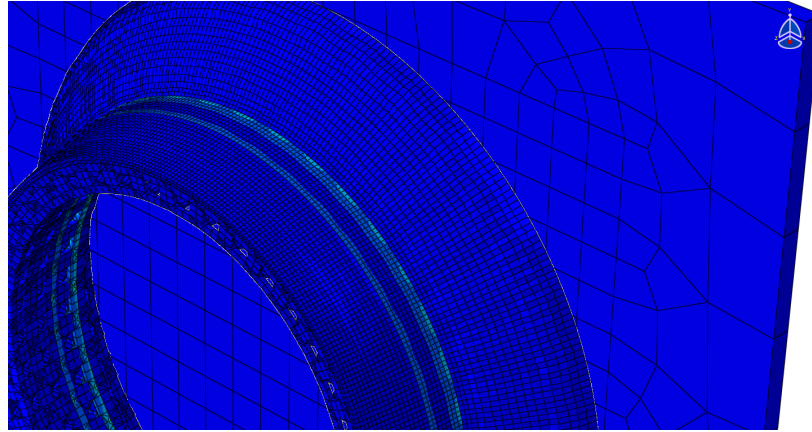


Figure 9.30: The stress concentration moves when material properties are altered

The largest stress concentration has now moved from the interface between the print bed and the part, to the layer that no longer fits the FGM methodology. This shows that the stress concentrations are being measured correctly.

The residual stress is measured to ensure it is below the yield stress of the constituent materials. If the residual stress anywhere in the part is above the constituent material yield stress, the part must be redesigned in order to reduce the stresses, otherwise the part will warp. If below yield stress levels but still undesirably high, the cooling conditions can be altered, or post production heat treatments can be applied.

The yield stress of the two constituent materials and the maximum residual stress in the part from figure 9.28 are shown in table 9.4.

Table 9.4: Yield stress of constituent materials

Material	Yield Stress
ABS	43 MPa
Carbon Fibre	2500 MPa
Max residual stress	55 kPa

The largest residual stress in the part is seen on the thinned struts within the structured cells closest to the interface of the print bed and the part. The value of this residual stress is 55 kPa, far below the yield stress value of either constituent material in the part. For this reason, no serious stress-related manufacturing problems are expected during deposition.

9.12.12 Conclusion

The heat flow guidelines were tested successfully on the robotic arm gripper in section 8. The set up is very similar in this section. The animation of the tool path shows

that the elliptical design effectively lays down each segment as expected. The residual stresses are low in this part when compared to the yield stresses - this is in part due to the relatively low thermal gradient between deposition temperature and ambient temperature. However, as mentioned in Section 8.2, these residual stress values are based on a heat flow model that is yet to be validated with physical experiments, and therefore the researcher cannot recommend the use of this technique until the user has validated their own heat flow values with physical experiments.

9.13 Conclusion

As stated, the manufacturing steps cannot be tested due to financial constraints on the project. This test of the guidelines, and the experimental stages of this thesis therefore conclude at this point, having shown that form, structure, material and manufacturing technique can be brought together successfully to reduce the mass of a robotic arm link. However, before funding constraints were realised, a design for physical experiments was made by the researcher in order to test the design guidelines. This experimental design is shown in Appendix B (chapter 13).

Chapter 10

Discussion

The discussion chapter will be broken into three stages, focussing on the research questions, the research methods used, and the overall approach of the work.

10.1 Reflection on research questions

The overall research question laid out in section 1.2 was:

how effectively can topology optimisation, structured cells, FGMs, alterations to form and additive manufacture be merged in order to reduce the mass of robotic arms?

and was divided into the following questions:

1. What effect does altering form have on the possibility of incorporating TO, structured cells and FGMs?
2. If AM manufacturing restrictions are put in place, are the stress-reduction benefits of FGMs present?
3. Does FGM + TO mixing work?
4. Does FGM + structured cell mixing work?
5. How effective are these mixing techniques? Use physical testing to find this out.
6. If the above techniques can be used to reduce the mass in robotic arm links?

Each question will be looked at in turn.

10.1.1 Q1) What effect does altering form have on the possibility of incorporating TO, structured cells and FGMs?

Ideally, this question should have prompted research into combining different shaped structural cells, as this may have allowed structured cells to be used in more applications that what the guidelines in this thesis allow. However, due to time and skill limitations, the influence of form on the feasibility of using TO, structured cells and FGMs was not explicitly tested. Rather, its effect was predetermined using rules that were put in place to dictate what forms could use what combination of TO, structured cells

and FGMs. These rules were established from known restrictions which are inherent in structured cells (of the same shape) and topology optimisation, mostly related to geometry. As said, this question ended up being a restriction rather than a route for greater exploration, and therefore it was not well-answered.

10.1.2 Q2) If AM manufacturing restrictions are put in place, are the stress-reduction benefits of FGMs present?

AM manufacturing restrictions were kept as generic as possible. This was done for one reason - it would mean that the restrictions could be applied to a wider range of AM techniques. With these generic restrictions, it could be seen that the stress-reduction benefits of FGMs are present, as is shown in the preliminary test case of Section 4, and in line with literature. However, there is an argument for incorporating technology-specific restrictions into the work - doing this would give finer tuning to the guidelines, in turn making them reflect each AM technology more closely, and therefore increasing their credibility. This is something which should be done in the future as there will be nuances with each technology which are currently missed. Therefore, while it can be said that this question was answered, it is perhaps not a fully rounded answer, as the additional technology-specific restrictions may alter the credibility of FGMs for reducing stresses when made using AM.

10.1.3 Q3) Does FGM + TO mixing work?

Computationally, with the material combinations discussed in the thesis and the generic restrictions discussed above, it can be said that the merging of FGM and TO is successful. This is of no great surprise, as the TO solver is well established in the FE software, and the FGMs were demonstrated to work computationally in the preliminary tests. However, no physical builds were made, and therefore potential issues with material incompatibility never had to be addressed - this could be a potential issue for real-world FGM combined with TO. That being said, that is an issue for FGMs themselves, not an issue that would be borne solely out of the combination of TO and FGMs -there is no reason to believe that an AM process that could make non-TO FGMs (as demonstrated in literature) and that could also produce TO parts (such as PBF) would not be able to make FGM-TO parts. Computationally, the main issue for combining FGMs and TO is material representation techniques, and the one used in this thesis (identical to that used by Zhang et al.^[217]) did produce positive results - lightweight parts with gradually-blended materials.

10.1.4 Q4) Does FGM + structured cell mixing work?

The answer to this question is very similar to that above - the concept worked computationally in this thesis, however, it was bounded. In this case Section 9 showed that, computationally, with the generic AM restrictions put in place to allow the FGMs to be manufactured and manually-built structured cells, parts could be successfully modelled. The modelled structures were both light (due to the structured cells) and had gradually-blended materials (due to the modelled FGM). However, no real-world examples were produced, so stating that “FGM and structured cells work” is a simplification which cannot currently be validated. In order to answer this question more confidently, the AM restrictions would have to be more specific, a larger range of structured cells would have to be tested, and the parts would have to be physically produced and tested. However, as stated above, it can be said that mixing FGMs and structured cells was computationally-successful when generic AM restrictions for producing FGMs and a limited sample of manually-built structured cells were used as boundaries.

10.1.5 Q5) How effective are these mixing techniques? Use physical testing to find this out.

As discussed previously in this thesis, physical testing was not carried out due to financial restrictions. In the researcher’s opinion, this lack of physical validation is the largest issue with this piece of work, and a priority for future work. Therefore, in order to evaluate this question, the answer must be based on the computer simulations. The researcher is confident of two things: a) that the software used provides accurate results, as its use is widespread throughout the engineering field, and b) that the inputs to the software were correct, albeit simplified, as they were based on values and equations from literature. “Effectiveness” can therefore be said to be “promising”, but that the ideas must be physically tested to fully answer this question.

10.1.6 Q6) If the above techniques can be used to reduce the mass in robotic arm links?

The answer to this question can be largely inferred from the previous answers - the researcher believes that, in their current state, the techniques show promise, and the possibility of them reducing the mass of robotic arm links would be described as “probable”. However, until the issues discussed above have been investigated further (material instability, generic AM restrictions, TO and structured cell integration in real life examples), it **cannot** be stated with any certainty that “the above techniques can be used to reduce the mass in robotic arm links”.

The answer to the overall research question is therefore that there is scope for topology optimisation, structured cells, FGMs, alterations to form and additive manufacture to be effectively and successfully merged in order to reduce the mass of robotic arm links, however, further work is required before it can be confidently said that combining these techniques will definitely produce lightweight parts that can be used in real world situations.

10.2 Reflection on research methods used

This section aims to discuss the different research methods used during the thesis. In this case, that is the literature review, followed by case studies and where possible, validation.

10.2.1 Literature Review

Unless heavily involved in a research field, a literature review is advised for any project. This work used a “classic” approach rather than “systematic”, a necessity given the relatively loose scope of the work, as it not only left the original/main review unbounded, but also allowed for further literature to be searched for at later points through the study, without any detriment to rationale used in the original/main review. If the work had a tighter scope, a systematic approach could have been used - argued by some to be more thorough, however, it would have been impractical for the reasons that the “classic” approach was beneficial. As can be argued with many literature reviews, there will be areas that could have been researched in more depth, however, the researcher believes that the review in this thesis found the required information needed to give both themselves and any reader the sufficient knowledge in order to undertake and/or digest the later work.

10.2.2 Case study

Overall, the use of case studies/test cases for this thesis was a good decision - test cases are a powerful technique to assess the function of a rule/guideline base as they have the capability to find any potential weaknesses. However, this capability is heavily influenced by the test case itself - one which is too “easy” will not bring out the weaknesses in a particular function, and vice-versa. The test cases in this thesis were all linked to robotics - mostly robotic arm links. As noted during the introduction, the guidelines themselves can be applied to any structural part requiring lightweighting, and there are undoubtedly test cases more demanding than those used in this thesis that could have been used (and more appropriate given the cost required to make a part as described in the thesis). As mentioned numerous times, physical testing would

have been ideal in this work as it could have been used as a validation method for both the guidelines and the test cases, thus giving more credence to the particular test cases in the thesis - either reinforcing their findings, or rejecting them and thus acting as a base for further development. All this being said however does not take away from the test case research method itself, and the researcher believes that the use of them in this thesis was the correct decision in order to prove out the concepts put forward, and the same decision would be made again, with or without physical testing.

10.3 Reflection on overall approach

This section will focus on the approach the researcher took, including any strengths and weaknesses of the work.

As discussed above, the use of literature review is near-mandatory, and test cases are a powerful technique for assessing capability, and one which would be used again if the project were to begin afresh. The greatest strength of the approach used was its ability to be reactive to the project situation - the guidelines were written based off the perceived difficulty of the first test case, and the further test cases were contrived based on the situation at the time, be it to further test aspects of the guidelines deemed important to evaluate further (in the case of the second test) or to fill the void of physical testing when it became clear this was not an option (in the case of the heat flow work). If a more rigid structure had been used, unforeseen avenues of research, such as the heat flow work, would never have been explored. Conversely to this, the lack of structure resulted in a project with a loose overall scope. It could be argued that this loose overall scope resulted in results that did not have as much impact as those which might have been generated from a project with a tighter scope - for example, if it was known from the outset that funds would not be available to produce and test physical parts, a different approach could have been taken that focussed on other areas in more depth, i.e., stability of material combinations. However, the nature of research often results in projects not following the intended path, and thus even if the project did have a tighter scope at the outset, unforeseen circumstances may have resulted in the requirement to change plans part way through the research.

Not a weakness per se, but rather a missed opportunity, was the use of robotics as a basis for test cases, rather than a field which would have a greater use case for the techniques described in this thesis. For example, if space or aerospace components were used as test cases, the merit of the techniques could have been more easily expressed by the researcher. In turn, the scepticism that quite rightly surrounded the application of the techniques to robotic arm links (both in terms of practical requirement and cost) would not be present. As said, this is a missed opportunity rather than a weakness, and

was a by-product that arose from the loose scope discussed above. If this project were to be run again, the initial topic of robotics would be changed to aerospace components. Although mentioned many times, the lack of physical testing cannot be ignored, as the lack of validation is deemed as the largest weakness in this body of work. The physical tests would not only have given insight into the direct practicalities of part production, they would also allowed for validation (or otherwise) of the heat flow code and resulting residual stress prediction. As mentioned above, the flexibility of scope meant that other work could be done to partially fill this gap - a positive of the approach used. The researcher had to concede to the outcome that the physical tests would not be possible and therefore conclude that the computational work in the guidelines was based on well-established mathematics and engineering principles which would indicate that the work itself is most-likely correct, however, this is far from an ideal outcome. Ideally, the physical tests would have been done, and the computational work could have been developed based on the experimental outcomes, overall resulting in a more robust piece of work.

Chapter 11

Summary of conclusions, contributions to knowledge and future work

11.1 Summary of conclusions

Small conclusions have been given throughout the thesis. This section aims to summarise these to give overall conclusions to the project.

- The literature highlighted that there were gaps in knowledge when combining FGMs, TO, AM and structured cells. In order to address the most significant of these, a test case was proposed.
- The test case showed that merging FGMs and TO was successful, when accessed in respect to reducing stress concentrations when compared to a part made from materials kept in distinct areas. It was noted that the list of possible material combinations was limited to those with similar melting temperatures and coefficients of thermal expansion, as this was deemed a reasonable boundary to place when reviewing material compatibility. Since the process is complex, and no guidelines currently exist to guide designers through the process, it was decided that a set of design guidelines should be written.
- Four focus areas that relate to lightweight part design have been addressed by the guidelines. Each step of the guidelines was iterated many times, but only the final flowcharts are shown. Rather than testing the entire design guidelines, to begin with, only the most important steps were evaluated. The first test case evaluated the computational testing steps (steps 7 and 8). Validation of the guidelines could only be done computationally, not physically, therefore it was not possible to state with certainty that the information contained within was viable. Rather, it could be stated that all techniques used had solid mathematical grounding, and therefore it could be confidently assumed that the information contained within was correct.
- The guidelines were successful in computationally designing and testing a robotic

arm gripper. The shape of the gripper was not axisymmetric around at least two axes, and therefore the guidelines led the designer to use topology optimisation. The optimised structure reduced the mass significantly, while keeping the displacement within tolerable limits, again, only computationally. A shortcoming of the design guidelines was the lack of consideration that heat flow during manufacture has on the mechanical properties of the final part. It was decided to add this into the work, due to the fact that physical experiments were not financially viable.

- The heat flow code written plotted the heat flow through the FGM robotic arm gripper, following the path set by the designer. Temperatures seen in the computation were as expected - up to the set deposition temperature, and cooling towards ambient temperature once the heat source was removed. However, since the the heat flow code could be validated, values should be taken as general trends, rather than specific temperatures at any point during the deposition. The development of the code required to combine FGMs, TO and heat flow considerations was noted as a non-trivial accomplishment. This additional step was therefore added to the design guidelines.
- The final test case for the guidelines ran through them in their entirety, ensuring that all points within worked as expected from a computational point of view. The arm link used in the first test case was used once again, though it was evaluated far more thoroughly this time around. The guidelines successfully introduced structured cells and functionally graded materials. and tested the heat flow during deposition, indicating that the yield stress of the constituent materials was below the residual stresses measured after simulating AM deposition. However, related to the point above, the yield stress information was based on outputs of the unvalidated heat flow computational work, and therefore simulated on an untested model - this was noted as a priority for future work. The manufacturing technique step of the guidelines could not be validated, as there was not sufficient capital in place to manufacture the test part. However, the experimental design was still written and shown in future work.

The conclusions show that, overall, the use of FGMs, structured cells and topology optimisation computationally-work for reducing the mass of robotic arm links. This necessity to rely on computer simulations for testing of the work rather than physical experiments was a financial restriction, and a realised short coming of the current body of research. However, the researcher is confident in the results of the computer simulations, based on the reliability of the software used and the certainty of the equations input to said software. Nonetheless, future work aims to complete physical experiments.

11.2 Contributions to knowledge

This thesis contains numerous knowledge contributions. The key knowledge contributions are listed, starting with the most significant:

- A final high level design process, giving the inputs and outputs required for every stage of lightweight robotic arm design. This has not been seen before in literature.
- The realisation that topology optimisation can be incorporated along with FGMs and structured cells to produce lightweight structures, as shown in the second and fourth test cases.
- The discovery that Abaqus can be used to successfully simulate the thermal transfer during additive manufacture of a part made using functionally graded materials.
- The creation of material application rules and mixing constraints. These rules and constraints are created to ensure the parts can be manufactured, based on the resolution of current AM hardware. A set of rules similar was not seen in literature.
- The unique approach for segmented parts using the developed distance indicators and rules to ensure consistent, repeatable material placement.

11.3 Future Work

Throughout the thesis, possibilities for future work have been seen. These are compiled in this section, in order from greatest impact to least impact.

- **Physical Experiments.** Physical experiments will allow the theoretical work in this thesis to be further validated. Although validated using simulations, the use of physical experiments adds an additional verification to the work.
- **In depth guidelines.** A comprehensive lead-through which shows how to set up the various stages in Abaqus that are needed for the design guidelines could be useful. At present, the designer must either have knowledge of Abaqus or take the time to learn it.
- **Research of material compatibility.** A boundary is currently in place in the thesis that states any material combination which has constituents with similar melt temperatures can be used in the FGM experiments. This neglects the significant possibility of material instability between the two materials when they

are combined at elevated temperatures. All proposed combinations should be physically tested to verify whether they are compatible, or not.

- **Update deposition temperatures.** Related to the above point, greater control of simulated deposition temperature during heat flow tests is required. Currently, a mid-point between the deposition temperatures of the constituent materials is taken, irrespective of the gradient between the temperatures (although only combinations with relatively low gradients are chosen). Ideally, this temperature should take into account the deposition temperatures of the constituent materials, and calculate a temperature that is best suited for both materials involved.
- **Develop scan paths.** Scan paths should be incorporated into the GUI. Doing this means the designer does not have to code the scan paths themselves, unless they want bespoke solution.
- **Wall thickness constraint.** The current wall thickness constraint is set at 3 mm. This should be exchanged for a rule which is more flexible, based on the geometry and loading of the current part.
- **Material selection GUI.** Currently in the design guidelines, material selection is based on graphs. In future, a GUI could be developed to aid the material selection process. This would be akin to that developed by Ashby^[201] for the Cambridge engineering selector.
- **Structured cell design.** A sub-step in the computational pre-processing stage that allows structured cells to be altered and tested before being incorporated into lightweight part would be useful. Structured cells would then be better developed for the arm link being designed for.
- **Material bonding characterisation.** Deepening the understanding of material bonding between layers during AM deposition will increase the accuracy of the simulations. This should be done for layer bonding between identical materials, and for layer bonding between non-identical materials.
- **Additional TO techniques.** Currently, the SIMP method is the only method used in the guidelines. This was chosen as it is well established. However, the other TO techniques have benefits which may be beneficial for designing lightweight robotic arm links. These should be tested and compared. Abaqus does not currently have the inbuilt functionality to use other techniques, hence it was not tested in this thesis.

Chapter 12

Appendix A: Python Code

12.0.1 Calculating number and thickness of layers

```
#-----  
# CALCULATING THE SLICE THICKNESSES FOR UNDER OBD  
#-----  
if OBD <= (200*AMMinRes*3): # OBD = Overall Blending Distance  
# Calculate interpolation values for the two slice thicknesses  
  
    NumberSUMLayers = int(OBD/(AMMinRes*3))  
    print 'Number SUMC Layers: ', NumberSUMLayers  
  
    SUMCThickness = float(OBD)/NumberSUMLayers  
    print 'SUMC Thickness :', SUMCThickness  
  
    LowerBoundSlices = (math.floor(SUMCThickness*(1/AMMinRes)))/(1/AMMinRes)  
    print 'Lower Bound Slices :', LowerBoundSlices  
  
    UpperBoundSlices = (math.ceil(SUMCThickness*(1/AMMinRes)))/(1/AMMinRes)  
    print 'Upper Bound Slices :', UpperBoundSlices  
  
    AbsoluteValueLowerBoundSlices = int(round((OBD-(NumberSUMLayers*UpperBoundSlices))/(LowerBoundSlices-UpperBoundSlices)))  
    print 'Absolute Value Lower Bound Slices:', AbsoluteValueLowerBoundSlices  
  
    AbsoluteValueUpperBoundSlices = NumberSUMLayers - AbsoluteValueLowerBoundSlices  
    print 'Absolute Value Upper Bound Slices:', AbsoluteValueUpperBoundSlices  
  
    FirstHalfLowerBoundSlice = int(AbsoluteValueLowerBoundSlices*0.5)  
    print 'First Half Lower Bound Slice :', FirstHalfLowerBoundSlice  
  
    SecondHalfLowerBoundSlice = (AbsoluteValueLowerBoundSlices - FirstHalfLowerBoundSlice)  
    print 'Second Half Lower Bound Slice :', SecondHalfLowerBoundSlice
```

Figure 12.1: AM slice thickness for under OBD

```

#-----
# CALCULATING THE SLICE THICKNESSES FOR ABOVE OBD
#-----

else:

    NumberSUMCAlterations = 199

    NumberSUMCLayers = 200

    # FINDING SUMC THICKNESS
    SUMCThickness = float(OBD) / NumberSUMCLayers
    print 'SUMC Thickness = ' + repr(SUMCThickness)

    # FINDING NUMBER OF AM LAYERS PER SUMC (USING INTERPOLATION)

    NumberAMLayersPerSUMC = SUMCThickness / AMMinRes
    print 'Number of AM Layers per SUMC = ' + repr(NumberAMLayersPerSUMC)

    # Finding Lower Limit

    LowerBoundSlices = AMMinRes * int(NumberAMLayersPerSUMC)
    print 'Lower Interpolation Bound = ' + repr(LowerBoundSlices)

    # Finding Upper Limit

    UpperBoundSlices = AMMinRes * math.ceil(NumberAMLayersPerSUMC)
    print 'Upper Interpolation Bound = ' + repr(UpperBoundSlices)

    if LowerBoundSlices != UpperBoundSlices:

        AbsoluteValueLowerBoundSlices = int(round((OBD-(NumberSUMCLayers*UpperBoundSlices))/(LowerBoundSlices-UpperBoundSlices)))
        print 'Absolute Value Lower Bound :', AbsoluteValueLowerBoundSlices

        AbsoluteValueUpperBoundSlices = NumberSUMCLayers - AbsoluteValueLowerBoundSlices
        print 'Absolute Value Upper Bound :', AbsoluteValueUpperBoundSlices

        FirstHalfLowerBoundSlice = int(AbsoluteValueLowerBoundSlices*0.5)
        print 'FirstHalfLowerBoundSlice :', FirstHalfLowerBoundSlice

        SecondHalfLowerBoundSlice = (AbsoluteValueLowerBoundSlices - FirstHalfLowerBoundSlice)
        print 'SecondHalfLowerBoundSlice :', SecondHalfLowerBoundSlice

        CompositionOffFGM = AbsoluteValueUpperBoundSlices * UpperBoundSlices + AbsoluteValueLowerBoundSlices * LowerBoundSlices

```

Figure 12.2: AM slice thickness for above OBD

12.0.2 Partitioning the part

```

#-----
# UNDERTAKING THE X DIRECTION PARTITIONING
#-----

for i in range(1, NumberofXSlices):
    # Step 1) - The line below draws the plane
    yzpl=mdb.models['Model-1'].parts[C].DatumPlaneByPrincipalPlane(offset=X+printLength*i, principalPlane=YZPLANE)
    # Step 2) - The line below carries out the physical partition
    mdb.models['Model-1'].parts[C].cells.findAt(((X+printLength*i, 0.0, 0.0), ))
    cells=mdb.models['Model-1'].parts[C].cells.getByBoundingBox()
    mdb.models['Model-1'].parts[C].PartitionCellByDatumPlane(cells, mdb.models['Model-1'].parts[C].datums[yzpl.id])

#-----
# UNDERTAKING THE Y DIRECTION PARTITIONING
#-----

for i in range(1, NumberofYSlices):
    # Step 1) - The line below draws the plane
    xzpl=mdb.models['Model-1'].parts[C].DatumPlaneByPrincipalPlane(offset=Y+printWidth*i, principalPlane=XZPLANE)
    # Step 2) - The line below carries out the physical partition
    mdb.models['Model-1'].parts[C].cells.findAt(((0.0, Y+printWidth*i, 0.0), ))
    cells=mdb.models['Model-1'].parts[C].cells.getByBoundingBox()
    mdb.models['Model-1'].parts[C].PartitionCellByDatumPlane(cells, mdb.models['Model-1'].parts[C].datums[xzpl.id])

```

Figure 12.3: Partitioning in the X and Y directions

```

#-----
# UNDERTAKING THE BELOW OBD PARTITIONING
#-----

if OBD <= (200*AMMinRes*3):
    if LowerBoundSlices != UpperBoundSlices:
        for i in range(1, FirstHalfLowerBoundSlice+1):
            # Step 1) - The line below draws the plane
            xypl = mdb.models['Model-1'].parts[C].DatumPlaneByPrincipalPlane(offset=Z+LowerBoundSlices*i, principalPlane=XYPLANE)
            # Step 2) - The line below carries out the physical partition
            mdb.models['Model-1'].parts[C].cells.findAt(((0.0, 0.0, Z+LowerBoundSlices*i), ))
            cells=mdb.models['Model-1'].parts[C].cells.getByBoundingBox()
            mdb.models['Model-1'].parts[C].PartitionCellByDatumPlane(cells, mdb.models['Model-1'].parts[C].datums[xypl.id])

        for i in range(1, AbsoluteValueUpperBoundSlices+1):
            # Step 1) - The line below draws the plane
            xypl = mdb.models['Model-1'].parts[C].DatumPlaneByPrincipalPlane(offset=(Z+LowerBoundSlices*FirstHalfLowerBoundSlice
            +UpperBoundSlices*i, principalPlane=XYPLANE)
            # Step 2) - The line below carries out the physical partition
            mdb.models['Model-1'].parts[C].cells.findAt(((0.0, 0.0, (Z+LowerBoundSlices*FirstHalfLowerBoundSlice
            +UpperBoundSlices*i), ))
            cells=mdb.models['Model-1'].parts[C].cells.getByBoundingBox()
            mdb.models['Model-1'].parts[C].PartitionCellByDatumPlane(cells, mdb.models['Model-1'].parts[C].datums[xypl.id])

        for i in range(1, int(SecondHalfLowerBoundSlice)):
            # Step 1) - The line below draws the plane
            xypl = mdb.models['Model-1'].parts[C].DatumPlaneByPrincipalPlane(offset=(Z+LowerBoundSlices*FirstHalfLowerBoundSlice
            +UpperBoundSlices*int(NumberSUMLayers-AbsoluteValueLowerBoundSlices)+LowerBoundSlices*i, principalPlane=XYPLANE)
            # Step 2) - The line below carries out the physical partition
            mdb.models['Model-1'].parts['Part-1'].cells.findAt(((0.0, 0.0, (Z+LowerBoundSlices*FirstHalfLowerBoundSlice
            +UpperBoundSlices*int(NumberSUMLayers-AbsoluteValueLowerBoundSlices)+LowerBoundSlices*i), ))
            cells=mdb.models['Model-1'].parts[C].cells.getByBoundingBox()
            mdb.models['Model-1'].parts[C].PartitionCellByDatumPlane(cells, mdb.models['Model-1'].parts[C].datums[xypl.id])

    else:
        for i in range (1, NumberSUMLayers+1):
            # Step 1) - The line below draws the plane
            xypl = mdb.models['Model-1'].parts[C].DatumPlaneByPrincipalPlane(offset=Z+SUMCThickness*i, principalPlane=XYPLANE)
            # Step 2) - The line below carries out the physical partition
            mdb.models['Model-1'].parts[C].cells.findAt(((0.0, 0.0, Z+SUMCThickness*i), ))
            cells=mdb.models['Model-1'].parts[C].cells.getByBoundingBox()
            mdb.models['Model-1'].parts[C].PartitionCellByDatumPlane(cells, mdb.models['Model-1'].parts[C].datums[xypl.id])

```

Figure 12.4: Partitioning when below OBD (Z direction)

```

#-----
# UNDERTAKING THE ABOVE OBD PARTITIONING
#-----
else:
    if LowerBoundSlices != UpperBoundSlices:
        for i in range(1, FirstHalfLowerBoundSlice+1):
            # Step 1) - The line below draws the plane
            xypl = mdb.models['Model-1'].parts[C].DatumPlaneByPrincipalPlane(offset=Z+LowerBoundSlices*i, principalPlane=XYPLANE)
            # Step 2) - The line below carries out the physical partition
            mdb.models['Model-1'].parts[C].cells.findAt(((0.0, 0.0, Z+LowerBoundSlices*i), ))
            cells=mdb.models['Model-1'].parts[C].cells.getByBoundingBox()
            mdb.models['Model-1'].parts[C].PartitionCellByDatumPlane(cells, mdb.models['Model-1'].parts[C].datums[xypl.id])

        for i in range(1, AbsoluteValueUpperBoundSlices+1):
            # Step 1) - The line below draws the plane
            xypl = mdb.models['Model-1'].parts[C].DatumPlaneByPrincipalPlane(offset=(Z+LowerBoundSlices*FirstHalfLowerBoundSlice)
            +UpperBoundSlices*i, principalPlane=XYPLANE)
            # Step 2) - The line below carries out the physical partition
            mdb.models['Model-1'].parts['Part-1'].cells.findAt(((0.0, 0.0, (Z+LowerBoundSlices*FirstHalfLowerBoundSlice)
            +UpperBoundSlices*i), ))
            cells=mdb.models['Model-1'].parts[C].cells.getByBoundingBox()
            mdb.models['Model-1'].parts[C].PartitionCellByDatumPlane(cells, mdb.models['Model-1'].parts[C].datums[xypl.id])

        for i in range(1, int(SecondHalfLowerBoundSlice)):
            # Step 1) - The line below draws the plane
            xypl = mdb.models['Model-1'].parts[C].DatumPlaneByPrincipalPlane(offset=(Z+LowerBoundSlices*FirstHalfLowerBoundSlice)
            +UpperBoundSlices*int(NumberSUMCLayers-AbsoluteValueLowerBoundSlices)+LowerBoundSlices*i, principalPlane=XYPLANE)
            # Step 2) - The line below carries out the physical partition
            mdb.models['Model-1'].parts['Part-1'].cells.findAt(((0.0, 0.0, (Z+LowerBoundSlices*FirstHalfLowerBoundSlice)
            +UpperBoundSlices*int(NumberSUMCLayers-AbsoluteValueLowerBoundSlices)+LowerBoundSlices*i), ))
            cells=mdb.models['Model-1'].parts[C].cells.getByBoundingBox()
            mdb.models['Model-1'].parts[C].PartitionCellByDatumPlane(cells, mdb.models['Model-1'].parts[C].datums[xypl.id])

    else:
        for i in range(1, NumberSUMCLayers+1):
            # Step 1) - The line below draws the plane
            xypl = mdb.models['Model-1'].parts[C].DatumPlaneByPrincipalPlane(offset=Z+SUMCThickness*i, principalPlane=XYPLANE)
            # Step 2) - The line below carries out the physical partition
            mdb.models['Model-1'].parts[C].cells.findAt(((0.0, 0.0, Z+SUMCThickness*i), ))
            cells=mdb.models['Model-1'].parts[C].cells.getByBoundingBox()
            mdb.models['Model-1'].parts[C].PartitionCellByDatumPlane(cells, mdb.models['Model-1'].parts[C].datums[xypl.id])

```

Figure 12.5: Partitioning when above OBD (Z direction)

12.0.3 Material creation

```
#-----  
# CALCULATING THE MATERIAL ALTERATION PERCENTAGES BETWEEN LAYERS - ONLY NEEDED FOR BELOW OBD  
#-----  
  
# CALCULATING THE MATERIAL ALTERATION FOR BELOW OBD (NOT NEEDED FOR ABOVE OBD, AS IT IS SET AT 0.5%)  
if OBD <= (200*AMMinRes*3):  
    NumberSUMCLayers = int(OBD / (AMMinRes * 3))  
    NumberSUMCAlterations = NumberSUMCLayers -1  
    HalfNumberSUMCAlterations = int(0.5*NumberSUMCAlterations)  
  
    print 'Number of SUMC Alterations :', NumberSUMCAlterations  
    print 'Number of SUMC Layers :', NumberSUMCLayers  
  
    BlendingPercentage = BP = float(100)  
  
    #####  
    # Blending from 100% material A to 100% material B  
  
    PercentageChangeBetweenEachSegment = BP / NumberSUMCAlterations  
    print 'PercentageChangeBetweenEachSegment = ' + repr(PercentageChangeBetweenEachSegment)+'%'  
  
    #####  
    # Finding Interpolation Limits  
  
    LowerInterpolateBoundMaterial = int(PercentageChangeBetweenEachSegment * 2) * 0.5  
    print 'Lower Interpolation Bound Material: ' + repr(LowerInterpolateBoundMaterial)  
  
    UpperInterpolateBoundMaterial = math.ceil(PercentageChangeBetweenEachSegment * 2) * 0.5  
    print 'Upper Interpolation Bound Material: ' + repr(UpperInterpolateBoundMaterial)  
  
    if LowerInterpolateBoundMaterial != UpperInterpolateBoundMaterial:  
        AbsoluteValueLowerBoundMaterial = int(round((BP-(NumberSUMCAlterations*UpperInterpolateBoundMaterial))  
        /(LowerInterpolateBoundMaterial-UpperInterpolateBoundMaterial)))  
        print 'Absolute Value Lower Bound Material: ', AbsoluteValueLowerBoundMaterial  
  
        AbsoluteValueUpperBoundMaterial = NumberSUMCAlterations - AbsoluteValueLowerBoundMaterial  
        print 'Absolute Value Upper Bound Material: ', AbsoluteValueUpperBoundMaterial  
  
        FirstHalfLowerBoundMaterial = int(AbsoluteValueLowerBoundMaterial*0.5)  
        print 'First Half Lower Bound Material: ', FirstHalfLowerBoundMaterial  
  
        SecondHalfLowerBoundMaterial = (AbsoluteValueLowerBoundMaterial - FirstHalfLowerBoundMaterial)  
        print 'Second Half Lower Bound Material: ', SecondHalfLowerBoundMaterial
```

Figure 12.6: Calculating the material alteration between layers

```

#-----
# CREATING MATERIAL - BELOW OBD
#-----
if OBD <- (200*MMinRes*3):
    if LowerInterpolateBoundMaterial != UpperInterpolateBoundMaterial:
        for i in range(0, FirstHalfLowerBoundMaterial+1):
            materialrep = 'FGM '+repr(i+1)
            DensityValue = Density1*(1-i*LowerInterpolateBoundMaterial/100) + Density2*(i*LowerInterpolateBoundMaterial/100)
            YMValue = YM1*(1-i*LowerInterpolateBoundMaterial/100) + YM2*(i*LowerInterpolateBoundMaterial/100)
            PRValue = PR1*(1-i*LowerInterpolateBoundMaterial/100) + PR2*(i*LowerInterpolateBoundMaterial/100)
            SPCValue = SpecHeatCap1*(1-i*LowerInterpolateBoundMaterial/100) + SpecHeatCap2*(i*LowerInterpolateBoundMaterial/100)
            CondValue = MatCon1*(1-i*LowerInterpolateBoundMaterial/100) + MatCon2*(i*LowerInterpolateBoundMaterial/100)
            A[B].Material(name=repr(materialrep))
            A[B].materials[repr(materialrep)].Density(dependencies=0, distributionType=UNIFORM, fieldName='',
            table=((DensityValue, ), ), temperatureDependency=OFF)
            A[B].materials[repr(materialrep)].setValues(materialIdentifier='')
            A[B].materials[repr(materialrep)].Elastic(dependencies=0, moduli=LONG_TERM, noCompression=OFF,
            noTension=OFF, table=((YMValue, PRValue), ), temperatureDependency=OFF, type=ISOTROPIC)
            A[B].materials[repr(materialrep)].Conductivity(table=((CondValue, ), ))
            A[B].materials[repr(materialrep)].SpecificHeat(table=((SPCValue, ), ), law=CONSTANTPRESSURE)

        for i in range(1, AbsoluteValueUpperBoundMaterial+1):
            materialrep = 'FGM '+repr(FirstHalfLowerBoundMaterial+i+1)
            DensityValue = Density1*(1-((FirstHalfLowerBoundMaterial*LowerInterpolateBoundMaterial/100)+
            (i*UpperInterpolateBoundMaterial/100))) + Density2*((FirstHalfLowerBoundMaterial*LowerInterpolateBoundMaterial/100)
            +(i*UpperInterpolateBoundMaterial/100))
            YMValue = YM1*(1-((FirstHalfLowerBoundMaterial*LowerInterpolateBoundMaterial/100)+
            (i*UpperInterpolateBoundMaterial/100))) + YM2*((FirstHalfLowerBoundMaterial*LowerInterpolateBoundMaterial/100)
            +(i*UpperInterpolateBoundMaterial/100))
            PRValue = PR1*(1-((FirstHalfLowerBoundMaterial*LowerInterpolateBoundMaterial/100)+
            (i*UpperInterpolateBoundMaterial/100))) + PR2*((FirstHalfLowerBoundMaterial*LowerInterpolateBoundMaterial/100)
            +(i*UpperInterpolateBoundMaterial/100))
            SPCValue = SpecHeatCap1*(1-((FirstHalfLowerBoundMaterial*LowerInterpolateBoundMaterial/100)
            +(i*UpperInterpolateBoundMaterial/100))) + SpecHeatCap2*((FirstHalfLowerBoundMaterial*LowerInterpolateBoundMaterial/100)
            +(i*UpperInterpolateBoundMaterial/100))
            CondValue = MatCon1*(1-((FirstHalfLowerBoundMaterial*LowerInterpolateBoundMaterial/100)
            +(i*UpperInterpolateBoundMaterial/100))) + MatCon2*((FirstHalfLowerBoundMaterial*LowerInterpolateBoundMaterial/100)
            +(i*UpperInterpolateBoundMaterial/100))
            A[B].Material(name=repr(materialrep))
            A[B].materials[repr(materialrep)].Density(dependencies=0, distributionType=UNIFORM, fieldName='',
            table=((DensityValue, ), ), temperatureDependency=OFF)
            A[B].materials[repr(materialrep)].setValues(materialIdentifier='')
            A[B].materials[repr(materialrep)].Elastic(dependencies=0, moduli=LONG_TERM, noCompression=OFF, noTension=OFF,
            table=((YMValue, PRValue), ), temperatureDependency=OFF, type=ISOTROPIC)
            A[B].materials[repr(materialrep)].Conductivity(table=((CondValue, ), ))
            A[B].materials[repr(materialrep)].SpecificHeat(table=((SPCValue, ), ), law=CONSTANTPRESSURE)

        for i in range(1, SecondHalfLowerBoundMaterial+1):
            materialrep = 'FGM '+repr(FirstHalfLowerBoundMaterial+AbsoluteValueUpperBoundMaterial+i+1)
            DensityValue = Density1*(1-((FirstHalfLowerBoundMaterial*LowerInterpolateBoundMaterial/100)+
            (AbsoluteValueUpperBoundMaterial*UpperInterpolateBoundMaterial/100)+(i*LowerInterpolateBoundMaterial/100)))
            + Density2*((FirstHalfLowerBoundMaterial*LowerInterpolateBoundMaterial/100)+
            (AbsoluteValueUpperBoundMaterial*UpperInterpolateBoundMaterial/100)+(i*LowerInterpolateBoundMaterial/100))
            YMValue = YM1*(1-((FirstHalfLowerBoundMaterial*LowerInterpolateBoundMaterial/100)+
            (AbsoluteValueUpperBoundMaterial*UpperInterpolateBoundMaterial/100)+(i*LowerInterpolateBoundMaterial/100)))
            + YM2*((FirstHalfLowerBoundMaterial*LowerInterpolateBoundMaterial/100)
            +(AbsoluteValueUpperBoundMaterial*UpperInterpolateBoundMaterial/100) +(i*LowerInterpolateBoundMaterial/100))
            PRValue = PR1*(1-((FirstHalfLowerBoundMaterial*LowerInterpolateBoundMaterial/100)
            +(AbsoluteValueUpperBoundMaterial*UpperInterpolateBoundMaterial/100)+(i*LowerInterpolateBoundMaterial/100)))
            + PR2*((FirstHalfLowerBoundMaterial*LowerInterpolateBoundMaterial/100)
            +(AbsoluteValueUpperBoundMaterial*UpperInterpolateBoundMaterial/100)+(i*LowerInterpolateBoundMaterial/100))
            SPCValue = SpecHeatCap1*(1-((FirstHalfLowerBoundMaterial*LowerInterpolateBoundMaterial/100)
            +(AbsoluteValueUpperBoundMaterial*UpperInterpolateBoundMaterial/100)+(i*LowerInterpolateBoundMaterial/100)))
            + SpecHeatCap2*((FirstHalfLowerBoundMaterial*LowerInterpolateBoundMaterial/100)
            +(AbsoluteValueUpperBoundMaterial*UpperInterpolateBoundMaterial/100)+(i*LowerInterpolateBoundMaterial/100))
            CondValue = MatCon1*(1-((FirstHalfLowerBoundMaterial*LowerInterpolateBoundMaterial/100)
            +(AbsoluteValueUpperBoundMaterial*UpperInterpolateBoundMaterial/100)+(i*LowerInterpolateBoundMaterial/100)))
            + MatCon2*((FirstHalfLowerBoundMaterial*LowerInterpolateBoundMaterial/100)
            +(AbsoluteValueUpperBoundMaterial*UpperInterpolateBoundMaterial/100)+(i*LowerInterpolateBoundMaterial/100))
            A[B].Material(name=repr(materialrep))
            A[B].materials[repr(materialrep)].Density(dependencies=0, distributionType=UNIFORM, fieldName='',
            table=((DensityValue, ), ), temperatureDependency=OFF)
            A[B].materials[repr(materialrep)].setValues(materialIdentifier='')
            A[B].materials[repr(materialrep)].Elastic(dependencies=0, moduli=LONG_TERM, noCompression=OFF,
            noTension=OFF, table=((YMValue, PRValue), ), temperatureDependency=OFF, type=ISOTROPIC)
            A[B].materials[repr(materialrep)].Conductivity(table=((CondValue, ), ))
            A[B].materials[repr(materialrep)].SpecificHeat(table=((SPCValue, ), ), law=CONSTANTPRESSURE)

    else:
        for i in range(0, NumberSUMLayers):
            materialrep = 'FGM '+repr(i+1)
            DensityValue = Density1*(1-i*LowerInterpolateBoundMaterial/100) + Density2*(i*LowerInterpolateBoundMaterial/100)
            YMValue = YM1*(1-i*LowerInterpolateBoundMaterial/100) + YM2*(i*LowerInterpolateBoundMaterial/100)
            PRValue = PR1*(1-i*LowerInterpolateBoundMaterial/100) + PR2*(i*LowerInterpolateBoundMaterial/100)
            SPCValue = SpecHeatCap1*(1-i*LowerInterpolateBoundMaterial/100) + SpecHeatCap2*(i*LowerInterpolateBoundMaterial/100)
            CondValue = MatCon1*(1-i*LowerInterpolateBoundMaterial/100) + MatCon2*(i*LowerInterpolateBoundMaterial/100)
            A[B].Material(name=repr(materialrep))
            A[B].materials[repr(materialrep)].Density(dependencies=0, distributionType=UNIFORM, fieldName='',
            table=((DensityValue, ), ), temperatureDependency=OFF)
            A[B].materials[repr(materialrep)].setValues(materialIdentifier='')
            A[B].materials[repr(materialrep)].Elastic(dependencies=0, moduli=LONG_TERM, noCompression=OFF,
            noTension=OFF, table=((YMValue, PRValue), ), temperatureDependency=OFF, type=ISOTROPIC)
            A[B].materials[repr(materialrep)].Conductivity(table=((CondValue, ), ))
            A[B].materials[repr(materialrep)].SpecificHeat(table=((SPCValue, ), ), law=CONSTANTPRESSURE)

```

Figure 12.7: Creating material when below OBD

```

#-----
# CREATING MATERIAL - ABOVE OBD (MATERIAL CHANGES BY UNIFORM 0.5% BETWEEN EACH LAYER)
#-----
else:
    NumberSUMCLayers = 200
    for i in range (0, NumberSUMCLayers):
        materialrep = 'FGM '+repr(i+1)
        DensityValue = Density1*(1 - (float(i)/NumberSUMCAIterations)) + Density2*(float(i)/NumberSUMCAIterations)
        YMValue = YM1*(1 - (float(i)/NumberSUMCAIterations)) + YM2*(float(i)/NumberSUMCAIterations)
        PRValue = PR1*(1 - (float(i)/NumberSUMCAIterations)) + PR2*(float(i)/NumberSUMCAIterations)
        SPCValue = SpecHeatCap1*(1 - (float(i)/NumberSUMCAIterations)) + SpecHeatCap2*(float(i)/NumberSUMCAIterations)
        CondValue = MatCon1*(1 - (float(i)/NumberSUMCAIterations)) + MatCon2*(float(i)/NumberSUMCAIterations)
        A[B].Material(name=repr(materialrep))
        A[B].materials[repr(materialrep)].Density(dependencies=0, distributionType=UNIFORM, fieldName='', table=((DensityValue,
        ), ), temperatureDependency=OFF)
        A[B].materials[repr(materialrep)].setValues(materialIdentifier='')
        A[B].materials[repr(materialrep)].Elastic(dependencies=0, moduli=LONG_TERM, noCompression=OFF, noTension=OFF,
        table=((YMValue, PRValue), ), temperatureDependency=OFF, type=ISOTROPIC)
        A[B].materials[repr(materialrep)].Conductivity(table=((CondValue, ), ))
        A[B].materials[repr(materialrep)].SpecificHeat(table=((SPCValue, ), ), law=CONSTANTPRESSURE)

```

Figure 12.8: Creating material when above OBD

12.0.4 Building print base for heat flow

```

#-----
# BUILDING PRINT BASE
#-----
A[B].ConstrainedSketch(name='Print_Base_Sketch', sheetSize=200.0)
A[B].sketches['Print_Base_Sketch'].rectangle(point1=(0.0-(2*PartLength/2), 0.0+(2*PartHeight/2)), point2=(0.0+(2*PartLength/2), 0.0-(2*PartHeight/2)))
A[B].Part(dimensionality=THREE_D, name=G, type=
DEFORMABLE_BODY)
A[B].parts[G].BaseSolidExtrude(depth=PrintBaseDepth, sketch=
A[B].sketches['Print_Base_Sketch'])

```

Figure 12.9: Determining dimensions and building print base

12.0.5 Meshing part

```

#-----
# CHOOSING AREAS TO MESH ON PART
#-----
listofcellsets=[]
for i in range(0,numberprintedcells):
    listofcellsets.append(A[B].parts[C].sets['Cell '+repr(i)].cells)
#-----
# SEEDING PART
#-----
A[B].parts[C].seedPart(deviationFactor=0.1, minSizeFactor=0.1, size=0.00045)
A[B].parts[C].setElementType(elemTypes=(elemType1, elemType2, elemType3), regions=(listofcellsets))
#-----
# MESHING PART
#-----
mdb.models['Model-1'].parts['Part-1'].generateMesh()

```

Figure 12.10: Seeding and meshing part

12.0.6 Writing raster scan path for heat flow

```

#-----
# CREATING THE CELLS AND CREATING THE SECTIONS
#-----

listofsets=[]
listofsections=[]
listoflocations=[]

# First segment
counter=0
for i in range(0, FirstHalfLowerBoundslice): # looping through z direction
    if counter==0:
        loop1=0
        loop2=1
        counter=1
    else:
        loop1=1
        loop2=0
        counter=0

    for j in range(loop1, NumberofYSlices,2): # looping through y direction
        if counter==1:
            yMod=j
        else:
            yMod=NumberofYSlices-j-1
        for k in range(0, NumberofXSlices):
            cells = mdb.models['Model-1'].parts[C].cells.getByBoundingBox(X+(k*printLength),Y+(j*printWidth),
                Z+(i*LowerBoundslices),X+((k+1)*printLength),Y+((j+1)*printWidth),Z+((i+1)*LowerBoundslices))
            if cells:
                materialrep = 'FGM '+repr(i+1)
                mdb.models['Model-1'].parts[C].Set(cells=cells, name='Cell '
                    +repr((i*(NumberofXSlices*NumberofYSlices))+(yMod*NumberofXSlices)+k))
                A[B].HomogeneousSolidSection(material= repr(materialrep), name= 'Section '
                    +repr((i*(NumberofXSlices*NumberofYSlices))+(yMod*NumberofXSlices)+k), thickness=None)
                #listofsets[setNumber]=((i*(NumberofXSlices*NumberofYSlices))+(yMod*NumberofXSlices)+k)
                listofsets.append((i*(NumberofXSlices*NumberofYSlices))+(yMod*NumberofXSlices)+k)

                listofsections.append((i*(NumberofXSlices*NumberofYSlices))+(yMod*NumberofXSlices)+k)
                # cellnumber = ((i*(NumberofXSlices*NumberofYSlices))+(yMod*NumberofXSlices)+k)
                # listoflocations=(A[B].parts[C].getCentroid(cells=cells))
                # fileout.writerow([cellnumber,listoflocations])

        for j in range(loop2, NumberofYSlices,2):
            if counter==1:
                yMod=j
            else:
                yMod=NumberofYSlices-j-1
            for k in range(NumberofXSlices-1, -1, -1):# looping through x direction
                cells = mdb.models['Model-1'].parts[C].cells.getByBoundingBox(X+(k*printLength),Y+(j*printWidth),
                    Z+(i*LowerBoundslices),X+((k+1)*printLength),Y+((j+1)*printWidth),Z+((i+1)*LowerBoundslices))
                if cells:
                    materialrep = 'FGM '+repr(i+1)
                    mdb.models['Model-1'].parts[C].Set(cells=cells, name='Cell '
                        +repr((i*(NumberofXSlices*NumberofYSlices))+(yMod*NumberofXSlices)+(NumberofXSlices-k-1)))
                    A[B].HomogeneousSolidSection(material=repr(materialrep), name= 'Section '
                        +repr((i*(NumberofXSlices*NumberofYSlices))+(yMod*NumberofXSlices)+(NumberofXSlices-k-1)), thickness=None)
                    listofsets.append((i*(NumberofXSlices*NumberofYSlices))+(yMod*NumberofXSlices)+(NumberofXSlices-k-1))
                    listofsections.append((i*(NumberofXSlices*NumberofYSlices))+(yMod*NumberofXSlices)+(NumberofXSlices-k-1))
                    # cellnumber=((i*(NumberofXSlices*NumberofYSlices))+(yMod*NumberofXSlices)+(NumberofXSlices-k-1))
                    # listoflocations=(A[B].parts[C].getCentroid(cells=cells))
                    # fileout.writerow([cellnumber,listoflocations])
                    #part_volume=mdb.models['Model-1'].parts[C].getVolume(cells=cells)

```

Figure 12.11: Writing blocks into files in raster scan pattern

12.0.7 Deactivating print deposits

```
#-----  
# CREATING STEP TO REMOVE ("TURN OFF") ALL PRINT MATERIAL  
#-----  
kstep = 2  
timeElapsed = 0.0  
A[B].HeatTransferStep(name='REMOVE PRINT MATERIAL', previous='Initial', timePeriod=1.0,  
    initialInc=0.1, maxInc=0.1, deltmx=1000.0)  
#-----  
# REMOVE ("TURN OFF") ALL PRINT MATERIAL  
#-----  
A[B].ModelChange(activeInStep=False, createStepName=  
    'REMOVE PRINT MATERIAL', includeStrain=False, name='REMOVE ALL PRINT MATERIAL', region=  
    A[B].rootAssembly.instances[D].sets['ALL PRINT'])
```

Figure 12.12: “Turning off” all print blocks for heat flow

12.0.8 Creating heat transfer conditions

```
#-----  
# CREATING A LIST OF EXPOSED SURFACES  
#-----  
mdb.models['Model-1'].rootAssembly.Surface(name='Exposed Surfaces', side1Faces=  
    mdb.models['Model-1'].rootAssembly.instances['Part-1-1'].faces.getByBoundingBox() +\  
    mdb.models['Model-1'].rootAssembly.instances['Print_Base-1'].faces.findAt(  
        (0, 0, PrintBaseDepth), ), ((0.0-(0.8*PartLength), 0.0+(0.8*PartHeight), PrintBaseDepth), ), ))  
#-----  
# CREATING A LIST OF ALL PRINT MATERIAL  
#-----  
A[B].parts[C].Set(cells=A[B].parts[C].cells.getByBoundingBox(), name='ALL PRINT')
```

Figure 12.13: Creating lists for heat flow conditions

```

#-----
# CREATING RADIATION CONDITION
#-----
|
A[B].RadiationToAmbient(ambientTemperature=AmbientTemp,
    ambientTemperatureAmp='', createStepName='REMOVE PRINT MATERIAL',
    distributionType=UNIFORM, emissivity=emissivityVal, field='', name='RADIATION',
    radiationType=AMBIENT, surface=A[B].rootAssembly-surfaces['Exposed Surfaces'])
#-----

# CREATING CONVECTION CONDITION
#-----

A[B].FilmCondition(name='CONVECTION',
    createStepName='REMOVE PRINT MATERIAL', surface=A[B].rootAssembly-surfaces['Exposed Surfaces'],
    definition=EMBEDDED_COEFF, filmCoeff=filmCoeffVal, filmCoeffAmplitude='',
    sinkTemperature=Temp0, sinkAmplitude='', sinkDistributionType=UNIFORM,
    sinkFieldName='')

```

Figure 12.14: Creating surface radiation and natural convection on all exposed surfaces

```

#-----
# CREATING SURFACE HEAT FLUX CONDITION FROM NOZZLE RADIATION
#-----

Top = A[B].rootAssembly.instances[H].faces.findAt(((0,0,PrintBaseDepth), ), ((0.0-(0.8*PartLength),
    0.0+(0.8*PartHeight), PrintBaseDepth), ), )

region = A[B].rootAssembly.Surface(side1Faces=Top, name='NozzleRadiation')
A[B].SurfaceHeatFlux(name='NozzleRadiation',
    createStepName='Print-1', region=region, magnitude=1.0,
    distributionType=USER_DEFINED)

```

Figure 12.15: Creating surface heat flux from nozzle radiation

12.0.9 Heating, depositing and cooling segments

```

#-----
# HEATING PRINT DEPOSIT MATERIAL
#-----

A[B].TemperatureBC(name='HEAT PRINT DEPOSIT',
    createStepName='REMOVE PRINT MATERIAL', region=A[B].rootAssembly.instances[D].sets['ALL PRINT'],
    fixed=OFF, distributionType=UNIFORM, fieldName='', magnitude=TempDeposit, amplitude=UNSET)

```

Figure 12.16: Heating print material

```

#-----
# CALCULATING VOLUME OF AN "AVERAGE" PRINT DEPOSIT (AVERAGING THE THICKNESS IN THE BLENDING DIRECTION);
# CALCULATING THE X, Y AND Z COORDINATES OF THE REMAINING CELLS SO THEY CAN BE WRITTEN INTO POSITION DATA FILE
# CALCULATING THE VOLUME OF EACH PRINT DEPOSIT;
# CALCULATING THE TIME THE LASER SPENDS ON EACH PRINT DEPOSIT
# WRITING POSITION DATA TO FILE FOR REMAINING PRINT DEPOSITS
# STEPS THAT REACTIVATE ALL REMAINING PRINT DEPOSITS
#-----

for i in range(1,numberprintedcells):
    printDepositNo=i
    cells = A[B].parts[C].sets['Cell '+repr(i)].cells
    listofcentroids=(A[B].parts[C].getCentroid(cells=cells,relativeAccuracy=0.01))
    XCentroidValue = listofcentroids[0]
    YCentroidValue = listofcentroids[1]
    ZCentroidValue = listofcentroids[2]

    VolumeofPrintDeposit = A[B].rootAssembly.getVolume(A[B].rootAssembly.instances[D].sets['Cell '+repr(i)].cells)
    PrintDepositTime = (VolumeofPrintDeposit/VolumeCompletelyDenseDeposit)*TimeforwholeDeposit
    FirstPrintDepositTime += PrintDepositTime

    fileout.writerow([printDepositID, XCentroidValue, YCentroidValue, ZCentroidValue,FirstPrintDepositTime])
    A[B].HeatTransferStep(name='Print-'+repr(printDepositNo), previous='Print-'+repr(printDepositNo-1),
        timePeriod=PrintDepositTime, initialInc=PrintDepositTime/2, minInc=PrintDepositTime/50000, maxInc=PrintDepositTime/2,
        deltmx=maxTempInc)

```

Figure 12.17: “Turning on” segments based on raster scan path list and calculating print time per deposit

```

#-----
# CREATING COOL DOWN STEP
#-----
A[B].HeatTransferStep(name='Cooling', previous='Print-'+str(numberprintedcells-1),
    timePeriod=CoolingTime, initialInc=CoolingTime/100, minInc=CoolingTime/5000, maxInc=CoolingTime/20, deltmx=maxTempInc)
A[B].boundaryConditions['Print-'+str(numberprintedcells-1)].deactivate('Cooling')

```

Figure 12.18: Cooling part down in order to find residual stresses

Chapter 13

Appendix B: Physical Experimentation

As mentioned, physical experiments were not done in this project due to financial constraints. However, a physical experiment set up has been created by the researcher, as funding issues were realised later in the project time line. This chapter describes the experimental set up, and how the results would be used.

13.1 Experimental Aim

The main aim of the experiment will be to investigate the binding between the FGM layers. This binding layer is the most important aspect, as it is least researched when compared to the other aspects of this work - the use of topology optimisation and structured cells. To investigate the binding layer, mechanical tests and inspection of the microstructure will be done.

13.2 Test block

In order to minimise the potential costs, the test block should be as small as possible. Reviewing literature, Dongare et al.^[218] created a scaled-down tensile test coupon design using simulations for additive manufactured parts based on ASTM E-8. The finalised test coupon itself has an overall length of 17.74 mm. The researchers in this paper fabricated a plate from Ti-6Al-4V and took 12 test coupons from it, at two different orientations, all on the same plane. Figure 13.1 contains the dimension indicators of test coupon. Table 13.1 contains the dimensions of the test coupon.

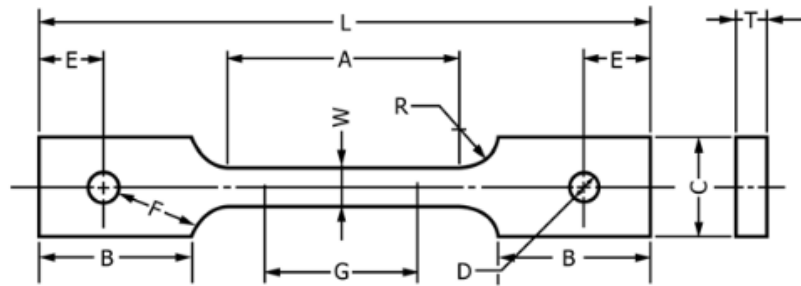


Figure 13.1: ASTM-E8 pin-loaded tension test coupon

Table 13.1: Scaled down test coupon dimensions. Adapted from^[218]

Feature	Standard ESTM-E8 coupon (mm)	Scaled down coupon (mm)
A - length of reduced section	57	3.4
B - length of grip section	50	5.92
C - width of grip section	50	6.05
D - diameter of pin hole	13	3
E - distance from hole to edge	40	3.02
F - distance from hole to fillet	13	3.4
G - gauge length	50	3.3
L - overall length	200	17.74
R - fillet radius	13	1.25
T - overall thickness	16	1
W - gauge width	12.5	1

The test block for the tests related to this thesis will use the same coupon dimension, but a different test block shape. A 3D solid model of the scaled down test coupon is shown in figure 13.2.

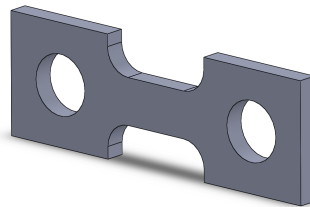


Figure 13.2: A 3D solid model of a single test coupon

There are two requirements for the test block:

1. Test coupons needs to be able to fit in two directions - perpendicular to one another, on the same plane.

2. There has to be four samples in each of the two directions - three for measurement to allow average values to be calculated, and a fourth as redundancy in the event one of the other three fails.

Eight test coupons are therefore needed. They are placed in four sets of two, each 2 mm apart. Each set of two is perpendicular to the previous two, giving four test coupons in one orientation, and the other four in the perpendicular orientation. Figure 13.3 shows the test coupons in this configuration.

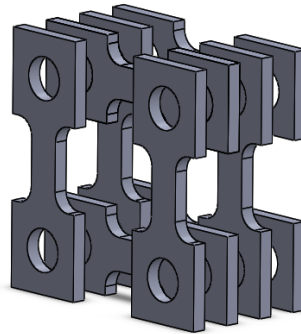


Figure 13.3: Configuration of the test coupons

The test block is designed to fit the configuration from figure 13.3 within. The final test coupon, attached to a simulated print bed, is shown in figure 13.4.

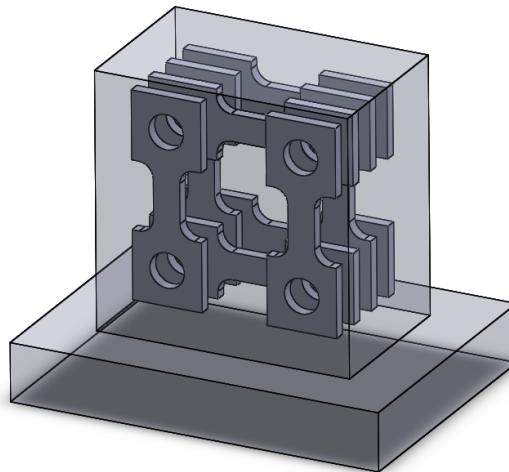


Figure 13.4: Test coupons in-situ within test block and print bed

13.3 Test coupon creation

The test block must first be made. The test coupons will be cut from the test block.

13.3.1 Making test block

The test block will be created on the two-powder feeder shown in figure 13.5.



Figure 13.5: Laser metal deposition apparatus, belonging to Laser Additive Solutions

This apparatus is capable of depositing constantly varying volumes of two materials, as needed for this test. This is done via the powder delivery speed, set using the RPM of the hopper delivery systems. The two material hoppers both feed into the same line. The powder feeder is controlled via a laser metal deposition CNC program.

13.4 Cutting the test coupons

Electrical discharge machining will be used to cut the test coupons from the test block. Features of the test coupons (pin holes) will also be cut using electrical discharge machining. This will be done in-house.

13.5 Tooling

As the test coupons were so small, tooling would need to be designed that could hold the specimens in the testing rig. In order to accurately measure the stress-strain behaviour of the test coupons, an extensionometer would be used. However, a “clip-on” contact extensionometer could not be used due to the size of the test coupons. A non-contact video extensionometer would therefore be used. This would measure the movement of two marks at either end of the gauge of the test coupon. The pin holes in the tooling would need to be very close to the edge to ensure the extensionometer could see these marks. Therefore, EN24, a high strength engineering steel, was chosen for the tooling. The tooling would fit into the 50 kN test rig using wedge grips on the rig. The other end of the tooling was designed with this in mind.

A 3D solid model of the designed tooling is shown in figure 13.6.

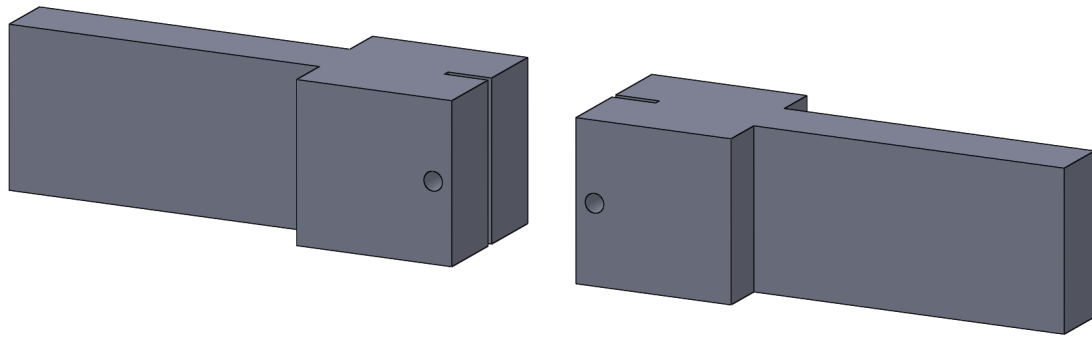


Figure 13.6: The tooling designed for the mechanical tests

The centre of the pin hole is 3 mm from the edge of the tooling. The pin hole itself is 3 mm in diameter. The distance from the edge of the pin hole to the edge of the tooling is thus 1.5 mm. This distance would allow marks to be placed on the test coupon for the video extensometer. A 7 mm deep by 1.2 mm wide slot was cut into the tooling to allow insertion of the 1 mm wide test coupon. The tooling was designed to be 25 mm wide, parallel to the pin direction. This large dimension would result in a low pressure being exerted by the pin, and thus limit deflection of the tooling around the pin hole. The tooling would be created in house.

13.6 Experiments to be conducted

The main object of the physical experimentation is the tensile tests. However, the remaining material from the test block can be used for additional tests, including hardness, X-ray diffraction and electron back scatter diffraction

13.6.1 Tensile test

As previously mentioned, tensile tests will be done on 2 sets of 3 test coupons - three parallel to the build direction, and three perpendicular to the build direction. These tests will give the stress-strain response of the FGMs in the two directions, and allow the FGM code to be updated.

13.6.2 Micro hardness test

A hardness test measures the resistance to plastic deformation of a material. This would be done at multiple points over the part, both in the build direction, and perpendicular to the build direction. This would allow the hardness of the FGM at different material constitution points to be measured. The hardness values would be compared to known values for the two constituent materials. A micro-hardness tester would be used, as it requires less surface area in order to record a measurement.

13.6.3 XRD

X-ray diffraction allows the atomic structure of the part to be measured. Knowing the atomic structure of the part will enhance understanding of the bonding between the FGM layers in the part. This information can be used to improve the FGM code to model the bonding layers more accurately. The XRD measurements will also give the residual stress values on the surface. These values can be compared to the simulated values. If anomalies exist, this knowledge can be used to alter the heat flow code.

13.6.4 EBSD

Electron back scatter diffraction is used to measure the orientation of the grains in the part. This orientation of the grains affects many mechanical properties of the part. Thus, knowing the crystallographic orientation of the part can explain many reasons for the mechanical properties that will be found from the tensile tests.

13.6.5 Residual stress test

XRD will give the surface residual stress values. To find the bulk residual stress values, the contour method would be used. The remaining material will be segmented into smaller pieces. Upon segmentation, the residual stresses will be released, which will result in the segments deforming. This deformation can be physically measured. The stresses measured when these deformed segments are fed into software and analytically “flattened” will be the bulk residual stresses. These can be compared to the values measured in the heat flow code. Updates can be made to the heat flow code in order to mimic these experimental values.

13.7 Conclusion

This chapter has described the physical tests that would be done in order to validate the work in this thesis experimentally. However, as mentioned, due to financial reasons, these tests will not be carried out within the research of this thesis.

References

- [1] S. Y. Nof. *Handbook of industrial robotics*, volume 1. John Wiley & Sons, 1999.
- [2] G. M. Mair. *Industrial Robotics*. Prentice Hall, 1988. ISBN 9780134632094. URL <https://books.google.co.uk/books?id=MOZjQgAACAAJ>.
- [3] P. Krži, F. Pušavec, and J. Kopa. Kinematic Constraints and Offline Programming in Robotic Machining. In *Technical Gazette*, volume 20, pages 117–124, 2013.
- [4] Kinova. Jaco² 6 DOF Robot Arm, 2015. URL <http://www.kinovarobotics.com/service-robotics/products/robot-arms/>.
- [5] Schunk. LWA 4P 6 DOF Robot Arm, 2013. URL <https://schunk.com/fileadmin/pim/docs/IM0012315.PDF>.
- [6] A. Albu-Schäffer, S. Haddadin, C. Ott, A. Stemmer, T. Wimböck, and G. Hirzinger. The DLR lightweight robot: design and control concepts for robots in human environments. *Industrial Robot: An International Journal*, 34(5):376–385, 2007. ISSN 0143-991X. doi: 10.1108/01439910710774386.
- [7] R. Bischoff, J. Kurth, G. Schreiber, R. Koeppel, A. Albu-Schaeffer, A. Beyer, O. Eiberger, S. Haddadin, A. Stemmer, G. Grunwald, and G. Hirzinger. <https://www.springer.com/gb/book/9783642303180>. *Robotics (ISR), 2010 41st International Symposium on and 2010 6th German Conference on Robotics (ROBOTIK)*, pages 1–8, 2010. ISSN 0143-991X. doi: 10.1108/01439910710774386.
- [8] Scorbot. ER-VII 6 DOF Robot Arm, 1996. URL <http://www.theoldrobots.com/scorbot.html>.
- [9] Staubli. TX90 6 DOF Robot Arm, 2015. URL <http://www.staubli.com/en/robotics/6-axis-scara-industrial-robot/medium-payload-6-axis-robot/6-axis-industrial-robot-tx90/>.
- [10] U. Robots. Universal Robots UR10, 2020. URL <https://www.universal-robots.com/products/ur10-robot/>.
- [11] H. Fang, L. Guo, and S. Bai. A Light Weight Arm Designed with Modular Joints. *Proceedings of the 3rd IFToMM Symposium on Mechanism Design for Robotics*, 33:47 – 54, 2015. doi: 10.1007/978-3-319-18126-4. URL <http://link.springer.com/10.1007/978-3-319-18126-4>.

- [12] L. Zhou and S. Bai. A New Approach to Design of a Lightweight Anthropomorphic Arm for Service Applications. *Journal of Mechanisms and Robotics*, 7(3):031001–031001–12, 2015. ISSN 1942-4302. doi: 10.1115/1.4028292. URL <http://mechanismsrobotics.asmedigitalcollection.asme.org/article.aspx?doi=10.1115/1.4028292>.
- [13] Y. Xiao, Z. Fan, W. Li, S. Chen, L. Zhao, and H. Xie. A Manipulator Design Optimization Based on Constrained Multi-objective Evolutionary Algorithms. *2016 International Conference on Industrial Informatics - Computing Technology, Intelligent Technology, Industrial Information Integration (ICIICII)*, pages 199–205, 2016. doi: 10.1109/ICIICII.2016.0056.
- [14] H. Yin, S. Huang, M. He, and J. Li. An overall structure optimization for a light-weight robotic arm. In *IEEE 11th Conference on Industrial Electronics and Applications (ICIEA)*, pages 1765–1770, 2016. ISBN 9781467386449. doi: 10.1109/ICIEA.2016.7603872.
- [15] Q. Meng, F. Xie, and X.-J. Liu. Topology optimization of the active arms for a high-speed parallel robot based on variable height method. In Y. Huang, H. Wu, H. Liu, and Z. Yin, editors, *Intelligent Robotics and Applications*, pages 212–224, Cham, 2017. Springer International Publishing. ISBN 978-3-319-65292-4.
- [16] P. Yao, K. Zhou, Y. Lin, and Y. Tang. Light-weight topological optimization for upper arm of an industrialwelding robot. *Metals*, 9(9), 2019. ISSN 20754701. doi: 10.3390/met9091020.
- [17] X. Lv, Y. Yang, W. Zeng, and D. Xu. Lightweight Design of Six-dof Tandem Manipulator Based on Additive Manufacturing Technology. *IOP Conference Series: Materials Science and Engineering*, 612(3), 2019. ISSN 1757899X. doi: 10.1088/1757-899X/612/3/032145.
- [18] X. Li, H. Shao, G. Li, W. Liu, and C. Liu. Static simulation and structure optimization of key parts of joint welding robots. *Proceedings of 2018 IEEE International Conference on Mechatronics and Automation, ICMA 2018*, pages 282–287, 2018. doi: 10.1109/ICMA2018.8484469.
- [19] E. C. Tsirogiannis and G. C. Vosniakos. Redesign and topology optimization of an industrial robot link for additive manufacturing. *Facta Universitatis, Series: Mechanical Engineering*, 17(3):415–424, 2019. ISSN 23350164. doi: 10.22190/FUME181219003T.

- [20] H. Luo, J. Fu, P. Wang, J. Liu, and W. Zhou. Design optimization of the ram structure of friction stir welding robot. *Mechanics of Advanced Materials and Structures*, 27(2):108–118, 2020. doi: 10.1080/15376494.2018.1471758.
- [21] H. N. G. Wadley. Multifunctional periodic cellular metals. *Philosophical transactions. Series A, Mathematical, physical, and engineering sciences*, 364(1838): 31–68, 2006. ISSN 1364-503X. doi: 10.1098/rsta.2005.1697.
- [22] L. Valdevit, Z. Wei, C. Mercer, F. W. Zok, and a. G. Evans. Structural performance of near-optimal sandwich panels with corrugated cores. *International Journal of Solids and Structures*, 43(16):4888–4905, 2006. ISSN 00207683. doi: 10.1016/j.ijsolstr.2005.06.073.
- [23] M. Walters, W. Prof, G. Prof, W. Master, and M. Engineering. Designing and analysing Kagome structures for crash safety applications. *Masters, Department of Mechanical Engineering, Eindhoven University of Technology, Eindhoven, MT*, 2005.
- [24] N. a. Fleck, V. S. Deshpande, and M. F. Ashby. Micro-architected materials: past, present and future. *Proceedings of the Royal Society A: Mathematical, Physical and Engineering Sciences*, 466(2121):2495–2516, 2010. ISSN 1364-5021. doi: 10.1098/rspa.2010.0215.
- [25] I. Ullah, J. Elambasseril, M. Brandt, and S. Feih. Performance of bio-inspired Kagome truss core structures under compression and shear loading. *Composite Structures*, pages 294–302, 2014. ISSN 02638223. doi: 10.1016/j.compstruct.2014.07.036. URL <http://www.sciencedirect.com/science/article/pii/S0263822314003596>.
- [26] D. J. Sypeck. Cellular truss core sandwich structures. *Applied Composite Materials*, 12(3-4):229–246, 2005. ISSN 0929189X. doi: 10.1007/s10443-005-1129-z.
- [27] F. W. Zok, S. a. Waltner, Z. Wei, H. J. Rathbun, R. M. McMeeking, and a. G. Evans. A protocol for characterizing the structural performance of metallic sandwich panels: Application to pyramidal truss cores. *International Journal of Solids and Structures*, 41(22-23):6249–6271, 2004. ISSN 00207683. doi: 10.1016/j.ijsolstr.2004.05.045.
- [28] J. Wang, A. Evans, K. Dharmasena, and H. Wadley. On the performance of truss panels with Kagomé cores. *International Journal of Solids and Structures*, 40(25): 6981–6988, dec 2003. ISSN 00207683. doi: 10.1016/S0020-7683(03)00349-4. URL <http://www.sciencedirect.com/science/article/pii/S0020768303003494>.

- [29] D. T. Queheillalt and H. N. G. Wadley. Cellular metal lattices with hollow trusses. *Acta Materialia*, 53(2):303–313, 2005. ISSN 13596454. doi: 10.1016/j.actamat.2004.09.024.
- [30] H. J. Rathbun, F. W. Zok, S. A. Waltner, C. Mercer, A. G. Evans, D. T. Queheillalt, and H. N. G. Wadley. Structural performance of metallic sandwich beams with hollow truss cores. *Acta Materialia*, 54(20):5509–5518, 2006. ISSN 1359-6454. doi: <http://dx.doi.org/10.1016/j.actamat.2006.07.016>. URL <http://www.sciencedirect.com/science/article/pii/S1359645406005325>.
- [31] T. Liu, Z. C. Deng, and T. J. Lu. Design optimization of truss-cored sandwiches with homogenization. *International Journal of Solids and Structures*, 43(25-26): 7891–7918, 2006. ISSN 00207683. doi: 10.1016/j.ijsolstr.2006.04.010.
- [32] L. Valdevit, A. J. Jacobsen, J. R. Greer, and W. B. Carter. Protocols for the optimal design of multi-functional cellular structures: From hypersonics to micro-architected materials. *Journal of the American Ceramic Society*, 94(SUPPL. 1): 15–34, 2011. ISSN 00027820. doi: 10.1111/j.1551-2916.2011.04599.x.
- [33] R. Biagi and H. Bart-Smith. In-plane column response of metallic corrugated core sandwich panels. *International Journal of Solids and Structures*, 49(26): 3901–3914, dec 2012. ISSN 00207683. doi: 10.1016/j.ijsolstr.2012.08.015. URL <http://www.sciencedirect.com/science/article/pii/S0020768312003605>.
- [34] J. Bauer, S. Hengsbach, I. Tesari, R. Schwaiger, and O. Kraft. High-strength cellular ceramic composites with 3D microarchitecture. *Proceedings of the National Academy of Sciences*, 111(7):2453–2458, 2014. ISSN 0027-8424. doi: 10.1073/pnas.1315147111. URL <http://www.pnas.org/cgi/doi/10.1073/pnas.1315147111>.
- [35] T. Hahn. *International Tables for Crystallography, Space-Group Symmetry*. International Tables for Crystallography. Wiley, 2005. ISBN 9780792365907. URL <https://books.google.co.uk/books?id=S3ij7{ }eHyoQC>.
- [36] H. N. G. Wadley, N. a. Fleck, and A. G. Evans. Fabrication and structural performance of periodic cellular metal sandwich structures. *Composites Science and Technology*, 63(16):2331–2343, 2003. ISSN 02663538. doi: 10.1016/S0266-3538(03)00266-5.
- [37] L. Ma, H.-y. Zheng, and L.-z. Wu. Mechanical Properties and Impulsive Response of 3D-Kagome Truss Core Sandwich Panel. *16th International Conference on Composite Materials*, pages 1–7, 2007.

- [38] D. Mahmoud and M. Elbestawi. Lattice Structures and Functionally Graded Materials Applications in Additive Manufacturing of Orthopedic Implants: A Review. *Journal of Manufacturing and Materials Processing*, 1(2):13, 2017. ISSN 2504-4494. doi: 10.3390/jmmp1020013. URL <http://www.mdpi.com/2504-4494/1/2/13>.
- [39] S. M. Giannitelli, D. Accoto, M. Trombetta, and A. Rainer. Current trends in the design of scaffolds for computer-aided tissue engineering. *Acta Biomaterialia*, 10(2):580–594, 2014. ISSN 18787568. doi: 10.1016/j.actbio.2013.10.024. URL <http://dx.doi.org/10.1016/j.actbio.2013.10.024>.
- [40] F. S. Bobbert, K. Lietaert, A. A. Eftekhari, B. Pouran, S. M. Ahmadi, H. Weinans, and A. A. Zadpoor. Additively manufactured metallic porous biomaterials based on minimal surfaces: A unique combination of topological, mechanical, and mass transport properties. *Acta Biomaterialia*, 53:572–584, 2017. ISSN 18787568. doi: 10.1016/j.actbio.2017.02.024. URL <http://dx.doi.org/10.1016/j.actbio.2017.02.024>.
- [41] C. Yan, L. Hao, A. Hussein, and P. Young. Ti-6Al-4V triply periodic minimal surface structures for bone implants fabricated via selective laser melting. *Journal of the Mechanical Behavior of Biomedical Materials*, 51:61–73, 2015. ISSN 18780180. doi: 10.1016/j.jmbbm.2015.06.024. URL <http://dx.doi.org/10.1016/j.jmbbm.2015.06.024>.
- [42] C. Han, Y. Li, Q. Wang, S. Wen, Q. Wei, C. Yan, L. Hao, J. Liu, and Y. Shi. Continuous functionally graded porous titanium scaffolds manufactured by selective laser melting for bone implants. *Journal of the Mechanical Behavior of Biomedical Materials*, 80(March 2017):119–127, 2018. ISSN 18780180. doi: 10.1016/j.jmbbm.2018.01.013. URL <https://doi.org/10.1016/j.jmbbm.2018.01.013>.
- [43] Y. Wang, Z. Luo, N. Zhang, and Q. Qin. Topological shape optimization of multifunctional tissue engineering scaffolds with level set method. *Structural and Multidisciplinary Optimization*, 54(2):333–347, 2016. ISSN 16151488. doi: 10.1007/s00158-016-1409-2.
- [44] O. Sigmund and K. Maute. Topology optimization approaches: A comparative review. *Structural and Multidisciplinary Optimization*, 48(6):1031–1055, 2013. ISSN 1615147X. doi: 10.1007/s00158-013-0978-6.
- [45] H. Lombaert. Level set method: Explanation, Mar. 2006.
- [46] X. Huang, A. Radman, and Y. M. Xie. Topological design of microstructures of cellular materials for maximum bulk or shear modulus. *Computational Materials*

- Science*, 50(6):1861–1870, 2011. ISSN 09270256. doi: 10.1016/j.commat.2011.01.030. URL <http://dx.doi.org/10.1016/j.commat.2011.01.030>.
- [47] G. I. N. Rozvany. A critical review of established methods of structural topology optimization. *Structural and Multidisciplinary Optimization*, 37(3):217–237, 2009. ISSN 1615147X. doi: 10.1007/s00158-007-0217-0.
- [48] A. Aremu, D. Brackett, I. Ashcroft, R. Wildman, R. Hague, and C. Tuck. An Adaptive meshing based BESO topology optimisation. In *9th World Congress on Structural and Multidisciplinary Optimization, June 13-17 2011, Shizuoka, Japan*, pages 1–10, 2011.
- [49] T. Zegard and G. H. Paulino. Bridging topology optimization and additive manufacturing. *Structural and Multidisciplinary Optimization*, 2015. ISSN 1615-147X. doi: 10.1007/s00158-015-1274-4.
- [50] M. Teimouri and M. Asgari. Multi-objective BESO topology optimization for stiffness and frequency of continuum structures. *Structural Engineering and Mechanics*, 72(2):181–190, 2019. ISSN 15986217. doi: 10.12989/sem.2019.72.2.181.
- [51] M. V. O. Araujo, E. N. Lages, and M. A. A. Cavalcante. Checkerboard free topology optimization for compliance minimization applying the finite-volume theory. *Mechanics Research Communications*, 108:103581, 2020. ISSN 00936413. doi: 10.1016/j.mechrescom.2020.103581. URL <https://doi.org/10.1016/j.mechrescom.2020.103581>.
- [52] O. Sigmund and J. Petersson. Numerical instabilities in topology optimization: A survey on procedures dealing with checkerboards, mesh-dependencies and local minima. *Structural Optimization*, 16(1):68–75, 1998. ISSN 09344373. doi: 10.1007/BF01214002.
- [53] A. Aremu, I. Ashcroft, R. Wildman, R. Hague, C. Tuck, and D. Brackett. The Effects of Bidirectional Evolutionary Structural Optimization Parameters on an Industrial Designed Component for Additive Manufacture. *Proceedings of the Institution of Mechanical Engineers, Part B: Journal of Engineering Manufacture*, 227(6):794–807, 2013. ISSN 0954-4054. doi: 10.1177/0954405412463857. URL <http://pib.sagepub.com/lookup/doi/10.1177/0954405412463857>.
- [54] M. P. Bendsøe and O. Sigmund. *Topology optimization: theory, methods, and applications*, volume 2nd Edition. Springer Science & Business Media, 2003. ISBN 3540429921. doi: 10.1063/1.3278595. URL <http://www.amazon.fr/Topology-Optimization-Theory-Methods-Applications/dp/3540429921>.

- [55] J. D. Hiller and H. Lipson. Multi material topological optimization of structures and mechanisms. *11th Annual Conference on Genetic and Evolutionary Computation*, pages 1521–1528, 2009. doi: 10.1145/1569901.1570105. URL <http://portal.acm.org/citation.cfm?doid=1569901.1570105>. URL <http://dl.acm.org/citation.cfm?id=1570105>.
- [56] O. Sigmund. On the usefulness of non-gradient approaches in topology optimization. *Structural and Multidisciplinary Optimization*, 43(5):589–596, 2011. ISSN 1615147X. doi: 10.1007/s00158-011-0638-7.
- [57] X. Huang and Y. M. Xie. Bi-directional evolutionary topology optimization of continuum structures with one or multiple materials. *Computational Mechanics*, 43(3):393–401, 2009. ISSN 01787675. doi: 10.1007/s00466-008-0312-0.
- [58] A. Zocca, P. Colombo, C. M. Gomes, and J. Günster. Additive Manufacturing of Ceramics: Issues, Potentialities, and Opportunities. *Journal of the American Ceramic Society*, 98(7):1983–2001, 2015. ISSN 00027820. doi: 10.1111/jace.13700. URL <http://doi.wiley.com/10.1111/jace.13700>.
- [59] Renishaw. AM Metal Powders, 2015. URL <http://www.renishaw.com/en/metal-powders-supply--31458>.
- [60] H. West, O. Harrysson, T. Horn, D. Cormier, R. Aman, and D. Marcellin-Little. Novel materials and structures fabricated by electron beam melting. *Microscopy and Microanalysis*, 21(S3):461–462, 2015.
- [61] I. Gibson, D. W. Rosen, and B. Stucker. *Additive manufacturing technologies: Rapid prototyping to direct digital manufacturing*. Springer, 2nd edition, 2014. ISBN 9781441911193. doi: 10.1007/978-1-4419-1120-9.
- [62] R. M. Mahamood, E. T. A. Member, M. Shukla, and S. Pityana. Functionally Graded Material : An Overview. *World Congress on Engineering*, III:2–6, 2012. ISSN 9881925223.
- [63] Y. Miyamoto, W. A. Kaysser, B. H. Rabin, A. Kawasaki, and R. G. Ford. *Functionally graded materials: design, processing and applications*, volume 5. Springer Science & Business Media, 2013.
- [64] T. Tan, N. Rahbar, S. M. Allameh, S. Kwofie, D. Dissmore, K. Ghavami, and W. O. Soboyejo. Mechanical properties of functionally graded hierarchical bamboo structures. *Acta Biomaterialia*, 7(10):3796–3803, 2011. ISSN 17427061. doi: 10.1016/j.actbio.2011.06.008.

- [65] F. Nogata and H. Takahashi. Intelligent functionally graded material: Bamboo. *Composites Engineering*, 5(7):743–751, 1995. ISSN 09619526. doi: 10.1016/0961-9526(95)00037-N.
- [66] S. Amada, Y. Ichikawa, T. Munekata, Y. Nagase, and H. Shimizu. Fiber texture and mechanical graded structure of bamboo. *Composites Part B: Engineering*, 28(1-2):13–20, 1997. ISSN 13598368. doi: 10.1016/S1359-8368(96)00020-0.
- [67] E. C. N. Silva, M. C. Walters, and G. H. Paulino. Modeling bamboo as a functionally graded material: lessons for the analysis of affordable materials. *Journal of Materials Science*, 41(21):6991–7004, 2006.
- [68] M. Niino, T. Hirai, and R. Watanabe. The functionally graded materials. *Journal of the Japan Society for Composite Materials*, 13:277 – 264, 1987.
- [69] T. Hirano, J. Teraki, and T. Yamada. On the design on functionally gradient materials. In *Proceedings of 1st International Symposium on Functionally Gradient Materials*, pages 5–10, Sendai, 1990.
- [70] W. G. Buttlar, G. H. Paulino, and S. H. Song. Application of graded finite elements for asphalt pavements. *Journal of engineering mechanics*, 132(3):240–249, 2006.
- [71] S. Gouasmi, A. Megueni, A. S. Bouchikhi, K. Zouggar, and A. Sahli. On the Reduction of Stress Concentration Factor Around a Notch Using a Functionally Graded Layer. *Materials Research*, 18:971–977, 2015. ISSN 1516-1439. URL http://www.scielo.br/scielo.php?script=sci_arttext&pid=S1516-14392015000500971&nrm=iso.
- [72] N. Tutuncu and M. Ozturk. Exact solutions for stresses in functionally graded pressure vessels. *Composites Part B: Engineering*, 32(8):683–686, 2001.
- [73] Y. Z. Chen and X. Y. Lin. Elastic analysis for thick cylinders and spherical pressure vessels made of functionally graded materials. *Computational Materials Science*, 44(2):581–587, 2008.
- [74] G. Anandakumar, N. Li, A. Verma, P. Singh, and J.-H. Kim. Thermal stress and probability of failure analyses of functionally graded solid oxide fuel cells. *Journal of Power Sources*, pages 6659 – 6670, 2010.
- [75] D. Li, W. Liao, N. Dai, G. Dong, Y. Tang, and Y. M. Xie. Optimal design and modeling of gyroid-based functionally graded cellular structures for additive manufacturing. *CAD Computer Aided Design*, 104:87–99, 2018. ISSN 00104485.

doi: 10.1016/j.cad.2018.06.003. URL <https://doi.org/10.1016/j.cad.2018.06.003>.

- [76] D. Chen and X. Zheng. Multi-material Additive Manufacturing of Metamaterials with Giant, Tailorable Negative Poisson's Ratios. *Scientific Reports*, 8(1):1–8, 2018. ISSN 20452322. doi: 10.1038/s41598-018-26980-7.
- [77] M. Niino and S. Maeda. Recent Development Status of Functionally Gradient Materials. *Isij International*, 30(9):699–703, 1990. ISSN 09151559. doi: 10.2355/isijinternational.30.699.
- [78] K. B. Hazlehurst, C. J. Wang, and M. Stanford. An investigation into the flexural characteristics of functionally graded cobalt chrome femoral stems manufactured using selective laser melting. *Materials and Design*, 60:177–183, 2014. ISSN 18734197. doi: 10.1016/j.matdes.2014.03.068. URL <http://dx.doi.org/10.1016/j.matdes.2014.03.068>.
- [79] Y. Li, Z. Feng, L. Hao, L. Huang, C. Xin, Y. Wang, E. Bilotti, K. Essa, H. Zhang, Z. Li, F. Yan, and T. Peijs. A Review on Functionally Graded Materials and Structures via Additive Manufacturing: From Multi-Scale Design to Versatile Functional Properties, 2020. ISSN 2365709X.
- [80] R. M. Mahamood and E. T. Akinlabi. *Functionally graded materials*. Springer, 2017.
- [81] V. Bhavar, P. Kattire, S. Thakare, S. Patil, and R. K. Singh. A Review on Functionally Gradient Materials (FGMs) and Their Applications. *IOP Conference Series: Materials Science and Engineering*, 229(1), 2017. ISSN 1757899X. doi: 10.1088/1757-899X/229/1/012021.
- [82] V. A. Popovich, E. V. Borisov, A. A. Popovich, V. S. Sufiiarov, D. V. Masaylo, and L. Alzina. Functionally graded Inconel 718 processed by additive manufacturing: Crystallographic texture, anisotropy of microstructure and mechanical properties. *Materials and Design*, 2017. ISSN 18734197. doi: 10.1016/j.matdes.2016.10.075.
- [83] B. Zhang, P. Jaiswal, R. Rai, and S. Nelaturi. Additive manufacturing of functionally graded objects: A review. In *Proceedings of the ASME 2016 International Design Engineering Technical Conferences and Computers and Information in Engineering Conference*, 2016.
- [84] T. P. Rajan and B. C. Pai. Developments in processing of functionally gradient metals and metal-ceramic composites: A review, 2014. ISSN 21941289.

- [85] R. Gabbrielli, I. G. Turner, and C. R. Bowen. Development of modelling methods for materials to be used as bone substitutes. *Key Engineering Materials*, 361-363 II:901–906, 2008. ISSN 10139826. doi: 10.4028/www.scientific.net/KEM.361-363.903. URL <http://opus.bath.ac.uk/1447/>.
- [86] A. Radman, X. Huang, and Y. M. Xie. Topology optimization of functionally graded cellular materials. *Journal of Materials Science*, 48(4):1503–1510, 2013. ISSN 00222461. doi: 10.1007/s10853-012-6905-1.
- [87] A. Biswas, V. Shapiro, and I. Tsukanov. Heterogeneous material modeling with distance fields. *Computer Aided Geometric Design*, 2004. ISSN 01678396. doi: 10.1016/j.cagd.2003.08.002.
- [88] X. Kou. *Computer-aided Design of Heterogeneous Objects*. PhD thesis, University of Hong Kong, 2006.
- [89] K.-H. Shin and D. Dutta. Constructive Representation of Heterogeneous Objects. *Journal of Computing and Information Science in Engineering*, 1(3):205, 2001. ISSN 15309827. doi: 10.1115/1.1403448. URL <http://computingengineering.asmedigitalcollection.asme.org/article.aspx?articleid=1399232>.
- [90] S. Suresh and A. Mortensen. Functionally graded metals and metal-ceramic composites: Part 2 Thermomechanical behaviour. *International Materials Reviews*, 42(3):85–116, 1997. doi: 10.1179/imr.1997.42.3.85. URL <https://doi.org/10.1179/imr.1997.42.3.85>.
- [91] P. Alfeld. Multivariate Perpendicular Interpolation. *SIAM Journal on Numerical Analysis*, 22(1):95 – 106, 1985.
- [92] V. Kumar, D. Burns, D. Dutta, and C. Hoffmann. A framework for object modeling. *Computer-Aided Design*, 31(9):541–556, 1999. ISSN 0010-4485. doi: [https://doi.org/10.1016/S0010-4485\(99\)00051-2](https://doi.org/10.1016/S0010-4485(99)00051-2). URL <http://www.sciencedirect.com/science/article/pii/S0010448599000512>.
- [93] E. L. Doubrovski, E. Y. Tsai, D. Dikovsky, J. M. P. Geraedts, H. Herr, and N. Oxman. Voxel-based fabrication through material property mapping: A design method for bitmap printing. *Computer-Aided Design*, 60:3–13, 2015. ISSN 0010-4485. doi: <https://doi.org/10.1016/j.cad.2014.05.010>. URL <http://www.sciencedirect.com/science/article/pii/S0010448514001067>.
- [94] T. Jackson. *Analysis of FGM Object Representation Methods*. PhD thesis, Massachusetts Institute of Technology, 2000.

- [95] M. Naebe and K. Shirvanimoghaddam. Functionally graded materials: A review of fabrication and properties, 2016. ISSN 23529407.
- [96] A. Gupta and M. Talha. Recent development in modeling and analysis of functionally graded materials and structures, 2015. ISSN 03760421.
- [97] T. Hirai. CVD Processing. *MRS Bulletin*, 20(1):45–47, 1995. doi: 10.1557/S0883769400048946.
- [98] M. Jain, R. K. Sadangi, W. R. Cannon, and B. H. Kear. Processing of functionally graded WC/Co/diamond nanocomposites. *Scripta Materialia*, 44(8):2099–2103, 2001. ISSN 1359-6462. doi: [https://doi.org/10.1016/S1359-6462\(01\)00882-X](https://doi.org/10.1016/S1359-6462(01)00882-X). URL <http://www.sciencedirect.com/science/article/pii/S135964620100882X>.
- [99] M. Kawase, T. Tago, M. Kurosawa, H. Utsumi, and K. Hashimoto. Chemical vapor infiltration and deposition to produce a silicon carbide–carbon functionally gradient material. *Chemical Engineering Science*, 54(15):3327–3334, 1999. ISSN 0009-2509. doi: [https://doi.org/10.1016/S0009-2509\(98\)00391-1](https://doi.org/10.1016/S0009-2509(98)00391-1). URL <http://www.sciencedirect.com/science/article/pii/S0009250998003911>.
- [100] M. R. Dorfman. Thermal spray applications, Part IV. *Advanced Materials and Processes*, 160(10):66–68, 2002. URL <https://www.scopus.com/inward/record.uri?eid=2-s2.0-0036803619&partnerID=40&md5=0cacfaebace83714784b299c95c0fe9c>.
- [101] K. H. Choi, H.-S. Kim, C. H. Park, G.-H. Kim, K. H. Baik, S. H. Lee, T. Kim, and H. S. Kim. High-temperature thermo-mechanical behavior of functionally graded materials produced by plasma sprayed coating: Experimental and modeling results. *Metals and Materials International*, 22(5):817–824, sep 2016. ISSN 2005-4149. doi: 10.1007/s12540-016-6110-x. URL <https://doi.org/10.1007/s12540-016-6110-x>.
- [102] C. Pan and B. Chen. Formation of the deformation twinning in austenitic stainless steel weld metal. *Journal of Materials Science Letters*, 14(24):1798–1800, jan 1995. ISSN 1573-4811. doi: 10.1007/BF00271011. URL <https://doi.org/10.1007/BF00271011>.
- [103] C. Hu. Technical Handbook for Surface Treatment, 1997.
- [104] K. A. Khor and Y. W. Gu. Effects of residual stress on the performance of plasma sprayed functionally graded ZrO₂/NiCoCrAlY coatings. *Materials Science and Engineering: A*, 277(1):64–76, 2000. ISSN 0921-5093. doi: [https://doi.org/10.1016/S0921-5093\(00\)00064-7](https://doi.org/10.1016/S0921-5093(00)00064-7).

1016/S0921-5093(99)00565-1. URL <http://www.sciencedirect.com/science/article/pii/S0921509399005651>.

- [105] V. Cannillo, L. Lusvardi, and A. Sola. Production and characterization of plasma-sprayed TiO₂-hydroxyapatite functionally graded coatings. *Journal of the European Ceramic Society*, 28(11):2161–2169, 2008. ISSN 0955-2219. doi: <https://doi.org/10.1016/j.jeurceramsoc.2008.02.026>. URL <http://www.sciencedirect.com/science/article/pii/S095522190800109X>.
- [106] M. Ivosevic, R. Knight, S. R. Kalidindi, G. R. Palmese, and J. K. Sutter. Adhesive/cohesive properties of thermally sprayed functionally graded coatings for polymer matrix composites. *Journal of Thermal Spray Technology*, 14(1):45–51, mar 2005. ISSN 1544-1016. doi: [10.1361/10599630522765](https://doi.org/10.1361/10599630522765). URL <https://doi.org/10.1361/10599630522765>.
- [107] Y. Watanabe, N. Yamanaka, and Y. Fukui. Control of composition gradient in a metal-ceramic functionally graded material manufactured by the centrifugal method. *Composites Part A: Applied Science and Manufacturing*, 29(5):595–601, 1998. ISSN 1359-835X. doi: [https://doi.org/10.1016/S1359-835X\(97\)00121-8](https://doi.org/10.1016/S1359-835X(97)00121-8). URL <http://www.sciencedirect.com/science/article/pii/S1359835X97001218>.
- [108] Y. Watanabe and Y. Fukui. Microstructures and mechanical properties of functionally graded materials fabricated by a centrifugal method. *Rec. Res. Devel. Metall. Mater. Sci.*, 4:51–93, 2000.
- [109] A. G. Arsha, E. Jayakumar, T. P. D. Rajan, V. Antony, and B. C. Pai. Design and fabrication of functionally graded in-situ aluminium composites for automotive pistons. *Materials & Design*, 88:1201–1209, 2015. ISSN 0264-1275. doi: <https://doi.org/10.1016/j.matdes.2015.09.099>. URL <http://www.sciencedirect.com/science/article/pii/S0264127515305074>.
- [110] S. Put, J. Vleugels, G. Anné, and O. V. der Biest. Functionally graded ceramic and ceramic-metal composites shaped by electrophoretic deposition. *Colloids and Surfaces A: Physicochemical and Engineering Aspects*, 222(1):223–232, 2003. ISSN 0927-7757. doi: [https://doi.org/10.1016/S0927-7757\(03\)00227-9](https://doi.org/10.1016/S0927-7757(03)00227-9). URL <http://www.sciencedirect.com/science/article/pii/S0927775703002279>.
- [111] P. X. Fu, X. H. Kang, Y. C. Ma, K. Liu, D. Z. Li, and Y. Y. Li. Centrifugal casting of TiAl exhaust valves. *Intermetallics*, 16(2):130–138, 2008. ISSN 0966-9795. doi: <https://doi.org/10.1016/j.intermet.2007.08.007>. URL <http://www.sciencedirect.com/science/article/pii/S0966979507001768>.

- [112] L. Lajoie and M. Suery. MODELLING OF PARTICLE SEGREGATION DURING CENTRIFUGAL CASTING OF Al-MATRIX COMPOSITES. In *Cast reinforced metal composites: proceedings of the International Symposium on Advances in Cast Reinforced Metal Composites: held in conjunction with 1988 World Materials Congress, Chicago, Illinois, USA, 24-30 September 1988*, page 15. ASM International, 1988.
- [113] L. Drenchev, J. Sobczak, S. Malinov, and W. Sha. Numerical simulation of macrostructure formation in centrifugal casting of particle reinforced metal matrix composites. Part 1: model description. *Modelling and Simulation in Materials Science and Engineering*, 11(4):635–649, jun 2003. doi: 10.1088/0965-0393/11/4/314. URL <https://doi.org/10.1088/0965-0393/11/4/314>.
- [114] L. Drenchev, J. Sobczak, S. Malinov, and W. Sha. Numerical simulation of macrostructure formation in centrifugal casting of particle reinforced metal matrix composites. Part 2: simulations and practical applications. *Modelling and Simulation in Materials Science and Engineering*, 11(4):651–674, jun 2003. doi: 10.1088/0965-0393/11/4/315. URL <https://doi.org/10.1088/0965-0393/11/4/315>.
- [115] J. W. Gao and C. Y. Wang. Modeling the solidification of functionally graded materials by centrifugal casting. *Materials Science and Engineering: A*, 292(2):207–215, 2000. ISSN 0921-5093. doi: [https://doi.org/10.1016/S0921-5093\(00\)01014-5](https://doi.org/10.1016/S0921-5093(00)01014-5). URL <http://www.sciencedirect.com/science/article/pii/S0921509300010145>.
- [116] T. P. D. Rajan, R. M. Pillai, and B. C. Pai. Characterization of centrifugal cast functionally graded aluminum-silicon carbide metal matrix composites. *Materials Characterization*, 61(10):923–928, 2010. ISSN 1044-5803. doi: <https://doi.org/10.1016/j.matchar.2010.06.002>. URL <http://www.sciencedirect.com/science/article/pii/S1044580310001853>.
- [117] Y. FUKUI. Fundamental Investigation of Functionally Gradient Material Manufacturing System using Centrifugal Force. *JSME international journal. Ser. 3, Vibration, control engineering, engineering for industry*, 34(1):144–148, 1991. doi: 10.1299/jsmec1988.34.144.
- [118] R. Mahmoodian, M. A. Hassan, M. Hamdi, R. Yahya, and R. G. Rahbari. In situ TiC–Fe–Al₂O₃–TiAl/Ti₃Al composite coating processing using centrifugal assisted combustion synthesis. *Composites Part B: Engineering*, 59:279–284, 2014.

- ISSN 1359-8368. doi: <https://doi.org/10.1016/j.compositesb.2013.12.016>. URL <http://www.sciencedirect.com/science/article/pii/S1359836813007464>.
- [119] X.-H. Zhang, J.-C. Han, S.-Y. Du, and J. V. Wood. Microstructure and mechanical properties of TiC-Ni functionally graded materials by simultaneous combustion synthesis and compaction. *Journal of Materials Science*, 35(8): 1925–1930, apr 2000. ISSN 1573-4803. doi: 10.1023/A:1004714402128. URL <https://doi.org/10.1023/A:1004714402128>.
- [120] I. J. Shon and Z. A. Munir. Synthesis of TiC, TiC-Cu composites, and TiC-Cu functionally graded materials by electrothermal combustion. *Journal of the American Ceramic Society*, 81(12):3243–3248, 1998. ISSN 00027820. doi: 10.1111/j.1151-2916.1998.tb02762.x.
- [121] D. E. Burkes and J. J. Moore. Microstructure and kinetics of a functionally graded NiTi–TiC_x composite produced by combustion synthesis. *Journal of Alloys and Compounds*, 430(1):274–281, 2007. ISSN 0925-8388. doi: <https://doi.org/10.1016/j.jallcom.2006.05.008>. URL <http://www.sciencedirect.com/science/article/pii/S0925838806004968>.
- [122] L. Besra and M. Liu. A review on fundamentals and applications of electrophoretic deposition (EPD). *Progress in Materials Science*, 52(1):1–61, 2007. ISSN 0079-6425. doi: <https://doi.org/10.1016/j.pmatsci.2006.07.001>. URL <http://www.sciencedirect.com/science/article/pii/S0079642506000387>.
- [123] D. M. Hulbert, A. Anders, D. V. Dudina, J. Andersson, D. Jiang, C. Unuvar, U. Anselmi-Tamburini, E. J. Lavernia, and A. K. Mukherjee. The Absence of Plasma in “Spark Plasma Sintering”. *Journal of Applied Physics*, 2008.
- [124] X. Tang, H. Zhang, D. Du, D. Qu, C. Hu, R. Xie, and Y. Feng. Fabrication of W–Cu functionally graded material by spark plasma sintering method. *International Journal of Refractory Metals and Hard Materials*, 42:193–199, 2014. ISSN 0263-4368. doi: <https://doi.org/10.1016/j.ijrmhm.2013.09.005>. URL <http://www.sciencedirect.com/science/article/pii/S0263436813001947>.
- [125] Z. Zhang, X. Shen, C. Zhang, S. Wei, S. Lee, and F. Wang. A new rapid route to in-situ synthesize TiB–Ti system functionally graded materials using spark plasma sintering method. *Materials Science and Engineering: A*, 565:326–332, 2013. ISSN 0921-5093. doi: <https://doi.org/10.1016/j.msea.2012.12.060>. URL <http://www.sciencedirect.com/science/article/pii/S0921509312017595>.
- [126] C.-Q. Hong, X.-H. Zhang, W.-J. Li, J.-C. Han, and S.-H. Meng. A novel functionally graded material in the ZrB₂–SiC and ZrO₂ system by spark plasma

- sintering. *Materials Science and Engineering: A*, 498(1):437–441, 2008. ISSN 0921-5093. doi: <https://doi.org/10.1016/j.msea.2008.08.032>. URL <http://www.sciencedirect.com/science/article/pii/S0921509308010460>.
- [127] S.-H. Lee, H. Tanaka, and Y. Kagawa. Spark plasma sintering and pressureless sintering of SiC using aluminum borocarbide additives. *Journal of the European Ceramic Society*, 29(10):2087–2095, 2009. ISSN 0955-2219. doi: <https://doi.org/10.1016/j.jeurceramsoc.2008.12.006>. URL <http://www.sciencedirect.com/science/article/pii/S0955221908006109>.
- [128] Z. Qiao, J. Räthel, L.-M. Berger, and M. Herrmann. Investigation of binderless WC–TiC–Cr₃C₂ hard materials prepared by spark plasma sintering (SPS). *International Journal of Refractory Metals and Hard Materials*, 38:7–14, 2013. ISSN 0263-4368. doi: <https://doi.org/10.1016/j.ijrmhm.2012.12.002>. URL <http://www.sciencedirect.com/science/article/pii/S0263436812002247>.
- [129] J. J. Sobczak and L. Drenchev. Metallic Functionally Graded Materials: A Specific Class of Advanced Composites. *Journal of Materials Science & Technology*, 29(4):297–316, 2013. ISSN 1005-0302. doi: <https://doi.org/10.1016/j.jmst.2013.02.006>. URL <http://www.sciencedirect.com/science/article/pii/S1005030213000340>.
- [130] M. Eriksson, M. Radwan, and Z. Shen. Spark plasma sintering of WC, cemented carbide and functional graded materials. *International Journal of Refractory Metals and Hard Materials*, 36:31–37, 2013. ISSN 0263-4368. doi: <https://doi.org/10.1016/j.ijrmhm.2012.03.007>. URL <http://www.sciencedirect.com/science/article/pii/S0263436812000571>.
- [131] J. H. Yu, C. B. Wang, Q. Shen, and L. M. Zhang. Preparation and properties of Si_p/Al composites by spark plasma sintering. *Materials & Design*, 41:198–202, 2012. ISSN 0261-3069. doi: <https://doi.org/10.1016/j.matdes.2012.05.007>. URL <http://www.sciencedirect.com/science/article/pii/S0261306912003081>.
- [132] M. Nemat-Alla, M., M. H. Ata, M. R. Bayoumi, and W. Khair-Eldeen. Powder Metallurgical Fabrication and Microstructural Investigations of Aluminum/Steel Functionally Graded Material. *Materials Sciences and Applications*, 2(12):1708–1718, 2011.
- [133] F. Watari, A. Yokoyama, H. Matsuno, R. Miyao, M. Uo, T. Kawasaki, M. Omori, and T. Hirai. Fabrication of Functionally Graded Implant and Its Biocompatibility. *Functionally Graded Materials in the 21st Century: A Workshop on Trends and Forecasts*, pages 187–190, 2001.

- [134] G. Jin, M. Takeuchi, S. Honda, T. Nishikawa, and H. Awaji. Properties of multilayered mullite/Mo functionally graded materials fabricated by powder metallurgy processing. *Materials Chemistry and Physics*, 89(2):238–243, 2005. ISSN 0254-0584. doi: <https://doi.org/10.1016/j.matchemphys.2004.03.031>. URL <http://www.sciencedirect.com/science/article/pii/S0254058404001762>.
- [135] R. Yamanoglu, I. Daoud, and E. A. Olevsky. Spark plasma sintering versus hot pressing – densification, bending strength, microstructure, and tribological properties of Ti₅Al_{2.5}Fe alloys. *Powder Metallurgy*, 61(2):178–186, 2018. doi: 10.1080/00325899.2018.1441777. URL <https://doi.org/10.1080/00325899.2018.1441777>.
- [136] A. Kawasaki and R. Watanabe. Evaluation of thermomechanical performance for thermal barrier type of sintered functionally graded materials. *Composites Part B: Engineering*, 28(1):29–35, 1997. ISSN 1359-8368. doi: [https://doi.org/10.1016/S1359-8368\(96\)00017-0](https://doi.org/10.1016/S1359-8368(96)00017-0). URL <http://www.sciencedirect.com/science/article/pii/S1359836896000170>.
- [137] P. Popoola, O. Fatoba, O. Popoola, and G. Farotade. Laser Engineering Net Shaping Method in the Area of Development of Functionally Graded Materials (FGMs) for Aero Engine Applications - A Review. *Fiber Laser*, 2:64, 2016. ISSN 00093084. doi: 10.5772/32009.
- [138] X. Deng, Y. Wang, J. Yan, T. Liu, and S. Wang. Topology Optimization of Total Femur Structure: Application of Parameterized Level Set Method Under Geometric Constraints. *Journal of Mechanical Design*, 2015. ISSN 1050-0472. doi: 10.1115/1.4031803.
- [139] M. G. Rashed, M. Ashraf, R. A. W. Mines, and P. J. Hazell. Metallic microlattice materials: A current state of the art on manufacturing, mechanical properties and applications. *Materials & Design*, 95:518–533, 2016. ISSN 0264-1275. doi: <https://doi.org/10.1016/j.matdes.2016.01.146>. URL <http://www.sciencedirect.com/science/article/pii/S0264127516301447>.
- [140] E. Brandl, C. Leyens, and F. Palm. Mechanical properties of additive manufactured Ti-6Al-4V using wire and powder based processes. In *IOP Conference Series: Materials Science and Engineering*, volume 26, pages 1–10. IOP Publishing, 2011.
- [141] ASTM International. ASTM International Technical Committee F42 on Additive Manufacturing Technologies, 2013. URL <http://www.astm.org/COMMIT/F42{ }Fact{ }Sheet{ }2015.pdf>.

- [142] S. L. Sing, Y. Miao, F. E. Wiria, and W. Y. Yeong. Manufacturability and mechanical testing considerations of metallic scaffolds fabricated using selective laser melting: a review. *Biomedical Science and Engineering*, 2(11), 2016. doi: 10.4081/bse.2016.11.
- [143] S. M. Ahmadi, R. Hedayati, R. K. A. K. Jain, Y. Li, S. Leeftang, and A. A. Zadpoor. Effects of laser processing parameters on the mechanical properties, topology, and microstructure of additively manufactured porous metallic biomaterials: A vector-based approach. *Materials & Design*, 134:234–243, 2017. ISSN 0264-1275. doi: <https://doi.org/10.1016/j.matdes.2017.08.046>. URL <http://www.sciencedirect.com/science/article/pii/S0264127517307980>.
- [144] I. Shishkovsky, F. Missemer, and I. Smurov. Direct Metal Deposition of Functional Graded Structures in Ti- Al System. *Physics Procedia*, 39:382–391, 2012. ISSN 1875-3892. doi: <https://doi.org/10.1016/j.phpro.2012.10.052>. URL <http://www.sciencedirect.com/science/article/pii/S1875389212025795>.
- [145] J. M. Wilson and Y. C. Shin. Microstructure and wear properties of laser-deposited functionally graded Inconel 690 reinforced with TiC. *Surface and Coatings Technology*, 207:517–522, 2012. ISSN 0257-8972. doi: <https://doi.org/10.1016/j.surfcoat.2012.07.058>. URL <http://www.sciencedirect.com/science/article/pii/S0257897212007487>.
- [146] K. V. Wong and A. Hernandez. A Review of Additive Manufacturing, 2012. ISSN 2090-5130.
- [147] J. M. Smith. Method and apparatus for creating three-dimensional objects by cross-sectional lithography, 2002. URL <https://www.google.com/patents/US6500378>.
- [148] H. Kim, J.-W. Choi, and R. Wicker. Scheduling and process planning for multiple material stereolithography. *Rapid Prototyping Journal*, 16(4):232–240, 2010. ISSN 1355-2546. doi: 10.1108/13552541011049243.
- [149] I. Gibson, D. W. Rosen, and B. Stucker. *Additive manufacturing technologies: Rapid prototyping to direct digital manufacturing*. Springer, 2010. ISBN 9781441911193. doi: 10.1007/978-1-4419-1120-9.
- [150] L. Thijs, F. Verhaeghe, T. Craeghs, J. V. Humbeeck, and J. P. Kruth. A study of the microstructural evolution during selective laser melting of Ti-6Al-4V. *Acta Materialia*, 58(9):3303–3312, 2010. ISSN 13596454. doi: 10.1016/j.actamat.2010.02.004. URL <http://dx.doi.org/10.1016/j.actamat.2010.02.004>.

- [151] D. Wang, Y. Yang, Z. Yi, and X. Su. Research on the fabricating quality optimization of the overhanging surface in SLM process. *The International Journal of Advanced Manufacturing Technology*, 65(9-12):1471–1484, 2013.
- [152] M. Balažić. Additive Manufacturing and 3D Printing LENS Technology. *EFESTO LLC*, nov 2013.
- [153] D. Gill. Laser Engineered Net Shaping. *Sandia National Laboratories*, 2002.
- [154] S. H. Mok, G. Bi, J. Folkes, and I. Pashby. Deposition of Ti-6Al-4V using a high power diode laser and wire, Part I: Investigation on the process characteristics. *Surface and Coatings Technology*, 202(16):3933–3939, 2008. ISSN 02578972. doi: 10.1016/j.surfcoat.2008.02.008.
- [155] S. H. Mok, I. Pashby, and J. Segal. Studies on the microstructures and mechanical properties of Ti-6Al-2Sn-4Zr-2Mo produced by direct laser deposition. In *3rd International WLT-conference on lasers in manufacturing, Munich*, pages 773–776, 2005.
- [156] B. Baufeld, E. Brandl, and O. Van Der Biest. Wire based additive layer manufacturing: Comparison of microstructure and mechanical properties of Ti-6Al-4V components fabricated by laser-beam deposition and shaped metal deposition. *Journal of Materials Processing Technology*, 211(6):1146–1158, 2011. ISSN 09240136. doi: 10.1016/j.jmatprotec.2011.01.018. URL <http://dx.doi.org/10.1016/j.jmatprotec.2011.01.018>.
- [157] A. Sola, D. Bellucci, and V. Cannillo. Functionally graded materials for orthopedic applications – an update on design and manufacturing. *Biotechnology Advances*, 34(5):504–531, 2016. ISSN 0734-9750. doi: <https://doi.org/10.1016/j.biotechadv.2015.12.013>. URL <http://www.sciencedirect.com/science/article/pii/S0734975015300689>.
- [158] M. Mahbod and M. Asgari. Elastic and plastic characterization of a new developed additively manufactured functionally graded porous lattice structure: Analytical and numerical models. *International Journal of Mechanical Sciences*, 155 (February):248–266, 2019. ISSN 00207403. doi: 10.1016/j.ijmecsci.2019.02.041. URL <https://doi.org/10.1016/j.ijmecsci.2019.02.041>.
- [159] S. Yu, J. Sun, and J. Bai. Investigation of functionally graded TPMS structures fabricated by additive manufacturing. *Materials and Design*, 182:108021, 2019. ISSN 18734197. doi: 10.1016/j.matdes.2019.108021. URL <https://doi.org/10.1016/j.matdes.2019.108021>.

- [160] R. B. Wicker and E. W. MacDonald. Multi-material, multi-technology stereolithography. *Virtual and Physical Prototyping*, 7(January 2015):181–194, 2012. ISSN 1745-2759. doi: 10.1080/17452759.2012.721119.
- [161] L. Ren, Z. Song, H. Liu, Q. Han, C. Zhao, B. Derby, Q. Liu, and L. Ren. 3D printing of materials with spatially non-linearly varying properties. *Materials and Design*, 156:470–479, 2018. ISSN 18734197. doi: 10.1016/j.matdes.2018.07.012. URL <https://doi.org/10.1016/j.matdes.2018.07.012>.
- [162] D. Kokkinis, F. Bouville, and A. R. Studart. 3D Printing of Materials with Tunable Failure via Bioinspired Mechanical Gradients. *Advanced Materials*, 30(19):1–9, 2018. ISSN 15214095. doi: 10.1002/adma.201705808.
- [163] H. L. Tekinalp, V. Kunc, G. M. Velez-Garcia, C. E. Duty, L. J. Love, A. K. Naskar, C. A. Blue, and S. Ozcan. Highly oriented carbon fiber–polymer composites via additive manufacturing. *Composites Science and Technology*, 105:144–150, 2014. ISSN 02663538. doi: 10.1016/j.compscitech.2014.10.009. URL <http://www.sciencedirect.com/science/article/pii/S0266353814003716>.
- [164] F. Ning, W. Cong, J. Qiu, J. Wei, and S. Wang. Additive manufacturing of carbon fiber reinforced thermoplastic composites using fused deposition modeling. *Composites Part B: Engineering*, 80:369–378, 2015. ISSN 13598368. doi: 10.1016/j.compositesb.2015.06.013. URL <http://www.sciencedirect.com/science/article/pii/S1359836815003777>.
- [165] Y. Li, H. Jahr, P. Pavanram, F. S. Bobbert, U. Puggi, X. Y. Zhang, B. Pouran, M. A. Leeflang, H. Weinans, J. Zhou, and A. A. Zadpoor. Additively manufactured functionally graded biodegradable porous iron. *Acta Biomaterialia*, 96:646–661, 2019. ISSN 18787568. doi: 10.1016/j.actbio.2019.07.013.
- [166] D. S. Al-Saedi, S. H. Masood, M. Faizan-Ur-Rab, A. Alomarah, and P. Ponnusamy. Mechanical properties and energy absorption capability of functionally graded F2BCC lattice fabricated by SLM. *Materials and Design*, 2018. ISSN 18734197. doi: 10.1016/j.matdes.2018.01.059.
- [167] Z. H. Liu, D. Q. Zhang, S. L. Sing, C. K. Chua, and L. E. Loh. Interfacial characterization of SLM parts in multi-material processing: Metallurgical diffusion between 316L stainless steel and C18400 copper alloy. *Materials Characterization*, 94:116–125, 2014. ISSN 10445803. doi: 10.1016/j.matchar.2014.05.001. URL <http://dx.doi.org/10.1016/j.matchar.2014.05.001>.
- [168] C. Tan, K. Zhou, and T. Kuang. Selective laser melting of tungsten-copper functionally graded material. *Materials Letters*, 237:328–331, 2019. ISSN 18734979.

doi: 10.1016/j.matlet.2018.11.127. URL <https://doi.org/10.1016/j.matlet.2018.11.127>.

- [169] L. Yan, Y. Chen, and F. Liou. Additive manufacturing of functionally graded metallic materials using laser metal deposition, 2020. ISSN 22148604.
- [170] C. Zhang, F. Chen, Z. Huang, M. Jia, G. Chen, Y. Ye, Y. Lin, W. Liu, B. Chen, Q. Shen, L. Zhang, and E. J. Lavernia. Additive manufacturing of functionally graded materials: A review. *Materials Science and Engineering A*, 764(August): 138209, 2019. ISSN 09215093. doi: 10.1016/j.msea.2019.138209. URL <https://doi.org/10.1016/j.msea.2019.138209>.
- [171] J. ZHU, H. ZHOU, C. WANG, L. ZHOU, S. YUAN, and W. ZHANG. A review of topology optimization for additive manufacturing: Status and challenges, 2021. ISSN 10009361.
- [172] J. S. Zuback, T. A. Palmer, and T. DebRoy. Additive manufacturing of functionally graded transition joints between ferritic and austenitic alloys. *Journal of Alloys and Compounds*, 2019. ISSN 09258388. doi: 10.1016/j.jallcom.2018.08.197.
- [173] D. K. Kim, W. Woo, E. Y. Kim, and S. H. Choi. Microstructure and mechanical characteristics of multi-layered materials composed of 316L stainless steel and ferritic steel produced by direct energy deposition. *Journal of Alloys and Compounds*, 774:896–907, 2019. ISSN 09258388. doi: 10.1016/j.jallcom.2018.09.390. URL <https://doi.org/10.1016/j.jallcom.2018.09.390>.
- [174] L. D. Bobbio, B. Bocklund, R. Otis, J. P. Borgonia, R. P. Dillon, A. A. Shapiro, B. McEnerney, Z.-K. Liu, and A. M. Beese. Characterization of a functionally graded material of ti-6al-4v to 304l stainless steel with an intermediate v section. *Journal of Alloys and Compounds*, 742:1031–1036, 2018.
- [175] Y. Su, B. Chen, C. Tan, X. Song, and J. Feng. Influence of composition gradient variation on the microstructure and mechanical properties of 316L/Inconel718 functionally graded material fabricated by laser additive manufacturing. *Journal of Materials Processing Technology*, 283(January), 2020. ISSN 09240136. doi: 10.1016/j.jmatprotec.2020.116702.
- [176] T. Liu, S. Guessasma, J. Zhu, W. Zhang, and S. Belhabib. Functionally graded materials from topology optimisation and stereolithography. *European Polymer Journal*, 2018. ISSN 00143057. doi: 10.1016/j.eurpolymj.2018.08.038.
- [177] Y. Zhang and A. Bandyopadhyay. Direct fabrication of compositionally graded Ti-Al₂O₃ multi-material structures using Laser Engineered Net Shaping. *Ad-*

- ditive Manufacturing*, 21(March):104–111, 2018. ISSN 22148604. doi: 10.1016/j.addma.2018.03.001. URL <https://doi.org/10.1016/j.addma.2018.03.001>.
- [178] J. Zhang, Y. Zhang, W. Li, S. Karnati, F. Liou, and J. W. Newkirk. Microstructure and properties of functionally graded materials ti6al4v/tic fabricated by direct laser deposition. *Rapid Prototyping Journal*, 2018.
- [179] S. Chandrasekaran, S. Hari, and M. Amirthalingam. Wire arc additive manufacturing of functionally graded material for marine risers. *Materials Science and Engineering A*, 792, aug 2020. ISSN 09215093. doi: 10.1016/j.msea.2020.139530.
- [180] A. Reichardt, A. A. Shapiro, R. Otis, R. P. Dillon, J. P. Borgonia, B. W. McEnerney, P. Hosemann, and A. M. Beese. Advances in additive manufacturing of metal-based functionally graded materials. *International Materials Reviews*, 66(1):1–29, 2021. ISSN 17432804. doi: 10.1080/09506608.2019.1709354.
- [181] B. Saleh, J. Jiang, R. Fathi, T. Al-hababi, Q. Xu, L. Wang, D. Song, and A. Ma. 30 Years of functionally graded materials: An overview of manufacturing methods, Applications and Future Challenges, nov 2020. ISSN 13598368.
- [182] M. Baumers and M. Holweg. Cost impact of the risk of build failure in laser sintering. *Solid Freeform Fabrication 2016: Proceedings of the 27th Annual International Solid Freeform Fabrication Symposium - An Additive Manufacturing Conference, SFF 2016*, 1910:1910–1921, 2016.
- [183] C. Lindemann, U. Jahnke, M. Moi, R. Koch, et al. Analyzing product lifecycle costs for a better understanding of cost drivers in additive manufacturing. In *23th Annual International Solid Freeform Fabrication Symposium—An Additive Manufacturing Conference. Austin Texas USA 6th-8th August*, 2012.
- [184] G. Costabile, M. Fera, F. Fruggiero, A. Lambiase, and D. Pham. Cost models of additive manufacturing: A literature review. *International Journal of Industrial Engineering Computations*, 8(2):263–282, 2016. ISSN 19232934. doi: 10.5267/j.ijiec.2016.9.001.
- [185] M. Baumers, C. Tuck, R. Wildman, I. Ashcroft, E. Rosamond, and R. Hague. Transparency Built-in: Energy Consumption and Cost Estimation for Additive Manufacturing Baumers et al. Energy and Cost Estimation for Additive Manufacturing. *Journal of Industrial Ecology*, 17(3):418–431, 2013. ISSN 15309290. doi: 10.1111/j.1530-9290.2012.00512.x.
- [186] M. Baumers, L. Beltrametti, A. Gasparre, and R. Hague. Informing additive manufacturing technology adoption: total cost and the impact of capac-

- ity utilisation. *International Journal of Production Research*, 55(23):6957–6970, 2017. ISSN 1366588X. doi: 10.1080/00207543.2017.1334978. URL <https://doi.org/10.1080/00207543.2017.1334978>.
- [187] M. Baumers and M. Holweg. On the economics of additive manufacturing: Experimental findings. *Journal of Operations Management*, 65(8):794–809, 2019. ISSN 02726963. doi: 10.1002/joom.1053.
- [188] K. Fritz and I. Y. Kim. Simultaneous topology and build orientation optimization for minimization of additive manufacturing cost and time. *International Journal for Numerical Methods in Engineering*, 121(15):3442–3481, 2020. ISSN 10970207. doi: 10.1002/nme.6366.
- [189] N. Hopkinson and P. Dicknes. Analysis of rapid manufacturing—using layer manufacturing processes for production. *Proceedings of the Institution of Mechanical Engineers, Part C: Journal of Mechanical Engineering Science*, 217(1): 31–39, 2003.
- [190] M. Schröder, B. Falk, and R. Schmitt. Evaluation of cost structures of additive manufacturing processes using a new business model. *Procedia Cirp*, 30:311–316, 2015.
- [191] G. Manogharan, R. A. Wysk, and O. L. Harrysson. Additive manufacturing—integrated hybrid manufacturing and subtractive processes: economic model and analysis. *International Journal of Computer Integrated Manufacturing*, 29(5): 473–488, 2016.
- [192] Y. Yang and L. Li. Cost modeling and analysis for Mask Image Projection Stereolithography additive manufacturing: Simultaneous production with mixed geometries. *International Journal of Production Economics*, 206(August):146–158, 2018. ISSN 09255273. doi: 10.1016/j.ijpe.2018.09.023. URL <https://doi.org/10.1016/j.ijpe.2018.09.023>.
- [193] A. Z. A. Kadir, Y. Yusof, and M. S. Wahab. Additive manufacturing cost estimation models—a classification review. *The International Journal of Advanced Manufacturing Technology*, 107(9):4033–4053, 2020.
- [194] J. Liao and D. R. Cooper. The environmental impacts of metal powder bed additive manufacturing. *ASME 2020 15th International Manufacturing Science and Engineering Conference, MSEC 2020*, 1:1–15, 2020. doi: 10.1115/MSEC2020-8476.

- [195] T. Kamps, M. Lutter-Guenther, C. Seidel, T. Gutowski, and G. Reinhart. Cost- and energy-efficient manufacture of gears by laser beam melting. *CIRP Journal of Manufacturing Science and Technology*, 21:47–60, 2018. ISSN 17555817. doi: 10.1016/j.cirpj.2018.01.002. URL <https://doi.org/10.1016/j.cirpj.2018.01.002>.
- [196] R. E. Laureijs, J. B. Roca, S. P. Narra, C. Montgomery, J. L. Beuth, and E. R. Fuchs. Metal additive manufacturing: Cost competitive beyond low volumes. *Journal of Manufacturing Science and Engineering, Transactions of the ASME*, 139(8):1–9, 2017. ISSN 15288935. doi: 10.1115/1.4035420.
- [197] M. Baumers, P. Dickens, C. Tuck, and R. Hague. The cost of additive manufacturing: Machine productivity, economies of scale and technology-push. *Technological Forecasting and Social Change*, 102:193–201, 2016. ISSN 00401625. doi: 10.1016/j.techfore.2015.02.015. URL <http://dx.doi.org/10.1016/j.techfore.2015.02.015>.
- [198] S. Y. Choy, C. N. Sun, K. F. Leong, and J. Wei. Compressive properties of functionally graded lattice structures manufactured by selective laser melting. *Materials and Design*, 131(June):112–120, 2017. ISSN 18734197. doi: 10.1016/j.matdes.2017.06.006. URL <http://dx.doi.org/10.1016/j.matdes.2017.06.006>.
- [199] W. D. Pilkey and D. F. Pilkey. *Peterson’s Stress Concentration Factors, Third Edition*. John Wiley & Sons, 2008. ISBN 9780470048245. doi: 10.1002/9780470211106.
- [200] F. Kreith and E. B. Magrab. Mechanical Engineering Handbook, CD-ROM Version. *Journal of Mechanical Design*, 1999. ISSN 10500472. doi: 10.1115/1.2829421.
- [201] M. F. Ashby. Materials Selection in Mechanical Design. *Design*, page 624, 2005. ISSN 0148-6608. doi: 10.1016/B978-1-85617-663-7.00011-4. URL http://www.knovel.com/web/portal/browse/display?{}_EXT{}_KNOVEL{}_DISPLAY{}_bookid=1472.
- [202] P. Muller, P. Mognol, and J. Y. Hascoet. Modeling and control of a direct laser powder deposition process for Functionally Graded Materials (FGM) parts manufacturing. *Journal of Materials Processing Technology*, 213(5):685–692, 2013. ISSN 09240136. doi: 10.1016/j.jmatprotec.2012.11.020. URL <http://dx.doi.org/10.1016/j.jmatprotec.2012.11.020>.

- [203] J. Zhuang, D. Gu, L. Xi, K. Lin, Y. Fang, and R. Wang. Preparation method and underlying mechanism of mwcnts/ti6al4v nanocomposite powder for selective laser melting additive manufacturing. *Powder Technology*, 368:59–69, 2020.
- [204] R. F. Gibson. *Principles of Composite Material Mechanics*. CRC Press, 1994. ISBN 0824753895. URL <http://www.loc.gov/catdir/toc/ecip0714/2007013616.html>.
- [205] P. Muller, J.-Y. Hascoet, and P. Mognol. Toolpaths for additive manufacturing of functionally graded materials (FGM) parts. *Rapid Prototyping Journal*, 20(6):511–522, 2014. ISSN 1355-2546. doi: 10.1108/RPJ-01-2013-0011. URL <http://www.scopus.com/inward/record.url?eid=2-s2.0-84919764704-&partnerID=tZ0tx3y1>.
- [206] J. Jhabvala, E. Boillat, T. Antignac, and R. Glardon. On the effect of scanning strategies in the selective laser melting process. *Virtual and Physical Prototyping*, 2010. ISSN 17452759. doi: 10.1080/17452751003688368.
- [207] R. Mertens, S. Clijsters, K. Kempen, and J.-p. Kruth. Optimization of Scan Strategies in Selective Laser Melting of Aluminum Parts With Downfacing Areas. *Journal of Manufacturing Science and Engineering*, 136:1–7, 2014. doi: 10.1115/1.4028620.
- [208] J. Kranz, D. Herzog, and C. Emmelmann. Design guidelines for laser additive manufacturing of lightweight structures in TiAl6V4. *Journal of Laser Applications*, S14001(27):1–17, 2015. doi: 10.2351/1.4885235.
- [209] M. Langelaar. Topology optimization of 3D self-supporting structures for additive manufacturing. *Additive Manufacturing*, 12:60–70, 2016. ISSN 22148604. doi: 10.1016/j.addma.2016.06.010.
- [210] T. S. Hunnewell, K. L. Walton, S. Sharma, T. K. Ghosh, R. V. Tompson, D. S. Viswanath, and S. K. Loyalka. Total hemispherical emissivity of ss 316l with simulated very high temperature reactor surface conditions. *Nuclear Technology*, 198(3):293–305, 2017.
- [211] B. P. Keller, S. E. Nelson, K. L. Walton, T. K. Ghosh, R. V. Tompson, and S. K. Loyalka. Total hemispherical emissivity of inconel 718. *Nuclear Engineering and Design*, 287:11–18, 2015.
- [212] L. González-Fernández, E. Risueño, R. Pérez-Sáez, and M. Tello. Infrared normal spectral emissivity of ti-6al-4v alloy in the 500–1150 k temperature range. *Journal of alloys and compounds*, 541:144–149, 2012.

- [213] Z. Kim, H., Cong, W., Zhang, H-C., Liu. Laser Engineered Net Shaping of Nickel-Based Superalloy Inconel 718 Powders onto AISI 4140 Alloy. *Materials*, 10(341): 18, 2017. doi: 10.3390/ma10040341.
- [214] E. Toolbox. Emissivity Coefficients Materials, 2003. URL https://www.engineeringtoolbox.com/emissivity-coefficients-d_{ }447.html.
- [215] T. E. Abioye, J. Folkes, and A. T. Clare. Journal of Materials Processing Technology A parametric study of Inconel 625 wire laser deposition. *Journal of Materials Processing Tech.*, 213(12):2145–2151, 2013. ISSN 0924-0136. doi: 10.1016/j.jmatprotec.2013.06.007. URL <http://dx.doi.org/10.1016/j.jmatprotec.2013.06.007>.
- [216] T. E. Abioye, D. G. McCartney, and A. T. Clare. Journal of Materials Processing Technology Laser cladding of Inconel 625 wire for corrosion protection. *Journal of Materials Processing Tech.*, 217:232–240, 2015. ISSN 0924-0136. doi: 10.1016/j.jmatprotec.2014.10.024. URL <http://dx.doi.org/10.1016/j.jmatprotec.2014.10.024>.
- [217] B. Zhang, P. Jaiswal, R. Rai, and S. Nelaturi. Additive Manufacturing of Functionally Graded Material Objects: A Review, dec 2018. ISSN 15309827.
- [218] S. Dongare, T. E. Sparks, J. Newkirk, and F. Liou. A mechanical testing methodology for metal additive manufacturing processes. In *Annual international solid freeform fabrication symposium*, pages 224–242, 2014.